UNIVERSITY OF CALIFORNIA SAN DIEGO

Assessment of the Seismic Behavior of Fully and Partially Grouted Reinforced Masonry Structural Systems through Finite Element Analysis and Shake-Table Testing

A dissertation submitted in partial satisfaction of the requirements for the degree

Doctor of Philosophy

in

Structural Engineering

by

Andreas A. Koutras

Committee in charge:

Professor P. Benson Shing, Chair
Professor Joel P. Conte
Professor Raymond A. de Callafon
Professor Francesco Lanza di Scalea
Professor José I. Restrepo

2019

The Dissertation of Andreas A. Koutras is approved, and it is acceptable in quality and form for publication on microfilm and electronically:

_____

_____

_____

_____

_____

Chair

University of California San Diego

2019

TABLE OF CONTENTS

LIST OF FIGURES

LIST OF TABLES

ACKNOWLEDGEMENTS

The research presented in this dissertation was conducted under the supervision of Professor P. Benson Shing at the University of California San Diego. The work conducted on the numerical modeling of fully grouted reinforced masonry was funded by the Federal Emergency Management Agency (FEMA) under the project ATC-116 of the Applied Technology Council. The research presented on the investigation of the seismic behavior of partially grouted reinforced masonry was funded by the Network for Earthquake Engineering Simulation (NEES) program of the National Science Foundation (NSF) under Award No. 1208208. The support of the NEES operation funds for the shake-table tests conducted at the UC San Diego NEES facility is also gratefully acknowledged. The Education and Research Foundation of the National Concrete Masonry Association also provided generous financial support for the shake-table tests of the partially grouted masonry structures.

I would like to thank the Department of Structural Engineering for awarding me the graduate fellowship in the first year of my studies, and the dissertation fellowship in the last quarter of my studies. I am also thankful to the Gerondelis Foundation for the additional financial support provided. I am most grateful to the A.G. Leventis Foundation for the generous financial support provided through its Educational Grants Program for graduate studies.

I would like thank the members of my dissertation committee, Professors Joel P. Conte, Raymond A. de Callafon, Francesco Lanza di Scalea, and José I. Restrepo for providing useful suggestions for my dissertation and for their inspiring courses which were invaluable for my research and my personal development in engineering. I am grateful to Professors Conte and

Restrepo for their interest in the progress of my work and for their advices over the course of my studies at UC San Diego.

I would like to express my deepest gratitude and appreciation to my advisor, Professor P. Benson Shing. His wise guidance and encouragement have been a great support during my doctoral studies at UC San Diego. I want to thank him for giving me the opportunity to work with a person of his expertise and integrity.

I am also grateful to Professors George Gazetas and Christos Zeris of the National Technical University of Athens (NTUA) for serving as my academic advisors during my undergraduate studies and for supporting and encouraging my applications for graduate studies in the U.S. I also wish to express my gratitude and respect to all my professors at the Department of Civil Engineering of NTUA for their dedication in providing top-quality education and research in Civil Engineering.

I am deeply grateful to Professor Ioannis Koutromanos for his interest in my research, his constructive comments, and his precious support over the years. I would further like to acknowledge him along with Dr. Mohammadreza Moharrami for providing me the computer code of their constitutive model for reinforcing steel, which has been used in this study.

I would like express my sincere gratitude to my former colleagues and friends: Dr. Marios Mavros for sharing the bond-slip element formulation, Dr. Alexandra Kottari for sharing her implementation of the cohesive-crack interface law, and Professor Juan Murcia-Delso for providing me with his cyclic bond-slip material law. I am grateful for their contributions and their valuable comments on my research. I would also like to thank Professor Andreas Stavridis for his

interest and input in my work. Special thanks are due to my colleague Mr. Jianyu Cheng for the excellent collaboration we had in various projects.

I further wish to thank Professor Arturo E. Schultz and Ms. Catherine Johnson of the University of Minnesota at Twin Cities, Professor Ahmad Hamid of Drexel University, and Professor Mohammad Bolhassani, formerly a graduate student at Drexel University, for providing me with the data of the quasi-static tests that they had conducted on partially grouted masonry walls.

The contribution of RCP Brick and Block of San Diego for their generous donation of the concrete masonry units used in the construction of the shake-table test structures is also gratefully acknowledged.

I also wish to acknowledge the members of the project technical committee and project review panel of ATC -116 for their valuable comments and suggestions on our work. I also want to thank Dr. Greg Kingsley and his team at KL&A Inc. for providing the design and preparing the drawings of the two-story building archetype examined in this dissertation.

I am grateful to the invaluable technical support provided by the engineering staff at the Livermore Software and Technology Corporation (LSTC) for the implementation of the constitutive models and elements in LS-DYNA.

I would like to thank the technical staff members of the Englekirk Structural Engineering Center and the Powell Structural Laboratories of UC San Diego for their professionalism, cooperation, and help in conducting the shake-table tests presented in this study. I am also grateful to my colleagues, the faculty, and the staff of the Department of Structural Engineering I had the

pleasure to interact or work with, and especially to my friends Mr. Konstantinos Anagnostopoulos, Dr. Vasileios Papadopoulos, and Dr. George Moutsanidis.

I further want to express my gratitude to the Greek-American family of Vangelis (Evans) and Irene Mylonas, who have been expressing their kindness, solidarity, and support to me from the beginning of my stay in San Diego

Finally, I wish to thank my family, my father Alexandros A. Koutras, my mother Efstratia (Efy) Tsifoutidou, and my sister Eleni, for their constant support and encouragement throughout my life. It is to them that I dedicate this dissertation.

Parts of Chapters 1 through 3 are a reprint of the material that will appear in Chapter 4 of the technical report titled "Developing Solutions to the Short-Period Building Performance Paradox: Study for Reinforced Masonry Buildings", which will be submitted to the Federal Emergency Management Agency by the Applied Technology Council for the project number ATC-116. The authors of Chapter 4 in the report are: the author of this dissertation, Jianyu Cheng, and P. Benson Shing. The report chapter was prepared under the supervision of Dr. Charles A. Kircher, who was the technical director of the ATC-116 project. The author of this dissertation is the primary investigator and the author of all the materials covered in this dissertation.

Parts of Chapters 4 and 5, are a reprint of the material that appears in the manuscript "Koutras A, Shing PB. Seismic Behavior of a Partially Grouted Reinforced Masonry Structure: Shake-Table Testing and Numerical Analyses" which has been submitted for publication to the Journal of Earthquake Engineering and Structural Dynamics in 2019. The author of this dissertation was the primary investigator and author of this manuscript.

VITA

2011 Diploma in Civil Engineering, National Technical University of Athens

2014 Master of Science in Structural Engineering, University of California San Diego

2019 Doctor of Philosophy in Structural Engineering, University of California San Diego

ABSTRACT OF THE DISSERTATION

Assessment of the Seismic Behavior of Fully and Partially Grouted Reinforced Masonry Structural Systems through Finite Element Analysis and Shake-Table Testing

by

Andreas A. Koutras

Doctor of Philosophy in Structural Engineering

University of California San Diego, 2019

Professor P. Benson Shing, Chair

Reinforced masonry (RM) structures are commonly found in North America including in areas of high seismicity. However, the ability of such buildings to meet the performance expectations of design codes for high-intensity earthquakes has not been thoroughly validated at the system level. Furthermore, the seismic behavior of partially grouted masonry (PGM) wall systems is not well understood. In this study, a detailed finite element (FE) analysis framework

has been developed to simulate the seismic response of RM structures through collapse. The framework combines smeared-crack shell elements and cohesive-crack interface elements to capture the fracture of masonry, and beam elements to simulate the nonlinear behavior of reinforcing bars. The strain penetration and dowel action that may develop in the reinforcing bars are also accounted for. To enhance robustness and accuracy, an element removal scheme has been introduced. This scheme is triggered in the event of reinforcement rupture or severe masonry crushing. The material models and interface elements have been implemented in a commercial program. The modeling scheme has been validated with experimental data from quasi-static and shake-table tests, and has been used to provide insight into the seismic resistance mechanisms of reinforced masonry structures and the influence of design details on their seismic performance.

Two full-scale shake-table tests were conducted to acquire a better understanding of the seismic performance of PGM wall systems. The first structure had design details that represent the current practice, while the second had improved design details including stronger vertical grouted elements and bed-joint reinforcement. It has been shown that the PGM structure constructed according to current practice could develop an adequate base-shear capacity but failed in a brittle manner, while the improved design details studied could enhance the ductility and shear capacity of the structure. The FE modeling scheme has been extended for analyzing PGM and has been validated with data from the two shake-table tests and quasi-static tests. The models are used to understand the distribution of lateral forces among the wall components of the two test structures, and to evaluate the shear-strength equation given in the design code. The code equation has been found to be adequate for these structures. A parametric study has been conducted to demonstrate the beneficial influence of continuous bond beams below window openings, double vertical grouted cells, and joint reinforcement on the seismic performance of a PGM structure.

1 INTRODUCTION

1.1 Background and Statement of Problem

Reinforced masonry (RM) has many desirable properties as a construction material, such as durability, energy efficiency, and fire resistance. It is being used in a number of countries, such as the United States, Canada, South America, Europe, China, Japan, New Zealand, Australia, and others, including regions of high seismicity. Each country follows different construction techniques and uses different types of masonry units. In North America, RM is used for low-rise residential, commercial, industrial, and school buildings. In these structures, RM shear walls are the primary members resisting lateral earthquake or wind loads and also gravity loads. These walls can have various configurations and their geometry is usually dictated by the architectural design. They can be squat and long walls, perforated walls, cantilever walls, or walls coupled with horizontal diaphragms or beams, and can have a cross section that is rectangular, T-shaped, L-shaped, I-shaped, or U-shaped. Figure 1.1 shows examples of some of the typical RM building configurations found in the U.S.

In modern practice, RM walls are generally constructed of hollow concrete masonry units. Steel reinforcing bars are placed within the units in continuous vertical cells and horizontal courses, and then grout is poured into the cavities, as shown in Figure 1.2. In North America, concrete masonry units that are most commonly used in structural walls have a nominal length, height, and width of 16 in., 8 in., and 8 in., respectively. For grouting, a concrete mix with the maximum aggregate size of 3/8 in. is used. Although RM walls have many commonalities with reinforced concrete shear walls, their seismic behavior can be more complex due to the heterogeneity of the constituent materials, the lack of confinement reinforcement, and the

condition that the spacing of the reinforcing bars is restricted by the spacing of the hollow cores in the units. Several experimental studies have been conducted on the response of RM shear walls under in-plane loads (e.g. Sveinsson et al. 1985, Shing et al. 1991, Voon 2007, Ahmadi 2012). The studies show that RM shear walls can exhibit either a flexure-dominated or a shear-dominated behavior depending on the shear-span ratio of the wall, amount of vertical and horizontal reinforcement, and the axial load applied. Slender walls are expected to be flexure-dominated while walls with a low shear-span ratio may exhibit a brittle shear-dominated behavior.

A flexure-dominated wall can exhibit severe toe crushing, followed by buckling of the exposed vertical reinforcing bars, as shown in Figure 1.3a. Toe crushing may jeopardize the effectiveness of the vertical bars if they are lap-spliced to the dowel bars at the wall base. Furthermore, tensile bond failure due to splitting cracks may occur at the wall ends reducing the effectiveness of the vertical reinforcement in resisting moment. After a buckled bar has been subjected to a few cycles of straightening and bending as the wall is displaced back and forward, bar fracture may soon follow as a result of low-cycle fatigue. This will lead to severe strength degradation of the wall. For a given displacement level, the extent of toe crushing depends on the axial compressive load, the amount of vertical reinforcement, and the shear-span ratio. To improve the ductility of flexure-dominated walls, detailing schemes have been proposed that incorporate confined boundary elements at the wall ends (Cyrier 2012, Banting and El-Dakhakhni 2012). However, those have not gained popularity in the masonry construction practice because of the architectural challenges that may arise and the increase in the construction cost.

The strength and behavior of a wall dominated by diagonal shear cracks depend on the shear-span ratio, the strength of the masonry, the aggregate-interlock action along the cracks, the amount of the shear reinforcement, and the applied axial compressive load. Proper anchorage is

important for the horizontal reinforcement to be effective. The vertical reinforcement may also contribute to the shear resistance through dowel action. However, this contribution is normally small as compared to that provided by the horizontal reinforcement, unless the top of the wall is so restrained in the vertical direction that diagonal tension can develop in the vertical reinforcement crossing the diagonal cracks as the cracks open. Under this condition, the wide opening of the diagonal cracks may also cause the rupture of the horizontal reinforcing bars. Shear-dominated walls subjected to high compression can also exhibit brittle shear failure due to the crushing of the compressive struts, as shown Figure 1.3b.

A wall may also develop base sliding. In that case, the resistance is provided by shear friction as well as the dowel action of the vertical reinforcement, and it depends on the magnitude of the axial compressive load on the wall and the amount of the vertical reinforcement.

Design provisions for RM in the U.S. are provided in TMS 402. Based on the reinforcement details as well as the maximum permitted vertical reinforcement, the code classifies RM shear walls into three categories: ordinary, intermediate, and special walls. Special RM walls are required to meet the most restrictive detailing requirements and are allowed to be used in the seismic design categories (SDC) D, E, or F of ASCE/SEI 7. For the seismic design of special RM shear wall systems, ASCE/SEI 7 specifies a response modification factor (R) of 5, expecting these walls to have a ductile behavior dominated by flexure. However, this is not always guaranteed by the codes or the design practice (NIST 2014). This is especially true for short-period masonry buildings, which may have walls with low shear-span ratios. Moreover, a wall system could behave very differently from what was assumed in the design process because the design might not have fully accounted for the system effects. For example, the designer may underestimate the coupling forces exerted by horizontal diaphragms on structural walls, and thereby overestimate the shear-

span ratio of the walls. This could result in walls whose behavior will be dominated by shear rather than flexure, as shown in a study by Stavridis et al. (2016), whose results are shown in Figure 1.4. Furthermore, the coupling forces of the horizontal diaphragms and the axial restraints exerted by walls orthogonal to the direction of the seismic action can change the axial forces in the walls and thereby their resistance mechanism as the wall system undergoes lateral displacements under seismic forces (Mavros et al. 2016).

The previously mentioned studies focused on fully grouted RM shear walls. Reinforced masonry walls can also be partially grouted. In that case, only the reinforced vertical cells and reinforced horizontal courses (bond beams) are grouted. Partially grouted masonry (PGM) is generally preferred in areas of low to moderate seismicity where the spacing of the grouted cells can be large, namely, more than 4 ft. Such walls are normally designed as ordinary walls and constitute the vast majority of masonry construction in the U.S. outside the West Coast. Experimental studies have shown that the behavior of PGM walls under lateral loads is very different from that of fully grouted walls (Schultz 1996; Voon and Ingham 2006, 2008; Maleki 2008; Minaie et al. 2010; Nolph and ElGawady 2011; Johnson and Schultz 2014; Bolhassani et al. 2016a, 2016b). PGM walls develop a more complex response primarily dominated by shear and governed by the interaction of the grouted and ungrouted parts. Studies have shown that PGM walls with large spacing of grouted cells can behave similarly to RC infill frames. Failure of PGM walls involves the opening of stair-stepped cracks along the mortar joints, cracking along the interface between grouted and ungrouted parts, sliding along the horizontal mortar joints, splitting or crushing of the ungrouted concrete units, shearing of the vertical grouted cells, crushing of the wall toes due to diagonal compression, and subsequent bar buckling. Figure 1.5 shows examples of damage patterns observed in PGM wall specimens that were tested.

Based on the design code, the shear strength of PGM walls is calculated from an equation that was originally developed with test data from fully grouted walls. Since the 2013 version of the code (MSJC 2013), a reduction factor of 0.75 has been added to the code-based shear strength of PGM walls in order to compensate for the higher strength values predicted by the original equation as compared to the wall strengths observed in PGM wall tests. Nonetheless, experimental studies have shown that the current code equation may still overestimate the shear strength of PGM walls that have large spacing of vertical grouted cells (ElGawady 2015; Bolhassani 2015). All previous studies on partially grouted masonry focused on the response of walls under quasi-static loading. The dynamic behavior of a PGM wall system under severe seismic forces is not well understood. Because of the lack of experimental and field data, the ability of a PGM building system to withstand a seismic event it is designed for has not been definitively confirmed.

In past earthquakes, most of the RM buildings sustained minor structural damage. For example, during the 1994 Northridge Earthquake, no serious damage was reported in RM buildings, and during the 2011 Christchurch Earthquake, only a small number of RM buildings got severely damaged. In the latter event, shear and flexural failures were observed in fully and partially grouted walls, as shown in Figure 1.6. The damage obtained was primarily attributed to the poor grouting of the walls, the improper placement of reinforcement, and the irregularities in the building geometry (Dizhur et al. 2011; EERI 2011; Centeno et al. 2014).

A numerical study was conducted under ATC 76 (NIST 2012) to determine the collapse probability of various archetype buildings under the maximum considered earthquake (MCE) following the FEMA P-695 methodology (FEMA 2009). Among the structural systems examined were buildings with special and ordinary RM shear walls. Despite the limited failures that RM buildings had during real earthquake events, the study suggested that low-rise RM structures may

not satisfy the safety threshold of 10% probability of collapse during the MCE. Nonetheless, the models used for that study were overly simplified and too conservative. The development of numerical models that can be reliably used to assess the collapse potential of RM buildings is essential.

Ideally, an analytical model used to simulate the inelastic behavior and assess the collapse potential of a reinforced masonry building must be capable of capturing the aforementioned failure mechanisms and the system effects that will influence the strength and ultimate behavior of the wall system. In particular, the model should have sufficient sophistication to accurately describe the physical mechanisms that govern the inelastic behavior, accounting for the influence of the wall geometry, reinforcement details, and boundary conditions on the failure mechanisms, which will determine the strength and displacement capacity of a wall.

1.2 Research Objectives and Scope

The research presented in this dissertation consists of two parts. The first part was funded by the Federal Emergency Management Agency (FEMA) under the project ATC-116. It was aimed to develop a refined, reliable and robust modeling approach for the nonlinear analysis of fully grouted RM wall systems under severe earthquake loads to the point of collapse. To this end, a finite element (FE) modeling scheme has been developed and validated with results from quasi-static wall tests and two full-scale shake-table tests of wall systems. The modeling scheme can simulate masonry cracking and crushing, bar buckling and bar fracture, dowel action, bond deterioration, and bar pullout, and accounts for geometric nonlinearity. The scheme combines smeared-crack shell elements with cohesive-crack interface elements and uses beam elements to model the reinforcing bars in a discrete manner. Strain penetration and dowel action are accounted for by using a bond-slip/dowel-action interface element to attach the beam elements representing

reinforcing bars to the adjacent masonry shell elements. The modeling scheme is complemented with an element removal strategy to enhance accuracy and robustness. The scheme is validated with data from quasi-static wall tests and dynamic shake-table tests. The analyses are performed in the finite element program LS-DYNA. To meet the special modeling needs for capturing the various failure mechanisms, new materials laws, bond-slip/dowel-action interface elements, and an element removal scheme have been implemented as user-defined features in LS-DYNA. The modeling scheme can be used to gain insight into the seismic behavior of building systems and generate data for the calibration of simplified models.

The second part of the dissertation focuses on research conducted in a project funded by the National Science Foundation (NSF). The project was a joint effort between researchers from the University of California San Diego, Drexel University, and the University of Minnesota at Twin Cities. The overall objectives of the project were to investigate the behavior of ordinary partially grouted masonry walls and wall systems under lateral loads, provide data from quasi-static tests and dynamic tests of PGM walls and wall systems, propose new design details that can enhance the ductility of these structures, and develop numerical tools that can predict the cyclic behavior of PGM structures in a realistic manner. Drexel University studied the response of planar walls designed with conventional reinforcing details and with an improved reinforcing scheme (Bolhassani et al. 2016a, 2016b, 2016c). The University of Minnesota tested masonry wall assemblages that had a window opening and wall flanges and investigated retrofit strategies (Johnson and Schultz 2014, 2015, 2018; Schultz and Johnson 2019).

The research conducted at the University of California San Diego and presented in this dissertation focused on the system-level behavior of PGM wall structures under earthquake loading and on the numerical modeling of the nonlinear cyclic response of PGM structures. To

this end, two full-scale, one-story structures were designed and tested on a shake table. The first structure was designed and detailed according to the current code provisions and practice. It had widely spaced vertical grouted cells and horizontal bond beams. The second structure represented an improved reinforcing scheme with vertical grouted elements that extended in two side-by-side cells (double grouted cells), horizontal bond beams, and bed-joint reinforcement. The structures were subjected to a series of dynamic tests using historical ground motion records that were scaled to various intensity levels. The intensity of the strongest motions applied exceeded two times the MCE. The results and findings from the tests are presented in the dissertation.

The experimental data have been used for the calibration and validation of finite elements models. The modeling scheme adopted is an extension of the scheme proposed for fully grouted walls, using a combination of smeared-crack shell elements and cohesive-crack interface elements. The mortar joints in the ungrouted part of the walls are modeled with cohesive-crack interface elements that can capture the fracture and sliding behavior of the joints, as well as the dilatation and compaction effects under cyclic loading. A new interface element has been developed to account for the cavity between the face shells of concrete units in an efficient manner. After the calibration and validation of the modeling scheme with results from quasi-static tests on wall segments, the scheme is used to simulate the dynamic response of the two shake-table test structures and to investigate the influence of bond beams, double grouted cells, and joint reinforcement on the behavior of the structures. The models have been also used to understand the distribution of the lateral load resistance of the wall components and to evaluate the shear-strength equation given in the design code.

1.3 Outline of Dissertation

Chapter 2 provides a summary of the available modeling methods for reinforced masonry and concrete structures. It presents the proposed finite element modeling scheme for fully grouted walls, and describes the constitutive models and elements used in the analyses. A simple and robust orthotropic concrete model is developed to simulate the compressive and tensile behavior of the smeared-crack shell elements. Furthermore, an existing bond-slip/dowel-action interface element is enhanced to account for large rotations. An element removal scheme is introduced to model the loss of material resistance due to the severe crushing of masonry and reinforcement rupture.

Chapter 3 presents the results from the verification analyses conducted on fully grouted walls and wall systems. The analyses include shear-dominated and flexure-dominated wall segments that were tested under quasi-static cyclic lateral displacements, and a two-story and a one-story full-scale shake-table test structure. The second structure was tested to a roof drift ratio that exceeded 13% and the data was used to validate the ability of the finite element modeling scheme to simulate the dynamic response up to a large drift level. Lastly, a study is conducted to simulate the dynamic response of a two-story commercial building archetype under biaxial earthquake excitations to the point of collapse. The building was designed based on the current code and has reinforced masonry shear walls and a steel gravity system.

Chapter 4 presents the modeling scheme developed for the analysis of partially grouted masonry walls and systems under lateral loading. The scheme is validated with results from quasi-static wall tests. Among the tests, walls with double grouted cells and joint reinforcement are examined.

Chapter 5 describes the experimental program on the testing of the first full-scale one-story PGM structure on a shake table. The structure has reinforcing details that represented the current

code provisions and design practice. The chapter presents the design approach, reinforcing details, construction, ground motions and scaling, structural response, and the analysis of the test data. A detailed finite element model of the test structure is developed and validated with the test results. The model has been used to understand the distribution of the lateral force resistance among the wall components, and to evaluate the shear-strength equation given in the design code. Furthermore, a parametric study has been conducted to demonstrate the importance of bond beams.

Chapter 6 presents the shake-table testing of the PGM second structure that was designed with the goal to improve the ductility of the building. Compared to the first structure, the second structure had double grouted vertical cells and joint reinforcement. The chapter presents the observations and findings from the shake-table tests and compares the response of the two structures. A detailed finite element model is developed for the second structure. After the model is validated with the results from the shake-table tests, it is used to examine the influence of double grouted vertical cells and joint reinforcement on the seismic behavior of the building. The numerical results are also used to evaluate the shear-strength equation of the design code.

Chapter 7 presents the conclusions and the needs for future research.

Part of this chapter is a reprint of the material that will appear in Chapter 4 of the technical report titled “Developing Solutions to the Short-Period Building Performance Paradox: Study for Reinforced Masonry Buildings” that will be submitted to the Federal Emergency Management Agency by the Applied Technology Council for the project number ATC-116. The authors of Chapter 4 in the report are: the author of this dissertation, Jianyu Cheng, and P. Benson Shing. The report chapter was prepared under the supervision of Dr. Charles A. Kircher, who was the technical director of the ATC-116 project. The author of this dissertation was the primary investigator and author of all the materials covered in this chapter of the dissertation.

Commercial building | Office building

Residential building | Warehouse building

Figure 1.1 Common building configurations with reinforced masonry shear walls in North America (courtesy of Dr. G. Kingsley).

RM wall layout | RM wall grouting and consolidation

Figure 1.2 Construction of RM walls.

(a) Sherman (2011)

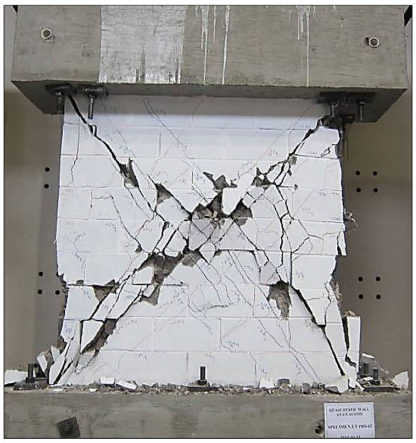

(b) Ahmadi (2012)

Figure 1.3 Flexure-dominated and shear-dominated failures in quasi-static tests of RM wall specimens.

(a) 3-story test structure

(b) Shear cracks in first-story walls after the tests

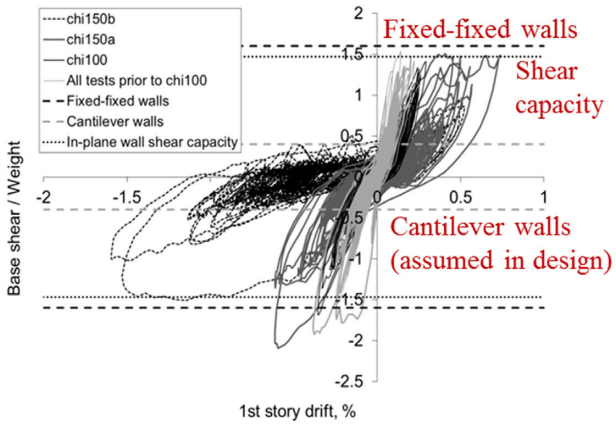

(c) Comparison of calculated capacity and experimental resistance

Figure 1.4 Behavior of the three-story structure tested by Stavridis et al. (2016) on a shake table.

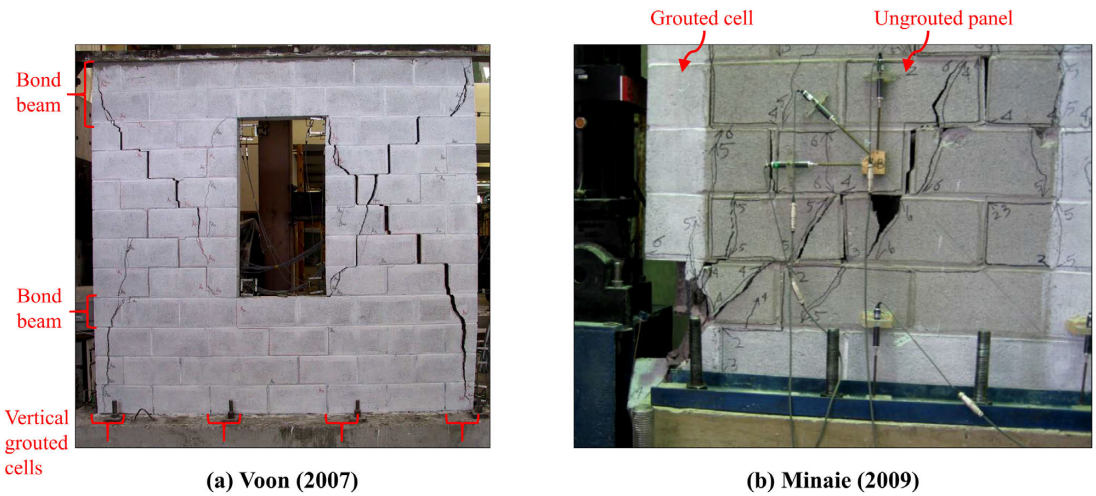

(a) Voon (2007) **(b) Minaie (2009)**

Figure 1.5 Damage in partially grouted wall tests: (a) perforated wall specimen B4 tested by Voon (2007); (b) diagonal compression failure in wall specimen PCL1 tested by Minaie (2009).

Courtesy of J. Ingham

Courtesy of J. Ingham

Centeno et al. (2014)

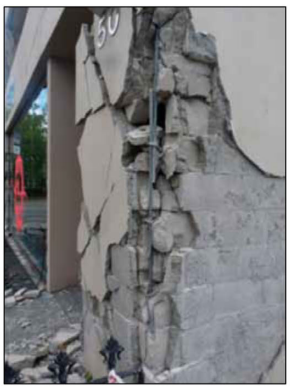

EERI Special Earthquake Report – May 2011

Figure 1.6 Damage observed in RM buildings after the 2011 Christchurch Earthquake.

2 FINITE ELEMENT MODELING OF GROUTED REINFORCED MASONRY

This chapter presents a detailed finite element (FE) analysis scheme that has been developed for the simulation of the inelastic response of reinforced masonry (RM) structures under earthquake loading. The proposed modeling scheme has been developed so that it can capture both flexure-dominated and shear-dominated failure modes and is intended to be used for the analysis of RM building systems through collapse. The scheme combines smeared-crack shell elements with discrete crack interface elements to capture crushing and tensile fracture of masonry, and uses beam elements to represent the steel reinforcement. The following sections provide a literature review of modeling methods developed in previous research, and presents the material models and elements used with the proposed FE modeling scheme.

2.1 Overview of Available Modeling Methods

The modeling of the inelastic response of RM wall systems subjected to static and dynamic loading is a challenging endeavor. Wall components in a RM wall system can exhibit one of several, or a combination of, different failure mechanisms, depending on the axial load exerted on the walls, the reinforcement details, the aspect ratio, and the boundary conditions. Slender cantilever walls are expected to have relatively ductile flexure-dominated behavior, while wall components with a low shear-span ratio tend to exhibit more brittle, shear-dominated behavior characterized by diagonal cracking or crushing. Walls with very low shear-span ratios can develop base sliding in lieu of diagonal cracking. Different modeling approaches with various degrees of sophistication can be used to analyze the response of RM structures under seismic loads. Because of the similarities between reinforced masonry and concrete, methods originally developed for the simulation of RC structures can be also applied for the analysis of RM structures. The available

modeling approaches may be divided into the following main categories: 1) frame models; 2) macro-models; 3) nonlinear truss models; and 4) FE models. A survey of the available methods is provided below.

The simplest approach to represent a masonry wall structure is through frame models. In these models, the vertical and horizontal wall components are represented by beam-column line elements, and the panel zones at the intersection of these components are usually modeled as rigid zones (Paulay and Priestley 1992). Figure 2.1 shows two simple examples. This method is particularly appealing for design because of its computational efficiency and its wide availability in commercial software of structural analysis. However, it is primarily intended to model flexure-dominated response. Depending on the required degree of accuracy, the inelastic behavior of beam elements can be assumed to be lumped at the element end nodes, or distributed along the element length using a fiber-section discretization.

With the lumped plasticity approach, rotational springs are used to represent the plastic-hinge response at the element ends. Their behavior is defined in terms of a moment-versus-rotation relation whose monotonic loading or back-bone curve can be calibrated with a moment-curvature sectional analysis. The assumption of an effective plastic hinge length and a constant axial load is needed. Some models may also account for the axial load-moment interaction. Load degradation due to masonry crushing, reinforcement buckling, or rupture needs to be accounted for a priori when determining the post-peak behavior of the backbone curve. The cyclic response can be described by selecting an appropriate hysteretic law that can represent phenomena such as cyclic strength and stiffness degradation, and pinching due to crack opening and closing or bar slip (e.g., Kunnath et al. 1990; Sivaselvan and Reinhorn 2000; Ibarra et al. 2005). Nonetheless, the parameters controlling the cyclic behavior of these models need be calibrated based on

experimental data or with analysis results from more refined models. In some models, rotational springs have been also used to indirectly account for shear-dominated response by assuming an equivalent moment-vs-rotation response (e.g., Takayanagi and Schnobrich 1979). In some other models, the nonlinear shear behavior of a member is represented by additional hysteretic shear springs placed in-series with the beam elements (e.g., Ambrisi and Filippou 1999; Elwood and Moehle 2008; LeBorgne and Ghannoum 2014; Burton and Deierlein 2013). These models are entirely empirical without predictive capabilities.

Beam-column elements with a fiber-section discretization and distributed plasticity can accurately capture the inelastic flexural behavior of RM walls, including axial load-moment interaction, as long as appropriate models are used for the uniaxial stress-strain behavior of masonry and steel reinforcement. Some of these models account for reinforcement buckling and rupture in an empirical manner (Girgin et al., 2018). In addition, several approaches have been proposed to account for the strain penetration effect, which can be modeled either in the state determination of the steel fibers assuming that part of the strain in a steel fiber is attributed to bar-slip (Monti and Spacone, 2000), or by introducing a zero-length fiber section at the element end using an appropriate stress-vs-slip material law to model the beam-end rotation due to strain penetration (Zhao and Srirathan 2007) or simply a rotational spring at the beam end (e.g., Ambrisi and Filippou 1999; LeBorgne and Ghannoum 2014; Girgin et al. 2018). The most commonly used beam formulations include displacement-based elements and force-based elements (Zeris and Mahin 1988; Spacone et al. 1996; Neuenhofer and Filippou 1997); the latter are advantageous in that they satisfy the internal equilibrium within the element. Such models can be extended to simulate the inelastic shear behavior of reinforced masonry and concrete members.

Several approaches have been proposed to incorporate the nonlinear shear behavior in beam-column elements with fiber discretization. Some of them assume a shear strain distribution along the cross section and account for the interaction between the normal and shear stresses at the fiber level by introducing a biaxial constitutive law for each fiber (e.g., Vecchio and Emara 1992; Petrangeli et al. 1999; Rose 2001; Jiang and Kurama 2010). Although they are more rigorous than the lumped plasticity models, they come at an increased computational cost and may still not be sufficiently reliable or robust to be used for the cyclic analysis of wall systems. A more simple approach is to model the shear response of a reinforced masonry or concrete section via a phenomenological shear force-vs-shear deformation hysteretic law (e.g., Marini and Spacone 2006). However, this approach is more empirical and cannot account for the flexure-shear interaction.

To simulate the response of reinforced concrete and masonry walls, several researchers have proposed multi-vertical-line-element models (MVLEM) or other macroelements. The first approach was introduced by Kabeyasawa et al. (1983), and since then it has been gradually improved by other researchers (e.g., Vulcano and Bertero, 1987; Colotti, 1993; Orakcal et al. 2004; Massone et al. 2006). A recent MVLEM has been proposed by Kolozvari et al. (2014a) and is schematically illustrated in Figure 2.2a. To capture shear-flexure interaction, the element includes a number of vertical panels whose response is governed by a biaxial concrete constitutive law. The model assumes that the relative rotation between the top and bottom faces of the element is concentrated at a distance of ch, as shown in Figure 2.2a. Although, the model is able predict well the response of flexure-dominated RC wall tests, it has not been shown as to whether it can accurately predict brittle shear failure (Kolozvari et al. 2014b).

Macro-elements have been developed as a computationally efficient approach intended for the seismic assessment and design of RC and masonry components controlled by shear. They usually consist of a two-dimensional panel component, which controls the shear response of the macro-element, and a set of springs placed at the perimeter of the panel that determine the flexural or sliding response. Calio et al. (2012) proposed a macro-element to simulate the in-plane behavior of unreinforced masonry structures. As shown in Figure 2.2b, it consists of four rigid hinge-connected beams forming the perimeter of a rectangular panel. Two diagonal springs govern the shear behavior of the panel, while vertical and horizontal springs placed at the perimeter of the panel control the flexural and sliding response as well as the interaction with the adjacent macro-elements. However, the definition of the uniaxial law assigned to the diagonal springs is vague. Penna et al. (2013) has proposed a macro-element intended to represent the in-plane response of masonry piers and spandrel beams within unreinforced masonry buildings. The panel shear strength was derived based on a frictional component and a cohesive component, while the cyclic response was modeled with a phenomenological hysteretic law. The macro-element was used to simulate quasi-static cyclic tests of unreinforced masonry walls and was able to predict the experimental response well. Another type of macro-element is the stringer and panel model, which is mainly for the design of shear-critical RC members. The model uses nonlinear stringers that resist the shear flow and nonlinear panels to represent RC panels (Blaauwendraad and Hoogenboom, 1996).

Beam elements with a fiber-section discretization or MVLEM's are able to accurately predict the response of flexure-dominated shear walls, given that appropriate material models are used to describe the behavior of concrete (or masonry) and steel reinforcement. Although several efforts have been made to allow these elements to capture shear-dominated response and shear-

flexure interaction in a rigorous manner, it is still not proven if they can be used to reliably predict brittle shear failures under cyclic load histories. Furthermore, frame models cannot accurately represent the geometry and stiffness of perforated walls which are common in reinforced masonry construction. On the other hand, macro-elements are based on empirical assumptions and are mainly intended for the simulation of shear-dominated panels rather than flexure-dominated shear walls. To overcome the limitations of the previous modeling methods, alternative approaches can be considered, such as nonlinear truss models or finite element models.

A nonlinear truss model idealizes a RC/RM wall component into an assemblage of diagonal, vertical, and horizontal truss elements, as shown in Figure 2.3. The diagonal elements are to simulate the inclined compression strut mechanism formed when a member is subjected to shear, while the vertical and horizontal elements are used to represent the steel reinforced and concrete resistance in these directions.

Truss models have been widely used to determine the capacity and evaluate the nonlinear behavior of RC structures and members. In design, they are commonly referred to as strut-and-tie models. The concept was first conceived in the early 1900s, where a strut-and-tie representation was used to model the shear transfer mechanism in RC concrete beams. Schlaich et al. (1987) developed design recommendations based on the strut-and-tie method. The current design codes, including Eurocode 2 (2004) and ACI 318-19 have also adopted strut-and-tie models to be used for the calculation of the capacity of RC members for situations in which the classic beam theory does not apply, such as deep beams, corbels, or cases with geometric or load discontinuities. Yun (2000) proposed the use of the strut-and-tie method as a nonlinear analysis tool to predict the monotonic response of RC members up to failure using simple material laws to represent the stress-strain response of concrete and reinforcing steel. Mazars et al. (2002) introduced a nonlinear truss

model, which had a fine mesh of diagonal, vertical, and horizontal truss elements, and was used to simulate the cyclic response of RC shear walls. Tomohiro (2004) proposed a lattice model which consisted of a mesh of vertical, horizontal, and diagonal truss elements at 45- and 135-degree angles. The mesh was enhanced with additional truss elements, referred to as arch elements that were used to model the dominant compressive struts expected to form along a structural member. He used 2D lattice models to analyze members under plane stress conditions and 3D lattices to account for the torsional behavior of beams and columns and to model frame structures subjected to bidirectional excitation. Park and Eom (2007) followed a similar approach to the one proposed by Mazars et al. (2002) but they used more refined material models. They also expressed the effect of transverse tension on the compressive resistance of the diagonal truss elements based on the modified compression field theory (MCFT) by Vecchio and Collins (1986). To et al. (2009) employed nonlinear truss models to analyze 2D multi-story RC frames subjected to static cyclic and dynamic loads. Panagiotou et al. (2012) developed a modeling framework using nonlinear truss models to capture the hysteretic response and failure modes of shear-dominated RC walls. Following the same assumption as in the modified compression field theory, a reduction factor was used to account for the effect of the transverse tensile strains on the compressive strength of the diagonal elements based on the element size selected. The compressive and tensile fracture energies of concrete were also regularized based on the element size. Their truss model was extended for three-dimensional analyses by Lu and Panagiotou (2013) by replacing the vertical truss elements with beam elements to model the out-of-plane flexural response of RC walls. The modified truss model, referred to as beam-truss model, was used to simulate cyclic quasi-static tests on RC flanged walls subjected to uniaxial and biaxial loading histories, and a shake-table test of a RC wall system subjected to bidirectional excitation. In all cases, the numerical results were

in good agreement with the experimental results. Moharrami et al. (2015a) improved the truss model of Panagiotou et al. (2012) by accounting for the contribution of the aggregate interlock to the shear resistance of inclined concrete cracks to simulate the response of shear-dominated RC columns, the cyclic response of RM shear walls tested quasi-statically, and the response of a two-story shear-wall structure that tested by Mavros et al. (2016) on a shake-table (Moharrami et al. 2015b). In any case, the numerical results were in good agreement with the experimental results.

Nonlinear truss models constitute a computationally efficient tool that can capture the response of both flexure and shear critical members, including brittle types of shear failure, as long as an appropriate angle of inclination is selected for the diagonal truss elements. However, the existing truss models cannot accurately represent more localized mechanisms and failures, such as the effect of strain penetration, pull-out of reinforcement, lap-slice failure, bar rupture, or dowel action. Furthermore, they cannot accurately account for the base sliding that may develop in lightly reinforced masonry walls that have low axial load. If a detailed analysis of the seismic response and damage of a RC/RM structure is required, nonlinear finite element models still remain the most powerful tool.

Nonlinear finite elements, in the form of continuum or shell elements, are being widely used for the analysis of RC/RM structures. To describe the effect of cracking, two main approaches are used: smeared-crack models (Rashid 1968) or discrete-crack models (Hillerborg et al. 1976). In the first approach, the effect of cracking is accounted for within the constitutive material laws used with continuum or shell elements, while in the second approach, discrete interface elements are used to explicitly model the displacement discontinuity across a crack. Although the discrete-crack approach can be more computationally demanding, due to the use of additional elements to model cracks, it can provide a more realistic representation of the crack pattern developed in a

member. However, the cracks allowed to develop depend on the locations of the discrete crack interface elements. A finer network of interface elements will produce more realistic crack patterns. In simulating brittle shear failure due to strongly localized diagonal cracks, explicit modeling of the dominant cracks may be necessary to circumvent the stress locking phenomenon that smeared-crack elements can present. Stress locking is essentially caused by the weak representation of the displacement discontinuity in a smeared-crack formulation that leads to the interlocking of the diagonal compressive stresses among the neighboring elements after the elements develop cracks (Rots and Blaauwendraad 1989; Lotfi and Shing 1991). Although other formulations that allow a strong representation of displacement discontinuities have been proposed, such as the extended or generalized finite element method (Fries and Belytschko 2010), formulations with cracks embedded in continuum elements (e.g., Manzoli and Shing 2006), and meshfree methods (e.g., Chen et al. 1996), they require a substantial effort to implement and their ability to model RC/RM structures under cyclic loading conditions in an efficient and robust manner has not been proven. Thus, the discrete-crack approach is still the most viable means for the simulation of shear failure associated with diagonal tensile cracking.

Several studies have demonstrated the smeared-crack approach can accurately simulate the flexural failure of RC shear walls and columns using plane stress, shells, or solid elements (e.g., Feenstra and de Borst 1995; Vecchio 1999; Kwan and Billington 2001; Faria et al. 2004; Noguchi and Uchida 2004; Murcia-Delso and Shing 2014; Moharrami and Koutromanos 2017). The steel reinforcement is represented as a layer smeared across concrete or masonry elements or by discrete truss or beam elements to model each reinforcing bar. When reinforcement is modeled in a discrete manner, the effect of bond-slip can be accounted for by using zero-length spring or interface

elements to connect the nodes of the reinforcement elements to the nodes of the concrete elements (Scordelis and Ngo 1967).

The discrete-crack approach has been primarily used for modeling components that are prone to shear failure. Stavridis and Shing (2010) combined cohesive-crack interface elements with smeared-crack plane-stress elements to model the response of non-ductile masonry-infilled RC frames under monotonic lateral loading. Truss elements were used to represent the steel reinforcement, and a discretization scheme was proposed for connecting the truss elements to the concrete elements as shown in Figure 2.4. Koutromanos et al. (2011) adopted the same discretization scheme, however, they used an improved cohesive-crack constitutive law (Koutromanos and Shing 2012) allowing them to simulate the cyclic and dynamic response of masonry-infill RC frames. The cohesive-crack model was also used to simulate a shear-dominated RC column that was tested quasi-statically (Koutromanos and Shing 2012). The predicted cyclic response and crack pattern were in a good agreement with the experimental results. Kottari (2016) extended the cohesive-crack model of Koutromanos and Shing (2012) to three-dimensions and used it together with solid elements to simulate shear failure in bridge abutment shear keys.

The finite element modeling of RM walls has received less attention. In most cases, plane stress or shell elements have been used to discretize RM walls. For RM walls, the steel reinforcement is typically placed as a single layer at the mid-thickness of the walls, and no confinement reinforcement is used. Seible et al. (1990) and Seible and Kingsley (1991) used plane-stress elements to model individual RM shear walls as well as RM wall systems under monotonic and cyclic loading. An orthotropic material law was adopted to represent the biaxial response of grouted masonry, and similar to that in the modified compression field theory (Vecchio and Collins 1986), the effect of transverse tension on the compressive resistance of masonry was considered.

They obtained satisfactory results and they also noted the mesh-size dependency of the numerical results when simulating the post-peak response of flexure-dominated walls. Lotfi and Shing (1991) evaluated the capability of smeared-crack plane-stress elements in predicting the lateral strength of flexure-dominated and shear-dominated RM shear walls. The compressive response of masonry was modeled with a J2-plasticity constitutive law and the steel reinforcement was represented as a smeared overlay with a bilinear material law. They obtained a good agreement with the experimental results for flexure-dominated walls; however, their model overestimated the lateral strength and ductility of shear-dominated wall specimens. The higher resistance obtained in the latter case was attributed to the stress locking phenomenon.

Mavros (2015) developed a FE modeling scheme to simulate the three-dimensional response of fully grouted reinforced masonry structures. In the proposed scheme, smeared-crack shell elements were combined with cohesive-crack interface elements to model the nonlinear behavior of masonry, and truss elements were used to model the reinforcing bars. Cohesive-crack interface elements were placed along the horizontal and vertical directions, as well as diagonally at 45-degree angles with a similar configuration as the one shown in Figure 2.4. However, additional interface elements were introduced to attach the reinforcement truss elements to the adjacent masonry shell elements to account for the bond-slip and dowel-action effects. The modeling scheme was extensively validated with shear and flexure-dominated wall tests as well as with the results from a two-story shake-table test structure. For the analyses, the finite element program FEAP (Zienkiewicz and Taylor, 2000) was used. In all cases, a very good agreement was obtained between the numerical and experimental results. However, a different discretization scheme had to be used depending on whether a wall specimen was dominated by flexure or shear.

Figure 2.5 shows the discretization schemes that Mavros (2015) proposed for the analysis of shear and flexure-dominated RM walls. To capture the response of flexure-dominated walls, shell elements of a smaller size were used in the region of the wall toes, and no cohesive-crack interface elements were included in these regions, as compared to the discretization proposed for shear-dominated walls. These modifications were needed because a network of interconnecting cohesive-crack interface elements could unduly increase the compressive resistance of a crushed region, and thus the flexural resistance of a wall, by carrying the compressive forces through their nodes even after the adjacent shell elements were crushed. On the other hand, discretizing shear-dominated walls with the scheme used for flexure-dominated walls could lead to an artificial increase of the shear resistance of the walls because the elimination of the cohesive-crack interface elements from the wall toes would increase the shear resistance of the compression toe. Furthermore, the aforementioned modeling scheme did not account for the buckling and rupture of the vertical reinforcement, which is largely responsible for post-peak load degradation of a flexure-dominated masonry wall.

2.2 Objective of Current Study

Most of the previous studies on the FE analysis of RM walls were not able to capture all the critical failure mechanisms and therefore the post-peak behavior of a wall in an accurate manner. A general modeling scheme that was suitable for both flexure-dominated and shear-dominated walls had been provided so far. It is difficult to predict a priori the dominant failure mode of a wall component in a building system before the analysis. Furthermore, most of the previous numerical studies on RM structures have been limited to the small-displacement regime. Yet, for the purpose of design code development, there is a pressing need to develop analysis tools

that can be used to evaluate the seismic performance of an RM building system undergoing large displacements to assess their collapse probability.

The objective of this study is to develop a FE modeling scheme that can simulate the response of both flexure- and shear-dominated RM walls and can be used for the analysis of RM building systems through collapse under severe earthquake loads. The scheme aims to capture both the cyclic response and induced damage in a realistic manner, accounting for masonry cracking and crushing, reinforcement buckling and rupture, dowel action, as well as bond deterioration and bar pull out.

2.3 Proposed Modeling Methodology for Grouted Reinforced Masonry

The FE modeling methodology proposed in this study is based on the scheme proposed by Mavros (2015) but aims to improve it in the following ways: 1) account for both flexure- and shear-dominated failures using the same discretization, 2) account for reinforcement buckling by using beam elements instead of truss elements and also account for reinforcement rupture, and 3) account for P-Delta effects. Four types of elements are used to model a RM wall: smeared-crack shell elements and cohesive-crack zero-thickness interface elements for the masonry, beam elements for the horizontal and vertical reinforcing bars, and additional interface elements for modeling bond-slip and dowel-action behaviors of reinforcing bars. The proposed discretization scheme for a typical wall is shown in Figure 2.6. The grouted masonry is modeled with triangular smeared-crack shell elements to simulate the compressive behavior of masonry as well as diffuse cracking. Each triangular element has two perpendicular sides that are 4 in. long. Cohesive-crack interface elements are used to represent dominant cracks in a discrete fashion. They are placed at a 45-degree angle to capture diagonal shear cracks in a realistic manner, avoiding stress locking that could be introduced by smeared-crack elements (Rots and Blaauwendraad 1989; Lotfi and

Shing 1991), and in the horizontal direction to allow for an accurate simulation of sliding along a cracked joint. They are also placed in the vertical direction to simulate possible vertical splitting cracks. The beam elements representing the reinforcing bars are connected to the shell elements through interface elements that allow the simulation of bond-slip and dowel-action without requiring a very refined mesh for masonry. For the beam elements, a steel material law that accounts for low-cycle fatigue and bar fracture is adopted. All the elements account for geometric nonlinearity.

Elements representing crushed masonry and fractured bars, as well as the interface elements connecting them to adjacent elements, are removed immediately after the respective failure occurs. This enhances the efficiency and robustness of the numerical computation, and also the accuracy of the numerical results. Removing the bond-slip/dowel-action elements after masonry crushing or bar rupture eliminates spurious restraints that could be introduced by these elements. The same is true for removing the cohesive-crack interface elements when the adjacent masonry crushes. The FE program LS-DYNA (LSTC, 2019) has been used as the platform, in which the required material models and the cohesive-crack and bond-slip/dowel-action interface elements have been implemented as user-defined features. The elements and material models used in this study, and the element removal scheme are further described in the following sections. The validation of the proposed modeling method with experimental results is presented in Chapter 3.

2.4 Smeared-crack Shell Elements

2.4.1 Element formulations

Grouted masonry is discretized with triangular shell elements. The triangular shell elements used have a computationally efficient formulation proposed by Kennedy et al. (1986), which is available in LS-DYNA. The formulation is based on the Reissner-Mindlin shell theory

accounting for through thickness shear strains and uses linear shape functions to approximate the mid-surface displacements and the rotations due to bending. To simulate the nonlinear out-of-plane flexural behavior of the walls, each shell element is assigned five through-thickness integration layers. Each layer has a single Gauss point and essentially represents a constant-strain plane-stress triangle. Large rigid-body rotations are handled by a co-rotational coordinate system that is updated based on the location of the three nodes of the element. The deformation component of the nodal rotation is obtained by subtracting the rigid-body rotation from the total nodal rotation.

2.4.2 Orthotropic model for masonry

The through-thickness shear stress-shear strain relation is assumed to be linearly elastic. The in-plane stress components at each integration point of the shell elements are calculated with a smeared-crack model that has been implemented in this study. The model is computationally efficient as compared to more refined models. It is used to simulate the compressive behavior as well as the tensile cracking of masonry or concrete. It adopts a simple and robust orthotropic material law with the nonlinear stress-strain relation in each of the two orthotropic directions described by a uniaxial law. The stress update in this model does not require iterations. The behavior of the material is characterized by two states, the uncracked state and the cracked state. As shown in Figure 2.7, before cracking, the axes of orthotropy are aligned and rotate with the directions of the principal strains. In this state, the stress update ensures that the axes of the principal strains coincide with the axes of the principal stresses. Cracking initiates when the maximum principal stress reaches the specified tensile strength, f_t, of the material. Beyond that point, the axes of orthotropy remain fixed, with directions parallel and perpendicular to the direction of the first crack. After this point, shear strain can develop with respect to the orthotropic directions, and the shear stress is related to the shear strain with an elastic-perfectly plastic law

with the yield strength assumed to be 50% of the tensile strength f_t to ensure numerical robustness. Another crack can develop in the direction perpendicular to the first crack when the tensile stress parallel to the first crack exceeds the tensile strength. In the orthotropic model, the Poisson's effect is neglected.

The uniaxial stress-strain law for tension and compression in each of the orthotropic directions is shown in Figure 2.8. In the tension regime, after crack initiation, it assumes an exponential function to model strain softening, and has stiffness degradation upon unloading and reloading. The reduced stiffness allows a complete crack closure during unloading. In the first compressive loading cycle, the material response is linearly elastic until reaching the stress f_o; after that, it is described by a parabolic function for pre-peak strain hardening and a linear function for post-peak strain softening. The monotonic response of the material in tension and compression is described by Eq. 2.1.

$$\sigma = \begin{cases} f_{res} & \text{for} \quad \varepsilon \le \varepsilon_u \\ f_{res} + \dfrac{f_m - f_{res}}{\varepsilon_0 - \varepsilon_u} \cdot \left(\varepsilon - \varepsilon_u\right) & \text{for} \quad \varepsilon_u \le \varepsilon \le \varepsilon_0 \\ a\varepsilon^2 + b\varepsilon + c & \text{for} \quad \varepsilon_0 \le \varepsilon \le f_o / E_m \\ E_m \cdot \varepsilon & \text{for} \quad f_o / E_m \le \varepsilon \le f_t / E_m \\ f_t \cdot \exp\left[\dfrac{-m_t\left(\varepsilon - f_t / E_m\right)}{f_t}\right] & \text{for} \quad f_t / E_m \le \varepsilon \end{cases} \qquad 2.1$$

The coefficients a, b, and c are calculated so that the slope of the parabolic function is zero at the strain ε_0 under which the compressive strength f_m develops. The parameter m_t defines the shape of the strain softening region in tension. Larger values of the parameter result in more rapid softening. The residual strength in compression, f_{res}, is assumed to be zero. Unloading in compression follows the initial stiffness until reaching zero stress. After reaching zero stress, the

stress remains zero during further strain increment in the same direction until the total strain becomes zero, after which tensile stress starts to develop. The residual plastic strain is denoted by ε_{pl} and is calculated during compressive loading as the strain at the intersection of the unloading branch with the zero-stress axis. Reloading in compression follows the same path, and compressive stress develops when the compressive strain becomes larger than ε_{pl} in magnitude. The material is considered to be completely crushed when the compressive strain along any of the two axes reaches ε_u. In the following discussion, the axes of orthotropy will be called axes α and β, and the axes of the principal strains will be denoted by 1 and 2. Principal axis 1 is defined as the axis of the maximum principal strain.

Crushing that initiates in one direction of orthotropy will compromise the strength that can develop in the other direction. Accounting for this phenomenon is important in modeling the cyclic response of masonry walls. To this end, it is assumed that the residual plastic strain ε_{pl} as a result of inelastic compression is the same for both orthotropic directions, and it has a value equal to the largest residual plastic strain, in absolute magnitude, that has been attained in any of the two directions, as calculated with Eq. 2.2.

$$\varepsilon_{pl} = \min\left\{\varepsilon_{\min,\alpha} - \sigma\left(\varepsilon_{\min,\alpha}\right)/E_m \ , \ \varepsilon_{\min,\beta} - \sigma\left(\varepsilon_{\min,\beta}\right)/E_m\right\} \qquad 2.2$$

in which $\varepsilon_{\min,\alpha}$ and $\varepsilon_{\min,\beta}$ are the peak compressive strains developed in the orthotropic directions, α and β, respectively. The behavior of the model under biaxial compression is shown by the numerical examples in Figure 2.9. Three loading scenarios are considered: 1) the material is subjected to simultaneous biaxial loading with equal magnitudes and strain rates in the two directions; 2) non-proportional loading with compression first applied along α-axis and then

unloading that is followed by compression applied along β-axis; and 3) proportional loading with compression applied simultaneously along α and β axes but with the strain in the direction of β-axis equal to half of that in the other direction. In the first scenario, the behaviors along the two axes are identical, and are the same as the behavior under uniaxial loading. The second scenario shows that prior damage in one loading direction will also reduce the compressive strength in the other. The third scenario shows that under proportional loading with unequal magnitudes, the direction with the larger deformation governs the damage and load degradation in both directions.

Even though this model more or less captures the biaxial loading effects observed in experiments, as discussed in Chen (2007), results from the first loading scenario do not exactly match experimental observations in that the compressive strength of concrete can increase by as much as 25% when subjected biaxial compression (Chen 2007). However, for reinforced masonry walls, this situation is rare. To properly account for the biaxial behavior of concrete or masonry, more refined but also more computationally demanding constitutive models can be used, e.g., the plane-stress J2-plasticity model adopted by Lotfi and Shing (1991), Koutromanos et al. (2011), and others, the three-dimensional concrete model proposed by Moharrami and Koutromanos (2016), the micro-plane model by Caner and Bažant (2013), and the damage-plasticity model by Lee and Fenves (1998).

To account for the reduction of tensile strength when the material has been damaged in compression, a reduction factor is applied to the tensile strength based on the peak compressive strain ever reached. However, it is assumed that the material can sustain its full uniaxial tensile strength if the peak compressive strain ever reached has not exceeded ε_0, which corresponds to the strain at the peak compressive stress. When the compressive strain exceeds ε_0, the tensile

strength f_t in Eq. 2.1 is reduced in proportion to the loss of the compressive resistance with respect to the peak strength with the formula shown in Eq. 2.3

$$f_t = f_{t,ini} \cdot \left(1 - \frac{\left\langle \varepsilon_0 - \min\left(\varepsilon_{\min,\alpha} \ , \varepsilon_{\min,\beta} \right) \right\rangle}{\varepsilon_0 - \varepsilon_u} \right) \tag{2.3}$$

in which $\langle \cdot \rangle$ represent Macaulay brackets and $f_{t,ini}$ is specified material property that denotes the uniaxial tensile strength. The same reduction is applied to the shear strength computed when the material is in the cracked state.

The material model is implemented in a shell element for strain-driven analysis, for which the strains change in an incremental manner. Let x and y axes define the in-plane local coordinates of the shell element. Consider that the values of the stresses $\boldsymbol{\sigma}^m = \left\{ \sigma_x^m \quad \sigma_y^m \quad \tau_{xy}^m \right\}^{\mathrm{T}}$ and the internal variables of the material model at step *m* have been updated for the given strain history. Now, the stresses $\boldsymbol{\sigma}^{m+1} = \left\{ \sigma_x^{m+1} \quad \sigma_y^{m+1} \quad \tau_{xy}^{m+1} \right\}^{\mathrm{T}}$ and the values of the internal variables at step *m*+1 need to be calculated given the strains $\boldsymbol{\varepsilon}^{m+1} = \left\{ \varepsilon_x^{m+1} \quad \varepsilon_y^{m+1} \quad \gamma_{xy}^{m+1} \right\}^{\mathrm{T}}$. For this purpose, the stress-update algorithms shown in Box 2.1 and Box 2.2 are used for the uncracked and cracked states of the orthotropic material model, respectively. As shown, the stress update is carried out in the orthotropic directions, α and β. The internal variables consist of $\varepsilon_{\max,\alpha}$, $\varepsilon_{\min,\alpha}$, $\varepsilon_{\max,\beta}$ and $\varepsilon_{\min,\beta}$, representing the maximum tensile strains and maximum compressive strains reached along the α and β directions. The angle of the orthotropic axes with respect to the x - y axes is denoted by θ and is measured in the counterclockwise direction. Before cracking, θ represents the direction of the maximum principal strains. After cracking, it represents the direction normal to the crack. The

stress and strain values in the two coordinate systems are related by the standard transformation relations as shown for the case of stress transformation by Eq. 1.4.

$$\begin{Bmatrix} \sigma_x^{m+1} \\ \sigma_y^{m+1} \\ \tau_{xy}^{m+1} \end{Bmatrix} = \mathbf{R}\left(-\theta^{m+1}\right) \begin{Bmatrix} \sigma_\alpha^{m+1} \\ \sigma_\beta^{m+1} \\ \tau_{\alpha\beta}^{m+1} \end{Bmatrix} \tag{2.4}$$

where

$$\mathbf{R}(\theta) = \begin{bmatrix} \cos^2\theta & \sin^2\theta & 2\cos\theta\sin\theta \\ \sin^2\theta & \cos^2\theta & -2\sin\theta\cos\theta \\ -\cos\theta\sin\theta & \cos\theta\sin\theta & \cos^2\theta - \sin^2\theta \end{bmatrix}$$

The orthotropic model is overlaid with smeared steel reinforcement. The steel layer has reinforcement in two orthogonal directions, $s1$ and $s2$, respectively. Let θ_{s1} be the angle of $s1$ with respect to x axis, measured in the counterclockwise direction. The stresses contributed by the reinforcement can be added to the stresses from the orthotropic smeared-crack model as shown in Eq. 2.5.

$$\boldsymbol{\sigma}_{tot}^{m+1} = \boldsymbol{\sigma}^{m+1} + \mathbf{R}\left(-\theta_{s1}\right) \begin{Bmatrix} \rho_1 \cdot \sigma_{s1} \\ \rho_2 \cdot \sigma_{s2} \\ 0 \end{Bmatrix}^{m+1} \tag{2.5}$$

in which σ_{s1} and σ_{s2} are the stresses in the reinforcing steel along the $s1$ and $s2$ axes, respectively, and ρ_1 and ρ_2 are the corresponding reinforcement ratios.

Given: internal variables $\varepsilon_{\min,\alpha}$ and $\varepsilon_{\min,\beta}$, and the strains $\boldsymbol{\varepsilon}^{m+1} = \left\{ \varepsilon_x^{m+1} \quad \varepsilon_y^{m+1} \quad \gamma_{xy}^{m+1} \right\}^{\mathrm{T}}$

If the material is uncracked:

1) Since the axes of orthotropy are parallel to the axes of the principal strains, the strain vector $\left\{ \varepsilon_\alpha^{m+1} \quad \varepsilon_\beta^{m+1} \right\}^{\mathrm{T}}$ and the angle θ^{m+1} are calculated as follows:

$$\varepsilon_\alpha^{m+1} = \frac{\varepsilon_x^{m+1} + \varepsilon_y^{m+1}}{2} + \sqrt{\left(\frac{\varepsilon_x^{m+1} - \varepsilon_y^{m+1}}{2} \right)^2 + \left(\frac{\gamma_{xy}^{m+1}}{2} \right)^2}$$

$$\varepsilon_\beta^{m+1} = \frac{\varepsilon_x^{m+1} + \varepsilon_y^{m+1}}{2} - \sqrt{\left(\frac{\varepsilon_x^{m+1} - \varepsilon_y^{m+1}}{2} \right)^2 + \left(\frac{\gamma_{xy}^{m+1}}{2} \right)^2}$$

$$\tan\left(2\theta^{m+1}\right) = \frac{\gamma_{xy}^{m+1}}{\varepsilon_x^{m+1} - \varepsilon_y^{m+1}}$$

2) Calculate $\sigma\left(\varepsilon_{\min,\alpha}\right)$ and $\sigma\left(\varepsilon_{\min,\beta}\right)$ with Eq. 2.1, and then ε_{pl} and f_t with Eqs. 2.2 and 2.3.

3) IF $\varepsilon_\alpha^{m+1} \geq \varepsilon_{pl}$ THEN

   IF $\varepsilon_\alpha^{m+1} \leq 0$ THEN $\sigma_\alpha^{m+1} = 0$ END

   IF $\varepsilon_\alpha^{m+1} > 0$ THEN $\sigma_{\alpha,TRIAL}^{m+1} = E_m \cdot \varepsilon_\alpha^{m+1}$, and set $\varepsilon_{\max,\alpha} = \varepsilon_\alpha^{m+1}$ if $\varepsilon_{\max,\alpha} < \varepsilon_\alpha^{m+1}$ END

   IF $\sigma_{\alpha,TRIAL}^{m+1} > f_t$ THEN set $\theta_{cr} = \theta^{m+1}$, and $\sigma_\alpha^{m+1} = f_t \cdot \exp\left[\dfrac{-m_t\left(\varepsilon_\alpha^{m+1} - f_t / E_m\right)}{f_t} \right]$ ELSE

   $\sigma_\alpha^{m+1} = \sigma_{\alpha,TRIAL}^{m+1}$ END

   ELSE

   IF $\varepsilon_\alpha^{m+1} \geq \varepsilon_{\min,\alpha}$ THEN $\sigma_\alpha^{m+1} = E_m \cdot \left(\varepsilon_\alpha^{m+1} - \varepsilon_{pl}\right)$

   ELSE calculate σ_α^{m+1} with Eq. 2.1 and set $\varepsilon_{\min,\alpha} = \varepsilon_\alpha^{m+1}$ END

   END

4) Update the stress σ_β^{m+1} for the second axis of orthotropy using the procedure in Step 3 with the subscript α replaced by β.

Box 2.1 Stress update algorithm when the orthotropic model is uncracked.

Given: internal variables $\varepsilon_{\min,\alpha}$ and $\varepsilon_{\min,\beta}$, $\varepsilon_{\max,\alpha}$ and $\varepsilon_{\max,\beta}$, and the strains $\boldsymbol{\varepsilon}^{m+1} = \left\{ \varepsilon_x^{m+1} \quad \varepsilon_y^{m+1} \quad \gamma_{xy}^{m+1} \right\}^{\mathrm{T}}$

If the material is cracked:

1) Set $\theta^{m+1} = \theta_{cr}$ and calculate the strains in the orthotropic system as follows: $\begin{Bmatrix} \varepsilon_\alpha^{m+1} \\ \varepsilon_\beta^{m+1} \\ \gamma_{\alpha\beta}^{m+1} \end{Bmatrix} = \mathbf{T}\left(\theta^{m+1}\right) \begin{Bmatrix} \varepsilon_x^{m+1} \\ \varepsilon_y^{m+1} \\ \gamma_{xy}^{m+1} \end{Bmatrix}$, with $\mathbf{T}(\theta) = \begin{bmatrix} \cos^2\theta & \sin^2\theta & \cos\theta\sin\theta \\ \sin^2\theta & \cos^2\theta & -\sin\theta\cos\theta \\ -2\cos\theta\sin\theta & 2\cos\theta\sin\theta & \cos^2\theta - \sin^2\theta \end{bmatrix}$.

2) Calculate $\sigma\left(\varepsilon_{\min,\alpha}\right)$ and $\sigma\left(\varepsilon_{\min,\beta}\right)$ with Eq. 2.1, and ε_{pl} and f_t with Eqs. 2.2 and 2.3.

3) IF $\varepsilon_\alpha^{m+1} \geq \varepsilon_{pl}$ THEN

   IF $\varepsilon_\alpha^{m+1} \leq 0$ THEN $\sigma_\alpha^{m+1} = 0$

   ELSE IF $\varepsilon_\alpha^{m+1} \leq \varepsilon_{\max,\alpha}$ THEN $\sigma_\alpha^{m+1} = f_t \cdot \exp\left[\dfrac{-m_t\left(\varepsilon_{\max,\alpha} - f_t / E_m\right)}{f_t} \right] \cdot \dfrac{\varepsilon_\alpha^{m+1}}{\varepsilon_{\max,\alpha}}$

   ELSE IF $\varepsilon_\alpha^{m+1} > \varepsilon_{\max,\alpha}$ THEN $\sigma_\alpha^{m+1} = f_t \cdot \exp\left[\dfrac{-m_t\left(\varepsilon_\alpha^{m+1} - f_t / E_m\right)}{f_t} \right]$ and set $\varepsilon_{\max,\alpha} = \varepsilon_\alpha^{m+1}$ END

   IF $\sigma_{\alpha,TRIAL}^{m+1} > f_t$ THEN $\sigma_\alpha^{m+1} = f_t \cdot \exp\left[\dfrac{-m_t\left(\varepsilon_\alpha^{m+1} - f_t / E_m\right)}{f_t} \right]$ ELSE $\sigma_\alpha^{m+1} = \sigma_{\alpha,TRIAL}^{m+1}$

   END.

   ELSE

   IF $\varepsilon_\alpha^{m+1} \geq \varepsilon_{\min,\alpha}$ THEN $\sigma_\alpha^{m+1} = E_m \cdot \left(\varepsilon_\alpha^{m+1} - \varepsilon_{pl}\right)$ ELSE calculate σ_α^{m+1} from Eq. 2.1 and set $\varepsilon_{\min,\alpha} = \varepsilon_\alpha^{m+1}$ END

   END

4) Update the stress σ_β^{m+1} for the second axis of orthotropy using the procedure in Step 3 with the subscript α replaced by β.

5) Calculate the shear stress in the cracked coordinate system as follows: $\tau_{\alpha\beta}^{m+1} = \min\left\{ \max\left\{ \tau_{\alpha\beta}^m + G \cdot \Delta\gamma, -0.5 f_t \right\}, 0.5 f_t \right\}$.

Box 2.2 Stress update algorithm when the orthotropic model is cracked.

2.4.3 Calibration of material parameters and verification analysis

The model involves a small number of material parameters that can be calibrated based on material tests and recommendations from the literature. However, the parameters controlling the strain softening in compression and tension are dependent on the size of the shell element to preserve the objectivity of the numerical results in the post-peak region (Bažant and Planas, 1998). For a given compressive or tensile strain-softening relation, the post-peak behavior of the numerical solution in compression or tension will be sensitive to the element size due to the localization of the plastic strain in one row of elements perpendicular to the direction of loading, which determines the total fracture energy release. To avoid this numerical artifact, the fracture energy release must be regularized so that the total energy release will not be affected by the element size.

To calibrate the behavior of masonry in compression, a set of six grouted masonry prism tests have been selected to determine the material parameters. The prisms were tested by Mavros (2015) and had dimensions of 24 x 16 x 8 in. Each prism was made out of three 16 x 8 x 8 in. concrete masonry units.

The prisms are discretized with triangular elements that have a vertical and horizontal side of 4 in., which is found to be convenient to model masonry components made of 16 x 8 x 8 in. units. Vertical displacement is imposed at the top nodes while the bottom nodes are simply supported. Figure 2.10 shows that there can be great variability in the post-peak response obtained from different masonry prisms of the same set. To match the results in an average sense, a value of 0.040 has been selected for the crushing strain ε_u. To regularize the behavior of the model in compression, the crushing strain ε_u has to be changed if the element size is changed so that the total fracture energy remains the same. Furthermore, based on the experimental data, the modulus

of elasticity of masonry E_m is considered to be equal to $600 f_m$, the stress f_o at the end of the linear branch is taken equal to $2/3\, E_m$, and the strain at peak compressive stress ε_0 is considered to be equal to 0.003, where f_m is the compressive strength of masonry prisms. The modulus of elasticity selected is lower than the value of $900 f_m$ specified by the masonry design code (TMS 402-16) because it better reflects the prism test results.

For the tensile regime, the tensile strength f_t can be assumed to be equal to 10% of f_m if no specific experimental data are available. The parameter m_t is mesh-size dependent and is determined based on the procedure described by Burchnall (2014) and the condition that the mode-I fracture energy ($G_{f,I}$) of masonry be equal to the product of the area under the post-peak uniaxial stress-strain curve and the element length (L_e). Based on this, the parameter m_t is calculated by Eq. 2.6.

$$m_t = \frac{L_e \cdot f_t^2}{G_{f,I}} \tag{2.6}$$

For this purpose, the length L_e of a triangular element can be assumed to be equal to the square root of its area. The mode-I fracture energy is a material parameter that needs to be specified. In this study, it is assumed to be 0.0004 kips/in based on the recommendation of Koutromanos and Shing (2012).

To verify the performance of the orthotropic model and the validity of the calibration method, a reinforced masonry wall specimen tested by Sherman (2011) is simulated using only smeared-crack shell elements. The layout of the wall specimen and the finite element model are shown in Figure 2.11. The wall was fully grouted with dimensions of 72 x 40 x 8 in. and had

reinforcement consisting of 5 #6 vertical bars and 9 #4 horizontal bars. The wall was tested as a cantilever under a constant vertical load of 48 kips and a cyclic lateral displacement history applied quasi-statically at the top. In the test, the wall developed a flexure-dominated failure with toe crushing and buckling of the exterior vertical bars, as shown in Figure 2.12. The wall is discretized with triangular shell elements that have two perpendicular sides with a length of 4 in. The vertical and horizontal reinforcement is smeared and is modeled with a bilinear law with kinematic hardening and a strain-hardening ratio of 1%. Elastic shell elements are used to model the concrete footing and loading beam. The compressive strength of masonry is 2.77 ksi and the tensile yield strengths of the vertical and horizontal reinforcement are 65.4 ksi and 66.2 ksi, respectively. The material parameters of the orthotropic model are specified as described above.

As shown in Figure 2.12a, the model can predict well the peak strength of the wall. The model can also predict well the extent of crushing along the length of the wall, as it is indicated by the compressive strains shown in Figure 2.12c. As expected, the model cannot capture the extent of crushing along the wall height due to the strain localization phenomenon. The difference in the shapes of the loading-unloading curves between the analysis and the experiment can be attributed to the linear hardening law used for the reinforcement in the analysis and the fact that bond-slip was not accounted for. The reduced resistance observed in the last cycle of testing was due to the buckling of the vertical bars; the model used here ignores this phenomenon. The model greatly overestimates the initial stiffness of the wall. This can be partly due to the perfect bond assumed between the reinforcement and the grout, and also to the fact that the lower tensile strength in the wall-footing interface is not modeled.

The performance of the smeared-crack shell elements will be worse for a shear-dominated wall due to the aforementioned stress locking phenomenon. A refined finite element modeling

scheme using a combination of smeared-crack shell elements, cohesive-crack interface elements, bond-slip/dowel action interface elements, discrete beam elements for the reinforcing bars, and an element removal scheme aims to address the deficiencies of the smeared-crack modeling approach.

2.5 Cohesive-Crack Interface Element

The smeared-crack approach is simple, computationally efficient, and can capture well the effect of diffused fine cracks in reinforced masonry structures. However, as already discussed, there are numerous problems inherent to smeared-crack models, such as the mesh-size dependency caused by the localization of plastic strains in the post-peak regime, and the stress locking phenomenon that prevents realistic modeling of the brittle shear behavior induced by diagonal tensile cracks. Furthermore, smeared-crack elements are unable to capture shear sliding that can develop along a crack. To resolve these deficiencies, the smeared-crack shell elements are combined with cohesive-crack interface elements. The cohesive-crack interface elements can model in a realistic manner diagonal and horizontal cracks and can alleviate the mesh-size sensitivity of the smeared-crack elements under tensile softening.

Several constitutive models with different degrees of sophistication have been proposed to simulate the fracture and friction behavior of discrete cracks in concrete or masonry structures. Among others, the models of Lotfi and Shing (1994), Cervenka (1994), Carol et al. (1997), Mehrabi and Shing (1997), Oliveira and Lourenço (2004), Puntel et al. (2006), and Koutromanos and Shing (2012) are based on an elasto-plastic formulation under the plane-stress condition that is intended for two-dimensional analyses of concrete and masonry structures. This study adopts a model proposed by Kottari (2016), which is an extension of the model of Koutromanos and Shing (2012) to three dimensions. The cohesive-crack model can simulate mixed-mode (mode-I, II, and III) fracture, crack opening and closing, and relative shear sliding in an interface. The model also

accounts for the reversible normal dilatation and irreversible compaction that occurs in an interface when it is subjected to cyclic shear deformation based on the formulation of Koutromanos and Shing (2012). The model is used together with a zero-thickness interface element that is available in LS-DYNA.

2.5.1 Interface element formulation

The interface element adopted is available in LS-DYNA. It has four nodes and a configuration shown in Figure 2.13. The first two nodes, namely nodes 1 and 2, define its bottom surface and the other two its top surface. In element's undeformed state, the nodes of the top and bottom surface are coincident. The element is formulated to be compatible with the shell elements used in this study in that it has six degrees of freedom per node. Furthermore, as in the shell elements, linear shape functions are used to interpolate the displacements and rotations along the top and bottom surfaces of the interface. The deformation of the interface is calculated from the relative displacement between the two surfaces and has three components. These consist of the relative normal displacement d_n and the two relative shear displacements d_t and d_s along the longitudinal and transverse axes of the element, respectively, as shown in Figure 2.13. The corresponding stress components consist of the normal stress σ_n and the two shear stresses τ_t and τ_s. The nodal forces and moments are obtained by the integration of the normal and shear stresses along the element surface using Gauss quadrature with four integration points.

The interface element has a co-rotational local coordinate system and can thus be used in analyses involving large rigid-body rotations. Its local coordinate system is updated at every step of the solution based on the position of the two shell elements that the interface is connected to. As shown in Figure 2.13, local axis q_1 defines the direction of out-of-plane shear, local axis q_2

defined the direction of in-plane shear, and local axis q_3 defines the direction of normal opening. The calculation of the element local coordinate system starts by establishing the direction of local axis q_2 as the average of the directions of the top and bottom sides of the element. Local axis q_1 is defined so that its direction is in the average direction of the out-of-plane vectors normal to the upper and lower shell elements, respectively, and is made orthogonal to axis q_2 through an orthogonalization operation. Local axis q_3 is calculated so that it is orthogonal to axes q_1 and q_2. The disadvantage of this approach is that the interface element needs to be connected to shell elements at both sides and track the Cartesian coordinates of eight nodes during the analysis. Furthermore, connecting more than one shell elements to a single side of an interface element may result in a coordinate system that is not desirable. Further details about the definition of the element local system and the formulation of the element can be found in LS-DYNA Theory Manual (2018).

2.5.2 Cohesive-crack interface law

The cohesive-crack material law that is used with the interface elements adopts an elasto-plastic formulation. The material law was originally developed by Koutromanos and Shing (2012) for two-dimensional finite-element models and was extended by Kottari (2016) for three-dimensional models. The constitutive model was implemented in the finite element analysis program LS-DYNA for the purpose of this study. In this section, the cohesive-crack interface law is briefly summarized to define the material parameters that govern the response of the cohesive-crack interface elements.

To account for the different deformation modes of an interface, namely, the crack normal opening, shear sliding, joint compaction, and normal dilatation, the relative displacement vector

of the interface element is decomposed into three components as it was originally proposed by Mehrabi and Shing (1997)

$$\mathbf{d} = \left\{ d_n \quad d_t \quad d_s \right\}^T = \mathbf{d}^e + \mathbf{d}^p + \mathbf{d}^g \tag{2.7}$$

where $\mathbf{d}^e = \left\{ d_n^e \quad d_t^e \quad d_s^e \right\}^T$ is the elastic part, $\mathbf{d}^p = \left\{ d_n^p \quad d_t^p \quad d_s^p \right\}^T$ is the plastic part, and $\mathbf{d}^g = \left\{ d_n^g \quad 0 \quad 0 \right\}^T$ is the geometric part. The latter has only a normal component that represents the reversible joint dilatation introduced by the wedging action of the joint asperities when the joint is subjected to shear sliding.

The inelastic behavior of the interface is governed by the yield criterion of Eq. 2.8. Any inelastic displacement increment should result in a stress state that satisfies the yield condition $F = 0$. If $F < 0$ means that the displacement increment was all elastic.

$$F = \tau_s^2 + \tau_t^2 - \mu^2 \cdot (\sigma - s)^2 - 2 \cdot r \cdot (\sigma - s) = 0 \tag{2.8}$$

The yield criterion describes the yield surface shown in Figure 2.14. The surface has the shape of a hyperboloid in the three-dimensional stress space but reduces to a two-dimensional hyperbola if the out-of-plane shear stress is equal to zero. The shape of the three-dimensional surface can be obtained by the revolution of the hyperbola about the normal stress axis. The hyperbola is defined in terms of the three material parameters, s, μ, and r, as shown in Eq. 2.8. Parameter s is the tensile strength of the interface, μ is the slope of the asymptotes of the hyperbola, and r is the radius of curvature at the apex of the hyperbola. The values of the three parameters can decrease based on the accumulation of damage in the interface, causing the yield surface to shrink and shift from its initial state to the residual state, as shown in Figure 2.14. The

following set of equations is used to describe the change of s, μ, and r with respect to the plastic work:

$$s = s_o\left(1 - \frac{\kappa_1}{G_{f,I}} - \frac{\kappa_2}{G_{f,II}}\right) \tag{2.9}$$

$$\mu = \left(\mu_o - \mu_r\right)e^{-\alpha\kappa_3} + \mu_r \tag{2.10}$$

$$r = \left(r_o - r_r\right)\cdot e^{-\beta\kappa_3} + r_r \tag{2.11}$$

where s_o, μ_o, r_o, μ_r, and r_r are the specified initial and residual values of the material parameters, defining the initial and residual yield surfaces; $G_{f,I}$ and $G_{f,II}$ are the specified mode-I and mode-II fracture energies; and κ_1 and κ_2, represent the cumulative plastic work associated to mode-I and mode-II fractures, respectively, while κ_3 represents the cumulative frictional work that is related to the smoothening of the sliding surface. Variables α and β are specified material properties that govern the rate of change of μ and r with respect to the plastic work. To simplify the terminology, parameter μ will be hereafter referred to as the friction coefficient because the yield criterion reduces to the Mohr-Coulomb criterion for low values of r.

Based on Kottari (2016), the reversible geometric dilatation is calculated incrementally as a function of the plastic shear displacement based on the following expression that is in rate form:

$$\dot{d}_n^g = \zeta_{dil}\dot{d}_{res}^p \tag{2.12}$$

where ζ_{dil} is the coefficient of dilatation and d_{res}^p is the magnitude of the resultant plastic shear displacement given by:

$$d_{res}^{p} = \sqrt{\left(d_{t}^{p}\right)^{2} + \left(d_{s}^{p}\right)^{2}} \tag{2.13}$$

The coefficient of dilatation is assumed to decrease as the magnitude of the plastic shear displacement increases based on the following equation:

$$\zeta_{dil} = \left(\zeta_{dil,o} - \zeta_{dil,r}\right) \cdot \exp\left(-\frac{d_{res}^{p}}{d_{0}}\right) + \zeta_{dil,r} \tag{2.14}$$

where $\zeta_{dil,o}$, $\zeta_{dil,r}$, and d_0 are specified material parameters that define the geometric profile of the asperities, with $\zeta_{dil,r} \le \zeta_{dil,o}$. As described in Koutromanos and Shing (2012), parameters $\zeta_{dil,o}$ and $\zeta_{dil,r}$ represent the values of the initial and residual slopes of the asperities under an increasing magnitude of shear displacement, while d_0 determines the rate of decrease of the slope. Upon removal of the plastic shear displacement, the coefficient of dilatation returns to its initial value $\zeta_{dil,o}$ indicating its reversible nature. In Eqs. 2.12 to 2.14 it is stipulated that the geometric profile of the asperities is axisymmetric about the axis normal to the surface of the interface, meaning that the amount of geometric dilatation depends only on the magnitude of the resultant plastic shear displacement and not on its direction.

The plastic component of the relative displacement vector shown in Eq. 2.7 includes the plastic shear displacements due to sliding, the plastic normal displacement due to tensile fracture, and the irreversible joint compaction. The plastic displacement vector is calculated incrementally based on a non-associated flow rule:

$$\dot{\mathbf{d}}^{p} = \dot{\lambda}\mathbf{m} \tag{2.15}$$

where $\dot{\lambda}$ is a plastic multiplier, and $\mathbf{m}$ is a vector that defines the direction of plastic flow. The direction of vector $\mathbf{m}$ is determined as follows. If the normal stress is compressive, vector $\mathbf{m}$ is determined from a plastic potential function Q as

$$\mathbf{m} = \frac{\partial Q}{\partial \boldsymbol{\sigma}} \tag{2.16}$$

where $\boldsymbol{\sigma} = \{\sigma_n \quad \tau_t \quad \tau_s\}^T$ is the vector of stresses and

$$Q = \frac{1}{2}\eta\tau_t^2 + \frac{1}{2}\eta\tau_s^2 + \frac{1}{2}\sigma^2 \tag{2.17}$$

The variable η is a specified material parameter that controls the amount of normal compaction for a given plastic shear displacement. Smaller values of η result in more severe compaction. If the normal stress is tensile, vector $\mathbf{m}$ takes a different form allowing for the behavior of the interface in tension and compression to be modeled independently. In that case, the components of vector $\mathbf{m}$ are determined from the equations:

$$m_1 = \frac{\sigma^{el} / D_{nn}}{\sqrt{\left(\frac{\sigma^{el}}{D_{nn}}\right)^2 + \left(\frac{\tau_t^{el}}{D_{tt}}\right)^2 + \left(\frac{\tau_s^{el}}{D_{tt}}\right)^2}}$$

$$m_2 = \frac{\tau_t^{el} / D_{tt}}{\sqrt{\left(\frac{\sigma^{el}}{D_{nn}}\right)^2 + \left(\frac{\tau_t^{el}}{D_{tt}}\right)^2 + \left(\frac{\tau_s^{el}}{D_{tt}}\right)^2}} \tag{2.18}$$

$$m_3 = \frac{\tau_s^{el} / D_{tt}}{\sqrt{\left(\frac{\sigma^{el}}{D_{nn}}\right)^2 + \left(\frac{\tau_t^{el}}{D_{tt}}\right)^2 + \left(\frac{\tau_s^{el}}{D_{tt}}\right)^2}}$$

where, σ^{el}, τ_t^{el} and τ_s^{el} are the components of an elastic predictor stress vector, and D_{nn} and D_{tt} are the elastic stiffness constants in the normal and shear directions, respectively.

Given the relative displacements of the interface, the plastic displacements, the geometric dilatation, and the normal and shear stresses of the interface are calculated as follows:

$$\sigma = -D_{nn}\left\langle d_{n1} - d_n \right\rangle + D_{nn}\left\langle d_n - d_{n2} \right\rangle \tag{2.19}$$

$$\tau_t = D_{tt}\left(d_t - d_t^p\right) \tag{2.20}$$

$$\tau_s = D_{tt}\left(d_s - d_s^p\right) \tag{2.21}$$

in which $\langle\cdot\rangle$ represent Macaulay brackets. As illustrated in Figure 2.15, parameters d_{n1} and d_{n2} define the range of values of the normal relative displacement for which the normal stress is equal to zero during unloading and reloading in the normal direction. This range depends on the amount of joint compaction, geometric dilatation, and plastic normal displacement under tension. Compressive stress develops only when d_n becomes smaller than d_{n1}, signifying that the crack has been fully closed. The two parameters evolve according to the following expressions:

$$\dot{d}_{n1} = -\left\langle \dot{d}_n^p \right\rangle + \dot{d}_n^g \tag{2.22}$$

$$\dot{d}_{n2} = \dot{d}_n^p \tag{2.23}$$

The numerical implementation of the cohesive-crack material model is presented in Kottari (2016) and Koutromanos and Shing (2012). Validation of the material model against experimental data for concrete and masonry can be found in Koutromanos and Shing (2012).

2.5.3 Behavior of the cohesive-crack interface model and selection of material parameters

In this study, the cohesive-crack material model has been used to simulate the fracture and sliding behavior of cracks in grouted and ungrouted masonry as well as mortar joints. The behavior of the model for each case is governed by a number of parameters that need to be specified. The values of some parameters can be determined based on recommendations in the literature when experimental data are not available, while others can be calibrated directly with material test data or indirectly with experimental data from wall tests. Table 2.1 shows the values for the material parameters used in analyses presented in the following chapters for cracks in grouted concrete masonry and mortar joints in ungrouted concrete masonry. To show how the two sets of material parameter values affect the response of the cohesive-crack model, a simple analysis is performed in LS-DYNA using a single interface element subjected to shear as shown in Figure 2.16.

The parameter values used for cracks in grouted masonry are determined as follows. The elastic stiffness constants of the interface are assigned very high values to avoid unrealistic deformation before cracking and crack penetration upon crack closing. The tensile strength s_o is assumed to be equal to the tensile strength $f_{t,ini}$ of grouted masonry. In the analyses presented in the following chapters, the tensile strength is assumed to be in the range of 8%-12% of the masonry compressive strength f_m. In the specific example, the tensile strength is taken equal to 0.3 ksi. The mode-I fracture energy $G_{f,I}$ is specified to be 0.0004 kips/in based on the recommendation of Koutromanos and Shing (2012) for concrete. The mode-II fracture energy is assumed to be 10 times the value of mode-I fracture energy. The values of the initial and residual friction coefficient are assumed to be 1.40 and 1.00, while parameters $\zeta_{dil,o}$, $\zeta_{dil,r}$, and d_o, which control the geometric dilatation, are assigned values 0.40, 0.001, and 0.40 respectively. The values shown in

Table 2.1 for the rest of the parameters, namely, r_o, r_r, α, β, and η, are similar to the ones proposed by Koutromanos and Shing (2012) for modeling cracks in concrete.

As shown in Table 2.2, the material parameters used for a mortar joint in ungrouted masonry reflect a lower tensile strength and a lower shear resistance as compared to those for a crack in grouted masonry. The normal stiffness of the interface is calculated based on the elastic modulus of the mortar and the thickness of the joint assuming uniaxial compression. For this purpose, the mortar joint is assumed to be 3/8 in. The elastic modulus of the mortar is selected so that when the interface is combined with the adjacent shell elements representing masonry units, the axial stiffness of the masonry assembly is well represented. The shear stiffness of the mortar joint is determined from the shear modulus and joint thickness. The shear modulus is calculated from the elastic modulus by assuming an isotropic material with Poisson's ratio equal to 0.2. The tensile strength assigned to the interface corresponds to the tensile bond strength between the mortar and the concrete masonry unit. The tensile strength of 0.10 ksi selected here has been used in analyses presented in the following chapters. The initial and residual friction coefficients are assumed to be 0.95 and 0.85, respectively. These values are consistent with the coefficient of friction obtained from direct shear tests conducted by Mehrabi (1994) on mortar joints in hollow concrete units. The mode-I and mode-II fracture energies are assumed to be half of the ones used for cracks in grouted masonry. Lower values are also used for r_o and for the parameters defining the geometric dilatation. The remaining parameters are assumed to be the same as for cracks in grouted masonry.

The model shown in Figure 2.16 is subjected to cyclic out-of-plane shear displacement under a constant compressive stress of 100 psi. The responses of the interface obtained for the two sets of material parameters are shown in Figure 2.17. It can be observed that the crack for grouted

masonry has a much higher cohesive resistance than the mortar joint and also develops a normal displacement that is governed by the reversible geometric dilatation. For the case of the mortar joint, the geometric dilatation is much lower, and the normal displacement is eventually controlled by the irreversible joint compaction.

2.6 Beam Elements for Steel Reinforcing Bars

Reinforcing steel bars are modeled with beam elements that have the formulation proposed by Hughes and Liu (LSTC 2019). This formulation accounts for geometric nonlinearity and is available in LS-DYNA. Although beam elements are computationally more demanding than truss elements, they can capture the effects of bar buckling and dowel action in a realistic manner. The beam elements used in this study have a single integration section along the length and a total of four fibers for the integration of stresses over the section.

The stress-strain response of each fiber is described by the uniaxial steel constitutive model of Kim and Koutromanos (2016). The model is essentially an improved formulation of the material law previously proposed by Dodd and Restrepo-Posada (1995) in that it eliminates the need for iterations in the stress update procedure and also allows for the calculation of the material tangent stiffness through a closed-form expression. This was achieved by introducing non-uniform rational *b*-splines (NURBS) to define in an explicit manner the hysteretic cyclic response of the material and circumvent the iterative procedure that the original model of Dodd and Restrepo-Posada (1995) required. The material model of Kim and Koutromanos (2016) also accounts for rupture under monotonic and cyclic loading using a criterion related to the accumulation of work under inelastic strains.

The material model can accurately describe the salient features of the monotonic and cyclic response of a steel reinforcing bar. It accounts for the yield plateau and subsequent strain hardening

under monotonic loading and the Bauschinger effect and kinematic hardening under cyclic loading. The cyclic response of the model is based on the monotonic stress-strain curve. The formulation of the material is in terms of the natural strains and natural (true) stresses since the monotonic response of a steel bar in tension and compression becomes practically symmetric (when no buckling occurs) when expressed in terms of these stress and strain measures as explained in Dodd and Restrepo (1995).

A total of seven material parameters are used for the description of the monotonic stress-strain curve as shown in Figure 2.18a. These consist of the initial elastic modulus E_s, the yield stress f_y, the strain ε_{sh} at the onset of strain hardening, the ultimate strength f_{su} and the corresponding strain ε_{su}, and the stress f_{sh1} and strain ε_{sh1} of a point that lies in the strain-hardening region. The strain-hardening region is defined as a curve that passes through points (ε_{sh}, f_y), (ε_{sh1}, f_{sh1}), and (ε_{su}, f_{su}) and has zero slope at the point of ultimate strength in the engineering stress-strain system. Based on the original material model of Dodd and Restrepo-Posada (1995), load reversals in the inelastic regime are generally described by a linear unloading region, which has an unloading modulus that is lower than E_s, and a curved region, as shown in Figure 2.18b. In the formulation of Kim and Koutromanos (2016), the curved region is described with quadratic NURBS that have three control points, as it is qualitatively depicted in Figure 2.18c.

Rebar rupture is accounted for in an empirical manner through a criterion that is based on a scalar variable, D. The criterion adopted is a uniaxial version of the one proposed by Huang and Mahin (2010) for the simulation of rupture due to low-cycle fatigue in structural steel members. Based on that, rupture occurs when the scalar variable D exceeds a critical threshold D_{cr}. The

evolution of D is associated with the accumulation of inelastic work under tensile stress and is defined by the following equation in rate form

$$\dot{D} = \begin{cases} \left(\dfrac{\dot{f}}{f_y} \right)^{2t} \dot{\varepsilon}_p, \text{ if } f > 0 \\ 0, \text{ otherwise} \end{cases} \tag{2.24}$$

where f is the stress, t is a material constant, and $\dot{\varepsilon}_p$ is the rate of plastic strain. When rupture is registered in all the fibers of a cross section, the corresponding beam element is considered ruptured.

The materials parameters that define the stress-strain response and the rupture criterion of the steel model can be determined from a given monotonic tensile stress-strain curve of a reinforcing bar. Parameter t is taken equal to 1.0, as suggested by Moharrami and Koutromanos (2017). Parameter D_{cr} is set equal to $D_{cr,mon}$, where $D_{cr,mon}$ is the value of D_{cr} required to capture the occurrence of rupture in a monotonic tensile test. Figure 2.19 shows an example of a stress-strain envelop that has been calibrated to match an experimentally obtained monotonic loading response up to the point the rebar specimen ruptured. Kim and Koutromanos (2016) have shown that using $D_{cr} = D_{cr,mon}$ can also predict well the occurrence of rupture under cyclic loading conditions for bars subjected to pure axial load. Figure 2.20 shows the response of the material model under a cyclic loading scenario and the evolution of D until rupture occurs. However, when the material model is used together with beam elements to simulate the response of reinforcing bars subjected to combined axial and bending deformation, Moharrami and Koutromanos (2017) found that D_{cr} should be increased to $2.4D_{cr,mon}$ to obtain reasonable agreement with experimental results. This threshold is adopted in this study.

2.7 Bond-Slip and Dowel Action Interface Element

The beam elements representing the steel reinforcement are attached to the masonry shell elements through interface elements that simulate the bond-slip and dowel-action behaviors of the reinforcing bars. The interface element used in this study has been implemented as a user-defined element in LS-DYNA using the formulation proposed by Mavros (2015) and Kottari et al. (2018), which allows for the connection of beam elements to shell elements that have a larger size. To model the bond slip and dowel action of bars, the bars often require a finer mesh than what is needed to model the nonlinear behavior of masonry or concrete. The adopted interface element formulation provides this flexibility. In this study, beam elements with lengths two to four times the bar diameter are used depending on the location of the reinforcing bar. To model bond-slip, the phenomenological bond-slip law developed by Murcia-Delso and Shing (2014) is adopted with certain modifications. To model the dowel-action effect, a simple uniaxial material law is proposed to simulate the lateral interaction of the bar with the adjacent concrete or masonry. To account for large rigid-body rotations, the interface element has been implemented with a local coordinate system that is updated based on the deformed configuration of the element. The original element by Mavros (2015) was limited to small rotations.

2.7.1 Element formulation

The interface element has 4 nodes. Nodes 1 and 2 are attached to the beam element representing the reinforcing bar, while nodes 3 and 4 are attached to the adjacent shell element representing the masonry or concrete, as shown in Figure 2.21. In the undeformed configuration, the steel and masonry sides are parallel to each other, while they can rotate with respect to each other during the analysis based on the positions of the four nodes. The element coordinate system is updated based on the deformed configuration of the element. Local axis x is defined so that it

is always along the direction of nodes 4 and 3, while local axes y and z are defined so that they are orthogonal to x and to each other. In the undeformed configuration, local axis z is specified as input so that it is normal to the plane of the wall.

The deformation of the interface element consists of four components that are calculated from Eq. 2.25: 1) the relative shear displacement (slip), $\tilde{u}$, between the bar and the masonry along the direction x, 2) the relative displacements $\tilde{v}$ and $\tilde{w}$ normal to the slip, along axes y and z respectively, which represent the deformation of the masonry or concrete adjacent to the bar and any gap created by the dowel action, and 3) the relative axial rotation $\tilde{\theta}_x$, along axis x, between the bar and the masonry or concrete. The element degrees of freedom associated with each deformation component are uncoupled from the rest.

$$\begin{Bmatrix} \tilde{u} \\ \tilde{v} \\ \tilde{w} \\ \tilde{\theta}_x \end{Bmatrix} = \begin{Bmatrix} u_{steel}(x) - u_{masonry}(x) \\ v_{steel}(x) - v_{masonry}(x) \\ w_{steel}(x) - w_{masonry}(x) \\ \theta_{x,steel}(x) - \theta_{x,masonry}(x) \end{Bmatrix} \tag{2.25}$$

The displacements and axial rotation of the steel and masonry or concrete sides are calculated with linear shape functions, N_1 and N_2, in parametric coordinates, based on the nodal displacements and axial rotations of nodes 1 and 2, and 4 and 3, respectively. To account for the fact that the steel side may have a smaller length than the masonry or concrete side, Mavros (2015) introduced separate parametric coordinates for the two sides, namely, η_m and η for the masonry and steel side respectively. The two coordinates are related through the following equation:

$$\eta_m = \alpha + \beta \cdot \eta \tag{2.26}$$

in which

$$\alpha = \frac{L_{14} - L_{23}}{L_{34}} \tag{2.27}$$

$$\beta = \frac{L_{12}}{L_{34}} \tag{2.28}$$

The lengths L_{12}, L_{23}, L_{14}, and L_{34} in Eqs. 2.27 and 2.28 are in the physical coordinate system and are calculated once, at the beginning of an analysis, as schematically shown in Figure 2.22.

The element nodal force vectors, $\mathbf{F_x}$, $\mathbf{F_y}$, and $\mathbf{F_z}$, along directions x, y, and z, respectively, and the nodal moment vector $\mathbf{M_x}$ about the x-axis are calculated as:

$$\begin{aligned}
\mathbf{F_x} &= \pi d_b \int_{-1}^{1} \mathbf{b}^T(\eta) \cdot \tau(\eta) \frac{L_{12}}{2} d\eta \\
\mathbf{F_y} &= d_b \int_{-1}^{1} \mathbf{b}^T(\eta) \cdot \sigma_x(\eta) \frac{L_{12}}{2} d\eta \\
\mathbf{F_z} &= d_b \int_{-1}^{1} \mathbf{b}^T(\eta) \cdot \sigma_z(\eta) \frac{L_{12}}{2} d\eta \\
\mathbf{M_x} &= \pi d_b \int_{-1}^{1} \mathbf{b}^T(\eta) \cdot t(\eta) \frac{L_{12}}{2} d\eta
\end{aligned} \tag{2.29}$$

with d_b the bar diameter, and $\mathbf{b}(\eta)$ the vector that relates each of the four deformation components to the corresponding nodal displacements or axial rotations of the interface element and is given by

$$\mathbf{b}(\eta) = \begin{bmatrix} N_1(\eta) & N_2(\eta) & -N_2(\alpha + \beta\eta) & -N_1(\alpha + \beta\eta) \end{bmatrix} \tag{2.30}$$

The integrals in Eq. 2.29 are evaluated with Gauss quadrature using two integration points. Stress component τ corresponds to the bond stress developed along the direction of the slip, while σ_y and σ_z, correspond to the stresses developed perpendicular to the slip due to dowel action along

directions y and z. Stress t represents the shear stress developed in the circumference of the bar due to relative axial rotation of the bar with respect to the masonry. The stress is calculated through an elastic-perfectly plastic law with a low yield strength so that the generated moments $\mathbf{M}_x$ will not exceed the cracking moment of the masonry shell elements. This done only for the purpose of restraining the free rotation of the bar. The interface element has no stiffness associated with the rotational degrees of freedom about axes y and z. The restraints at these degrees of freedom are provided by the stiffness of the shell and beam elements the bond-slip/dowel-action interface is attached to.

2.7.2 Proposed co-rotational local coordinate system

To account for large rigid-body rotation, the element local system is updated at every step of the analysis. The directions of the local axes are calculated based on the nodal displacements and rotations of nodes 3 and 4. In this way, the local system of the interface element will depend only on the deformed configuration of the masonry or concrete shell element rather than of the reinforcement beam element, which may experience larger deformations. To obtain the element local system, a set of three orthonormal vectors is defined at each of the two nodes. The set of the three vectors will be hereafter referred to as the nodal triads. Figure 2.23 illustrates the nodal triads of nodes 3 and 4. The nodal triads at nodes 3 and 4 consist of the unit vectors $\mathbf{r}_{31}$, $\mathbf{r}_{32}$, $\mathbf{r}_{33}$ and $\mathbf{r}_{41}$, $\mathbf{r}_{42}$, $\mathbf{r}_{43}$ respectively, while the unit vectors of the element local system along the directions of the x, y, and z axes are named $\mathbf{v}_x$, $\mathbf{v}_y$, and $\mathbf{v}_z$ respectively. All the aforementioned vectors are column vectors. In the initial (undeformed) configuration, the nodal triads coincide with the element local system with $\mathbf{r}_{31}$ and $\mathbf{r}_{41}$ being coincident to $\mathbf{v}_x$, and $\mathbf{r}_{32}$ and $\mathbf{r}_{42}$ being coincident to

$\mathbf{v}_y$. During the analysis, the nodal triads are updated based on the nodal rotations at each respective node. Each nodal triad is updated through its respective rotation matrix.

At a step n of the analysis, the rotation matrices $\mathbf{R}_3^n = \begin{bmatrix} \mathbf{r}_{31}^n & \mathbf{r}_{32}^n & \mathbf{r}_{33}^n \end{bmatrix}$ and $\mathbf{R}_4^n = \begin{bmatrix} \mathbf{r}_{41}^n & \mathbf{r}_{42}^n & \mathbf{r}_{43}^n \end{bmatrix}$ associated with the respective nodal triads represent the rotation operation of the unit vectors $\mathbf{e}_1$, $\mathbf{e}_2$, $\mathbf{e}_3$ of the global coordinate system to the unit vectors of the respective triad. Several approaches can be used to update the nodal rotation matrices from step n to n+1. One approach is to use the second-order accurate formula proposed by Hughes and Winget (1980). Based on this, the rotation matrix $\mathbf{R}_\mathbf{I}^{n+1}$ of node I at step n+1 is calculated through the equation:

$$\mathbf{R}_\mathbf{I}^{n+1} = \left(\mathbf{I} - \frac{1}{2}\mathbf{S}\left(\Delta\boldsymbol{\theta}_\mathbf{I}\right) \right)^{-1} \left(\mathbf{I} + \frac{1}{2}\mathbf{S}\left(\Delta\boldsymbol{\theta}_\mathbf{I}\right) \right) \mathbf{R}_\mathbf{I}^n \tag{2.31}$$

where $\Delta\boldsymbol{\theta}_\mathbf{I} = \begin{bmatrix} \Delta\theta_{IX} & \Delta\theta_{IY} & \Delta\theta_{IZ} \end{bmatrix}^\mathrm{T}$ the rotation increments in the global coordinate system at node I from step n to n+1, and $\mathbf{S}\left(\Delta\boldsymbol{\theta}_\mathbf{I}\right)$ is a skew-symmetric tensor given by

$$\mathbf{S}\left(\Delta\boldsymbol{\theta}_\mathbf{I}\right) = \begin{bmatrix} 0 & -\Delta\theta_{IZ} & \Delta\theta_{IY} \\ \Delta\theta_{IZ} & 0 & -\Delta\theta_{IX} \\ -\Delta\theta_{IY} & \Delta\theta_{IX} & 0 \end{bmatrix} \tag{2.32}$$

Another approach is to express the rotation matrix as a function of four parameters called quartenions. In general, these are collectively represented as one quantity with a scalar part $\overline{q}$ and a vector part $\mathbf{q}$. For a rotation vector $\boldsymbol{\theta} = \begin{bmatrix} \theta_X & \theta_Y & \theta_Z \end{bmatrix}^T$ the quartenions are defined as

$$\overline{q} = \cos\frac{\theta}{2}, \qquad \mathbf{q} = \begin{bmatrix} \frac{\theta_X}{\theta}\sin\frac{\theta}{2} & \frac{\theta_Y}{\theta}\sin\frac{\theta}{2} & \frac{\theta_Z}{\theta}\sin\frac{\theta}{2} \end{bmatrix}^T \tag{2.33}$$

in which, $\theta = \left(\boldsymbol{\theta}^{\mathrm{T}}\boldsymbol{\theta}\right)^{1/2}$ the magnitude of the rotation vector.

Given the quartenions at node I at step n+1, the rotation matrix at step n+1 can be obtained by:

$$\mathbf{R}_{\mathbf{I}}^{n+1} = 2\left(\overline{q}_{I,n+1}^{2} - \frac{1}{2}\right)\mathbf{I} + 2\mathbf{q}_{I,n+1}\mathbf{q}_{I,n+1}^{T} + 2\overline{q}_{I,n+1}\mathbf{S}\left(\mathbf{q}_{I,n+1}\right) \tag{2.34}$$

in which, the tensor $\mathbf{S}\left(\mathbf{q}_{I,n+1}\right)$ is defined from Eq. 2.32. The quartenions at step n+1 are calculated based on the quartenions at step n using the equations:

$$\begin{aligned} \overline{q}_{I,n+1} &= \overline{q}_{I,n}\overline{q}_{I,2} - \mathbf{q}_{I,n}^{T}\mathbf{q}_{I,2} \\ \mathbf{q}_{I,n+1} &= \overline{q}_{I,n}\mathbf{q}_{I,2} + \overline{q}_{I,2}\mathbf{q}_{I,n} - \mathbf{q}_{I,n} \times \mathbf{q}_{I,2} \end{aligned} \tag{2.35}$$

in which, $\overline{q}_{I,2}$ and $\mathbf{q}_{I,2}$ are the quartenions related to the incremental rotation from step n to step n+1 and are obtained by substituting the incremental rotation $\Delta\boldsymbol{\theta}_{\mathbf{I}}$ in Eq. 2.33.

In this study, the quartenion approach is used to update the rotation matrices of nodes 3 and 4 at the beginning of every step of the analysis. This approach requires that the four quaternions of each node are stored as history variables of the element. Having calculated the nodal rotation matrices $\mathbf{R}_{\mathbf{3}}^{n+1}$ and $\mathbf{R}_{\mathbf{4}}^{n+1}$ of nodes 3 and 4 respectively, an average rotation matrix $\mathbf{R}_{\mathbf{av}}^{n+1} = \left[\mathbf{r}_{\mathbf{av1}}^{n+1} \quad \mathbf{r}_{\mathbf{av2}}^{n+1} \quad \mathbf{r}_{\mathbf{av3}}^{n+1}\right]^{T}$ can be obtained. To calculate $\mathbf{R}_{\mathbf{av}}^{n+1}$ through $\mathbf{R}_{\mathbf{3}}^{n+1}$ and $\mathbf{R}_{\mathbf{4}}^{n+1}$, the procedure described in Crisfield (1990) is adopted. Once the average rotation matrix is calculated, it is corrected so that $\mathbf{r}_{\mathbf{av1}}^{n+1}$ becomes coincident to $\mathbf{v}_{\mathbf{x}}^{n+1}$, which is defined along the direction of nodes 4 and 3. Based on Crisfield (1990), the other two element local vectors are calculated in an approximate manner through:

$$\mathbf{v}_{\mathbf{y}}^{n+1} = \mathbf{r}_{\mathbf{av2}}^{n+1} - \frac{(\mathbf{r}_{\mathbf{av2}}^{n+1})^T \mathbf{v}_{\mathbf{x}}^{n+1}}{2}\left(\mathbf{v}_{\mathbf{x}}^{n+1} + \mathbf{r}_{\mathbf{av1}}^{n+1}\right)$$
$$\mathbf{v}_{\mathbf{z}}^{n+1} = \mathbf{r}_{\mathbf{av3}}^{n+1} - \frac{(\mathbf{r}_{\mathbf{av3}}^{n+1})^T \mathbf{v}_{\mathbf{x}}^{n+1}}{2}\left(\mathbf{v}_{\mathbf{x}}^{n+1} + \mathbf{r}_{\mathbf{av1}}^{n+1}\right) \quad 2.36$$

2.7.3 Bond-slip and dowel-action material laws

The stress-strain response for slip along the x-axis of the interface element is based on the cyclic bond-slip law proposed by Murcia-Delso and Shing (2014). The model was originally developed for reinforcing bars embedded in well-confined concrete and was intended to be used for three-dimensional analyses with solid elements representing concrete. The monotonic and cyclic behaviors of the model are shown in Figure 2.24. The model simulates bond-strength deterioration caused by bar slip, cyclic bar-slip reversals, tensile yielding of the bar, and concrete splitting caused by the wedging action effect of the ribs of the reinforcing bar. To simulate the wedging action effect, the model introduces a radial compressive stress normal to the direction of the bar. In the absence of confining reinforcement, the radial compressive stress could cause the tensile splitting of concrete in a 3D model as well as the normal opening of the bond interface. The latter will result in a decrease of the bond resistance. However, with the use of shell elements to model masonry or concrete, the confinement effect and splitting cracks cannot be accounted for. Therefore, the effects of the wedging action of the ribs are not considered in this study.

In the bond-slip model, the total bond resistance is decomposed into two components, the bearing resistance attributed to the bearing forces exerted by the ribs of the bar, and the friction resistance. Murcia-Delso and Shing (2014) proposed the following equation for the calculation of the total bond resistance for initial loading and for loading beyond the maximum slip ever attained by previous cycles:

$$\tau = \rho_n \left(\rho_{b,s} \cdot \rho_{b,c} \cdot \tau_b + \rho_{f,s} \cdot \rho_{f,c} \cdot \tau_f \right) \tag{2.37}$$

in which τ_b and τ_f are the bearing and friction resistances given as a function of slip $\tilde{u}$ for an elastic bar subjected to monotonic pull-out; ρ_n is a reduction factor that depends on the interface opening normal to the slip; $\rho_{b,s}$ and $\rho_{f,s}$ are factors that account for the reduction of the bearing and friction resistance due to the yielding of the reinforcing bar; and $\rho_{b,c}$ and $\rho_{f,c}$ are factors that account for the bond deterioration under cyclic loading. In this study, τ_b and τ_f are assumed to have the same behavior for positive and negative values of slip. The bearing and friction resistances are defined in terms of the peak bond strength ($\tau_{\max}$), the slip at which the peak strength is attained (s_{peak}), the clear spacing between the bar ribs (s_R), the slip at the onset of softening (s_2), and the residual bond strength (τ_{res}), based on the following set of equations:

$$\tau_b(\tilde{u}) = \begin{cases} 4(\tau_{\max} - \tau_{res}) \dfrac{\tilde{u}}{s_{peak}} & \text{for } 0 \le |\tilde{u}| < 0.1 s_{peak} \\ sign(\tilde{u}) \cdot (\tau_{\max} - \tau_{res}) \left[1 - 0.6 \left(\dfrac{|\tilde{u}| - s_{peak}}{0.9 s_{peak}} \right)^4 \right] & \text{for } 0.1 s_{peak} \le |\tilde{u}| < s_{peak} \\ sign(\tilde{u}) \cdot (\tau_{\max} - \tau_{res}) & \text{for } s_{peak} \le |\tilde{u}| < s_2 \\ sign(\tilde{u}) \cdot (\tau_{\max} - \tau_{res}) \left[1 - \dfrac{|\tilde{u}| - s_2}{s_R - s_2} \right] & \text{for } s_2 \le |\tilde{u}| < s_R \\ 0 & \text{for } |\tilde{u}| \ge s_R \end{cases} \tag{2.38}$$

$$\tau_f(\tilde{u}) = \begin{cases} 4\tau_{res} \dfrac{\tilde{u}}{s_{peak}} & \text{for } 0 \le |\tilde{u}| < 0.1 s_{peak} \\ sign(\tilde{u}) \cdot \tau_{res} \left[1 - 0.6 \left(\dfrac{|\tilde{u}| - s_{peak}}{0.9 s_{peak}} \right)^4 \right] & \text{for } 0.1 s_{peak} \le |\tilde{u}| < s_{peak} \\ sign(\tilde{u}) \cdot \tau_{res} & \text{for } |\tilde{u}| > s_{peak} \end{cases} \tag{2.39}$$

The behavior of the model under monotonic and cyclic loading is specified from the five parameters defining the monotonic response. The slip value s_2 and the residual bond strength τ_{res} are set equal to $s_2 = 1.1 s_{peak}$ and $\tau_{res} = 0.25\tau_{\max}$ per recommendation of Murcia-Delso and Shing (2014) for well-confined concrete. If experimental data are not available, Murcia-Delso and Shing (2015) have recommended that the values of $\tau_{\max}$, s_{peak}, and s_R be estimated from the compressive strength of concrete in ksi (f_c') and the bar diameter (d_b) with the equations:

$$\begin{aligned} \tau_{\max} &= 2.4\left(\frac{f_c'}{5.0}\right)^{0.75} \\ s_{peak} &= 0.07 d_b \\ s_R &= 0.5 d_b \end{aligned} \qquad 2.40$$

The coefficient ρ_n shown in Eq. 2.37 is a function of the interface opening normal to the direction of the slip and was originally introduced to account for the reduction of the bond resistance due to the opening of splitting cracks. However, in this study, splitting cracks are not modeled. This coefficient ρ_n is used instead to account for the reduction of the bond resistance due to deformation caused by the dowel action normal to the slip. Following the work of Murcia-Delso and Shing (2014), coefficient ρ_n is calculated by:

$$\rho_n = \begin{cases} 1 & \text{for } d_{\max} \le 0.5 h_R \\ 2\left(1 - d_{\max} / h_R\right) & \text{for } 0.5 h_R < d_{\max} \le h_R \\ 0 & \text{for } d_{\max} > h_R \end{cases} \qquad 2.41$$

in which, $d_{\max} = \max\left(\sqrt{\tilde{v}^2 + \tilde{w}^2}\right)$ is the maximum resultant dowel deformation ever attained during the analysis. Parameter h_R represents the rib height of the reinforcing bar and here is approximately assumed to be equal to $0.075 h_R$. The factors $\rho_{b,c}$ and $\rho_{f,c}$ shown in Eq. 2.37 are

reduction factors that account for the bond deterioration due to cyclic loading. Both factors depend on the user-specified parameter s_R and on the values of the maximum slips, $s_{\max}^{+}$ and $s_{\max}^{-}$, attained in the positive and negative directions. Factor $\rho_{b,c}$ is calculated by:

$$\rho_{b,c} = 1.2e^{-2.7\left(\bar{s}_{\max}/s_R\right)^{0.8}} \leq 1 \tag{2.42}$$

in which, $\bar{s}_{\max}$ is given by:

$$\bar{s}_{\max} = 0.75\max\left(s_{\max}^{+},\ s_{\max}^{-}\right) + 0.25\left(s_{\max}^{+} + s_{\max}^{-}\right) \tag{2.43}$$

Factor $\rho_{f,c}$ is calculated by the expression:

$$\rho_{f,c} = 1 - \min\left(\frac{s_{\max}^{+} + s_{\max}^{-}}{s_R},\ 1\right)\left(1 - e^{-0.45\left(s_{cum}/s_R\right)^{0.75}}\right) \tag{2.44}$$

where s_{cum} is considered to be zero before the slip exceeds the slip at the peak resistance, s_{peak}, for the first time. In the above expressions, $s_{\max}^{-}$ is equal to the absolute value of the peak negative slip. The reduction factors $\rho_{b,c}$ and $\rho_{f,c}$ are applied to the bond stress once the load is reversed. Details about the expressions of the reduction factors $\rho_{b,s}$ and $\rho_{f,s}$, as well as other parameters controlling the cyclic response of the bond-slip model, can be found in Murcia-Delso and Shing (2014).

The model adopted here assumes that the bar is embedded in well-confined concrete and ignores the effect of splitting cracks as discussed above. However, for reinforced masonry walls, good confinement is hard to achieve. Hence, splitting failure could occur and weaken the bond. To distinguish between confined and unconfined conditions in reinforced masonry, the criterion proposed for reinforced concrete by Eligehausen and Bigaj-van Vliet in CEB/FIP MC90 (1999) is

adopted. Based on that, in the absence of transverse reinforcement, confined conditions prevail if the minimum clear cover around the bar is larger than $5\,d_b$, otherwise, unconfined conditions are assumed. The clear cover is defined as the clear distance from the reinforcing bar to the exterior face of the wall. Based on this criterion, for a reinforced masonry wall with an actual thickness of 7.625 in., confined conditions are assumed for bar sizes of #3, #4, and #5, while unconfined conditions are assumed for bars of larger size. For confined conditions, the values of the modeling parameters recommended by Murcia-Delso and Shing (2014), as discussed above, are used. For unconfined conditions, the values are modified to account for premature bond failure due to splitting cracks. Eligehausen and Bigaj-van Vliet in CEB/FIP MC90 (1999) provide a range of values for the parameters $\tau_{\max}$, τ_{res}, and s_R depending on the bond quality in unconfined concrete. The values proposed were based on the experimental data from bond-slip tests. For good bond quality, they assumed that $\tau_{\max} = 0.762\left(f_c'\right)^{0.5}$, $\tau_{res} = 0.114\left(f_c'\right)^{0.5}$, and $s_R = 0.04$ in., while for poor bond quality, they assumed that $\tau_{\max} = 0.381\left(f_c'\right)^{0.5}$, $\tau_{res} = 0.057\left(f_c'\right)^{0.5}$, and $s_R = 0.10$ in. For the slip values of s_{peak} and s_2, they assumed that $s_{peak} = s_2 = 0.024$ in. in either case. This study adopts the value of $\tau_{\max}$ for good bond quality and the values of τ_{res} and s_R for poor bond quality. The use of the lower value of s_R, which is given for good bond quality, is avoided because it would lead to a very brittle bond-slip response that could make the analysis convergence harder. Table 2.2 summarizes the values adopted in this study for the bond-slip model under confined and unconfined conditions. In either case, the bond strength is calculated using the masonry prism strength (f_m') in lieu of f_c'. Figure 2.25 compares the monotonic bond stress-vs-slip response for the case of a #6 bar embedded in grouted concrete masonry with a prism strength of 3 ksi under confined and unconfined conditions.

The masonry behavior in dowel action along each of the element local axes *y* and *z* is represented by a simple uniaxial material law in terms of the masonry bearing stress σ_y (or σ_z) versus the interface deformation $\tilde{v}$ (or $\tilde{w}$), as shown in Figure 2.26. The behavior along each of the two axes is considered to be independent of the other. Under monotonic loading, the material is initially elastic-perfectly plastic with an initial stiffness K_d and a yield stress σ_d; beyond the deformation d_1, it shows a post-peak softening behavior described by a linear function until a specified residual strength is reach at deformation d_u, as shown in Figure 2.26. Unloading occurs with a stiffness higher than the initial stiffness, and after the stress reaches zero, it remains zero for further deformation increment in the same direction. The deformation at which the material is fully unloaded represents a gap. The gap depends on the maximum deformation ever reached and can be different in the positive and negative directions. Reloading follows the initial stiffness once the gap is closed.

In lack of experimental data on the dowel action response of bars embedded in reinforced masonry, the initial stiffness K_d and yield strength σ_d are determined with the dowel force-vs-displacement law of Dulacska (1972), which was derived from experimental results on dowel bars embedded in well-confined reinforced concrete. The calibration is performed with a simple model consisting of a dowel bar embedded in masonry and subjected to increasing shear displacement along a frictionless joint, as shown in Figure 2.27. The values of the deformation parameters d_1 and d_u are determined in an ad hoc manner by matching results of reinforced masonry wall analyses to quasi-static wall test data, as presented in the following chapter. The residual dowel stress is taken equal to $0.01\sigma_d$.

The model proposed by Dulacska (1972) to describe the dowel force (F) as a function of the applied shear displacement (Δ) is given by:

$$\Delta = \frac{3F}{d_b 10^3}\sqrt{\frac{1}{f_g}\tan\left(\frac{F}{F_d}\frac{\pi}{2}\right)} \qquad 2.45$$

in which, f_g is the compressive strength of the grout, F_d is the dowel strength, and F is in kips. The dowel strength is calculated with Eq. 2.46 as a function of the compressive strength of the grout (f_g), the diameter of the bar (d_b), the yield strength of the bar (f_y), and the angle (δ) that the bar forms with the outward normal vector to the crack plane. In this study, angle δ is assumed to be 45 degrees for the elements connecting the bars to the masonry in the vicinity of a diagonal crack in the wall.

$$F_d = 0.2 d_d^2 f_y \left(\sqrt{\sin^2\delta + \frac{f_g}{0.03 f_y}} - \sin\delta\right) \qquad 2.46$$

Based on Eq. 2.46, bars crossing a diagonal crack in a wall will have a lower dowel strength than a bar that is perpendicular to a crack (i.e. for $\delta = 0$). For example, if a grout strength of 3.5 ksi and a reinforcement yield strength of 60 ksi is used in Eq. 2.46, the reduction in dowel strength for a 45-degree angle is about 40%.

The equations proposed by Dulacska (1972) assume that the dowel force (F) and displacement (Δ) are parallel to the crack plane. For an inclined crack plane, the dowel force component that is perpendicular to the direction of the bar can be obtained as $F\cos\delta$, which is equal to $0.707F$ for a 45-degree angle crack. However, considering that in the analyses of RM walls, some of the cracks crossing the reinforcing bars will be perpendicular to the bars, this condition is ignored and the dowel force F calculated with Eq. 2.45 for an angle δ equal to 45

degrees is assumed to2.47 occur in the direction perpendicular to the bar. This is to avoid excessive reduction of the resistance contributed by dowel action. The same assumption is made for the dowel displacement Δ.

Figure 2.27 compares the dowel force-displacement curve obtained with Eqs. 2.45 and 2.46 and the response obtained using the simple model. The reinforcing bar is assumed to be #4 with a yield strength of 60 ksi and embedded in masonry with a grout strength of 3.5 ksi. The angle δ in Eq. 2.46 is set to 45 degrees based on the previous discussion. The relative displacements thresholds d_1 and d_u are specified to be equal to 0.03 in. and 0.06 in., respectively. The same values are used in the analyses presented in following chapters.

The reduction of the bond and dowel resistances due to the compressive crushing of the surrounding masonry is modeled by introducing a strength reduction factor k. The factor is equal to 1.0 before the onset of crushing of masonry (i.e., when the peak compressive strain has not exceeded ε_0, the strain at the peak stress) and is reduced to zero when the peak masonry compressive strain ever developed (ε_m) exceeds ε_u, as given by Eq. 2.48, in which $\langle\cdot\rangle$ represent Macaulay brackets. The peak compressive strain of masonry (ε_m) is approximately represented by the axial strain at the masonry side of the interface element. The reduced bond and dowel resistances are given by Eq. 2.49.

$$k(\varepsilon_m) = 1 - \frac{\langle \varepsilon_o - \varepsilon_m \rangle}{\varepsilon_o - \varepsilon_u} \geq 0 \tag{2.48}$$

$$\begin{aligned} \tau_{red} &= k(\varepsilon_m) \cdot \tau \\ \sigma_{y,red} &= k(\varepsilon_m) \cdot \sigma_y \\ \sigma_{z,red} &= k(\varepsilon_m) \cdot \sigma_z \end{aligned} \tag{2.49}$$

2.8 Proposed Element Removal Scheme

The FE modeling scheme is complemented with a new non-local element removal procedure. Element removal is employed to help avoid numerical problems that can be caused by severe element distortion and unrestrained degrees of freedom, to model bar buckling and rupture in a natural manner, and to simulate loss of contact under certain conditions in cohesive interface elements. In this strategy, element removal is triggered by masonry crushing, bar rupture, or an excessive relative displacement in a cohesive-crack interface element. However, removal is not local to the triggering element. When all the integration points in a shell element satisfy the condition for compressive failure (i.e. compressive strain exceeds the strain ε_u), the shell element, all the adjacent cohesive-crack interface elements, and all the bond-slip/dowel-action interface elements connected to the shell element are removed. This aims to eliminate undesired spurious resistance introduced by the remaining cohesive-crack and bond-slip/dowel-action interface elements after the adjacent shell element has been completely crushed. When all the fibers of a beam element cross section have registered rupture, the beam element is removed, and the adjacent bond-slip/dowel-action interface element is removed. A cohesive-crack interface element is removed to simulate the loss of contact when at least one of the element's integration points registers out-of-plane sliding that is larger than the thickness of the wall. The element removal scheme is completed by removing any masonry shell element that remains attached to other shell or cohesive crack interface elements through only one of its sides.

The FE element analysis program, LS-DYNA, allows for element removal, but only in a local manner. To implement the non-local element removal scheme within the existing framework of the program, the following steps have been followed. First, all the elements that are adjacent to a given element are identified and their identification numbers (element ID's) are stored as internal

constants in the given element. This process is performed only at the beginning of the analysis and is repeated for every shell, beam, and interface element. A global vector, which can be accessed by all elements during the analysis, is formed with each entry containing information about whether or not an element has been removed. For the shell elements and beam elements once compressive failure or rupture is detected at an integration point, the stresses at the failed integration point are set to zero for all subsequent steps of the analysis. When all the integration points of the element have failed or ruptured, the element is removed. The entry in the global vector corresponding to the removed element is then updated to signal the removal to the adjacent elements. In implicit analysis, the element removal is performed at the end of a converged step.

The element removal scheme is demonstrated with the examples shown in Figure 2.28 and Figure 2.29. In the first example, a #4 bar is embedded in a masonry prism and the prism is subjected to compression. It can be seen that bar buckling occurs once the masonry shell elements are crushed and get removed together with the adjacent bond-slip/dowel-action interface elements. In the second example, a #4 bar is embedded in two masonry prisms. The nodes of the bottom prism are fixed and those of the top prism are subjected to an upward vertical displacement. The reinforcing bar is assumed to have the stress-strain response shown in Figure 2.19. It can be seen that when the reinforcing bar beam element gets ruptured and removed, the adjacent bond-slip interface element is also removed. In both examples, the masonry prism strength is assumed to be 2.5 ksi.

Part of this chapter is a reprint of the material that will appear in Chapter 4 of the technical report titled “Developing Solutions to the Short-Period Building Performance Paradox: Study for Reinforced Masonry Buildings” that will be submitted to the Federal Emergency Management Agency by the Applied Technology Council for the project number ATC-116. The authors of

Chapter 4 in the report are: the author of this dissertation, Jianyu Cheng, and P. Benson Shing. The report chapter was prepared under the supervision of Dr. Charles A. Kircher, who was the technical director of the ATC-116 project. The author of this dissertation was the primary investigator and author of all the materials covered in this chapter of the dissertation.

Table 2.1 Material parameters for the cohesive-crack model used in the analyses of a single interface element.

Material parameter	Crack in grouted masonry	Mortar joint	Material parameter	Crack in grouted masonry	Mortar joint
D_{nn} (ksi/in)	5000	300	$G_{f,I}$ (kips/in)	0.0004	0.0002
D_{tt} (ksi/in)	5000	125	α (in/kip)	2000	2000
s_o (ksi)	0.30	0.10	β (in/kip)	2200	2200
μ_o	1.40	0.95	$\zeta_{dil,o}$	0.40	0.10
μ_r	1.00	0.85	$\zeta_{dil,r}$	0.001	0.001
r_o (ksi)	0.05	0.02	d_o	0.40	0.04
r_r (ksi)	0.01	0.01	η	300	300

Table 2.2 Material parameters for bond-slip material law under confined and unconfined conditions.

Material parameter	Confined conditions	Unconfined conditions
s_{peak}	$0.07d_b$	0.024 in.
s_2	$1.1s_{peak}$	0.024 in.
s_R	$0.5d_b$	0.10 in.
τ_{max}	$2.4(f'_m/5.0)^{0.75}$	$0.762(f'_m)^{0.5}$
τ_{res}	$0.25\tau_{max}$	$0.057(f'_m)^{0.5}$

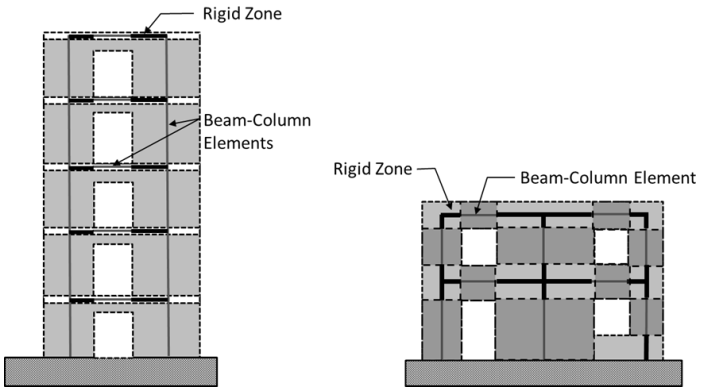

Figure 2.1 Frame models for masonry wall systems (from NIST 2014).

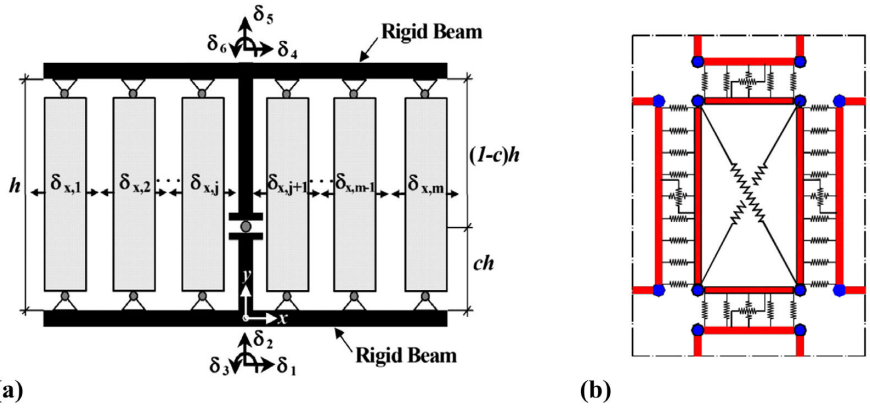

Figure 2.2 Modeling strategies for the seismic analysis of concrete and masonry structures: (a) multi-vertical-line-element for RC/RM shear walls (from Kolozvari et al. 2014); (b) macro-element for unreinforced masonry panel (from Calio et al. 2012).

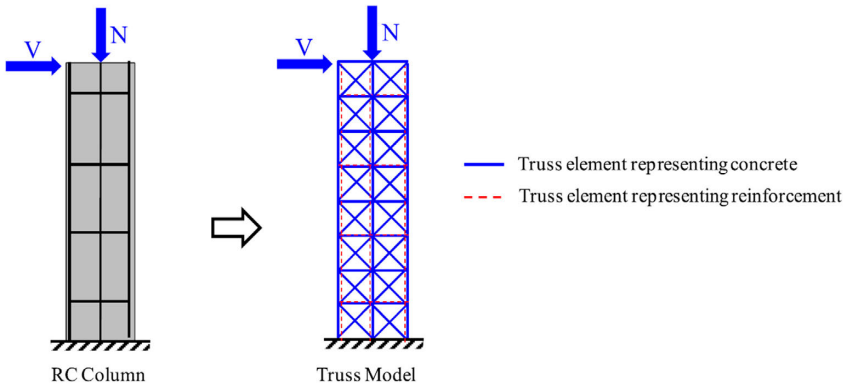

Figure 2.3 Nonlinear truss model representation of a RC column (from Moharrami et al. 2015).

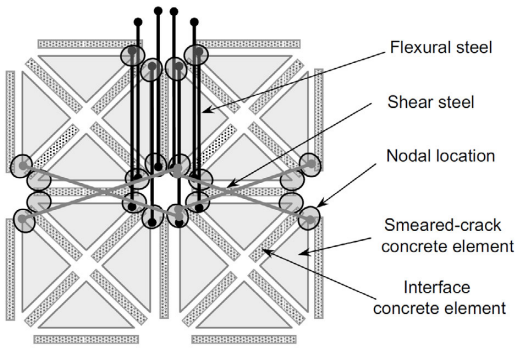

Figure 2.4 Finite-element discretization scheme proposed by Stavridis and Shing (2010) for the analysis of RC members (from Stavridis and Shing 2010).

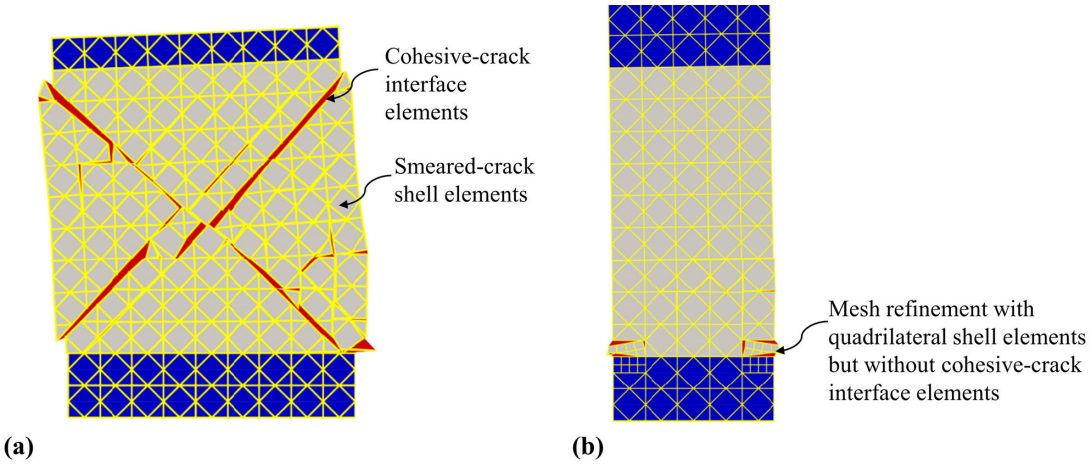

Figure 2.5 Discretization scheme proposed by Mavros (2015) for: (a) shear-dominated wall tests; (b) flexure-dominated wall tests (courtesy of Mavros 2015).

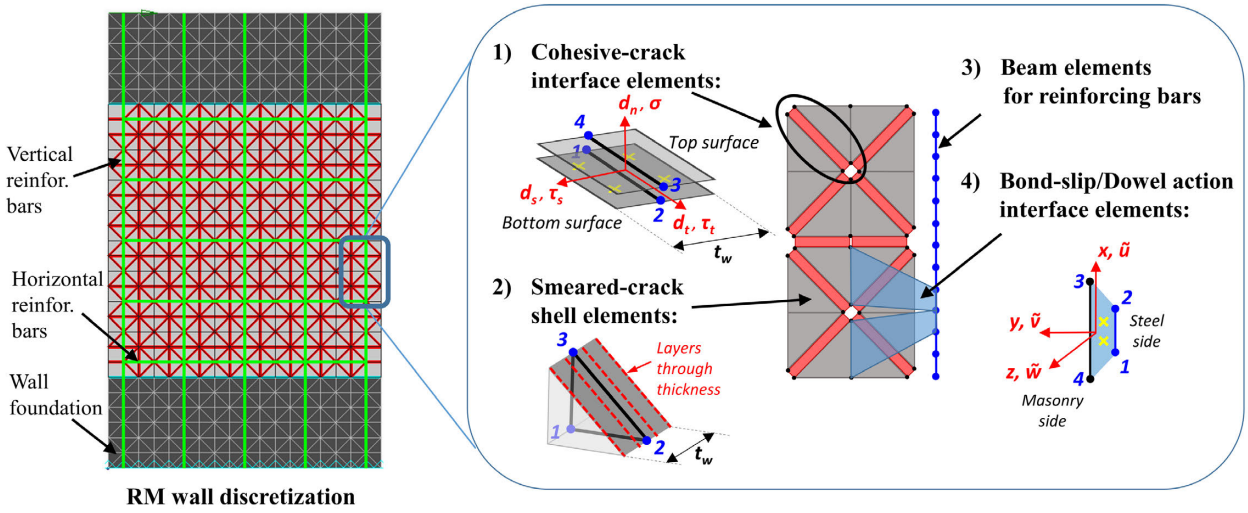

Figure 2.6 Proposed discretization scheme for RM walls.

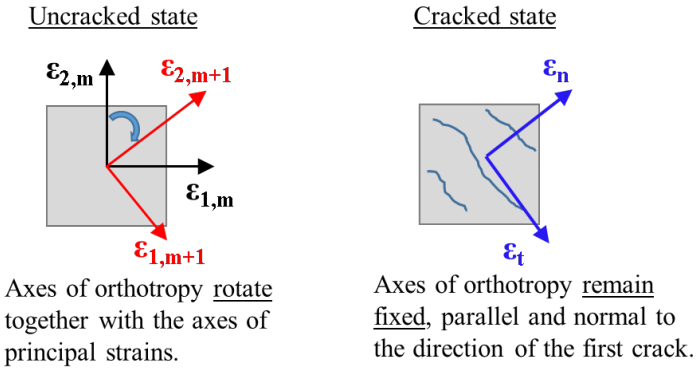

Figure 2.7 States of the orthotropic model for concrete or masonry.

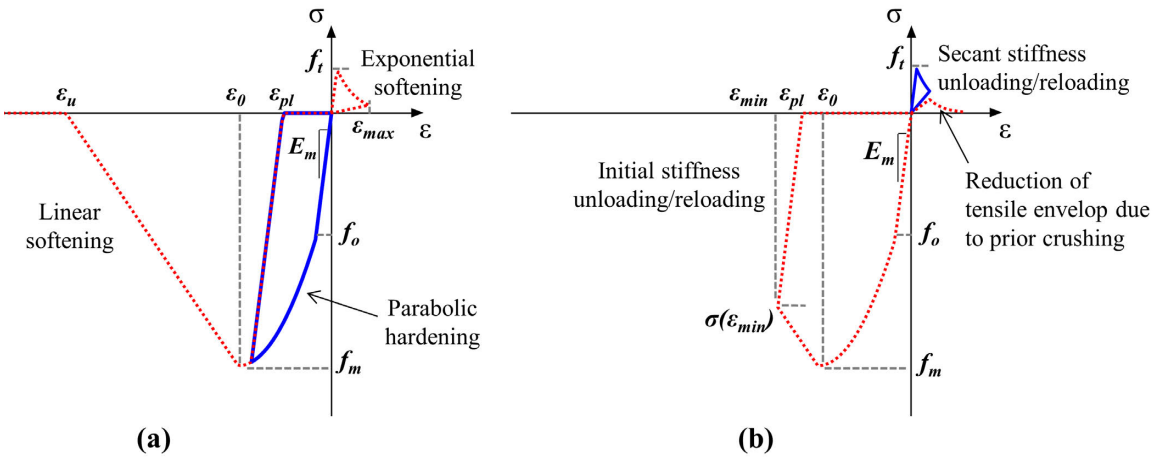

Figure 2.8 Uniaxial stress-strain relation of the orthotropic model for masonry and concrete: (a) material initially loaded in compression; (b) material initially loaded in tension.

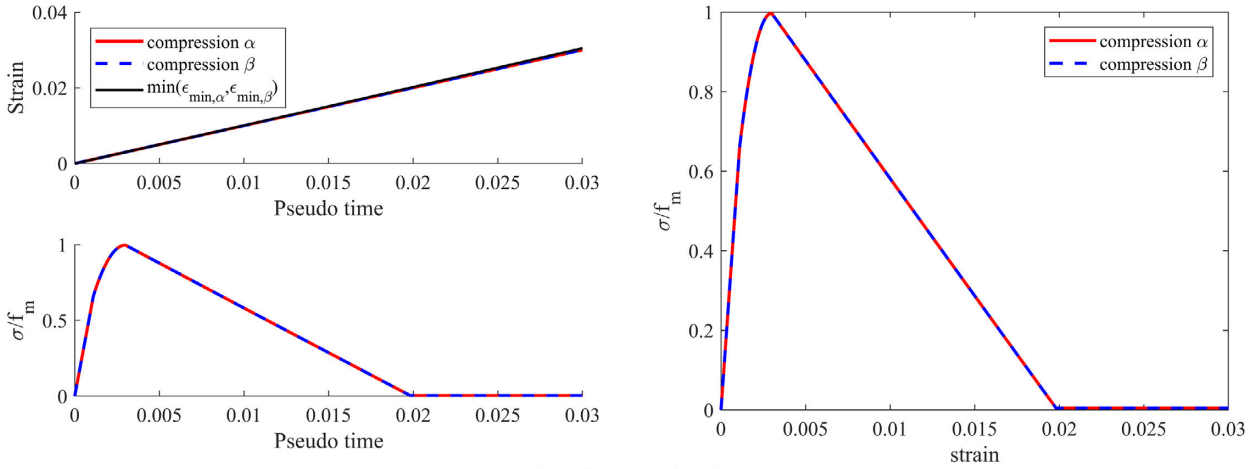

(a) Scenario 1

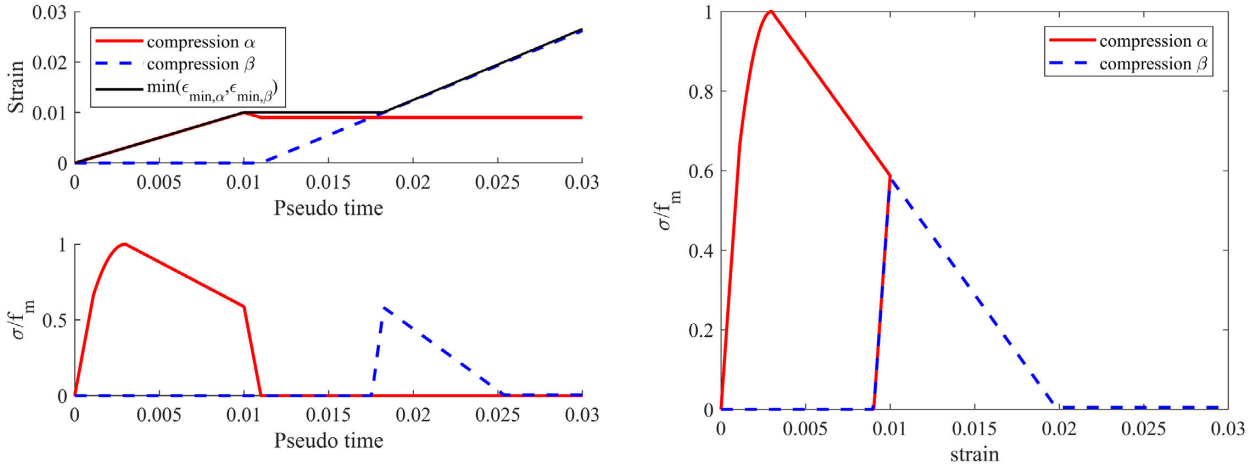

(b) Scenario 2

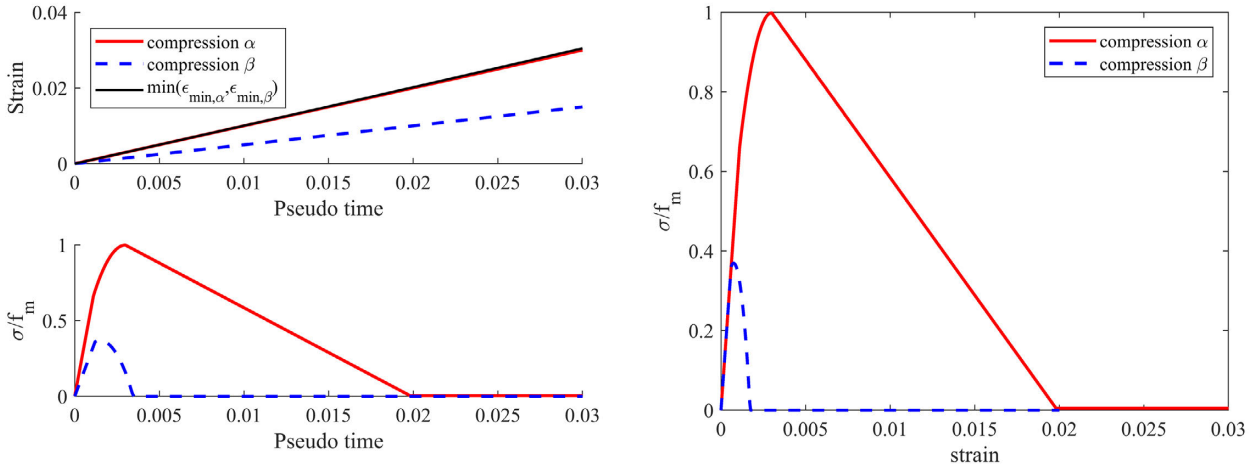

(c) Scenario 3

Figure 2.9 Behavior of the orthotropic model under biaxial compression for three loading scenarios. The sign convention for the plots has been reversed so that compression is positive.

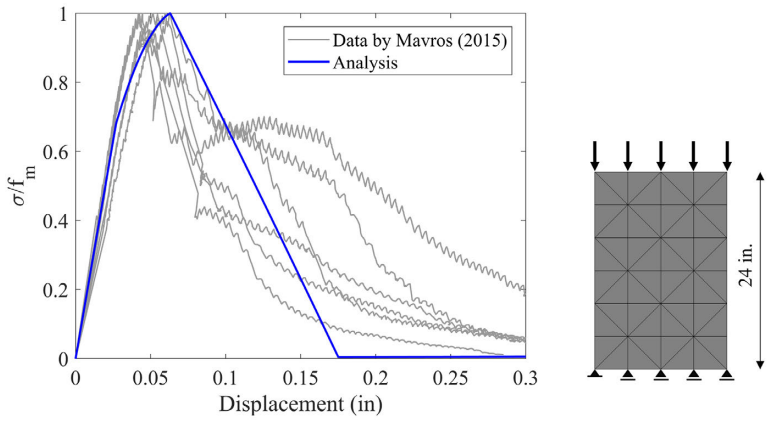

Figure 2.10 Simulation of grouted masonry prism tests.

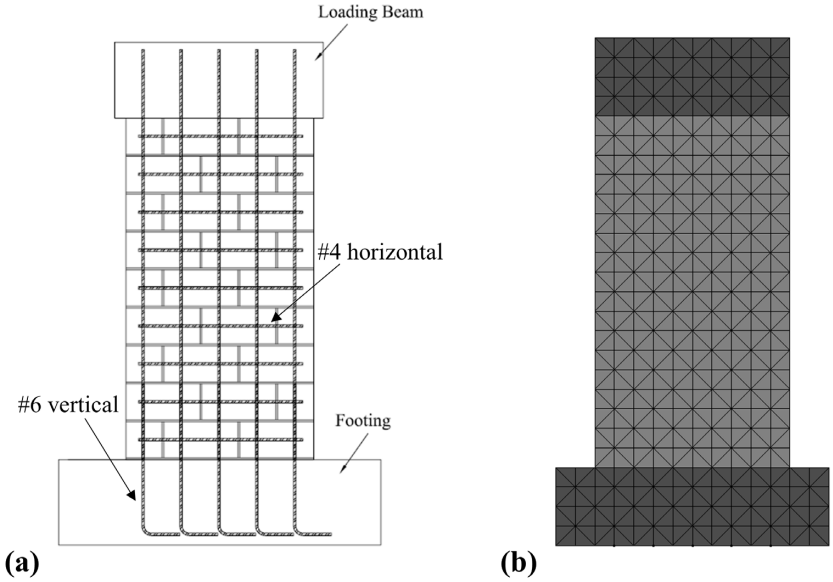

Figure 2.11 Reinforced masonry wall tested by Sherman (2011); (a) wall layout; (b) finite-element model using only smeared-crack shell elements.

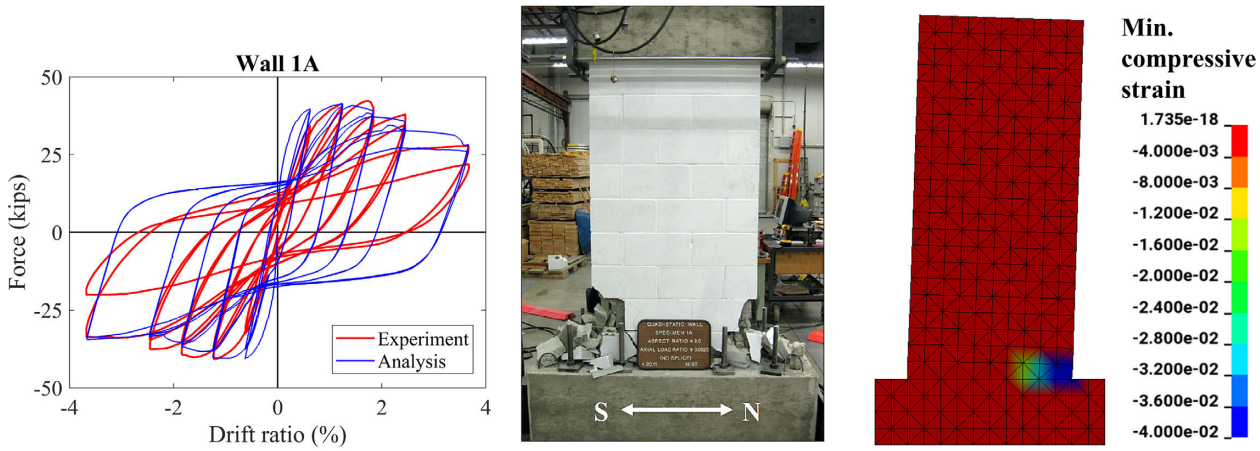

Figure 2.12 Analysis of wall specimen 1A tested by Sherman (2011) using only smeared-crack shell elements; (a) comparison of hysteresis loops; (b) damage in the test (Sherman 2011); (c) crushing predicted by the model at the peak positive drift of the last cycle.

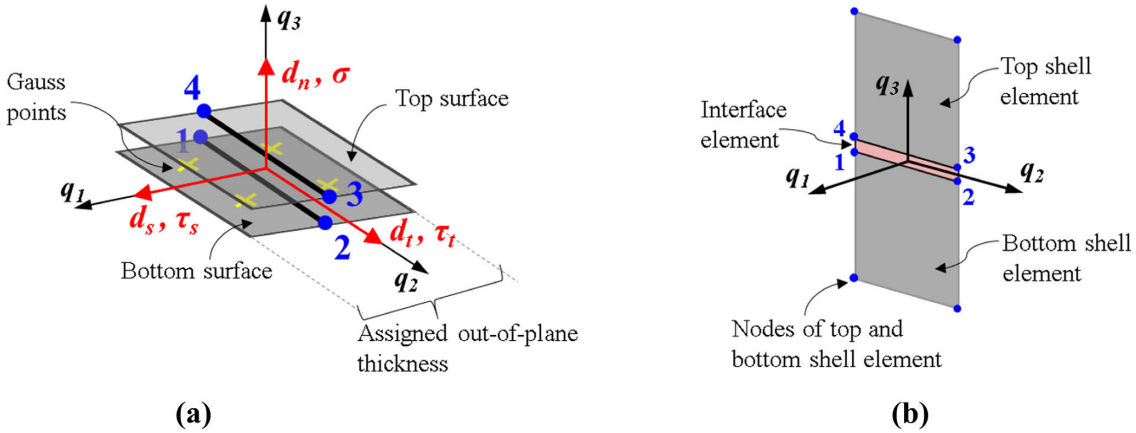

Figure 2.13 Interface element configuration. (a) Local coordinate system, deformation and stress components; (b) Connectivity with top and bottom shell elements.

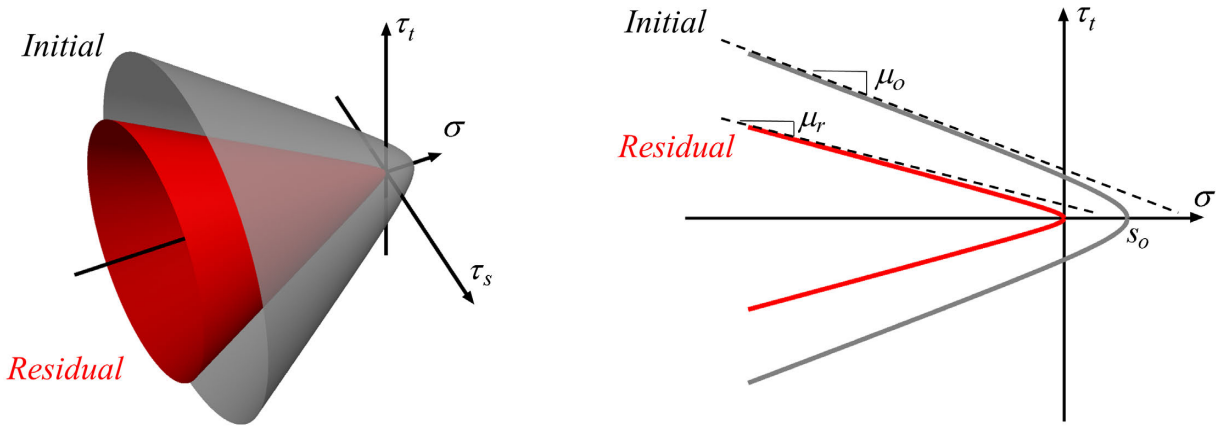

(a) Yield surface in three dimensions **(b) Yield surface in two dimensions**

Figure 2.14 Initial and residual yield surface of the cohesive-crack material model.

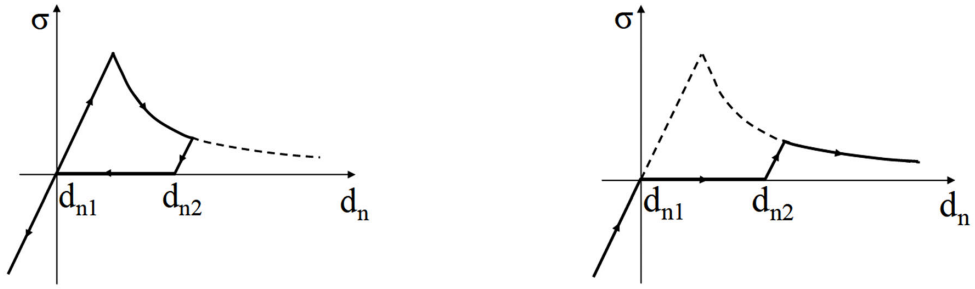

(a) Normal loading and unloading **(b) Normal reloading**

Figure 2.15 Uniaxial behavior of the interface model in tension and compression (from Koutromanos and Shing 2012).

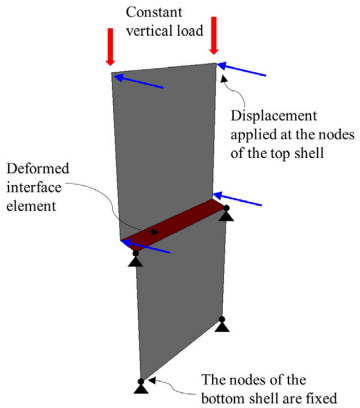

Figure 2.16 Model used for the analysis of a single interface element in LS-DYNA.

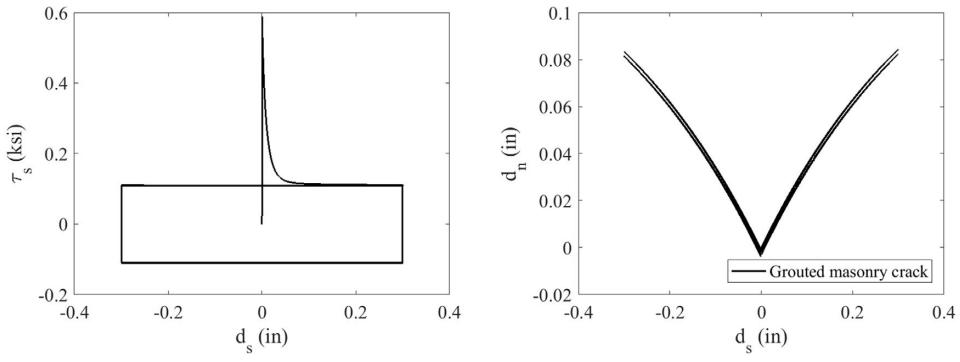

(a) Grouted masonry crack

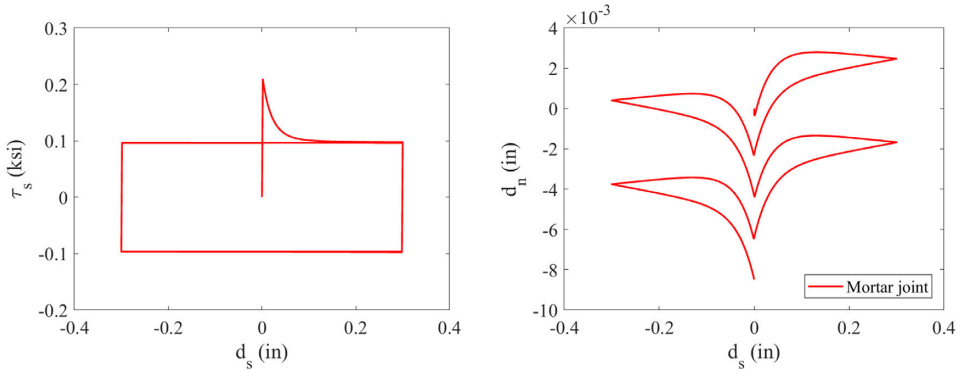

(b) Mortar joint

Figure 2.17 Response of the interface element in terms of shear stress -vs- applied horizontal relative displacement and vertical relative displacement -vs- applied horizontal relative displacement. (a) Case of a discrete crack in grouted concrete masonry; (b) case of a mortar joint in ungrouted concrete masonry.

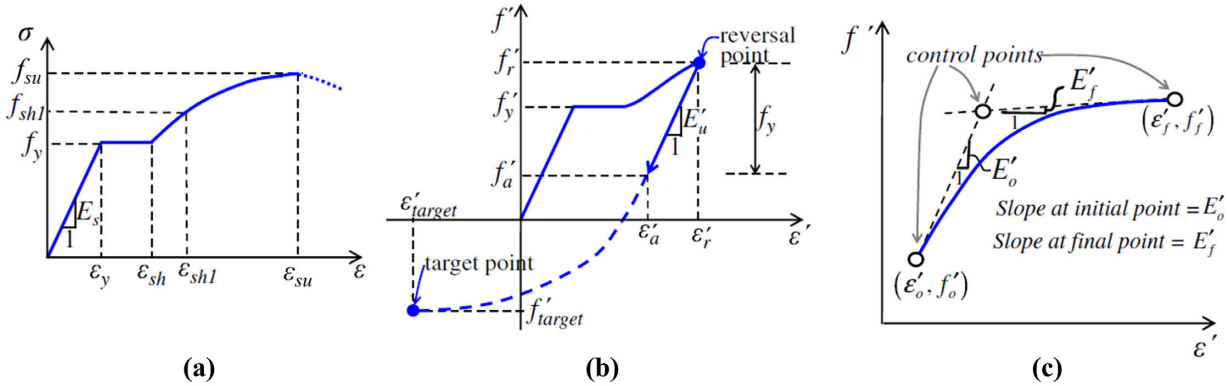

(a) **(b)** **(c)**

Figure 2.18 Behavior of the reinforcing steel model: (a) monotonic tensile curve; (b) reversal behavior shown in terms of natural strain and true stress; (c) NURBS to describe the reversal curve (figure from Kim and Koutromanos, 2016).

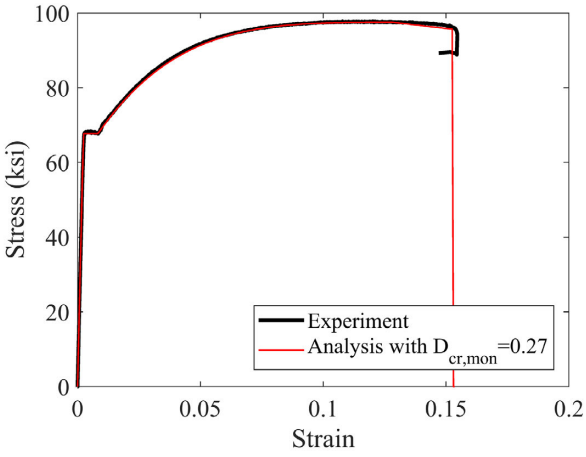

Figure 2.19 Calibration of the monotonic tensile stress-strain curve.

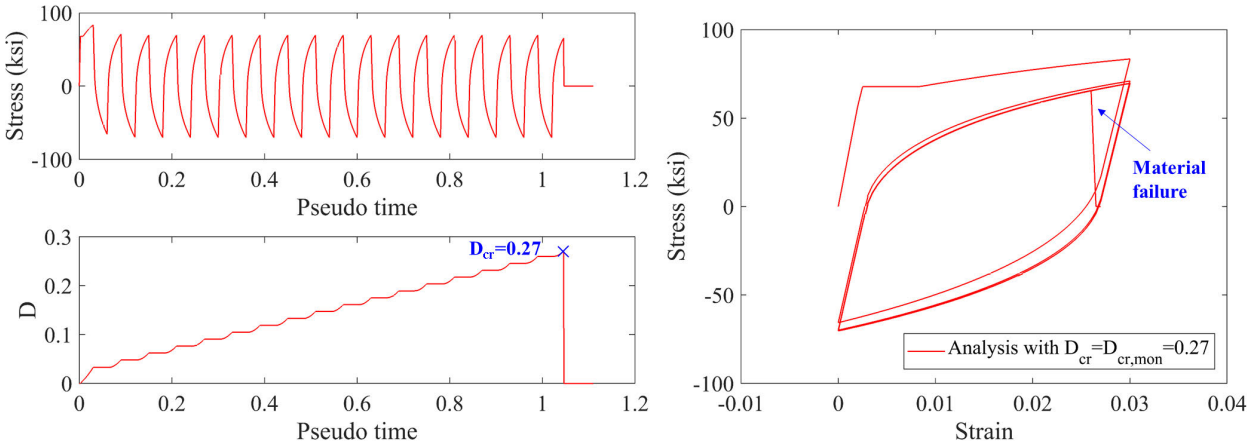

Figure 2.20 Cyclic response of the steel material until failure.

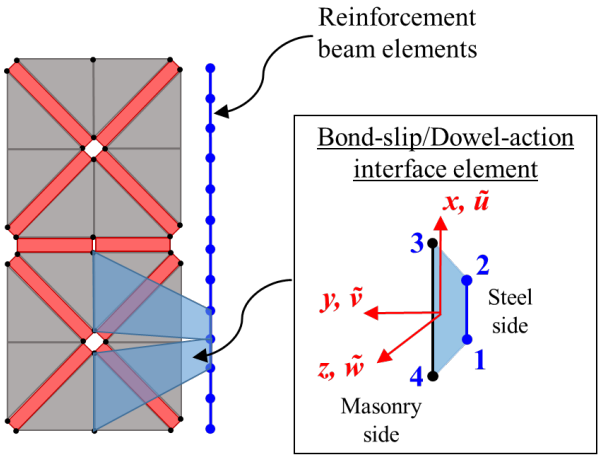

Figure 2.21 Bond-slip/dowel-action interface elements used to connect the reinforcing bars to masonry.

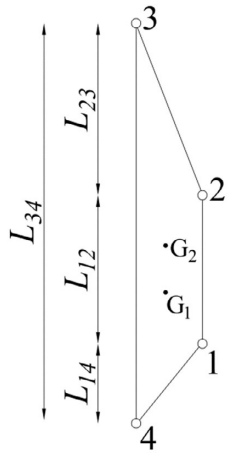

Figure 2.22 Bond-slip/dowel-action interface element lengths (from Mavros 2015).

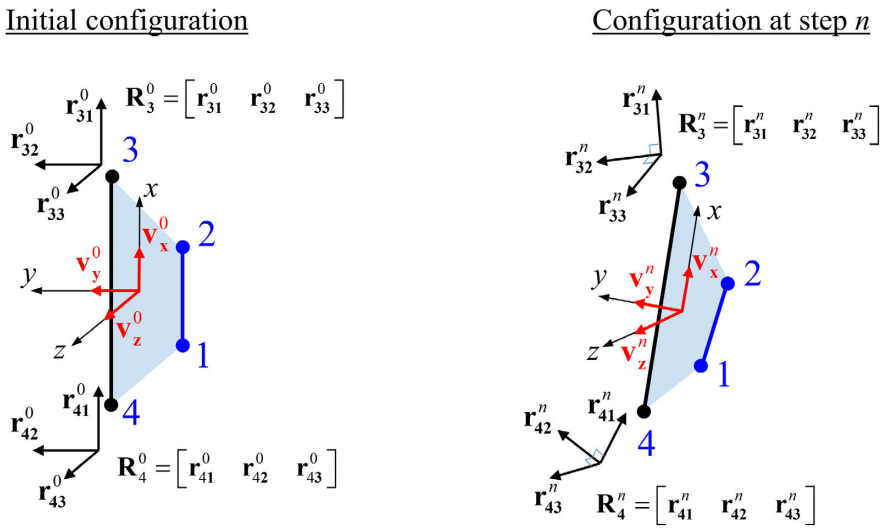

Figure 2.23 Nodal triads and element local coordinate system of the bond-slip/dowel-action interface element.

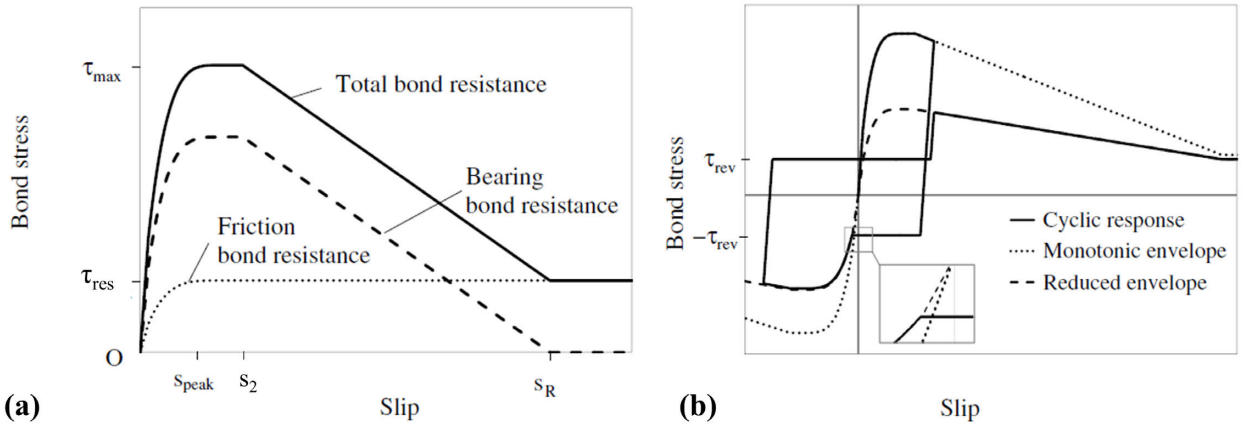

Figure 2.24 Bond stress-versus-slip law: (a) monotonic response; (b) cyclic response (from Murcia-Delso and Shing 2014).

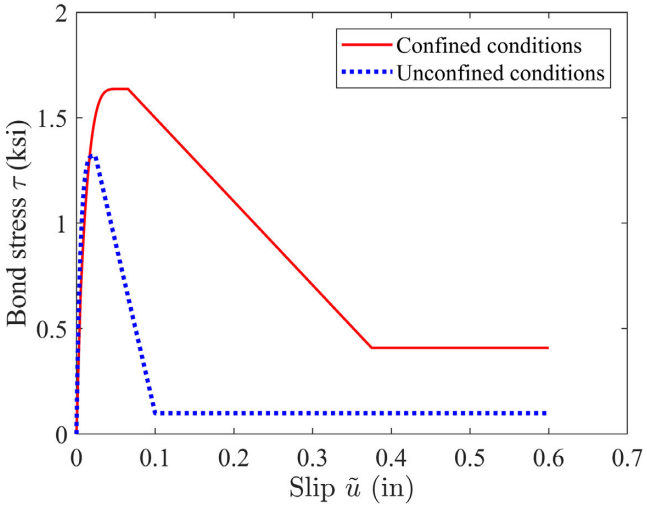

Figure 2.25 Comparison of monotonic bond-slip response for confined and unconfined conditions.

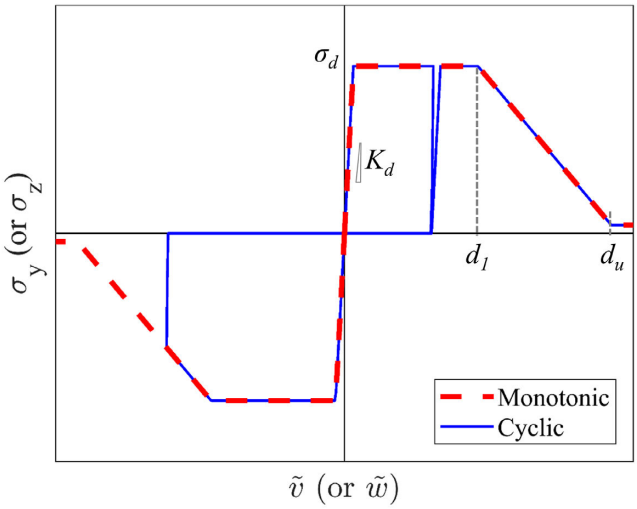

Figure 2.26 Material law used in the bond-slip/dowel-action interface element to model dowel action in reinforced masonry.

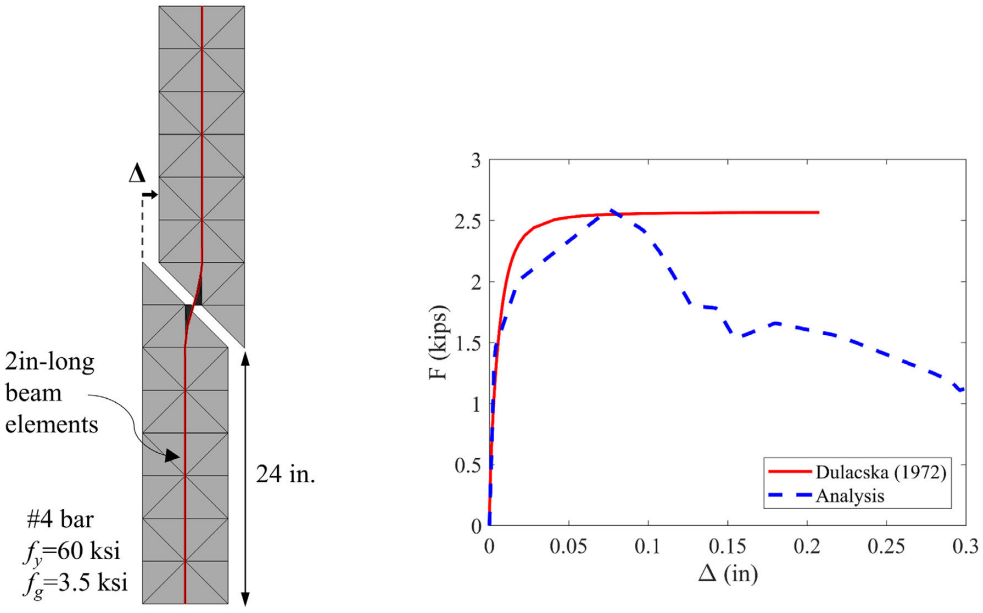

Figure 2.27 Calibration of the initial stiffness and yield stress of the dowel-action material law using a simple model.

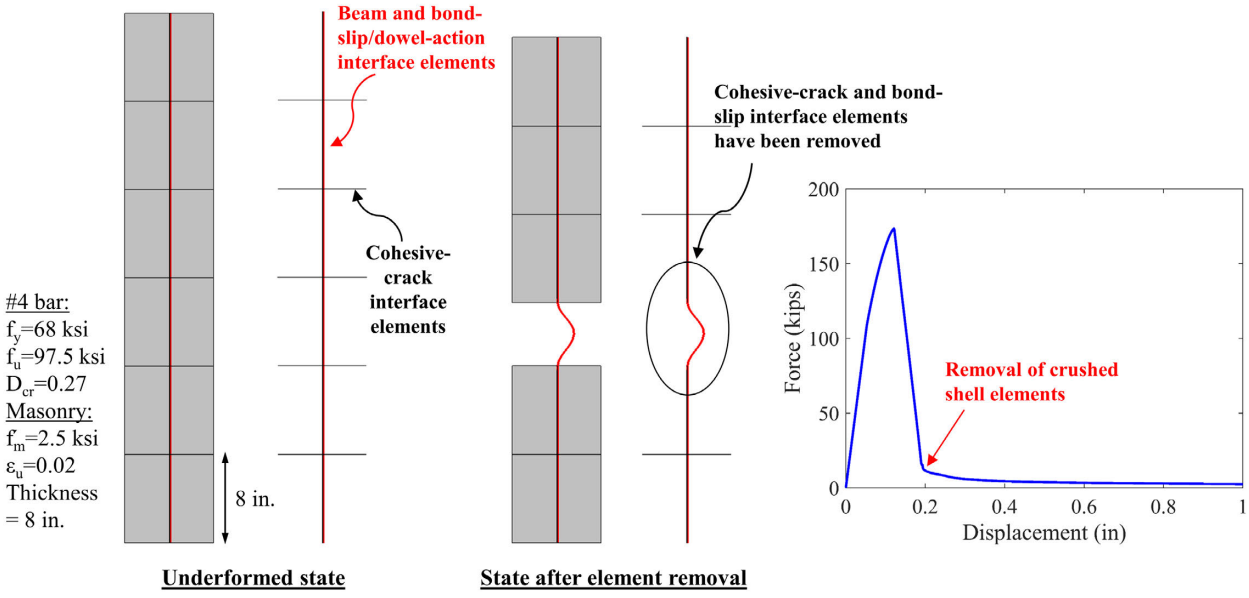

Figure 2.28 Element removal due to masonry crushing.

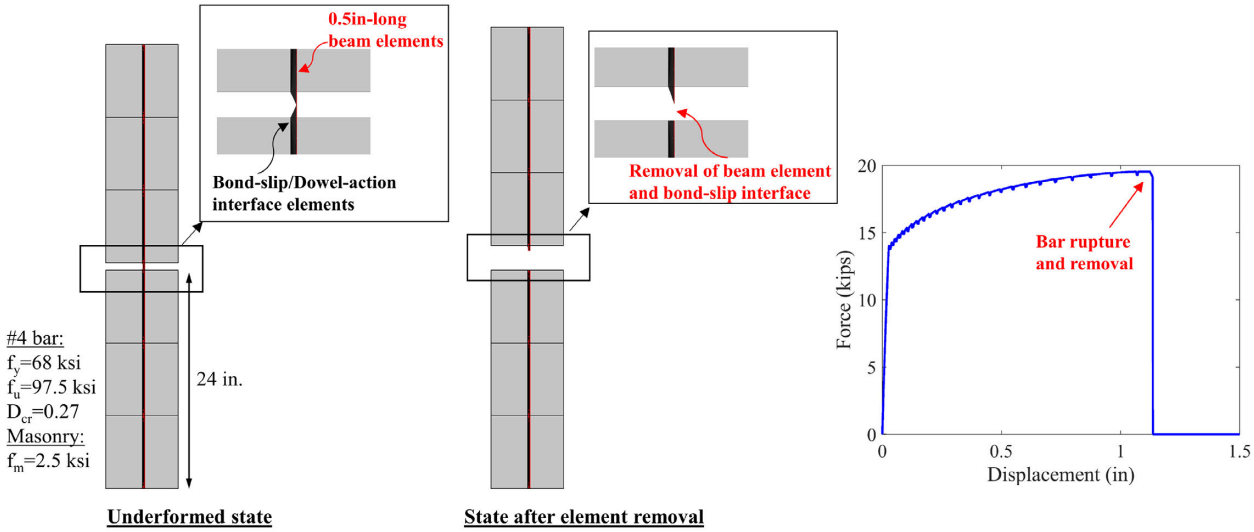

Figure 2.29 Element removal due to rupture of a reinforcing bar embedded in masonry.

3 VALIDATION OF MODELING SCHEME FOR GROUTED REINFORCED MASONRY

The proposed finite element (FE) modeling scheme is validated with experimental results from quasi-static and dynamic tests. To demonstrate the capability of the modeling scheme to capture the different possible failure mechanisms of RM shear walls, quasi-static tests on wall segments exhibiting shear-dominated and flexure-dominated behaviors are studied. The same discretization scheme is used for the analysis of all the wall segments regardless of the failure mode obtained in the tests. Emphasis is also placed on the selection of the material parameters. The material strengths are based on the data provided in the respective test reports, while the parameters defining the cyclic behavior and damage evolution of the constitutive models are calibrated in a consistent manner among the various wall tests simulated. To verify the capability of the modeling scheme in predicting the response of RM wall systems subjected to earthquake loading, the response of two RM structures tested on a shake table is simulated. Both structures were tested under unidirectional base excitation using a sequence of ground motions. The first structure had two-stories and wall components that were shear-dominated. The structure reached a peak first-story drift ratio of 1.9% under the strongest earthquake motion of the testing sequence. The second structure is studied to demonstrate the capability of the modeling scheme in capturing the structural response at larger lateral drifts. It had a single story and was tested up to a lateral drift ratio that exceeded 13%.

3.1 Discretization Proposed for RM Wall Segments

Reinforced masonry walls are normally constructed of hollow concrete masonry units and have reinforcing bars placed at the centers of the hollow cores. Thus, the vertical reinforcement

spacing is always a multiple of the distance between the centers of two adjacent cores. For typical concrete units used in North America, the center-to-center core spacing is 8 in. The first vertical bar from a wall edge is placed at a distance of 4 in. from the edge. The horizontal reinforcing bars are placed more or less at the mid-height of the bond beams; and the height of a bond beam is 8 in. The finite element discretization scheme adopted here takes into account the geometric properties of masonry construction. Figure 3.1a shows the representative discretization scheme used for a RM wall segment. In the mesh shown, the shell elements have been shrunk to better illustrate the locations of the zero-thickness interface elements that are inserted between the shell elements. The beam elements used to model the reinforcing bars are also shown. They are attached to the shell elements through bond-slip/dowel-action interface elements. The nodes of the mesh are placed at the mid-thickness of the wall. The triangular shell elements selected for the discretization of RM walls have vertical and horizontal sides that are 4 in. long. This allows the cohesive-crack interface elements to be placed at 45-degree angles as well as in the horizontal and vertical directions. Furthermore, 4 in. is the largest element size that still permits the beam elements representing the reinforcing bars to be placed at positions reflecting the actual locations. Selecting a smaller shell element size, such as 2 in., would lead to a severe and unrealistic localization of compressive strain at the base of flexure-dominated walls. It would also result in an unrealistically short buckling length for the vertical reinforcement.

Reinforcing bars are modeled with 2-inch long beam elements. This element size has been shown to be sufficiently small in capturing the bond-slip response (Mavros 2015). However, it is not small enough to accurately simulate the curvature along a bar that is subjected to dowel action. To properly model the bending of reinforcement due to the dowel action, beam elements with a length smaller than one bar diameter would have been needed. However, this is not needed in the

present study because the dowel action is treated in an empirical manner by having the initial stiffness and strength of the interface model representing the dowel response directly calibrated with Dulacska's equation (1972), as described in the previous chapter.

The connection of the vertical and horizontal reinforcement to the masonry shell elements is illustrated in Figure 3.1b. The region shown corresponds to the base course of a wall, right above the foundation. The foundation is modeled with elastic shell elements. Cohesive-crack interface elements are placed along the wall-foundation interface to model possible sliding of the wall at the base and also account for the lower tensile bond strength that the base interface may have compared to tensile strength of masonry. As shown in Figure 3.1b, the vertical bar elements are attached to the shell elements that are directly in contact with the wall-foundation interface. These shell elements are expected to experience higher compressive strains in a flexure-dominated wall segment and will be removed when the compressive failure of the elements occurs. Thus, buckling of the adjacent vertical bar elements can naturally occur. As it has been described in the previous chapter, the resistance of the bond-slip/dowel-action interface elements is gradually reduced based on the compressive strain in the masonry. Reinforcement splices are modeled explicitly by simulating each of the lap-spliced bars with a separate set of beam and bond-slip/dowel-action interface elements.

In RM wall construction, when horizontal reinforcing bars are required to provide the necessary shear strength, they should terminate with a 180-degree hook around the vertical bar at each end. In the model, the horizontal bars are assumed to terminate 4 in. away from the wall end and are connected to the vertical bar, as shown in Figure 3.2a. The hooks are modeled by using a bond-slip element that has a very high bond strength to connect the beam element at the end to the shell element. When modeling a flanged RM wall, the horizontal bars of the web are extended

beyond the flanged-web interface and are again anchored with a very strong bond-slip interface element to the shell element. An example of the discretization of a flange-web intersection of a T-wall is shown in Figure 3.2b. In practice, a 90-degree or 180-degree hook is used to anchor the horizontal bars of the web in the flange.

The toes of a wall are discretized in a slightly different manner than the rest of the wall. As shown in Figure 3.2a, instead of having triangular elements, the first two rows in the mesh at each wall corner have two quadrilateral smeared-crack elements separated by a horizontal cohesive crack interface. This is to better simulate the shear-compression resistance of masonry in the compression toes. In the analysis of some shear-dominated walls, it has been found that the use of triangular shell elements connected with a diagonal interface at a wall toe results in premature failure and load drop as soon as the first major diagonal crack forms. For consistency, the modified scheme is applied to both shear-dominated and flexure-dominated wall segments, although it is not needed for the latter. For wall segments with fixed-fixed end conditions, this modification is also applied at the sides of the top course. The quadrilateral elements used have four Gauss integration points in each layer across the element thickness. The element is removed when compressive failure has been registered in all the sampling points. Compressive failure is defined for the smeared-crack model as the state when the peak compressive strain has exceeded the strain ε_u at which the compressive resistance has dropped to zero.

3.2 Analyses of Quasi-Static Wall Tests

Quasi-static tests on shear-dominated and flexure-dominated RM wall segments are used for the validation of the proposed finite element modeling scheme. The tests were conducted by Ahmadi (2012), Kapoi (2012), Sherman (2011), Voon (2007), He and Priestley (1992), and Shing et al. (1991) and covered a wide range of configurations in terms of reinforcement details,

boundary and loading conditions, and wall aspect ratios. Table 3.1 summarizes the configuration of the test specimens. Table 3.2 shows the average material strengths as obtained from the respective test reports. Each specimen is identified with the name used in the corresponding experimental study. The reinforcement details and test setup of each study are shown in Figure 3.3 to Figure 3.8. The calibration of material parameters and analysis results are presented in the following sections. The limitations of the FE models are also discussed.

The nonlinear analyses are conducted by applying static displacements at the top of the walls. For the numerical analysis, an iteration scheme that consists of Broyden-Fletcher-Goldfarb-Shanno (BFGS) iterations and modified Newton-Raphson iterations is used. The modified Newton-Raphson iterations are performed using the initial stiffness of the material laws.

3.2.1 Calibration of material parameters

The material models for the smeared-crack shell elements, cohesive-crack interface elements, reinforcement beam elements, and bond-slip/dowel-action interface elements have a number of material parameters to calibrate. The values of many of these parameters are not available from experimental studies conducted on masonry walls, which usually provided only the compressive strength of the masonry and grout, and the yield and tensile strengths of the steel reinforcement. These include material parameters that define the compressive, tensile, and shear fracture of the masonry cohesive-crack interfaces, and the stiffness, strength, and softening of the masonry material in the dowel-action model. The values of these parameters have to be calibrated based on recommendations provided in the literature or in an ad hoc manner to match wall test data. It should be noted that one of the objectives of this validation study is to determine an approach procedure and method to calibrate these material parameters that can best characterize the behavior of reinforced masonry walls and can be used to model masonry building systems.

Some of the basic material parameters assume more or less the same values for all the modeled wall tests, while others are related to the material strengths. The values of the material parameters used in the analyses of the wall segments are summarized in Table 3.3 and Table 3.4.

The masonry prism strength (f'_m) and grout strength (f'_g) have been obtained directly from the values reported in Table 3.2. Stress-strain data from masonry prisms tested in compression are not available in any of the aforementioned studies. Apart from the masonry prism strength, the material law of the smeared-crack shell elements has a number of parameters to specify, as shown in Figure 2.8. In the analyses, the modulus of elasticity (E_m) is assumed to be equal to $600 f'_m$, the stress at the end of the linear branch in compression (f_o) is assumed to be equal to $2/3 f'_m$, and the strain at peak compressive strength (ε_0) is taken equal to 0.003, as described in the previous chapter. The values assumed for the tensile strength of masonry (f_t) are in the range of 8-11% of f'_m, as shown in Table 3.3. The masonry strain at compressive failure (ε_u) is assumed to be in the range of 0.03-0.04 for the element size selected. These values are based on the analyses of masonry prisms that were tested in compression, as shown in the previous chapter.

The cohesive-crack material law is used with the interface elements representing discrete cracks in masonry as well as with the elements simulating the wall-foundation interface. For masonry cracks, the tensile bond strength (s_o) is equal to the tensile strength of masonry. The mode-I fracture energy ($G_{f,I}$) is specified to be 0.0002 kips/in and mode-II fracture energy ($G_{f,II}$) is assumed to 10 times the value of the mode-I fracture energy, as recommended by Koutromanos and Shing (2012). The initial coefficient of friction (μ_o) is assumed to be equal to 1.2, which is lower than the value of 1.4 recommended by ACI 318-14 for concrete placed monolithically.

However, this difference is justifiable because of the smaller aggregate size typically used in a masonry grout mix. For the residual coefficient of friction (μ_r), a value of 1.0 is adopted, which is recommended by TMS 402 for masonry placed against a roughened concrete surface. Parameters $\zeta_{dil,o}$, $\zeta_{dil,r}$, and d_o that control the geometric dilatation, are assigned values of 0.40, 0.001, and 0.40, respectively. The values of the parameters for the wall-foundation interface depend on whether the foundation surface has been intentionally roughened or not before the construction of the wall. For a roughened surface, the friction coefficient is assumed to be equal to 1.0, otherwise, it is set equal to 0.7, as prescribed by TMS 402. For a surface that has not been intentionally roughened, lower values are also assumed for the parameters controlling the geometric dilation, as shown in Table 3.3. The values used for the rest of the parameters of the cohesive-crack material law are shown in Table 2.1 and are based on recommendations of Koutromanos and Shing (2012).

The values of the material parameters of the reinforcement beam elements were obtained from Table 3.2 whenever possible. For the wall tests that do not provide the monotonic stress-strain response of the steel reinforcing bars, values of the parameters that define the hardening behavior of reinforcing steel have to be assumed, as shown in Table 3.4. For these walls, the value of parameter D_{cr} (i.e. the parameter that controls the tensile failure of steel) is assumed to be 0.55, which is a relatively conservative value. For wall specimens 1A, Spec. 5, and F2, for which the monotonic stress-strain reinforcement data are available, the value of D_{cr} is determined based on the procedure described in the previous chapter. Nonetheless, no reinforcement rupture was reported in any of the wall tests considered.

The parameters controlling the monotonic response of the bond-slip law in the bond-slip/dowel-action interface elements are determined based on the confinement condition assumed for a reinforcing bar. A reinforcing bar is assumed to be confined when the clear masonry cover around the bar exceeds 5 bar diameters (d_b). Otherwise, the bar is assumed to be unconfined. In the confined case, it is assumed that the bond resistance can develop without the opening of splitting cracks, while in the unconfined case, it is assumed that splitting cracks will compromise the bond resistance. As explained in the previous chapter, the bond-slip law used for the confined case adopts the properties proposed by Murcia-Delso and Shing (2015), while the bond-slip law used for the unconfined case assumes a lower bond-strength and has a more rapid bond degradation for increasing slip based on recommendations of Eligehausen and Bigaj-van Vliet (1999). The parameters used for either case are presented in detail in Section 2.7.3. The bond strength is calculated based on the masonry prism strength. Confined bond conditions are always assumed within a wall foundation or a RC loading beam. The bond strength of the respective bond-slip/dowel-action interface elements is calculated based on concrete strength.

The dowel model used in this study adopts a uniaxial material law in terms of the masonry bearing stress developed under dowel action and the dowel deformation, as described in Section 2.7.3. The material law is elastic-perfectly plastic in the pre-softening region and has a linear softening branch that starts at a deformation d_1 and reaches a residual resistance equal to 1% of the yield strength at a deformation d_u. The initial stiffness and yield strength of the masonry material law are calibrated based on the equation proposed by Dulacska (1972) for the dowel strength of a bar embedded in concrete, as described in the previous chapter. The dowel strength is calculated using the grout strength. The values adopted for d_1 and d_u are 0.03 in. and 0.06 in., respectively, and have been indirectly deduced from the load-displacement response of wall tests.

In the wall foundation, the dowel law of the bond-slip/dowel-action interface elements is assigned no softening. The dowel response is calibrated so that it matches the force-displacement curve proposed by Dulacska (1972).

3.2.2 Simulation of shear-dominated tests

Wall specimens A2, Spec. 5, and UT-PBS-02 were tested by Voon (2007), Shing et al. (1991), and Ahmadi (2012), respectively, and were all shear-dominated. Wall specimen UT-PBS-02 was tested under fixed-fixed end conditions, while the other two were tested as cantilevers. Wall A2 had no axial load applied, while walls Spec. 5 and UT-PBS-02 were subjected to 100 psi and 188 psi of constant axial compressive stress, respectively, as shown in Table 3.1. Furthermore, wall A2 did not contain any horizontal reinforcement. In the tests, all three walls developed diagonal shear cracks, and in the case of UT-PBS-02, severe crushing occurred along the diagonal strut in both loading directions. The FE discretization developed for the three walls is shown in Figure 3.9.

Figure 3.10 compares the damage obtained at the end of the tests and the analyses. For clarity, the deformation in the numerical models has been amplified by 3 times. In all cases, the model is able to produce a realistic damage pattern, which is mainly governed by diagonal cracks and compressive failure of masonry. Compressive failure of masonry triggered element removal in the analysis of Spec. 5 and UT-PBS-02. However, the damage in the analysis of Spec. 5 indicates toe crushing, which was not observed in the test. For wall UT-PBS-02, the model is able to capture the crushing of the diagonal compressive struts, but not to the extent observed in the test. In the model, crushing localized only at the compression toes while in the test, crushing occurred along the diagonal struts and was more severe in the middle portion of the wall. This is in part due to the

spurious localization of compressive strains in elements undergoing softening in the analysis, and in part to the localization of damage along the diagonal discrete crack interface elements.

Figure 3.11 compares the force-displacement response curves obtained in the tests and the analyses of the three shear-dominated walls. It can be observed that the models can capture reasonably well the lateral strength of the walls and the load degradation observed in the tests. The calculated peak lateral strengths for walls A2, Spec. 2, and UT-PBS-02 differ from the test results by 3%, 2%, and 5%, respectively. In the analysis of wall UT-PBS-02, load degradation appears to occur more rapidly than that in the test. This can be explained by the localization of the compressive failure across a smaller area in the model (e.g. only at the wall toes) than in the test. Nonetheless, the model is able to capture the residual capacity of the wall.

The model accounts for the various mechanisms of shear resistance after diagonal tensile cracking occurs in a wall segment. These include the shear resistance of masonry in the compressive toe, the friction resistance along the surface of a crack, the resistance provided by the horizontal reinforcement, and the dowel action of the vertical reinforcement. The lateral resistance developed before diagonal cracking is governed by the tensile strength of masonry, which is also accounted for. Thus, the modeling scheme can be used as a reliable tool to determine the lateral load response of shear-critical wall segments.

3.2.3 Simulation of flexure-dominated tests

The second group of wall segments analyzed consists of specimens C2, 1A and 1B, UT-W-13, and F2, which were tested by Kapoi (2012), Sherman (2011), Ahmadi (2012), and He and Priestley (1992), respectively. All walls were flexure dominated. Walls C2, 1B, and UT-W-13 had vertical bars that were lap-spliced at the base, while walls 1A and F2 had no lap splices within the plastic hinge zone, as shown in Table 3.1. Although ASCE/SEI 7-16 does not permit the use of lap

splices within plastic hinge zones of special reinforced masonry shear walls, TMS 402 (2016) does not prohibit them. Walls 1A and 1B were tested by Sherman (2011) to examine the influence of lap splices on the flexural behavior of a wall. The two walls had identical configurations with the only variable being the lap-splices of the vertical bars in wall 1B. Wall F2 was a flanged wall with a T-shaped cross section. It is selected for the validation analyses because flanged walls are very common in reinforced masonry construction. All the aforementioned wall specimens were tested as cantilevers. The various damage modes observed among the tests, include horizontal flexural cracking, masonry crushing at the compression toes, buckling of vertical reinforcing bars, and lap-splice failure. Reinforcement rupture was not observed in any of the wall tests examined. In the analyses, the strain at which the compressive strength of masonry drops to zero is assumed to be $\varepsilon_u = 0.040$ for all walls except for wall UT-W-13 for which a value of $\varepsilon_u = 0.030$ is adopted. The discretization of the walls is shown in Figure 3.12. Figure 3.13 to Figure 3.17 compare the experimental and numerical results in terms of damage patterns and force-displacement response curves. It can be observed that for all cases, crushing occurs only at the first row of elements (4 in. high) above the footing because of the strain localization phenomenon.

Wall 1A is the only rectangular wall examined that did not have lap splices at the base. In the test, it showed toe crushing that extended up to the second course from the base and buckling of the vertical bars adjacent to the toes. The analysis predicts well the experimental cyclic response apart from the last two cycles, in which the model presents higher hysteretic energy dissipation than the wall specimen, as shown in Figure 3.14. This is mainly due to the fact that the model is not able to correctly capture the extent of crushing along the height of the wall, and therefore, cannot accurately represent the buckling behavior of the exposed vertical bars with the correct unsupported length. In the analysis, the unsupported length is equal to the height of the smeared-

crack shell elements, which is equal to 4 in., while in the test, the unsupported length is close to 16 in. Furthermore, the longer unsupported length of the vertical bars at the crushed toes in the test may have also reduced the tensile strains in the bar and subsequently the plastic strain energy dissipated.

Wall C2 had #4 vertical bars with 16 in. lap splices at the base, while wall 1B had #6 vertical bars with 33 in. lap splices at the base. Both walls were subjected to the same axial compression, as shown in Table 3.1. Reinforcement buckling did not occur in any of the two tests. In both tests, vertical splitting cracks were observed at the toes of the walls. These cracks can be attributed to the high compressive stress in masonry in the toe regions and to the slip of the vertical reinforcing bars near the two edges when they were subjected to high tension. In the analyses, a similar degree of crushing was observed at the base of the two walls, and it was a bit more severe than that observed in the tests, as shown in Figure 3.13 and Figure 3.15. The pinching observed in the last cycle of the force-displacement response for both tests is partly due to slip of the vertical dowel bars. This is more obvious in the response of wall 1B, in which the hysteretic energy dissipation diminished drastically in the last two cycles, as compared to the response of wall 1A. The models capture this effect to some extent. The more severe crushing obtained in the analysis is likely due to the lower slip of the vertical dowel bars and therefore the higher tensile stress developed.

Wall UT-W-13 had #6 vertical bars with 33 in. lap splices at the base and the top. As shown in Figure 3.16, the damage in the test consisted of spalling and crushing at the wall toes. Crushing was more severe at the north toe of the wall and was accompanied by the buckling of the exposed vertical reinforcing bar. Reinforcement buckling was not observed in the south toe. As shown in Figure 3.16, rapid load degradation was observed in both directions after the applied displacement

at the top exceeded 2.5 in., which corresponds to a drift ratio of 1.7%. The load degradation and low hysteretic energy dissipation obtained in subsequent cycles can be partly attributed to lap-splice failure and excessive slip of the vertical reinforcing bars. The FE model is able to capture well the cyclic response and load resistance up a displacement of 2 in. In subsequent cycles up to 5 in. of displacement, the model is more ductile and develops a higher hysteretic energy dissipation than the actual specimen. This is due to the lower amount of bar slip obtained in the analysis. It is also partly due to the inability of the model in capturing the bar buckling observed in the test. Eventually, lap-splice failure occurs in the analysis during the cycle with a displacement amplitude of 6 in. and the resistance of the model drops. The small amount of resistance that can be seen in the last cycle of the analysis is attributed to the frictional component of the bond resistance developed along the vertical dowel bars. This lateral load resistance is similar to that developed in the test. The severe crushing obtained in the analysis is again due to the inability of the model to capture the lap-splice failure as early as that observed the test. In the analysis, toe crushing initiated at a displacement of 3 in., while in the test, crushing started when the applied displacement reached 2 in.

Wall F2 was a T-shaped flanged wall with #4 vertical bars and no lap splices at the base. The damage obtained in the tests consisted of severe crushing in the web. This led to the rapid load degradation observed in the positive direction of the force-displacement curves shown in Figure 3.17. The crushing damage extended up to the third course from the base as can be observed from the picture provided in the test report (He and Priestley, 1992), which is included in Figure 3.17. No reinforcement rupture occurred in the test. The analysis captures well the experimental response in both directions up to the point that the extreme vertical bar in the web of the model

ruptures in tension. Figure 3.17 shows the rupture of the bar during the last large excursion to the negative direction after the crushing of the web.

3.2.4 Improved modeling scheme for flexure-dominated walls

The previous analyses show that the FE modeling scheme can capture well the cyclic response of flexure-dominated walls until softening begins. The limitation of the models lies on the fact that they are not able to simulate the actual extend of crushing damage along the height of flexure-dominated walls. Although the fracture energy of the smeared-crack model has been regularized to account for the strain localization effect with respect to the element size, the softening behavior of the walls is still not captured accurately. This is because the models cannot reproduce well the actual unsupported length of the reinforcing bars after the surrounding masonry has been lost due to crushing and cannot simulate the loss of the bond in the vertical bars due to the compressive damage that extends beyond the height of the elements at the base (which is 4 in. for the current models). Compressive damage could be the complete crushing of masonry or the formation of splitting cracks due to compression that can reduce the bond strength between the vertical reinforcing bars and the surrounding grout. To alleviate strain localization, constitutive models that are based on the concepts of nonlocal damage representation (e.g. Bazant and Lin 1988; Grassl and Jirasek 2006) or gradient-depended plasticity (e.g. de Borst and Muhlhaus 1992; Peerlings et al. 1998) can be pursued.

In this study, a simple non-local approach is proposed to account for the extent of crushing along the height of a wall. The approach is empirical and is based on an a priori assumption of the height of the crushed region. Based on the damage observed in wall tests (Kapoi 2012; Sherman 2011; Ahmadi 2012; and He and Priestley 1992), crushing is assumed to extend along a height (H_c) that is equal to 20% of the height (H_L) of a cantilever wall or 20% of the effective height,

which is measured from a fixed end to the point of inflection. In the original analysis scheme proposed here, the resistance of the bond-slip/dowel-action interface elements is gradually reduced as the adjacent masonry softens. This is achieved by multiplying the bond and dowel resistance of the interface elements by a reduction factor k, which is calculated based on the axial strain attained at the masonry side of the interface elements. When a smeared-crack shell element crushes and gets removed, the bond-slip/dowel-action interface elements connected to the crushed shell element are also removed. To address the strain localization issue, this scheme is modified as follows considering a cantilever flexure-dominated wall in which strain localization occurs at the base. Upon the crushing and removal of a smeared-crack element at the base, the bond-slip/dowel-action interface elements within the entire height of the assumed crushed region (within H_c) are removed. Before removal, the value of the reduction factor k for these bond-slip/dowel-action interface elements is based on the masonry compressive strain closest to the wall base.

The analyses of the flexure-dominated wall tests are repeated with the proposed scheme. The height (H_c) of the crushed region is specified to be 16 in. for walls C2, 1A, and 1B, and 28 in. for walls UT-W-13 and F2. Figures Figure 3.18 to Figure 3.22 show the damage obtained at the end of the analysis of each wall, and compare the force-displacement curves obtained with this modified approach to the experimental response and the response obtained with the original scheme. In the analysis of wall C2, the modified scheme results in less crushing at the base, which better resembles the damage obtained in the test (see Figure 3.13). However, the difference in the force-displacement response is very small compared to the original result. In the analysis of walls 1A and 1B, the modified scheme results in slightly more extended crushing along the base. The analyses also show rebar buckling, which was however not reported in the tests. For wall UT-W-13, the modified scheme provides improved the response of the model. For wall F2, the modified

scheme does not show reinforcement rupture, and the numerical response in the negative direction matches better the experimental response, as shown in Figure 3.22.

3.3 Time-history Analysis of a Two-Story Shake-Table Test Structure

To validate the ability of the proposed FE modeling scheme to simulate the dynamic response of RM wall systems, a two-story structure that was tested on a shake-table is examined. The structure was tested by Mavros et al. (2016) under a sequence of unidirectional ground motions, which were applied at a progressively increasing intensity. The structure was symmetric about the plane aligned with the direction of the input motion, and had the same layout and reinforcement details in both stories. In each story, the wall parallel to the direction of shaking (in-plane wall) had a window and a door opening. The three piers in the first story are named W1, W2, and, W3, as shown in Figure 3.23. Piers W1 and W3 had a T-shaped cross section, while pier W2, the middle one, had a rectangular cross section. The structure had four rectangular walls perpendicular to the direction of the shake-table motion, as shown in Figure 3.23. They are called the out-of-plane walls. The reinforcement details of the structure are shown in Figure 3.24. The reinforcement consisted of #4 vertical and horizontal bars. They were placed with a spacing of 16 in. on-center in the in-plane walls and the vertical bars in the wall flanges had a spacing of 8 in. Each of the out-of-plane walls had 3 #4 vertical bars and #4 horizontal bars spaced at 16 in. on center. The floor and roof system consisted of 8-inch hollow core planks with a 3-inch cast in-place RC topping. Dowel bars were used to tie floor and roof slab to the walls. During construction, the precast planks were initially supported only by the out-of-plane walls. Details about the design of structure can be found in Mavros et al. (2016).

The structure was tested with a sequence of 9 earthquake motions, all from the El Centro record of the 1979 Imperial Valley Earthquake, which was scaled to different intensity levels. The

last motion of the sequence was the strongest one with an intensity equal to the level of the Maximum Considered Earthquake (MCE), corresponding to the Seismic Design Category (SDC) D, the structure was designed for. During the tests, wall piers W2 and W3 behaved in a shear-dominated manner developing diagonal shear cracks, while the slender pier W1 had a combined flexure- and shear-dominated behavior. The damage obtained at the three wall piers by the end of the testing sequence is shown in Figure 3.25. The out-of-plane walls developed only horizontal flexural cracks. The walls in second story developed some fine cracks before the damage localized in the first-story walls. No reinforcement rupture or buckling was observed in any of the walls.

The FE model developed for the test structure is shown in Figure 3.26. The in-plane walls and wall flanges of the first story are discretized with the proposed discretization scheme. The four out-of-plane walls are discretized with rectangular 8 x 8 in. smeared-crack shell elements using cohesive-crack interface elements only in the horizontal direction. The vertical reinforcement of the out-of-plane walls is modeled with discrete beam elements and bond-slip/dowel-action interface elements are included, while the horizontal reinforcement is smeared over the shell elements. The walls in the second story had little damage and are all modeled with smeared-crack shell elements and smeared reinforcement. Cohesive-crack interface elements are not included in the second story to reduce the computational cost. The floor and roof slab are modeled with elastic shell elements and are attached to the out-of-plane and in-plane masonry walls through stiff elastic horizontal interface elements. The walls of the second story are attached to the walls of the first story through stiff elastic interface elements too. Bond-slip/dowel-action interface elements are used for the starter bars extended from the first story into the second story.

To mimic the construction sequence that can affect the distribution of the vertical load among the walls, the stiffness of each group of the elastic horizontal interface elements described

above is engaged sequentially during the application of the gravity load in the analysis. The gravity-load analysis is performed in four stages. In the first stage, the weight of the first-story walls is applied. In the second stage, the stiffness of the slab interface elements above the webs of the out-of-plane first-story walls is activated and then the weight of the first-floor slab is applied. In the third stage, the stiffness of the slab interface elements along the webs of the in-plane first-story walls is activated as well as the stiffness of the interface elements placed between the bottom and top story walls and the weight of the second-story walls is applied. In the last stage, the stiffness of the bond-slip/dowel-action interface elements of the starter bars extended into the second story is activated; the stiffness of the slab interface elements above the webs of the out-of-plane second-story walls is also activated. The weight of the second-floor slab is applied and then the stiffness of the slab interface elements above the webs of the in-plane second-story walls is activated. The gravity load is exerted by the mass multiplied by the acceleration of gravity. Once applied, the gravity load remains constant throughout the analysis. After completion of the gravity-load analysis, the time-history analysis is performed. Instead of applying base acceleration, an inertial force is applied which is equal to the mass times the negative base acceleration. The analysis program distributes the inertial force at each node based on the nodal mass.

The time-history analysis is performed with the implicit time-integration scheme proposed by Bathe (2007). The scheme has a desirable numerical damping characteristic to suppress spurious high-frequency modes that could be induced by the cracking of masonry. Additionally, Rayleigh damping is prescribed with a damping ratio of 0.5% for the first and second modes that are predominant along the direction of the shake-table motion. The stiffness proportional part of the Rayleigh damping is based on the initial stiffness of the shell and beam elements. However, for the cohesive-crack and bond-slip/dowel-action interface elements, no stiffness proportional

damping is applied because of their high initial stiffness. The initial first-mode period and second-mode period of the model are calculated to be 0.087 s and 0.031 s respectively. The first-mode period of the actual test structure was 0.077 s (Mavros et al. 2016). In the time-history analysis, the last five motions of the testing sequence are applied sequentially in a single run. In the test, motions applied prior to these five did not cause any discernible damage, and are thus omitted from the simulation. The five motions are labeled as El Centro 43%, 86%, 108%, 145%, and 160%. The material parameters used in the analysis are shown in Table 3.5. In the analysis, the original element removal scheme is used since most of the damage obtained in the test occurred in the shear-dominated piers. The modified (non-local) element removal scheme will not affect the response of shear-dominated wall segments.

The analysis results obtained from the sequence of the five motions are compared to the experimental results in Figure 3.27 to Figure 3.29. In general, the model predicts well the experimental response and the final damage patterns of the three wall piers. However, the model slightly overestimates the peak first-story drift developed during El Centro 145% and 160% motions, the last two of the sequence.

3.4 Time-history Analysis of a Structure Tested to Large Drifts on a Shake Table

The ability of the modeling scheme to capture the behavior of a RM structure at large lateral drifts is evaluated with the results obtained from the shake-table tests conducted on a single-story RM wall system. The structure was designed by Cheng et al. (2019), including the author of this dissertation, and was tested under unidirectional excitation to a roof drift that exceeded 13%. The configuration of the test structure is shown in Figure 3.23. The building had two planes of symmetry about the east-west and the north-south directions. The masonry wall system consisted of two T-walls that had their webs aligned with the direction of the shake-table motion (east-west)

and six out-of-plane rectangular walls. The roof slab consisted of 8-inch-thick hollow core planks and a 3-inch-thick RC topping. To attain the target roof mass, four RC blocks were placed on the roof slab. Each block was 16.5 ft. x 10 ft. x 10 in., as shown in Figure 3.24, and was attached to the roof slab with post-tensioning rods. The structure was designed so that the webs of the T-walls would develop a shear-dominated failure mode. The vertical and horizontal reinforcement placed in the web of the T-walls consisted of #4 vertical bars spaced at 8 in. on center and #3 horizontal bars spaced at 16 in. on center. The wall flanges and the out-of-plane walls were reinforced with #4 vertical bars spaced at 16 in. on center and #3 horizontal bars spaced at 16 in. as well. The structure was tested with a sequence of 7 ground motions using records obtained from the 1994 Northridge Earthquake. Motions 1 to 6 were scaled versions of the record from the Mulholland station during the 1940 Northridge Earthquake and were applied at 45%, 90%, 120%, 90%, 133%, and 160% of the original intensity, respectively. In Motion 7, the Rinaldi record was applied with the acceleration history scaled by 130%.

The initial period of the structure was estimate to be 0.090 s by the white-noise excitation applied before Motion 1. By the end of Motion 5, the fundamental period of the structure increased by 37%. Nonetheless, visible damage first occurred during Motion 6 (160% Mulholland). Figure 3.25 shows the damage developed during Motion 6 and Motion 7. During Motion 6, diagonal shear cracks and horizontal flexural cracks developed in the webs of W1 and W2, and masonry spalling occurred in the toe of the web of W1. Furthermore, vertical cracks appeared along the web-flange interface. During Motion 7, the final motion, the structure reached a peak drift ratio of 13.3% and sustained severe but without collapsing. As shown in Figure 3.25, wide diagonal cracks opened along the wall webs and extended along the web-flange interface. Severe crushing occurred in the wall webs but also in the wall flanges and even at the top of the out-of-plane walls. All the

horizontal bars placed in the wall webs ruptured with the exception of the bar placed in the topmost course below the roof slab. In some of the bars, rupture occurred at two locations along their length. Rupture also occurred in the extreme vertical bar at the web of W2 at the height of the wall-foundation interface. The locations of rupture are marked in Figure 3.25 as well.

Figure 3.33 shows the FE model developed for the test structure. The T-walls are discretized with the proposed modeling scheme placing cohesive-crack interface elements in the horizontal and vertical direction as well as at 45-degree and 135-degree angles. In the out-of-plane rectangular walls, the cohesive-crack interfaces are placed only in the horizontal direction since no diagonal or vertical cracks are expected to form in these walls. The vertical bars, including the dowel bars placed between the roof slab and the walls, are modeled with beam elements which are connected to the adjacent masonry shell elements with bond-slip/dowel-action elements based on the proposed methodology. The horizontal reinforcement of the out-of-plane walls is modeled as smeared reinforcement. The roof slab is modeled with elastic shell elements whose nodes are placed along the mid-thickness of the slab. Elastic shell elements are also used to model the RC blocks. Rigid beam elements are used to model the vertical offset between the height of the center of mass of the roof slab and the center of mass of the RC blocks. This approach assumes that full composite action can develop between the blocks and roof slab. The modulus of elasticity assigned to the shell elements of the roof and blocks is 2,500 ksi. Table 3.6 shows the calibration of the material properties used in the analyses of the structure for the smeared-crack shell elements, cohesive-crack interface elements, reinforcing bar beam elements, and bond-slip/dowel-action interface elements. The masonry tensile strength is assumed to be about 8% of the masonry prism strength. For the coefficient of friction of cracked masonry, the value of 1.20 is used which has been also adopted in all the analyses presented in the previous sections. A coefficient of friction

equal to 1.0 is used for the wall-foundation interface since the interface was intentionally roughened in the test. The values used for the parameters of the reinforcing steel model have been calibrated based on the monotonic tensile stress-strain curves obtained from samples of the bars used in the construction of structure. The samples were tested to fracture. The fundamental period of the model is determined though eigenvalue analysis and it is equal to 0.082 s. This is slightly lower than the initial fundamental period (0.090 s) measured for the test structure.

The model is subjected to the measured histories of Motions 5, 6, and 7 in a single run. Since no discernible damage occurred prior to Motion 6 in the test, motions 1 to 4 are omitted from the analysis. Figure 3.34 compares the numerical to experimental results in terms of the displacement time history of the roof and the base shear versus roof displacement hysteresis curves. In Motions 5 and 6, the model appeared to be stiffer than the test structure. The lower stiffness developed in the test can be attributed to the deterioration in the bond between the vertical bars and the grout caused during Motions 1 to 5 under consecutive displacement cycles of low amplitude. The model is not able to simulate this effect. Figure 3.35 shows the cracks formed in the analysis of Motion 6. In Motion 7, the model is able to capture the rapid load degradation that occurred during the first displacement excursion in the positive direction. The load drop is primarily caused by the rupture of the horizontal bars. Nonetheless, in the following cycles, the model overestimated the resistance of the structure likely because it cannot capture the extent of crushing observed in the test, as shown in Figure 3.35. Furthermore, the reinforcing bars ruptured in more locations in the test than in the analysis. Nonetheless, given the complexity of the damage mode obtained in the test, the results of the analyses are deemed satisfactory.

3.5 Case Study of a Commercial Building Archetype Subjected to Severe Earthquake Loading

There is a pressing need from the design codes to assess the seismic performance of modern RM buildings under severe earthquakes. Buildings designed based on the current seismic design criteria (ASCE/SEI 7) are presumed to have a probability of collapse lower than 10% when subjected to the maximum considered earthquake (MCE). However, there has been no rational analysis to support this assertion. The finite element (FE) modeling scheme developed for the analysis of RM structures has been validated with results from shear- and flexure-dominated quasi-static wall tests as well as with results from the shake-table tests of two full-scale RM wall systems. One of the two wall systems examined had been tested up to the verge of collapse experiencing severe shear failure including rupture of horizontal reinforcement. In all cases, the models were able to capture reasonably well the cyclic load-displacement response and damage pattern observed in the tests. Therefore, the proposed modeling scheme can be used as a predictive tool for assessing the collapse potential of real-world RM wall structures under strong base excitation and provide insight into their seismic behavior. This section demonstrates the use of the proposed FE modeling scheme for the analysis of a two-story commercial building archetype subjected to severe earthquake loading.

3.5.1 Building design

Figure 3.36 shows the configuration of the building archetype considered for this case study. The building has two stories and is symmetric along the longitudinal (x-direction) and transverse (z-direction) directions. The footprint of the building has dimensions of 96 ft. x 48 ft., and the story height is 12 ft. The lateral load resisting system consists of six RM shear walls located at the perimeter of the building. The four corner walls have an L-shaped cross section, while the

two middle walls are rectangular. The gravity load is partly resisted by the RM shear walls and partly by a steel frame. Figure 3.37 and Figure 3.38 show the framing plans and the design details of the walls and steel members. The building was designed by KL&A Inc. (FEMA 2019) according to current codes and practice. The building was designed for a high seismic intensity site with a design spectrum corresponding to seismic design category (SDC) D_{max}, as defined in FEMA P-695. The walls were designed as special RM shear walls following the provisions of TMS 402 (2016). In the design, the walls were assumed to behave as cantilevers neglecting any coupling introduced by the horizontal diaphragms. Using a response modification factor (R) of 5, as permitted by ASCE/SEI 7 for special RM walls, the seismic base shear coefficient (C_s) was determined to be equal to 0.20. The steel frame was designed to resist only gravity loads. As shown in Figure 3.37, the floor system consists of a composite concrete slab, while the roof system consists of a metal deck. In both levels, apart from the main beams spanning between the steel columns and walls, beam joists have been placed along the longitudinal direction of the building. The beam joists are supported on the lateral main beams and on the corner walls.

The RM walls were designed with 8-inch-thick concrete masonry walls. The compressive strength of masonry was specified to be 2,000 psi. The horizontal and vertical reinforcement of the walls consists of Grade 60 #5 bars, as shown in Figure 3.38. The vertical loads assumed in the design are as follows: the dead and live loads for the floor are 80 psf and 50 psf, respectively, while those for the roof are 20 psf and 30 psf, respectively. The weight of the cladding placed along the perimeter of the building between the masonry walls is assumed to be 20 lbs per square foot.

3.5.2 Development of the finite element model

Figure 3.39 shows the FE model developed for the building archetype. Damage was expected to primarily localize in the bottom story. Therefore, only the bottom-story walls are

modeled with the detailed scheme described in Section 2.3. The upper-story walls are modeled in a less refined fashion, for the sake of computational efficiency, with smeared-crack shell elements and smeared reinforcement described by a bilinear material law. This is deemed sufficient to capture the mild damage expected to develop in the upper story. The triangular shell elements used in the walls have 6-inch long perpendicular sides and four layers through the thickness. The steel columns and beams in the gravity system are modeled with fiber-section beam-column elements that have the Hughes-Liu formulation (LSTC 2019) and are assigned a bilinear material law. Each column is discretized with eight elements per story. The columns are assumed to be hinge-connected to the base plate. According to the design details, the beams are connected to the orthogonal supporting beams and columns through clip angles, which do not provide much moment or axial force restraints at the ends of the connected beams, and thereby will not allow the development of a strong composite action between the beams and the floor slab at these locations. To account for this, the beams under the floor slab of the archetype are connected to the supporting beams and the columns with stiff zero-length springs that do not transmit moments or axial forces but provide strong translational restraints in the vertical and lateral directions. Beams are connected to the walls in the same way. The beams for the roof decks have regular hinge connections except for the beam joists which are connected to the supporting beams without the axial restraint.

The floor and roof diaphragms are modeled with nonlinear shell and beam elements. The modeling approach pursued intends to provide a good approximation of the stiffness of the diaphragms, and to capture the strengths and failure behaviors. According to the design, the floor diaphragm has a concrete slab cast on a corrugated steel pan with 2.0-in.-high ribs running along the transverse direction (z-direction) of the building (see Figure 3.36 for the coordinate system).

The distance of the top surface of the concrete slab to the top of the ribs is 3.0 in., and the slab contains temperature and shrinkage steel running perpendicular to the ribs with an amount meeting the minimum requirement of ACI 318. To simplify modeling, the ribs are not explicitly represented. The slab is assumed to have a uniform thickness of 4 in. including the concrete topping and a 0.0474-in.-thick bottom layer representing the steel pan. The steel layer is set to act only along the direction of the ribs. The concrete layer of the shell elements is modeled with the material law described in Section 2.4.2. The temperature and shrinkage steel is accounted for as smeared reinforcement. The centroids of the steel beams and shell elements are offset vertically to model the bending stiffness and capacity of the composite section correctly.

The roof diaphragm is a light corrugated steel deck with 1.5-in.-high ribs spanning along the transverse direction (*z*-direction) of the building. The deck panels are stitched together with fasteners and supported on the steel joists and the main beams. Experimental studies by Tremblay et al. (2004) have shown that the in-plane shear stiffness and strength of metal decks greatly depend on the stiffness and strength of the panel-to-panel side-lap connections and deck-to-frame connections. For this building, the deck-to-frame connections consist of puddle welds placed at a 36/7 pattern (Luttrell 1995), while the side-lap connections consist of #10 screws spaced at 12 in. on center along the side laps. For the corrugated panels, beam elements with a fiber-section discretization are used to simulate the bending stiffness of the ribs, and shell elements are used to provide the in-plane resistance. Each beam has an I-shaped cross section that represents the bending stiffness of the ribs over a 36-in.-wide panel. To ensure that no additional in-plane shear resistance can be introduced by the bending of the beams, the moments at the ends of each beam element about the axis perpendicular to the deck are released. The nonlinear in-plane shear response of the shell elements is calibrated to represent both the behavior of the panel and that of

the connectors. Figure 3.40d shows the arrangement of the beam and shell elements in the discretization of the deck. The deck shell elements are assigned a two-dimensional elasto-plastic constitutive law adopted from the material library of LS-DYNA. The constitutive law has an effective stress - versus - effective plastic strain hardening/softening relation. Hardening is linear in the pre-peak regime and is followed by linear softening in the post-peak regime until a constant residual strength is reached. The initial stiffness and strength of the shell elements under simple shear were determined from the guidelines of the Steel Deck Institute (SDI) Design Manual (Luttrell 1995). The deck has been assumed to remain elastic up to 40% of the peak strength.

The effective strain at peak strength and the residual strength of the constitutive law were calibrated with the test data of Essa et al. (2003) on a roof deck diaphragm with fasteners similar to those used for the building archetype. Figure 3.40 shows the deck specimen tested by Essa et al. (2003) and the experimental cyclic and monotonic response under shear. The test specimen was simulated by using shell elements with dimensions 36 in. x 30 in, which is similar to the size of those used in the roof diaphragm of the FE model of the archetype. Based on the experimental results, the parameters of the constitutive law have been determined so that the peak shear strength occurs at a shear angle of 0.008 rad and that the residual strength is 20% of the peak strength and is reached at a shear angle of 0.20 rad. Figure 3.40c also shows the response of the model under monotonic and cyclic shear for the same deck configuration as in Essa et al. but with the properties of the deck panels and fasteners used in the archetype building. The diaphragm of the archetype is stronger than the test specimen because it has a thicker steel panel, namely 0.0474 in. versus 0.0295 in., and has panel-to-frame welds located in every flute (36/7 pattern) rather than in every other flute. This is accounted for in the model. The side-lap connections consist of screws spaced at 12

in. in both the archetype and the test of Essa et al. Furthermore, the width of the deck panels and the rib-height are the same in both the archetype and the test of Essa et al.

In the FE model of the building, the shell elements representing the roof and floor diaphragms are directly connected to the shell elements of the walls. Owing to the large variation in the type and detailing of the connectors in practice, the flexibility and failure of the diaphragm-to-wall connections are not considered in the model. Further details about the modeling of the diaphragms in this building archetype can be found in FEMA (2019).

3.5.3 Time-history analyses

Time-history analyses have been performed using three sets of ground motion records selected from the far-field records of the FEMA P-695 data base. Each record has two components of horizontal acceleration. Figure 3.41 shows the ground acceleration time histories and acceleration response spectra for these records, as well as the MCE spectrum for SDC D_{max}. Records 1 and 2 were obtained from the 1994 Northridge Earthquake, while Record 3 was obtained from the 1987 Superstition Hills Earthquake. The three records have distinct characteristics in terms of the spectral shapes and durations of strong motion. Analyses have been conducted with the records scaled to the MCE and 2xMCE. Table 3.7 shows the scaling factors applied to each record for the two intensity levels. The records were scaled by matching the spectral acceleration of the record at the code-based period to that of the MCE or 2xMCE. Among the two components, the scaling was based to the one with the highest spectral acceleration at the code-based period. Based on FEMA P-695, the code-based period of the archetype building is 0.25 s.

The gravity and seismic mass used in the analyses are based on the following load combination: $1.05D + 0.25L$ (with D and L being the dead and live loads, respectively), according to the FEMA P-695 procedure. This results in a total building weight of 872 kips (excluding the

foundation). In the model, the mass is distributed among the nodes according to the density of the elements. As in the analyses of the shake-table structures, the time-history analyses of the archetype are performed using the time-integration scheme proposed by Bathe (2007). Furthermore, Rayleigh damping is prescribed with a damping ratio of 0.1% in the first and fifth significant modes. Its stiffness proportional part is based on the initial stiffness of the shell and beam elements. No stiffness proportional damping is applied to the cohesive-crack and bond-slip/dowel-action interface elements.

Table 3.8 shows the values of the material properties assigned to the masonry smeared-crack shell elements, reinforcement beam elements, and cohesive-crack and bond-slip/dowel-action interface elements. Expected values have been assumed for the masonry prism strength, masonry grouted strength, and for the reinforcement yield and tensile strengths. For the rest of the parameters, consistency is maintained with the values used in the validation analyses presented in the previous sections.

The RM walls of the archetype were designed as cantilever walls following the code provisions for special RM shear walls. Therefore, they were expected to behave in a flexure-dominated manner developing crushing at the base due to flexure. To account for the extent of crushing above the base, the approach presented in Section 3.2.4 is used. As described in Section 3.2.4, the approach is based on an a priori assumption of the height H_c of the crushed region and aims to represent the unsupported length of the bars due to crushing. As described in Section 3.2.4, the bond and dowel resistance of the bond-slip/dowel-action interface elements that lie within the assumed crushed region are reduced as a function of the compressive strain registered at the wall top or bottom. The bond-slip/dowel-action interface element within the height H_c will get

removed when the shell element at the base gets removed due to crushing. The height H_c of the crushed region is specified to be equal to 20% of the distance between the inflection point of the wall and the wall end. For the archetype building, a trial analysis with the MCE-level motions was conducted to identify the location of the inflection point of the first-story walls. It was found that the inflection point of the corner walls is located at a distance of 80%-90% of the story height above the base, while the inflection point of the middle walls is located at the mid-height of the first story. Therefore, at the base of the corner and middle walls, H_c is assumed to be equal to 24 in. and 14 in., respectively. At the top of the first-story walls, H_c should be equal to 4 in. and 14 in. for the corners and middle walls, respectively. However, to simplify the present analyses, the approach of Section 3.2.4 has been employed only for the bottom of the walls, while H_c at the top of the walls is assumed to be equal to the height of the shell elements, namely 6 in.

Figure 3.42 through Figure 3.45 show the response of the building model under Records 1 and 2. The results are presented in terms of the time-history response of the first-story drift ratio and the hysteresis loops of the base shear versus the first-story drift ratio developed in the *x* and *z* directions. The base shear shown is normalized by the building weight of 872 kips. The base shear does not include the inertia of the footings. Record 3 was the least demanding out of the three. When scaled at the MCE and 2xMCE levels, the structure reaches a peak first-story drift of 1.6% and 6.3%, respectively. In the analyses with the three records, the structure develops a peak base shear that is about 3 times the design base shear (on average), which corresponds to a seismic base shear coefficient of 0.20. The higher capacity is partly due to the influence of the floor diaphragm which restrains the top of the bottom-story walls from rotating, and thereby, reduces the effective shear span ratio of the walls. Figure 3.46 shows the damage obtained during Record 1 when scaled to the MCE and 2xMCE levels, and the damage obtained during Record 2 when scaled to 2xMCE.

Failure concentrated in the bottom story walls with severe crushing occurring at the base of the walls. The crushing was due to flexure in the middle walls, and due to combined flexure and shear in the corner walls. Diagonal shear cracks occurs in both sides of the flanged walls, however, their opening is controlled by the horizontal reinforcement. Several of the vertical bars buckle and rupture near the base. Rupture of horizontal bars occurs only during the motion with Record 1 scaled at the MCE level. In this motion, two horizontal bars along the *z*-direction of the corner wall rupture as shown in Figure 3.46a. The results also show that Record 1 was the most demanding and caused the building to collapse when applied with the intensity of 2xMCE. Nonetheless, the first-story drift ratio exceeds 10% when approaching collapse. During the analyses, the damage in the second story primarily occurs in the form of flexural cracks right above the floor slab, causing the smeared reinforcement to yield.

Part of this chapter contains the material that will appear in Chapter 4 of the technical report titled "Developing Solutions to the Short-Period Building Performance Paradox: Study for Reinforced Masonry Buildings" that will be submitted to the Federal Emergency Management Agency by the Applied Technology Council for the project number ATC-116. The authors of Chapter 4 in the report are the author of this dissertation, Jianyu Cheng, and P. Benson Shing. The report chapter was prepared under the supervision of Dr. Charles A. Kircher, who was the technical director of the ATC-116 project. The author of this dissertation was the primary investigator and author of all the materials covered in this chapter of the dissertation.

Table 3.1 Design details of quasi-static wall tests.

Wall ID	Tested by	L_w (in)	H_w (in)	H_L (in)	t_w (in)	Reinforcement		Lap splices	Applied axial load (kips)	End condi-tions	Failure mode
						Vert.	Hor.				
A2	Voon (2007)	70.9	70.9	70.9	5.512	D20 @ 15.7 in.	1 x R6	No splices	0.0	Canti-lever	Shear
Spec. 5	Shing et al. (1991)	72.0	72.0	72.0	5.625	#7 @ 16 in.	#3 @ 16 in.	No splices	40.5	Canti-lever	Shear
UT-PBS-02	Ahmadi (2012)	72.0	72.0	72.0	7.625	#6 @ 16 in.	#4 @ 16 in.	24 in. (mid-height)	103.0	Fixed-ends	Shear
C2	Kapoi (2012)	40.0	72.0	80.0	7.625	#4 @ 8 in.	#4 @ 8 in.	16 in. (base)	48.0	Canti-lever	Flexure
1A	Sherman (2011)	40.0	72.0	79.3	7.625	#6 @ 8 in.	#4 @ 8 in.	No splices	48.0	Canti-lever	Flexure
1B	Sherman (2011)	40.0	72.0	79.3	7.625	#6 @ 8 in.	#4 @ 8 in.	33 in. (base)	48.0	Canti-lever	Flexure
UT-W-13	Ahmadi (2012)	48.0	136.0	144.0	7.625	#6 @ 8 in.	#4 @ 16 in.	33 in. (base/top)	45.75	Canti-lever	Flexure
F2	He and Priestley (1992)	45.625 (web) 104.0 (flange)	136.0	144.0	5.625	#4 @ 16 in.	#4 @ 8 in. (web) #4 @ 8 in. (flange)	20 in. (mid-height)	81.0	Canti-lever	Flexure

L_w, H_w, and t_w represent the length, height, and thickness of a masonry wall.
H_L is the height at which the lateral load was applied.
In wall F2, the length of the web includes the thickness of the flange.

Table 3.2 Material properties of wall specimens.

Material property	Wall ID							
	A2	**Spec. 5**	**UT-PBS-02**	**C2**	**1A**	**1B**	**UT-W-13**	**F2**
Masonry prism compressive strength, f'_m (ksi)	2.55	2.64	3.11	3.04	2.77	3.04	4.45	2.60
Grout prism compressive strength, f'_g (ksi)	n.a.	3.02	5.97	5.53	6.49	5.53	4.67	5.64
Reinf. size [vert. / hor.]	D20 / R6	#7 / #3	#6 / #4	#4 / #4	#6 / #4	#6 / #4	#6 / #4	#4 / #4
Reinf. yield strength, f_y (ksi) [vert. / hor.]	46.1 / 47.1	72 / 57	63.2 / 62.4	65.3	65.4 / 66.2	64.7 / 65.3	61.1 / 65.0	75.9
Reinf. tensile strength, f_u (ksi) [vert. / hor.]	66.2 / n.a.	105 / 82	102.7 / 100.5	n.a.	n.a.	n.a.	101.9 / 102.3	117.2
Reinf. strain at ultimate strength, ε_u [vert. / hor.]	0.20 / n.a.	0.15 / 0.15	n.a.	n.a.	n.a.	n.a.	n.a.	0.10
Reinf. strain at beginning of strain hardening, ε_{sh}	0.02 / n.a.	0.013 / 0.02	n.a.	n.a.	n.a.	n.a.	n.a.	0.006
Reinf. strain and stress at a point (ε_{sh1}, σ_{sh1}) within the hardening region [vert. / hor.]	(0.03, 49.2) / n.a.	(0.04, 89.0) / (0.05, 72.0)	n.a.	n.a.	n.a.	n.a.	n.a.	(0.03, 93.4)

Table 3.3 Material parameters of smeared-crack shell elements and cohesive-crack interfaces used in the analyses of wall segments.

Material parameters	Wall ID							
	A2	**Spec. 5**	**UT-PBS-02**	**C2**	**1A**	**1B**	**UT-W-13**	**F2**
				Smeared-crack shell elements				
f_m **(ksi)**	2.55	2.64	3.11	3.04	2.77	3.04	4.45	2.60
f_o **(ksi)**	1.70	1.76	2.07	2.03	1.85	2.03	2.97	1.73
E_m **(ksi)**	1530	1584	1866	1824	1662	1824	2670	1560
f_t **(ksi)**	0.20	0.33	0.35	0.30	0.27	0.30	0.44	0.30
ε_0	0.003	0.003	0.003	0.003	0.003	0.003	0.003	0.003
ε_u	0.040	0.040	0.040	0.040	0.040	0.040	0.030	0.040
				Cohesive-crack interface elements				
D_{nn} / D_{tt} **(ksi/in)**	5000	5000	5000	5000	5000	5000	5000	5000
s_o **(ksi)**	0.20	0.30	0.35	0.30	0.27	0.30	0.44	0.30
μ_o / μ_r	1.2 / 1.0	1.2 / 1.0	1.2 / 1.0	1.2 / 1.0	1.2 / 1.0	1.2 / 1.0	1.2 / 1.0	1.2 / 1.0
r_o / r_r **(ksi)**	0.05 / 0.01	0.05 / 0.01	0.05 / 0.01	0.05 / 0.01	0.05 / 0.01	0.05 / 0.01	0.05 / 0.01	0.05 / 0.01
$G_{f,I}$ **(kips/in)**	0.0002	0.0002	0.0002	0.0002	0.0002	0.0002	0.0002	0.0002
$G_{f,II}$ **(kips/in)**	0.002	0.002	0.002	0.002	0.002	0.002	0.002	0.002
$\zeta_{dil,o}$ / $\zeta_{dil,r}$	0.40 / 0.001	0.40 / 0.001	0.40 / 0.001	0.40 / 0.001	0.40 / 0.001	0.40 / 0.001	0.40 / 0.001	0.40 / 0.001
d_o **(in)**	0.40	0.40	0.40	0.40	0.40	0.40	0.40	0.40
				Cohesive-crack interface elements at base				
D_{nn} / D_{tt} **(ksi/in)**	5000	5000	5000	5000	5000	5000	5000	5000
s_o **(ksi)**	0.20	0.20	0.20	0.20	0.20	0.20	0.20	0.20
μ_o / μ_r	1.0 / 1.0	1.0 / 1.0	0.7 / 0.7	1.0 / 1.0	1.0 / 1.0	1.0 / 1.0	0.7 / 0.7	0.7 / 0.7
r_o / r_r **(ksi)**	0.05 / 0.01	0.05 / 0.01	0.05 / 0.01	0.05 / 0.01	0.05 / 0.01	0.05 / 0.01	0.05 / 0.01	0.05 / 0.01
$G_{f,I}$ **(kips/in)**	0.0002	0.0002	0.0002	0.0002	0.0002	0.0002	0.0002	0.0002
$G_{f,II}$ **(kips/in)**	0.002	0.002	0.002	0.002	0.002	0.002	0.002	0.002
$\zeta_{dil,o}$ / $\zeta_{dil,r}$	0.40 / 0.001	0.40 / 0.001	0.10 / 0.001	0.40 / 0.001	0.40 / 0.001	0.40 / 0.001	0.10 / 0.001	0.10 / 0.001
d_o **(in)**	0.40	0.40	0.05	0.40	0.40	0.40	0.05	0.05

Table 3.4 Material parameters of reinforcement beam and bond-slip/dowel-action interface elements used in the analyses of wall segments.

Material parameters	Wall ID							
	A2	**Spec. 5**	**UT-PBS-02**	**C2**	**1A**	**1B**	**UT-W-13**	**F2**
	Reinforcement beam elements							
Size [vert. / hor.]	D20 / R6	#7 / #3	#6 / #4	#4 / #4	#6 / #4	#6 / #4	#6 / #4	#4 / #4
f_y (ksi)	46.1 / 47.1	72.0 / 57.0	63.2 / 62.4	66.0	65.4 / 66.2	64.7 / 65.3	61.1 / 65.0	75.9
f_u (ksi)	66.2	105 / 82	102.7 / 100.5	105.0	105	105.0	101.9 / 102.3	117.2
E_s (ksi)	29000	29000	29000	29000	29000	29000	29000	29000
ε_{sh}	0.02	0.013 / 0.02	0.01	0.01	0.01	0.01	0.01	0.006
(ε_{sh1} , f_{sh1})	(0.03, 49.2)	(0.04, 89) / (0.05, 72)	(0.03, 84)	(0.03, 84)	(0.03, 84)	(0.03, 84)	(0.03, 84)	(0.03, 93.4)
ε_{su}	0.20	0.15	0.12	0.12	0.12	0.12	0.12	0.10
D_{cr}	0.76	0.63 / 0.60	0.55	0.55	0.55	0.55	0.55	0.55
	Bond-slip/Dowel-action interface elements							
Masonry strength used for bond strength (ksi)	2.55	2.64	3.11	3.04	2.77	3.04	4.45	2.60
Confinement conditions [vert. / hor.]	Unconf. / Confined	Unconf. / Confined	Unconf. / Confined	Conf.	Unconf. / Confined	Unconf. / Confined	Unconf. / Confined	Confined
Grout strength used for dowel strength (ksi)	2.55	3.02	5.97	5.53	6.49	5.53	4.67	5.64
Dowel model d_1 / d_u (in)	0.03 / 0.06	0.03 / 0.06	0.03 / 0.06	0.03 / 0.06	0.03 / 0.06	0.03 / 0.06	0.03 / 0.06	0.03 / 0.06

Table 3.5 Material parameters used in the analysis of the two-story shake-table test.

Smeared-crack shell elements

f_m (ksi)	2.50
f_o (ksi)	1.67
E_m (ksi)	1500
f_t (ksi)	0.35
ε_o	0.003
ε_u	0.040

Cohesive-crack interface elements

D_{nn} / D_{tt} (ksi/in)	5000
s_o (ksi)	0.35
μ_o / μ_r	1.2 / 1.0
r_o / r_r (ksi)	0.05 / 0.01
$G_{f,I}$ (kips/in)	0.0002
$G_{f,II}$ (kips/in)	0.002
$\zeta_{dil,o}$ / $\zeta_{dil,r}$	0.40 / 0.001
d_o (in)	0.40

Cohesive-crack interface elements at base

D_{nn} / D_{tt} (ksi/in)	5000
s_o (ksi)	0.20
μ_o / μ_r	0.7 / 0.7
r_o / r_r (ksi)	0.05 / 0.01
$G_{f,I}$ (kips/in)	0.0001
$G_{f,II}$ (kips/in)	0.001
$\zeta_{dil,o}$ / $\zeta_{dil,r}$	0.10 / 0.001
d_o (in)	0.05

Reinforcement beam elements

Size	#4
f_y (ksi)	63.2
f_u (ksi)	102.7
E_s (ksi)	29000
ε_{sh}	0.01
(ε_{sh1} , f_{sh1})	(0.02, 80.0)
ε_{su}	0.15
D_{cr}	0.7

Bond-slip/Dowel-action interface elements

Masonry strength used for bond strength (ksi)	2.5
Confinement conditions	Confined
Grout strength used for dowel strength (ksi)	3.5
Dowel model d_l / d_u (in)	0.03 / 0.06

Table 3.6 Material parameters used in the analysis of the one-story shake-table test.

Smeared-crack shell elements

f_m (ksi)	3.0
f_o (ksi)	2.0
E_m (ksi)	1800
f_t (ksi)	0.25
ε_o	0.003
ε_u	0.040

Cohesive-crack interface elements

D_{nn} / D_{tt} (ksi/in)	5000
s_o (ksi)	0.25
μ_o / μ_r	1.2 / 1.0
r_o / r_r (ksi)	0.05 / 0.01
$G_{f,I}$ (kips/in)	0.0002
$G_{f,II}$ (kips/in)	0.002
$\zeta_{dil,o}$ / $\zeta_{dil,r}$	0.40 / 0.001
d_o (in)	0.40

Cohesive-crack interface elements at base

D_{nn} / D_{tt} (ksi/in)	5000
s_o (ksi)	0.10
μ_o / μ_r	1.0 / 1.0
r_o / r_r (ksi)	0.05 / 0.01
$G_{f,I}$ (kips/in)	0.0001
$G_{f,II}$ (kips/in)	0.001
$\zeta_{dil,o}$ / $\zeta_{dil,r}$	0.40 / 0.001
d_o (in)	0.40

Reinforcement beam elements [vert./hor.]

Size	#4 / #3
f_y (ksi)	68.0 / 75.0
f_u (ksi)	99.0 / 106.0
E_s (ksi)	29000
ε_{sh}	0.010 / 0.006
(ε_{sh1} , f_{sh1})	(0.03, 85.0) / (0.025 93.0)
ε_{su}	0.12 / 0.11
D_{cr}	0.79 / 0.60

Bond-slip/Dowel-action interface elements

Masonry strength used for bond strength (ksi)	3.0
Confinement conditions	Confined
Grout strength used for dowel strength (ksi)	4.5
Dowel model d_1 / d_u (in)	0.03 / 0.06

Table 3.7 Scaling of the three records used for the time-history analyses of the commercial building archetype.

Intensity	Acceleration scaling factors		
	Record 1	Record 2	Record 3
MCE	1.25	1.33	1.80
2xMCE	2.50	2.66	3.60

Table 3.8 Material parameters used in the analysis of the commercial archetype.

Smeared-crack shell elements

f_m (ksi)	2.50
f_o (ksi)	1.67
E_m (ksi)	1500
f_t (ksi)	0.25
ε_o	0.003
ε_u	0.047

Cohesive-crack interface elements

D_{nn} / D_{tt} (ksi/in)	5000
s_o (ksi)	0.25
μ_o / μ_r	1.2 / 1.0
r_o / r_r (ksi)	0.05 / 0.01
$G_{f,I}$ (kips/in)	0.0002
$G_{f,II}$ (kips/in)	0.002
$\zeta_{dil,o}$ / $\zeta_{dil,r}$	0.40 / 0.001
d_o (in)	0.40

Cohesive-crack interface elements at base

D_{nn} / D_{tt} (ksi/in)	5000
s_o (ksi)	0.10
μ_o / μ_r	1.0 / 1.0
r_o / r_r (ksi)	0.05 / 0.01
$G_{f,I}$ (kips/in)	0.0001
$G_{f,II}$ (kips/in)	0.001
$\zeta_{dil,o}$ / $\zeta_{dil,r}$	0.40 / 0.001
d_o (in)	0.40

Reinforcement beam elements

Size	#5
f_y (ksi)	68.0
f_u (ksi)	102.0
E_s (ksi)	29000
ε_{sh}	0.010 / 0.03
(ε_{sh1} , f_{sh1})	(0.03, 85.0)
ε_{su}	0.11
D_{cr}	0.55

Bond-slip/Dowel-action interface elements

Masonry strength used for bond strength (ksi)	2.50
Confinement conditions	Confined
Grout strength used for dowel strength (ksi)	3.50
Dowel model d_1 / d_u (in)	0.03 / 0.06

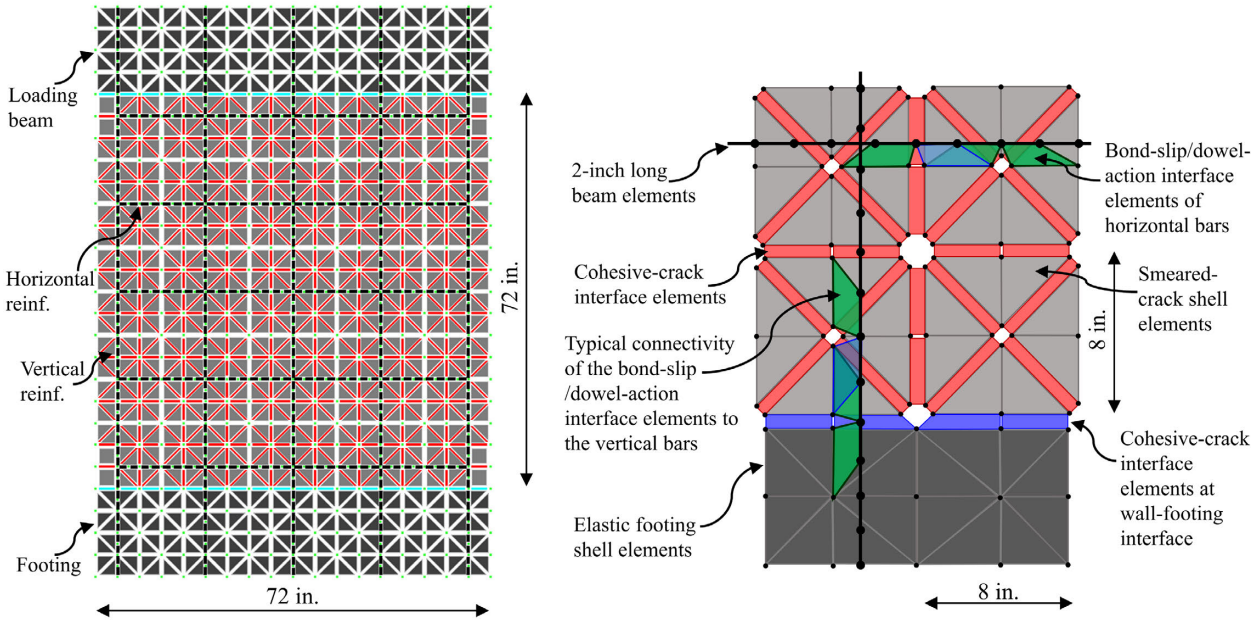

Figure 3.1 Proposed discretization for RM wall segments. (a) Mesh of a wall; (b) schematic of element connectivity within a wall.

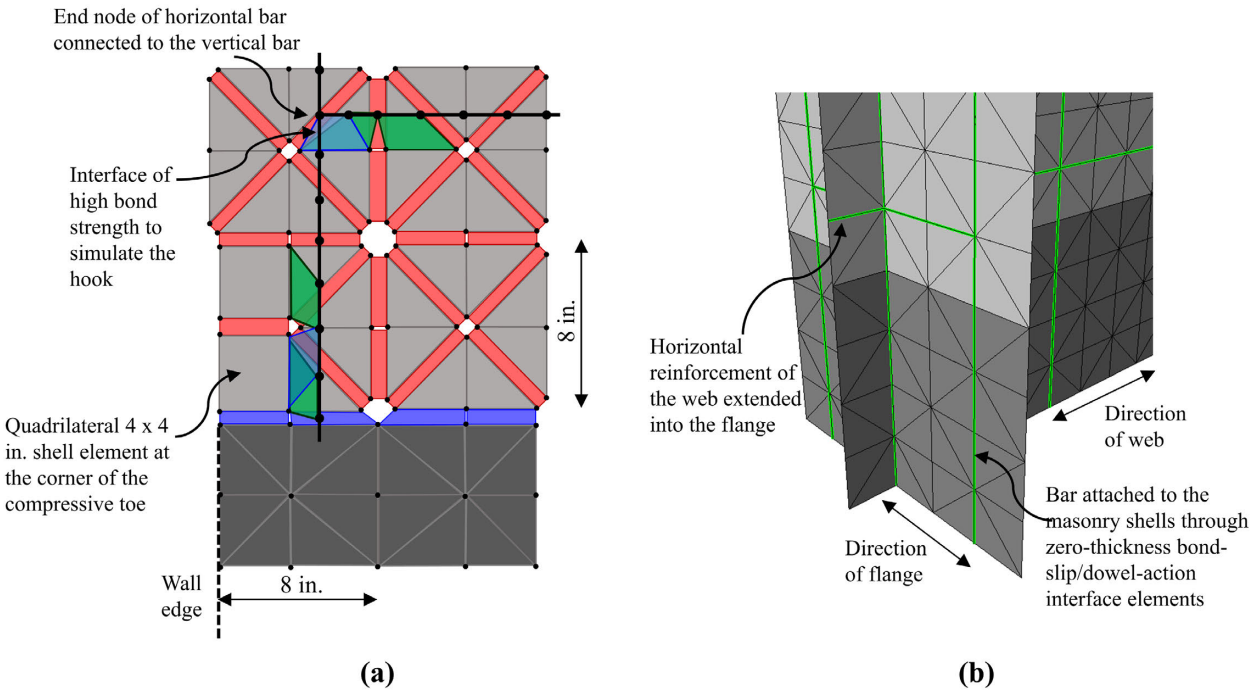

Figure 3.2 Proposed discretization scheme at the edge of a RM wall. (a) Schematic for a planar wall; (b) mesh for a flanged wall.

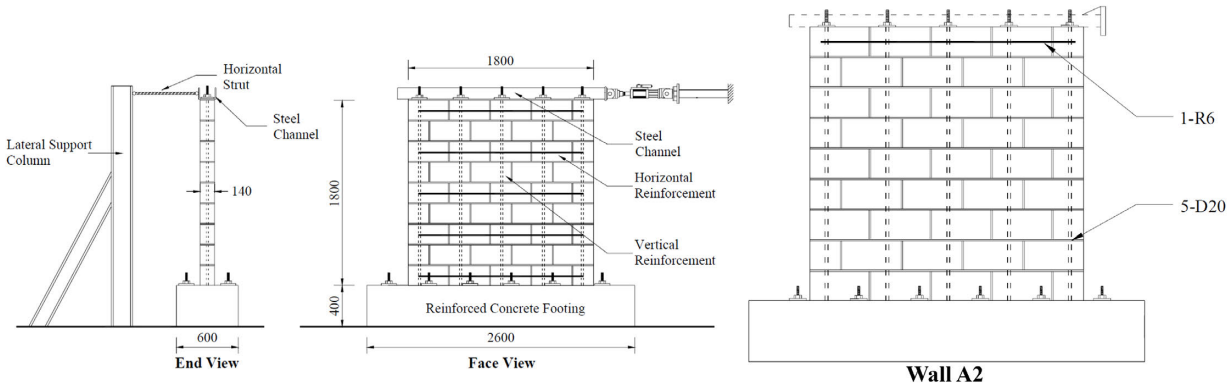

(a) Test setup **(b) Reinforcement detail**

Figure 3.3 Test setup and reinforcement details of wall specimen A2 (Voon 2007).

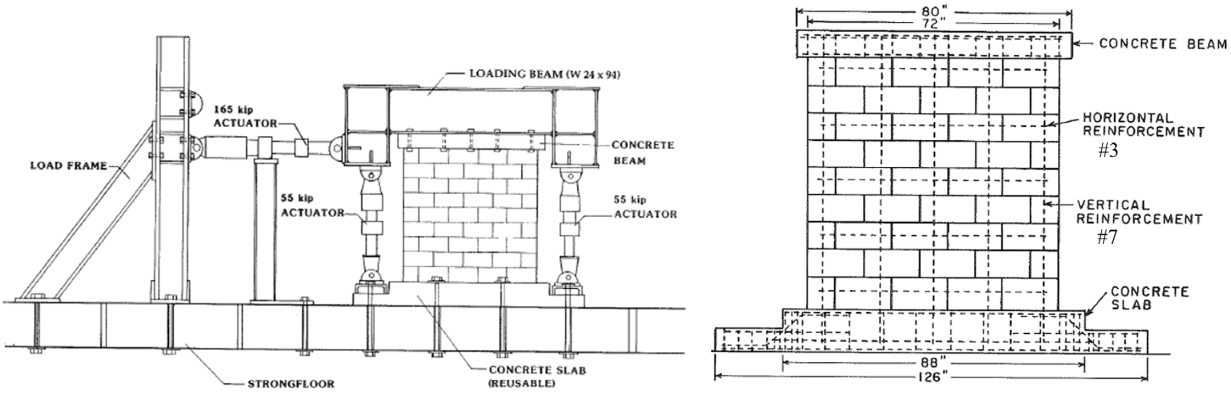

(a) Test setup **(b) Reinforcement detail**

Figure 3.4 Test setup and reinforcement details of wall specimen Spec. 5 (Shing et al. 1991).

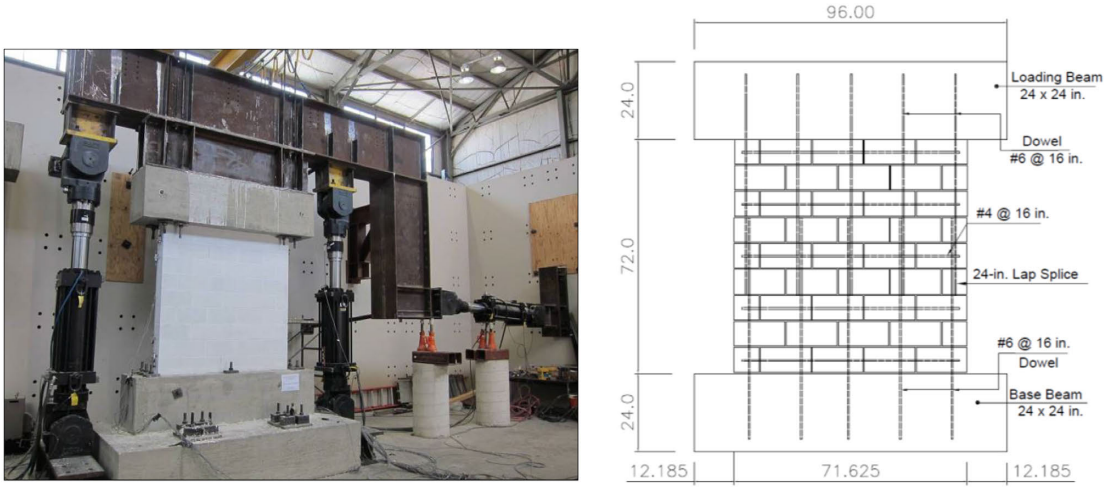

(a) Test setup **(b) Reinforcement detail**

Figure 3.5 Test setup and reinforcement details of wall specimen UT-PBS-02 (Ahmadi 2012).

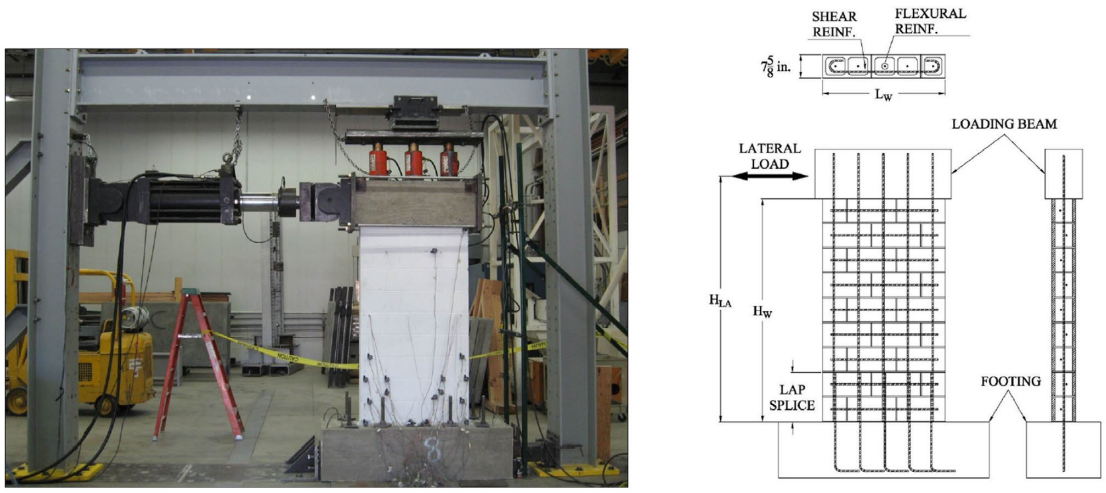

(a) Test setup **(b) Reinforcement detail**

Figure 3.6 Test setup and typical reinforcement layout for wall specimens C2, 1A, and 1B (Kapoi 2012).

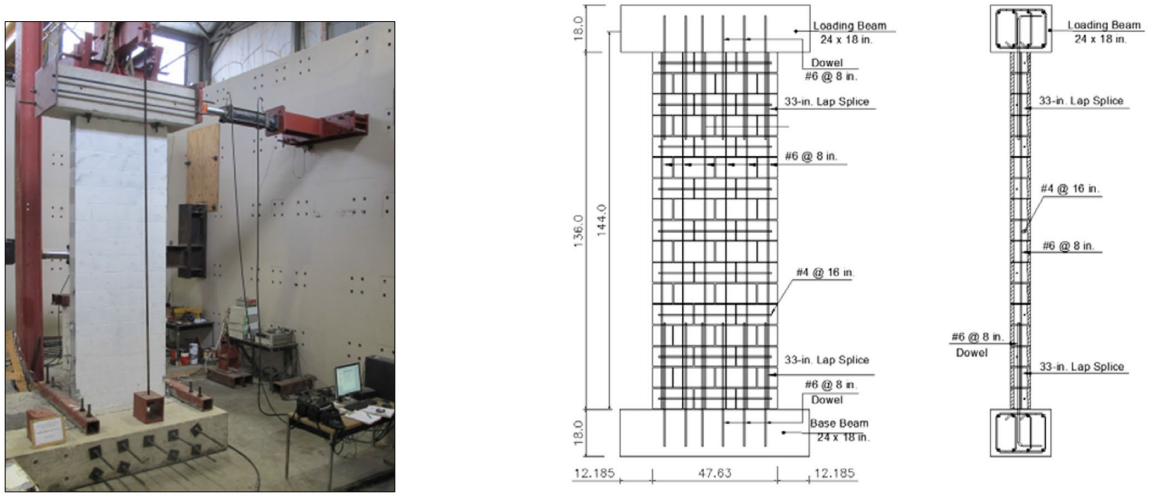

(a) Test setup **(b) Reinforcement detail**

Figure 3.7 Test setup and reinforcement details of wall specimen UT-W-13 (Ahmadi 2012).

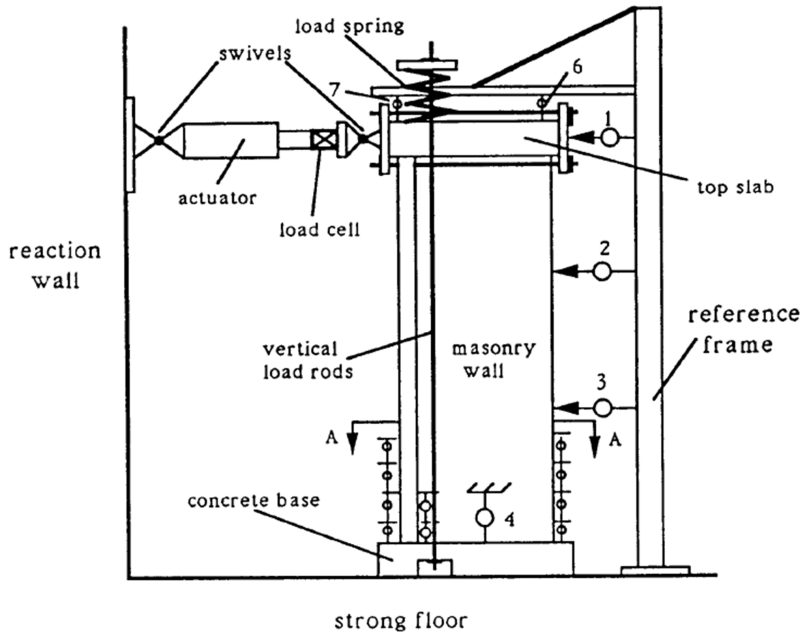

(a) Test setup

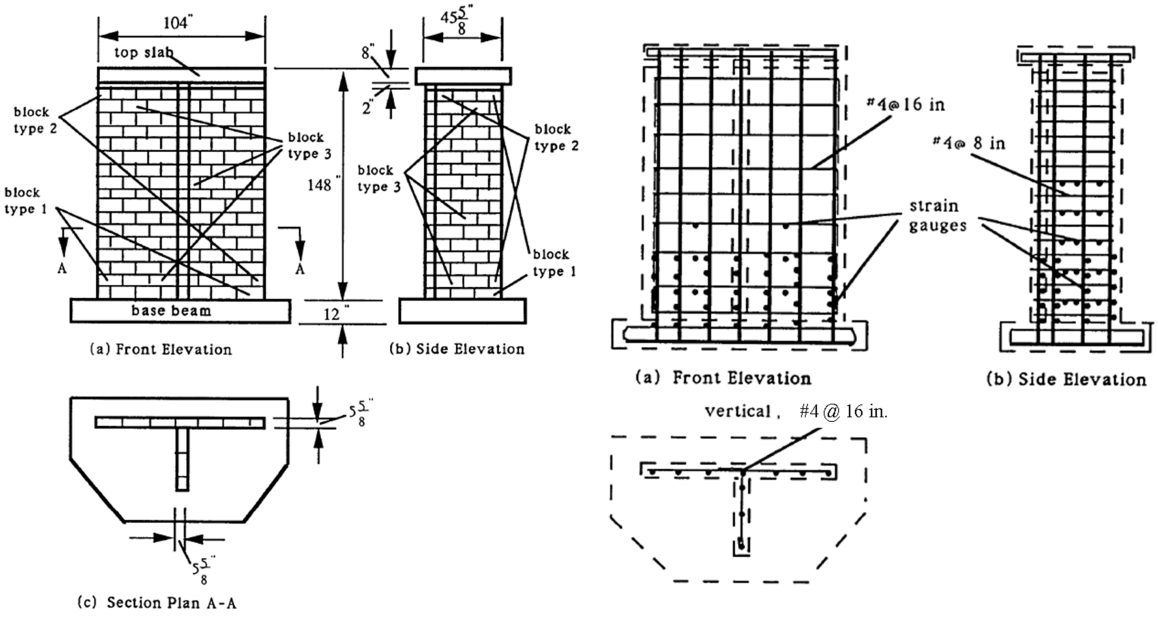

(b) Reinforcement details

Figure 3.8 Test setup and reinforcement details of wall specimen F2 (He and Priestley 1992).

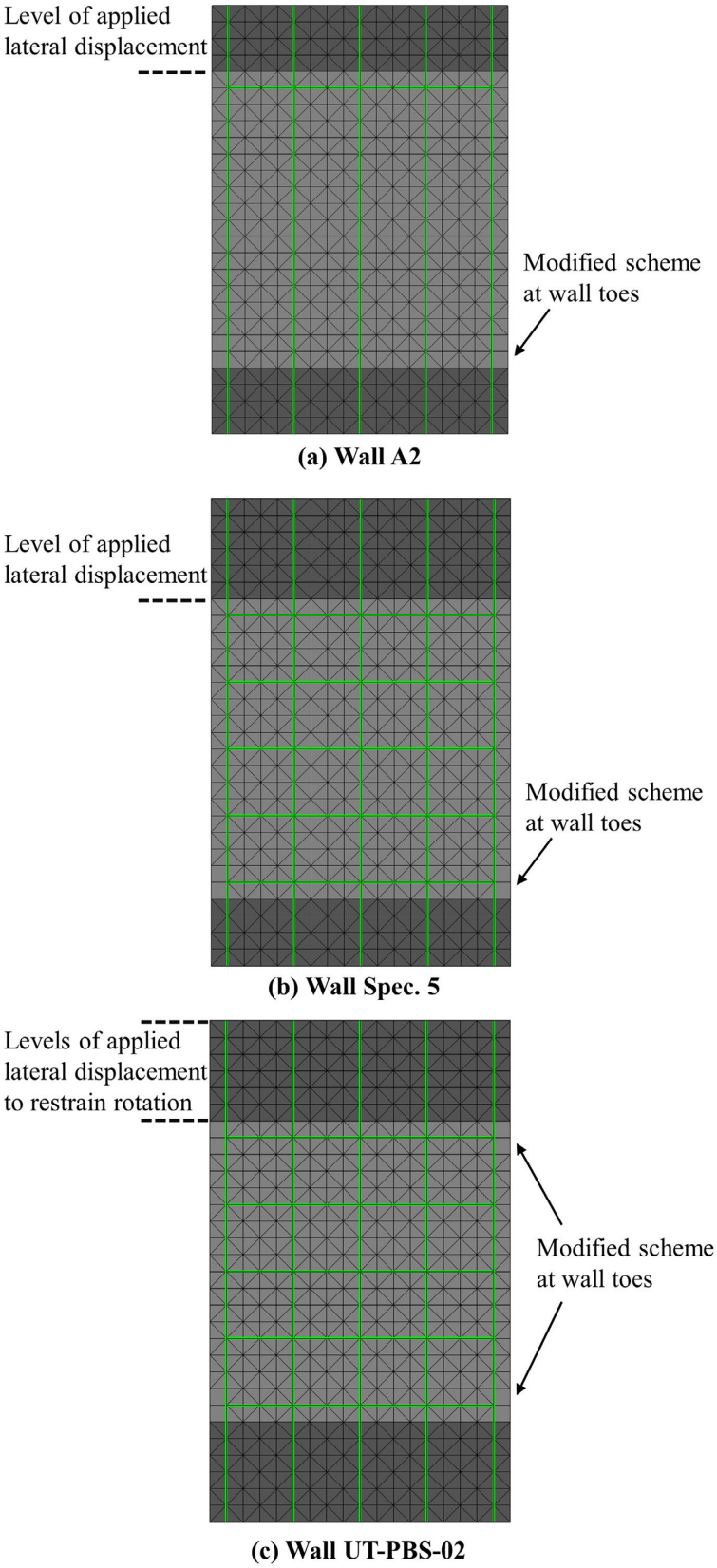

Figure 3.9 FE discretization of shear-dominated wall specimens.

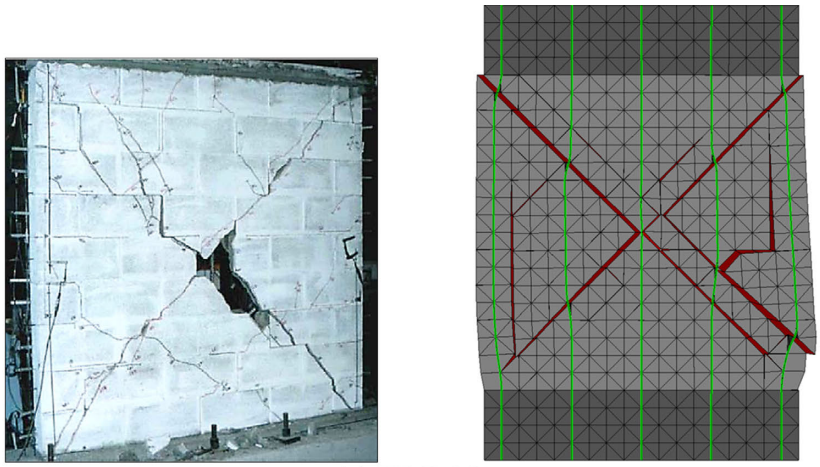

(a) Wall A2

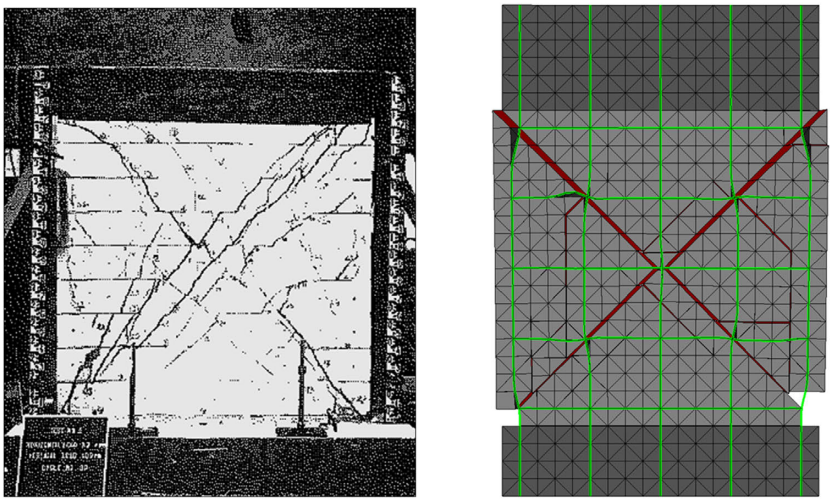

(b) Wall Spec. 5

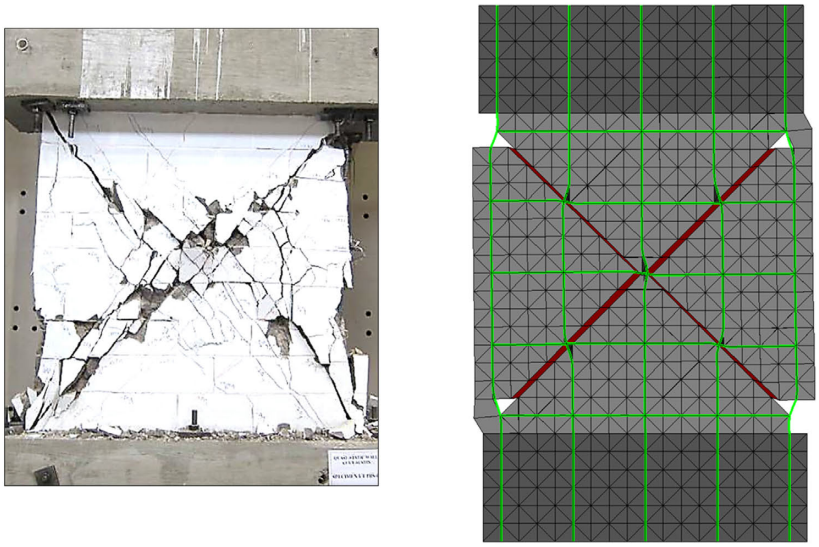

(c) Wall UT-PBS-02

Figure 3.10 Comparison of damage obtained in the tests and analyses of shear-dominated walls.

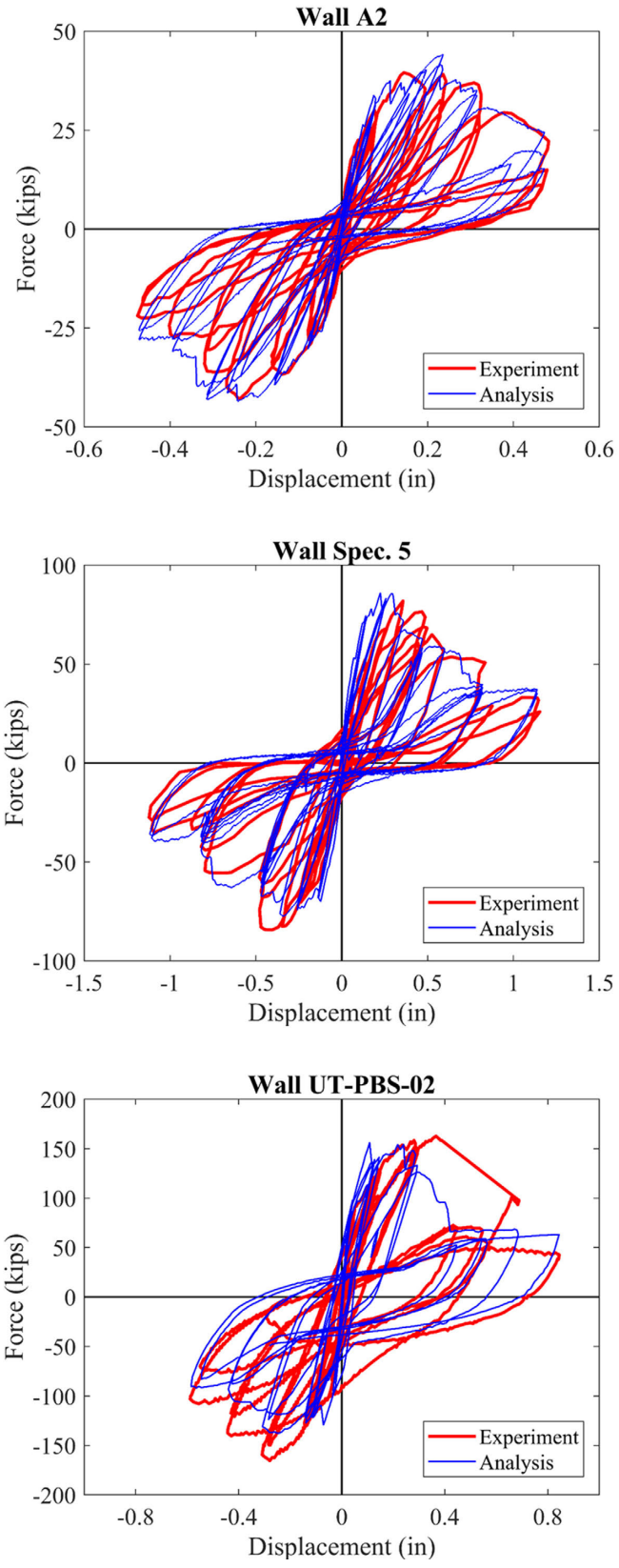

Figure 3.11 Comparison of experimental and numerical results for the shear-dominated wall specimens.

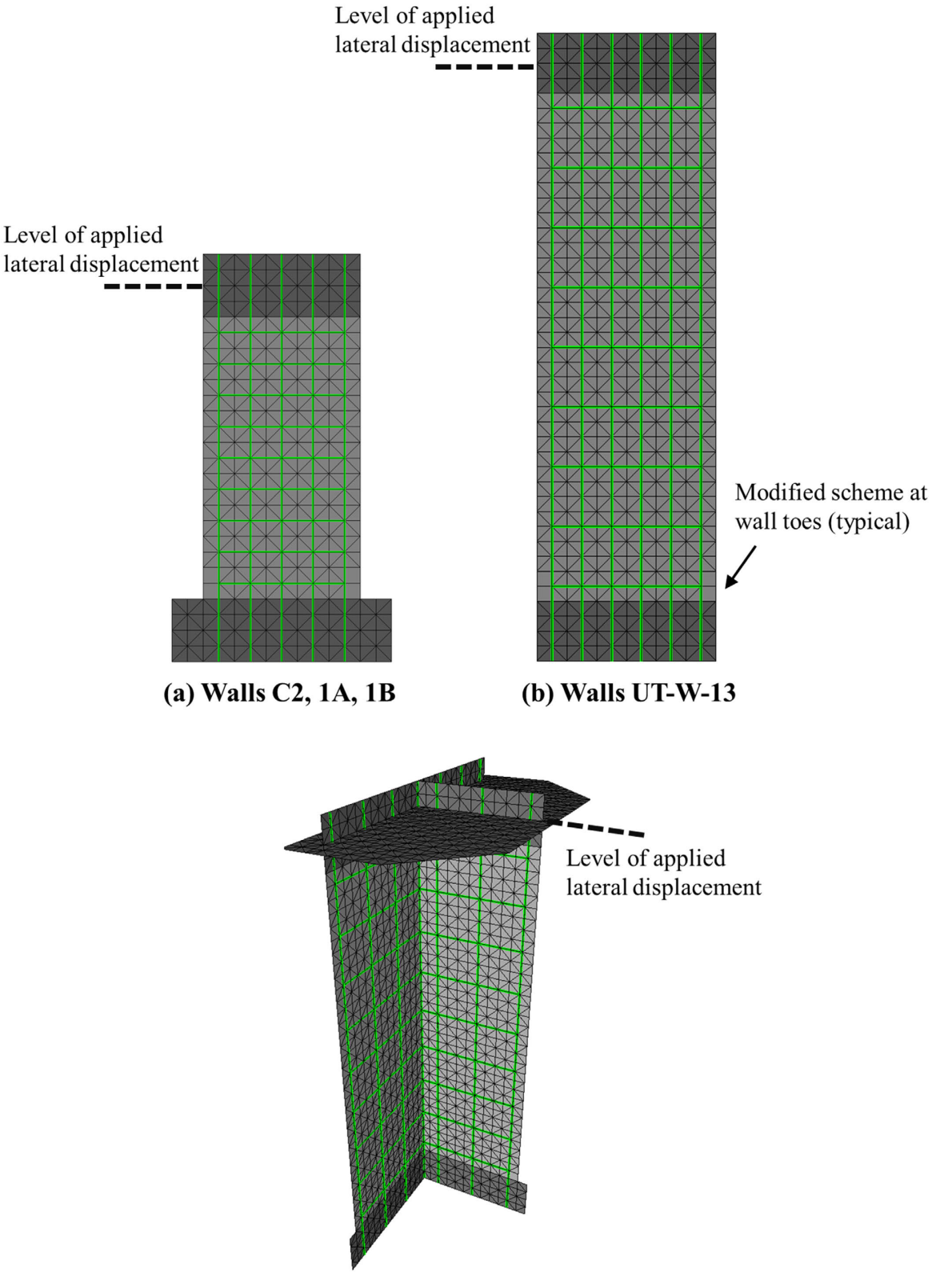

Figure 3.12 FE discretization of flexure-dominated wall segments.

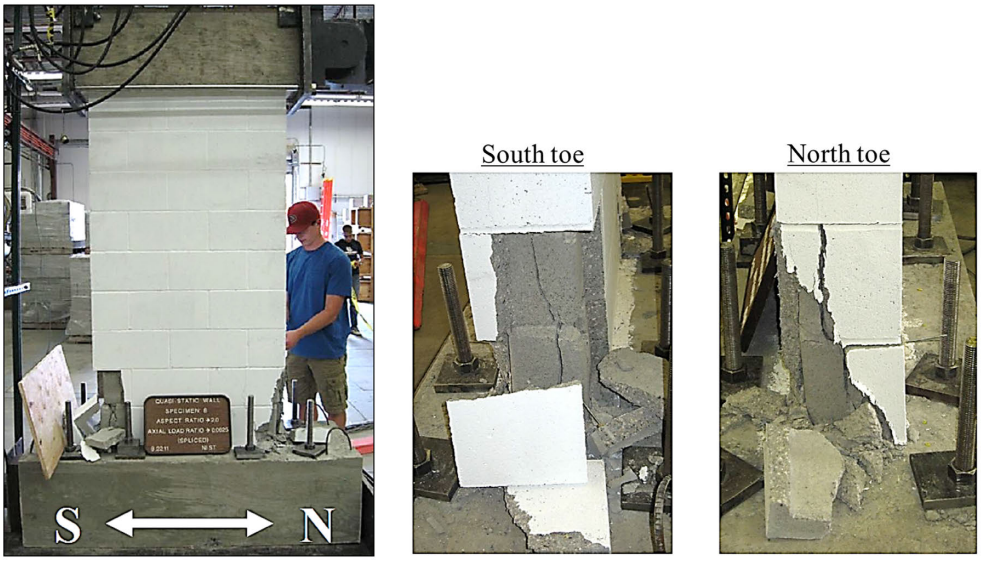

(a) Damage in test

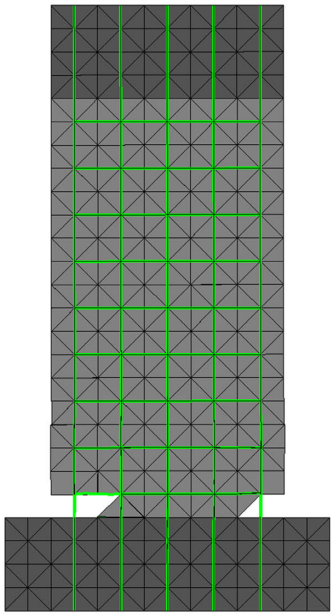

(b) Damage in analysis

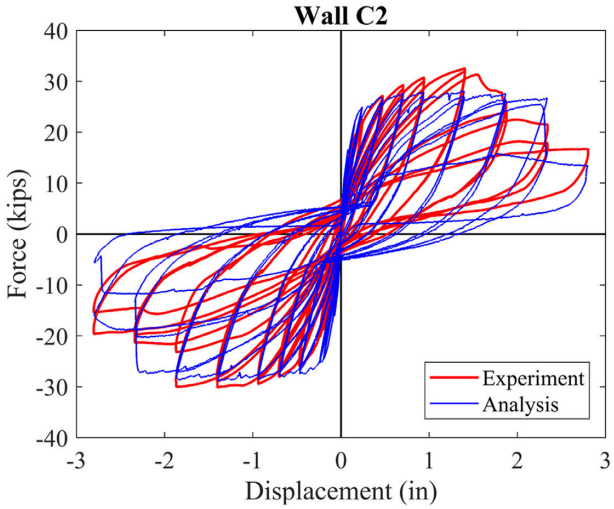

(c) Force-displacement response

Figure 3.13 Comparison of numerical and experimental results for wall C2.

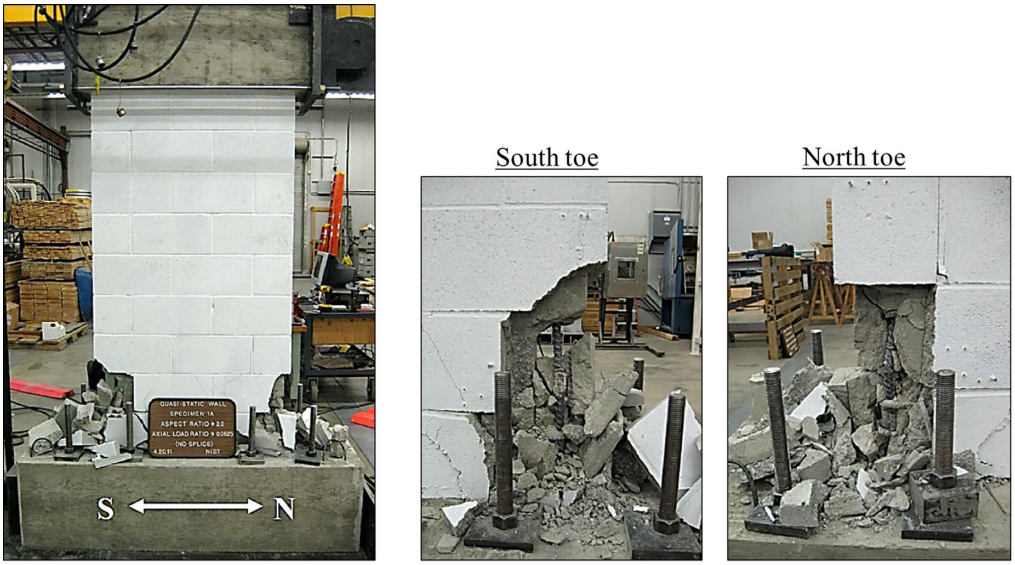

(a) Damage in test

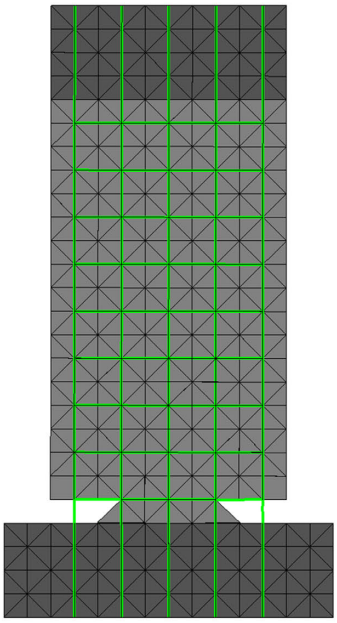

(b) Damage in analysis

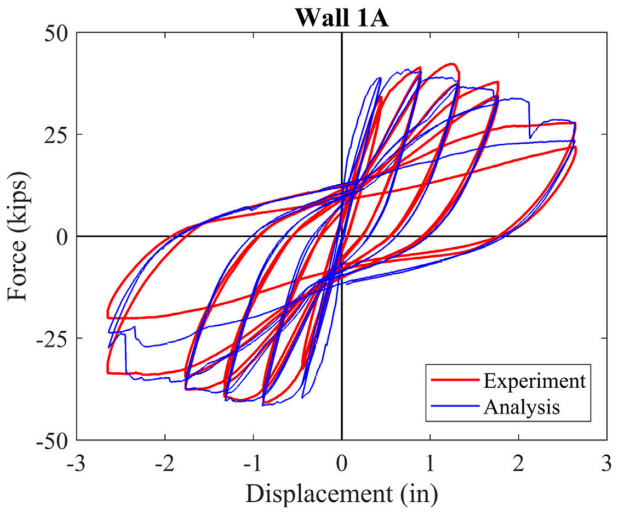

(c) Force-displacement response

Figure 3.14 Comparison of numerical and experimental results for wall 1A.

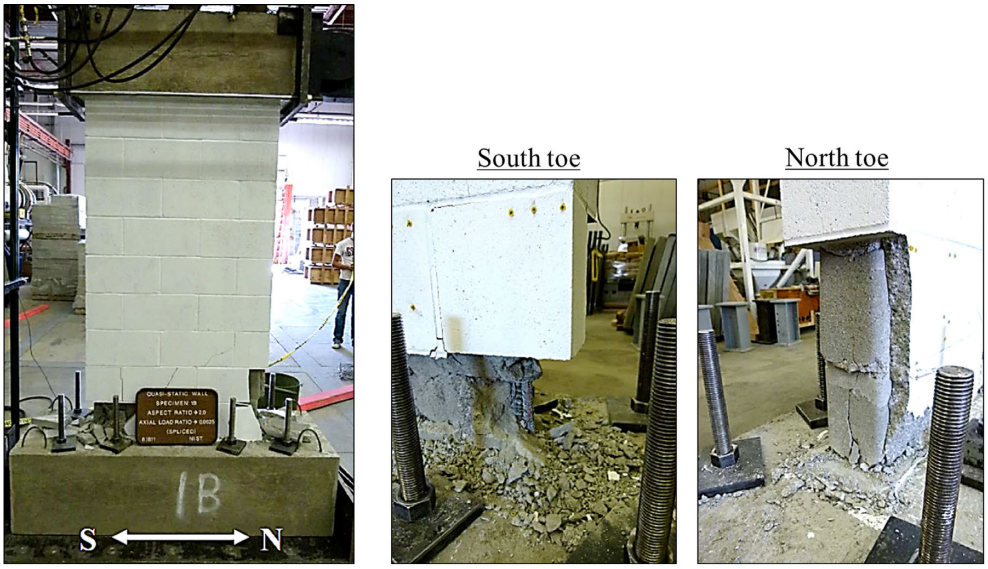

(a) Damage in test

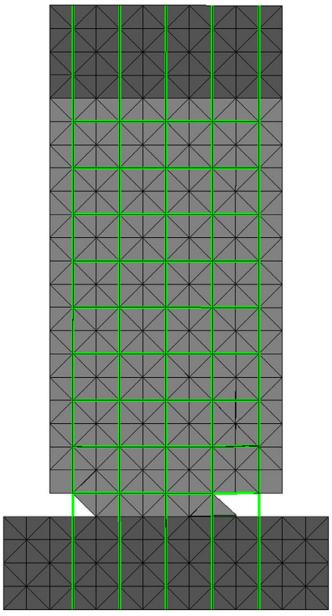

(b) Damage in analysis

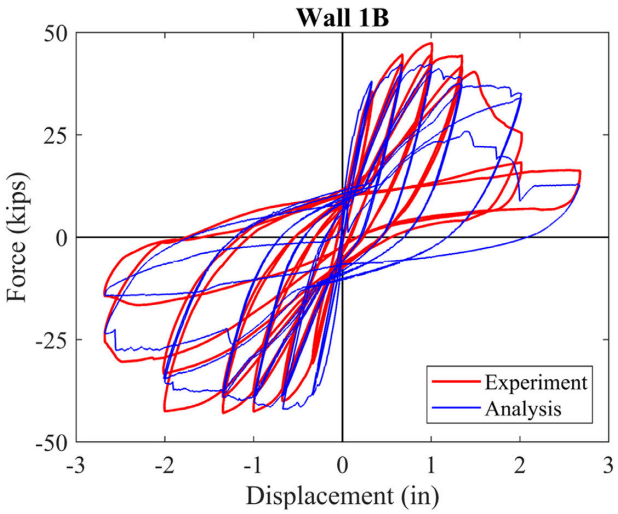

(c) Force-displacement response

Figure 3.15 Comparison of numerical and experimental results for wall 1B.

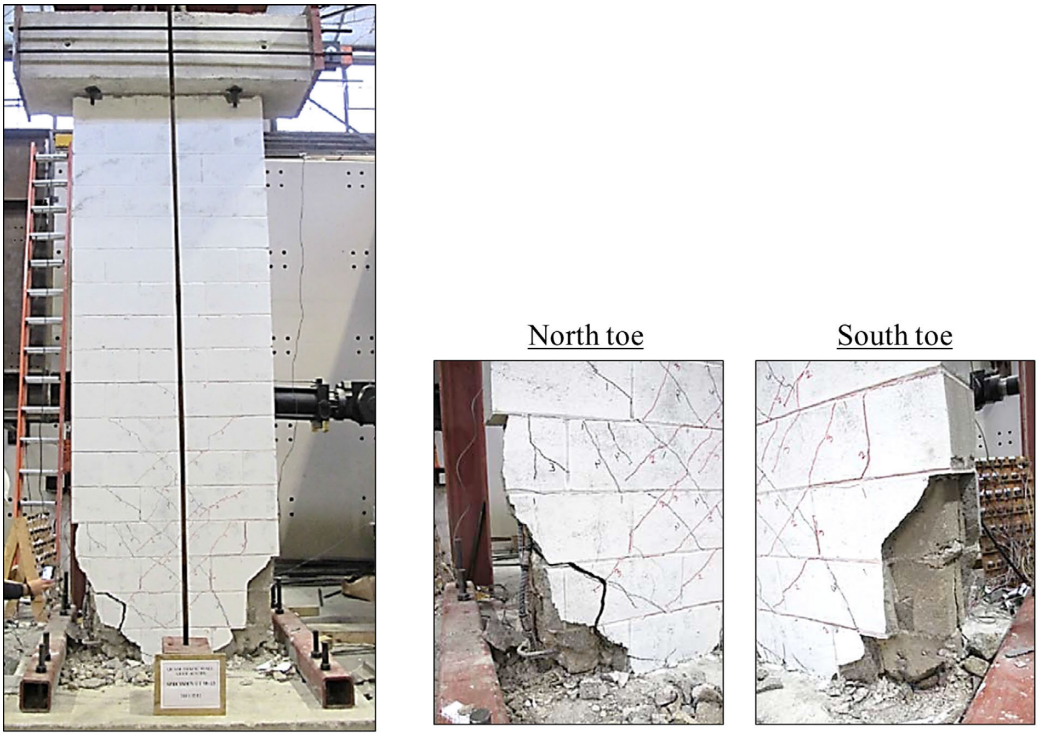

(a) Damage in test

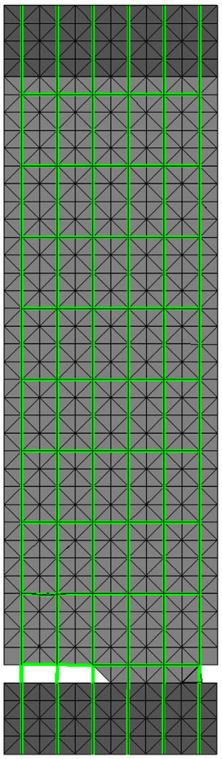

(b) Damage in analysis

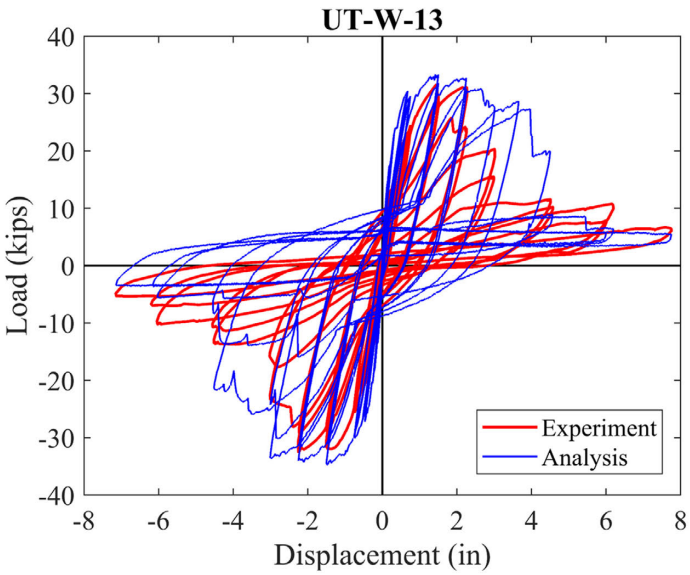

(c) Force-displacement response

Figure 3.16 Comparison of numerical and experimental results for wall UT-W-13.

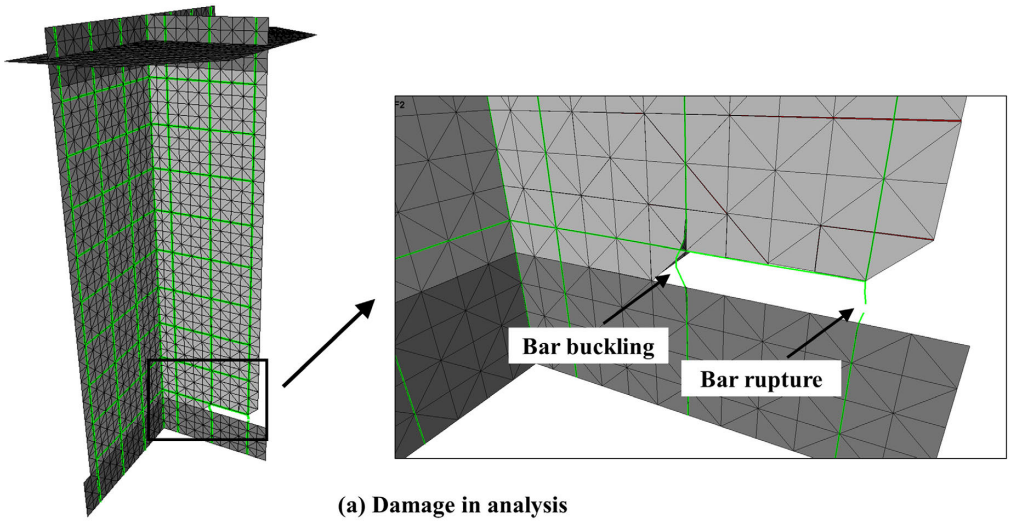

(a) Damage in analysis

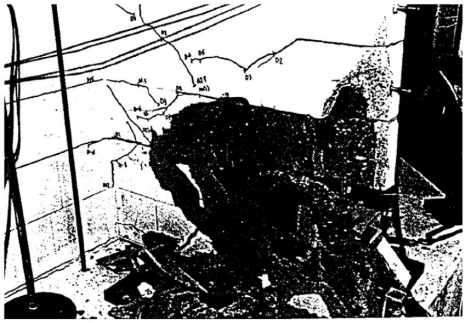

(b) Damage in web after the test

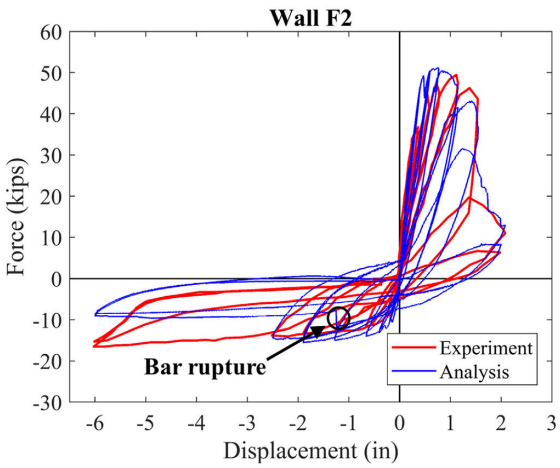

(c) Force-displacement response

Figure 3.17 Comparison of numerical and experimental results for wall F2.

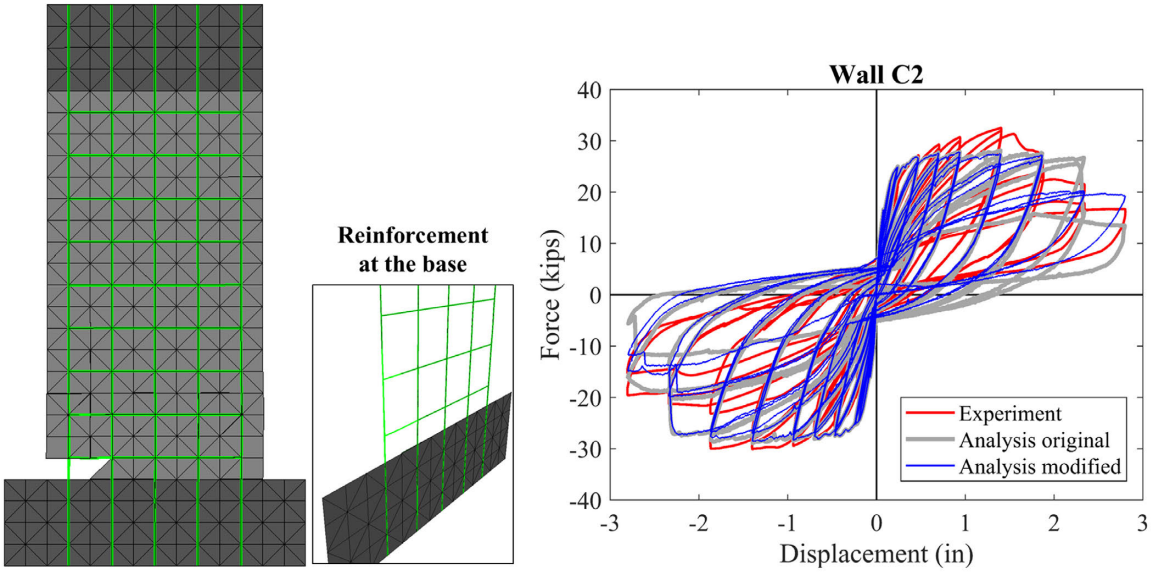

Figure 3.18 Analysis of wall C2 using the modified element removal scheme.

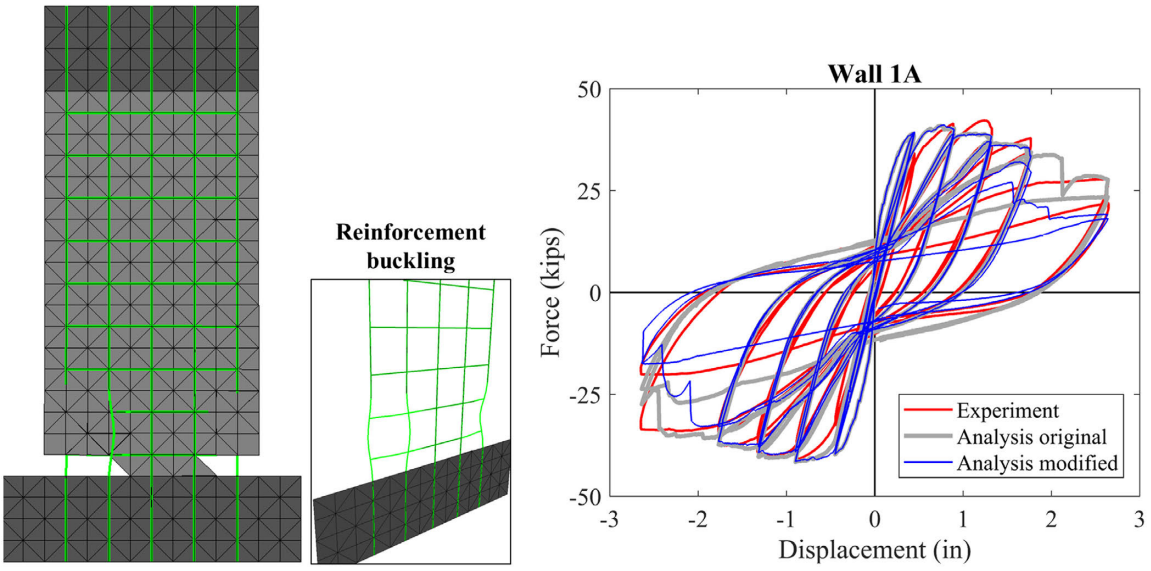

Figure 3.19 Analysis of wall 1A using the modified element removal scheme.

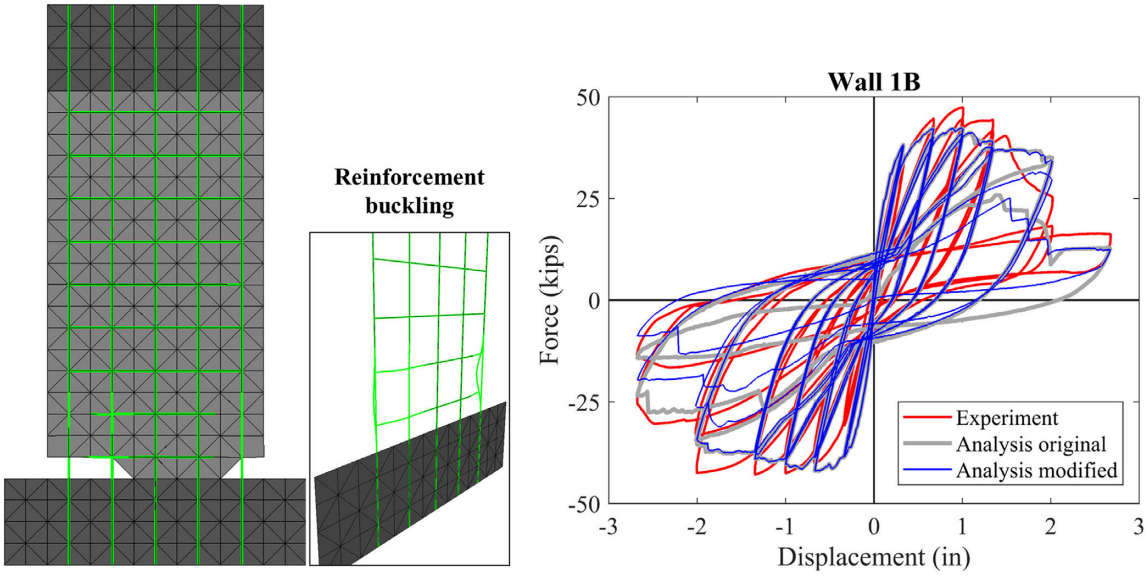

Figure 3.20 Analysis of wall 1B using the modified element removal scheme.

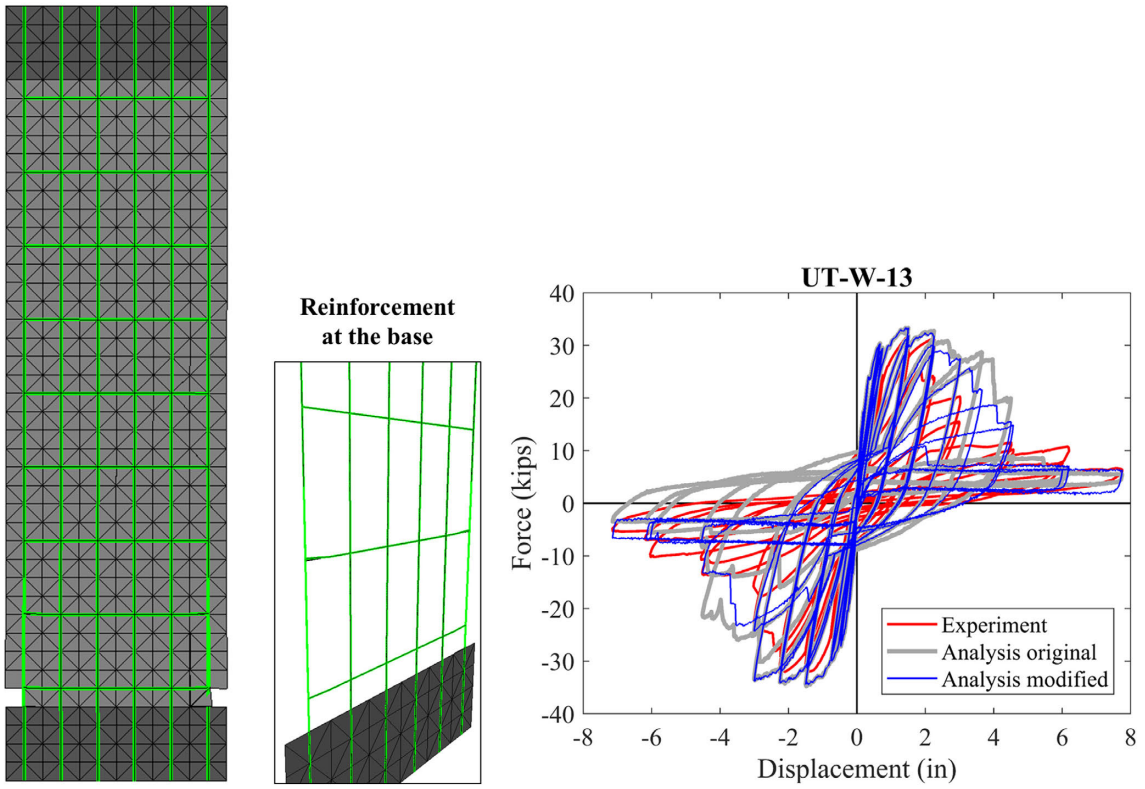

Figure 3.21 Analysis of wall UT-W-13 using the modified element removal scheme.

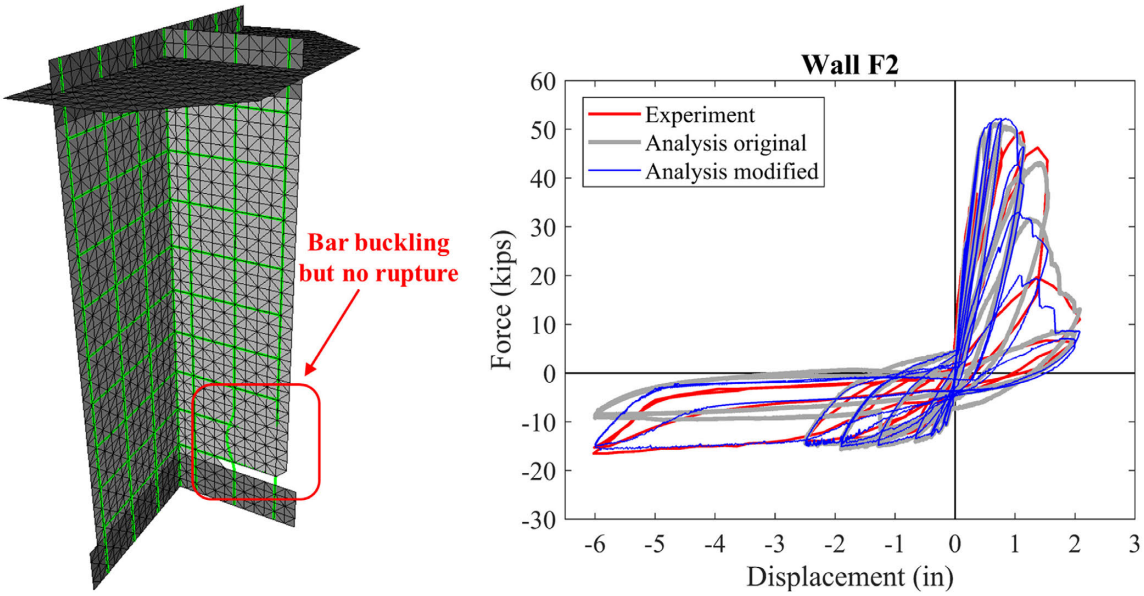

Figure 3.22 Analysis of wall F2 using the modified element removal scheme.

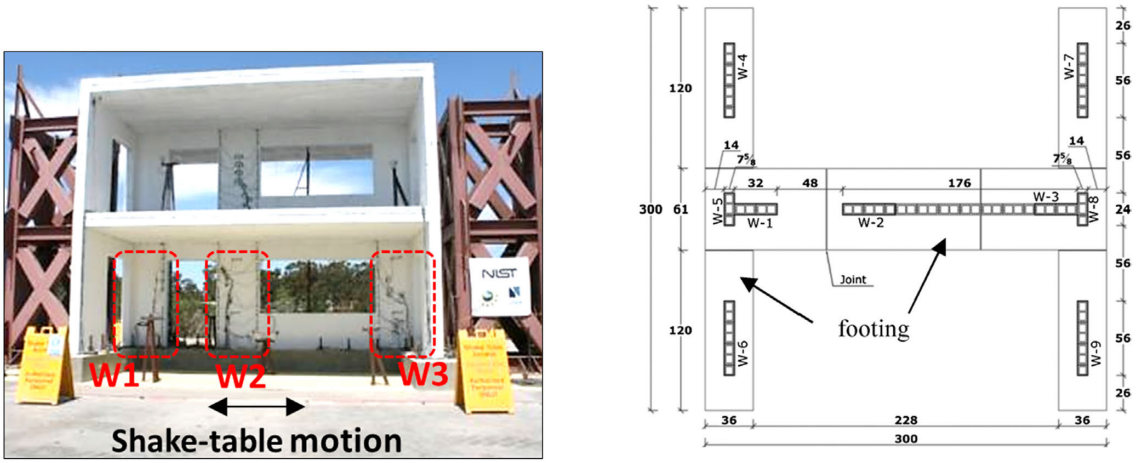

(a) (b)

Figure 3.23 Two-story test structure. (a) Test setup; (b) plan view (from Mavros et al. 2016).

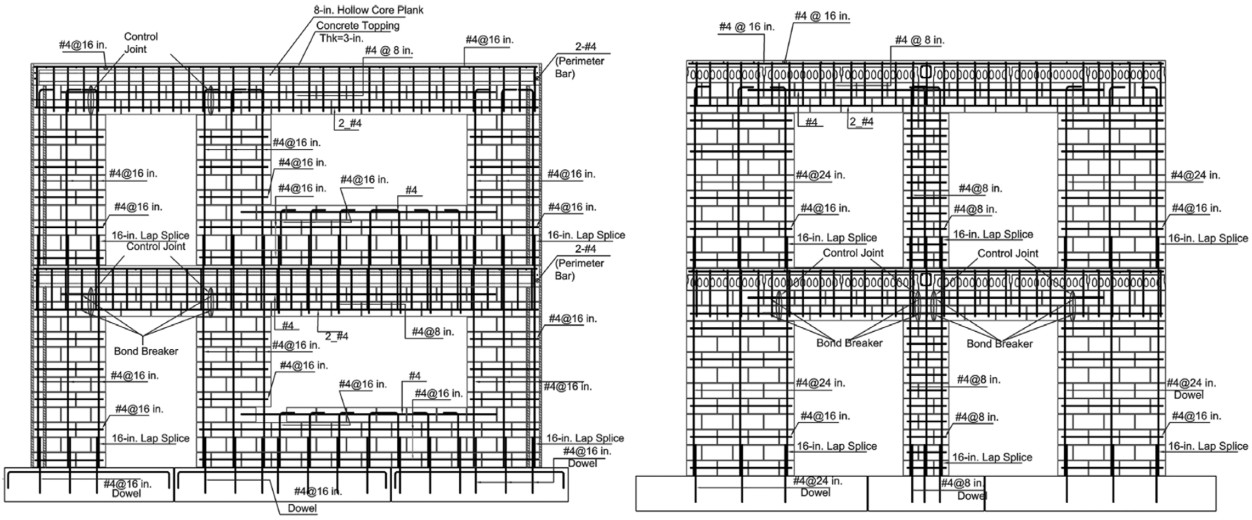

(a) (b)

Figure 3.24 Reinforcement details. (a) In-plane walls; (b) out-of-plane walls (from Mavros et al. 2016).

Figure 3.25 Damage patterns in the three wall piers at the end of the testing sequence (from Mavros et al. 2016).

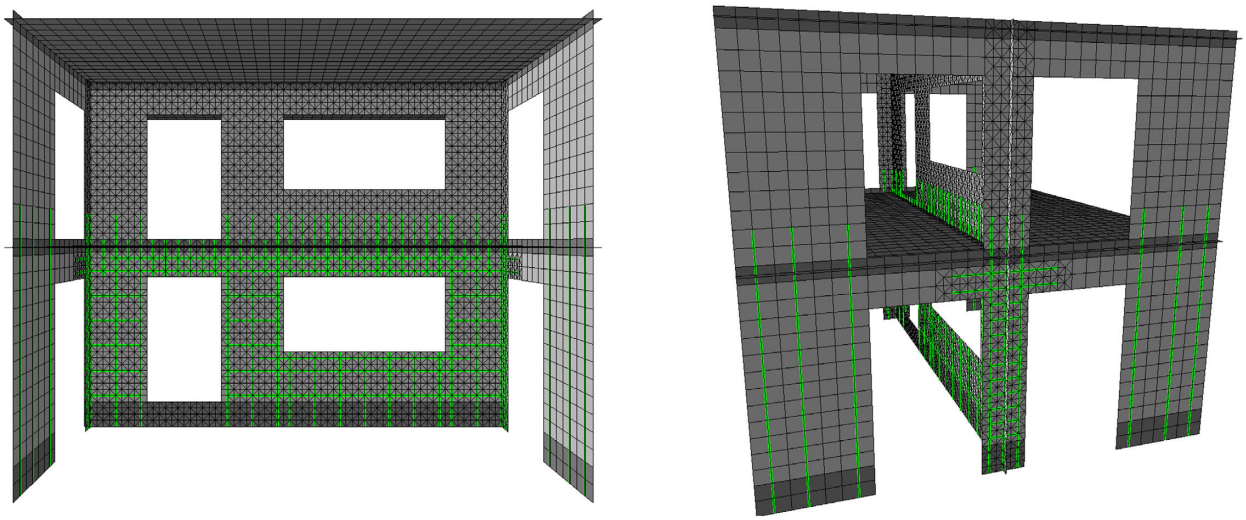

Figure 3.26 Finite element discretization of the two-story test structure.

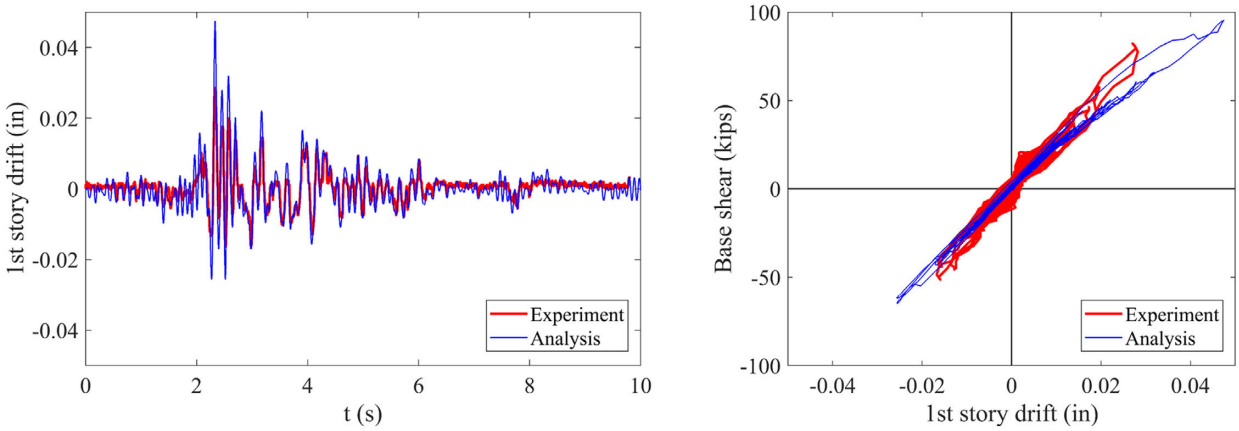

(a) El Centro 43%

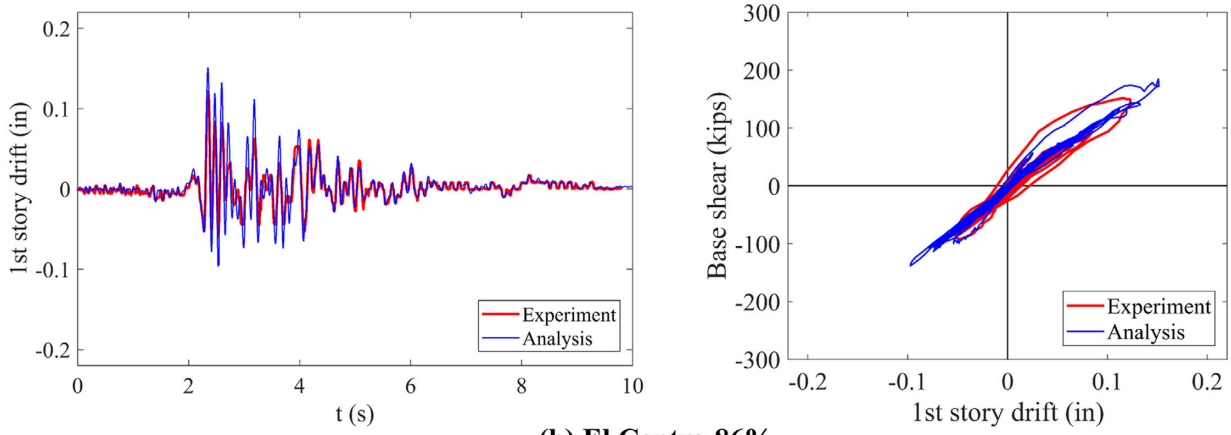

(b) El Centro 86%

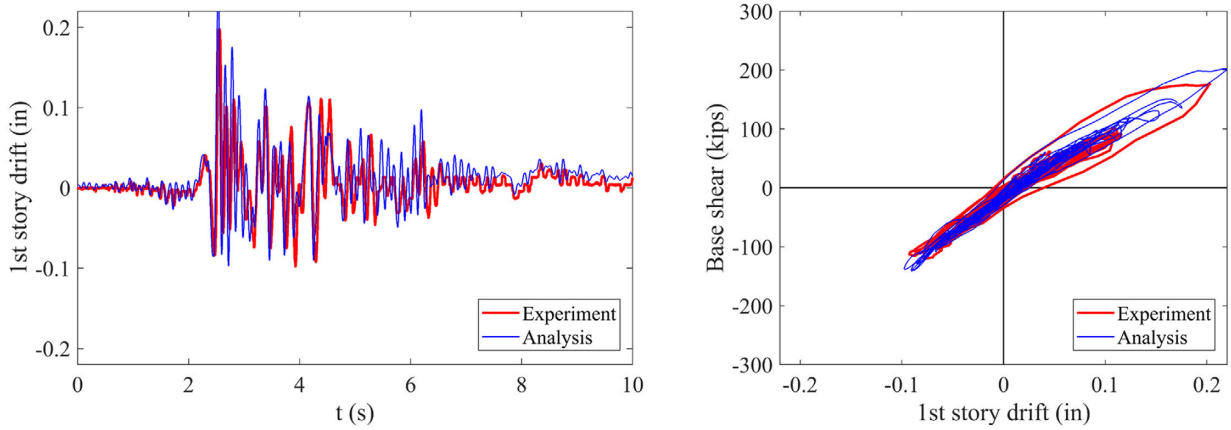

(c) El Centro 108%

Figure 3.27 Time-history analysis results of the two-story structure under El Centro 43%, 86%, and 108%.

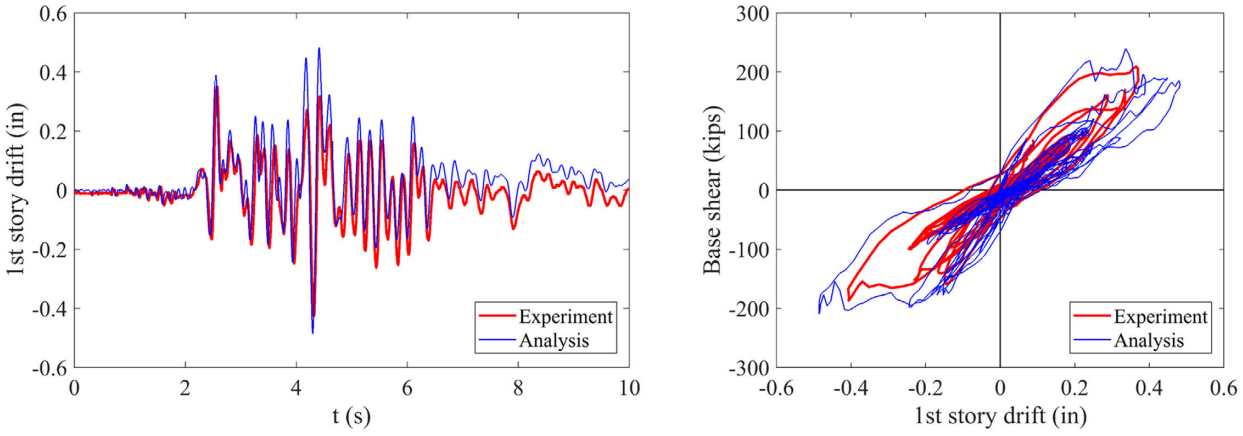

Figure 3.28 Time-history analysis results of the two-story structure under El Centro 145%.

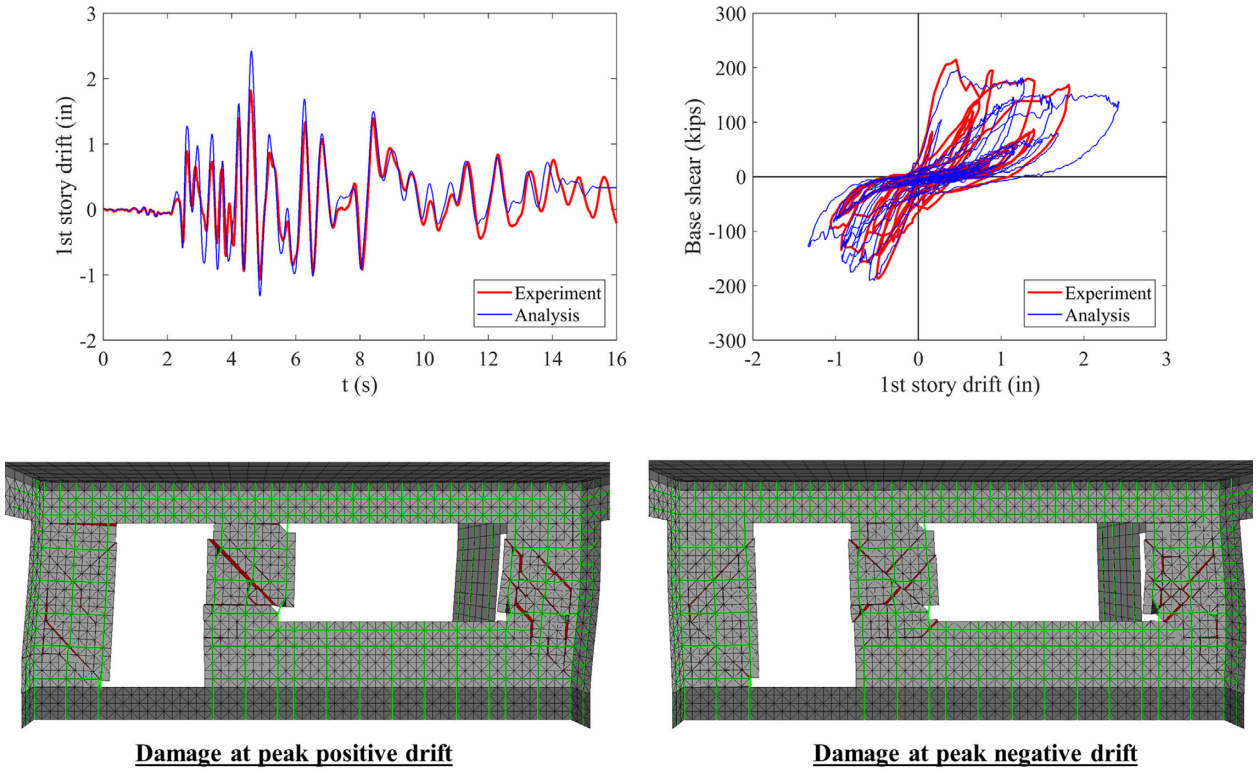

Figure 3.29 Time-history analysis results of the two-story structure and damage in the first story under El Centro 160% (deformation is magnified by 2 times).

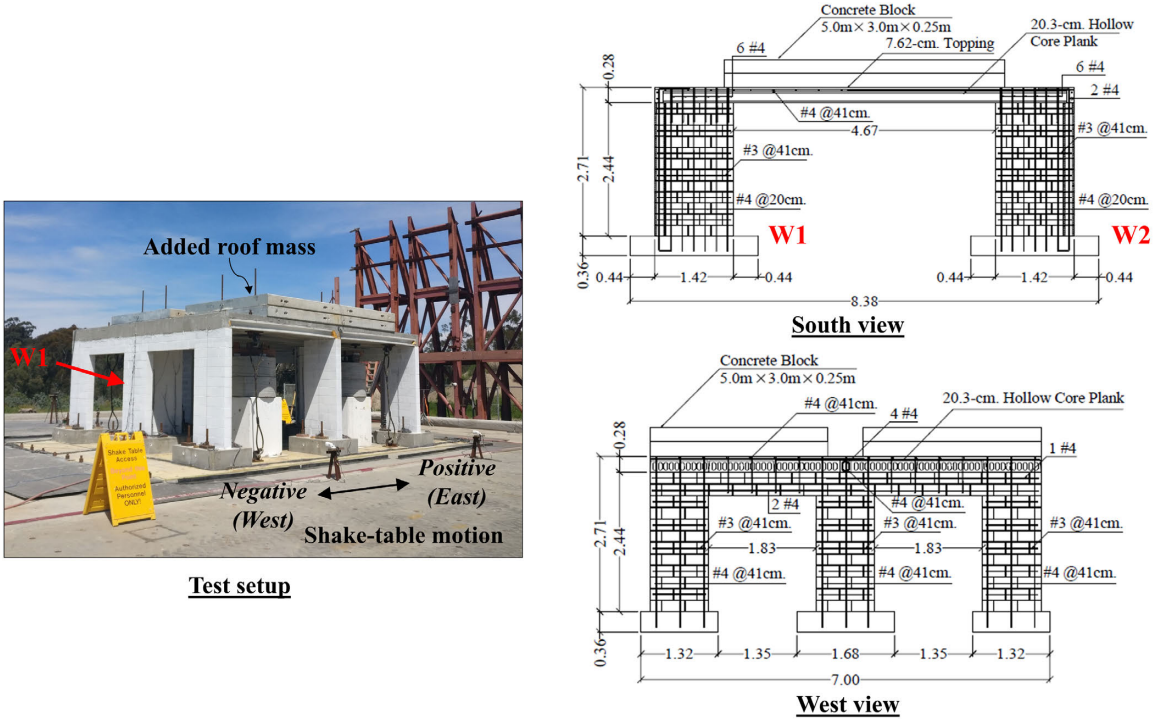

Figure 3.30 Test setup and reinforcing details of the one-story shake-table test structure (from Cheng et al. 2019). Dimensions in meters.

W1 W2

Figure 3.31 Cracks in the webs of the T-walls after Mulholland 160% (Motion 6).

South view

Wall 1

Wall 2

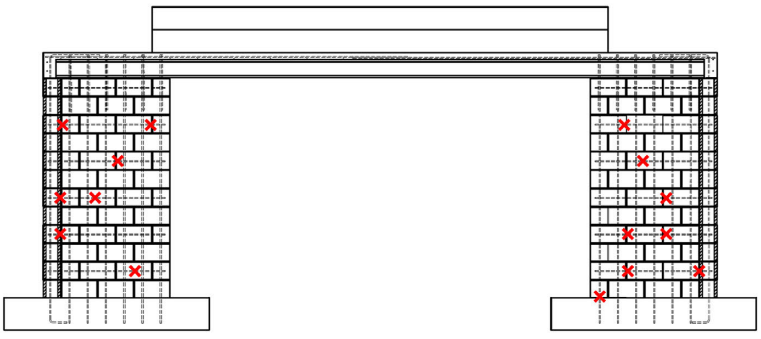

Locations of bar rupture
(courtesy of J. Cheng)

Figure 3.32 Damage in the one-story shake-table test structure after Rinaldi 130%.

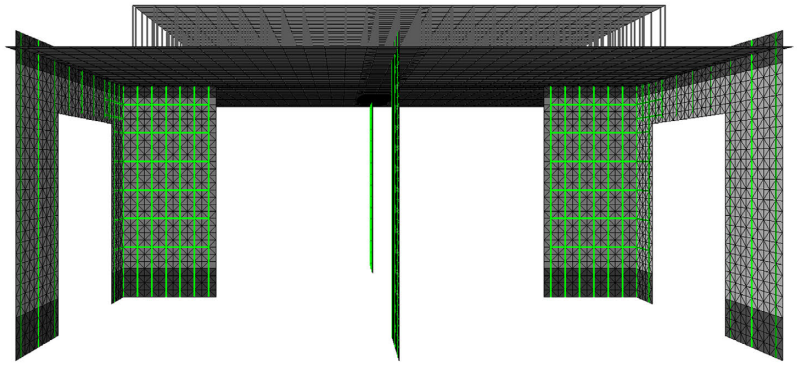

South view

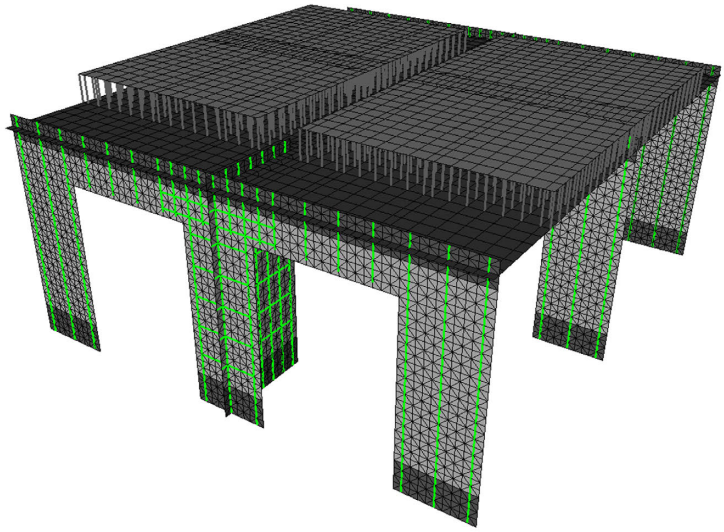

South-west view

Figure 3.33 Finite element model of the one-story shake-table test structure.

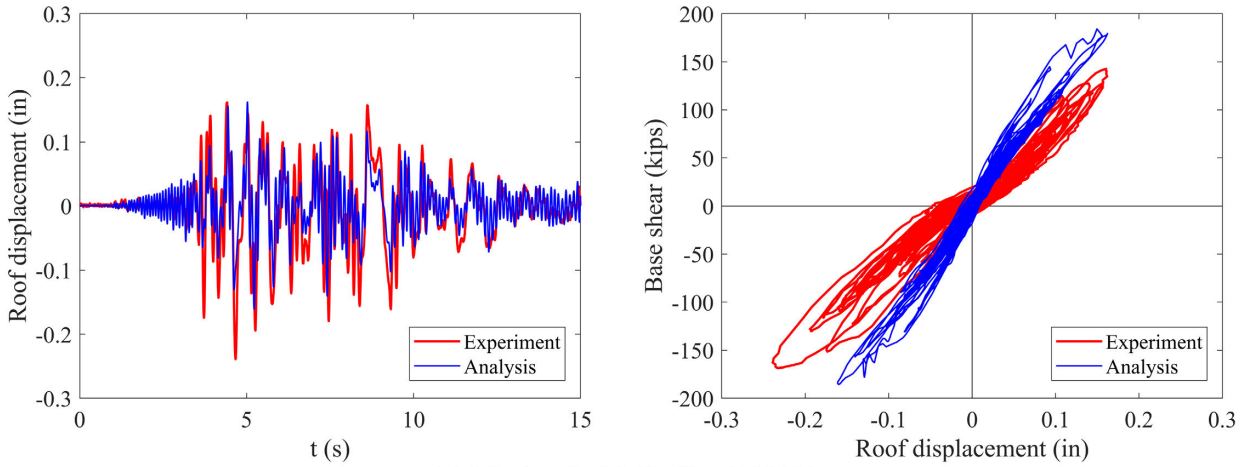

(a) Motion 5: Mulholland 133%

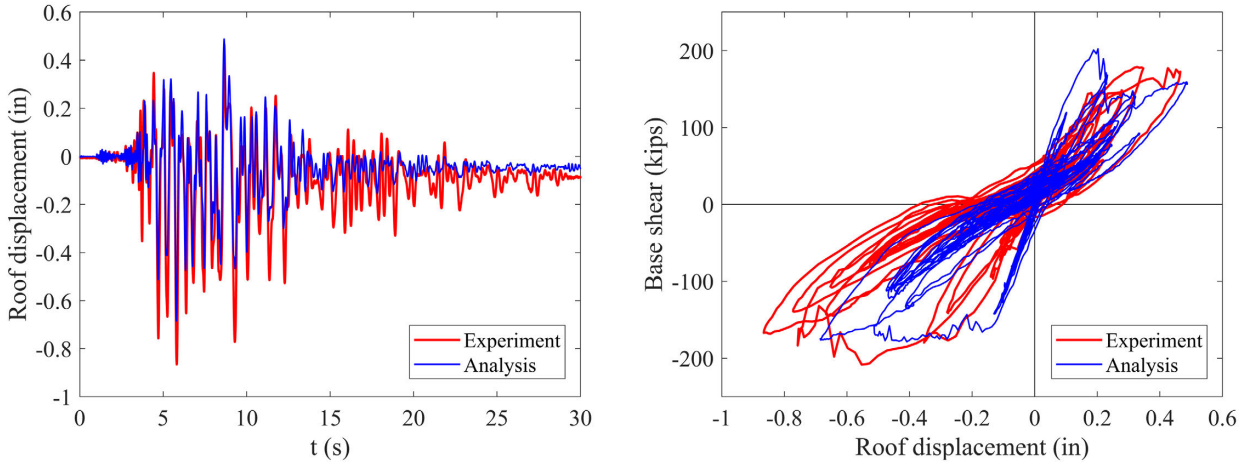

(b) Motion 6: Mulholland 160%

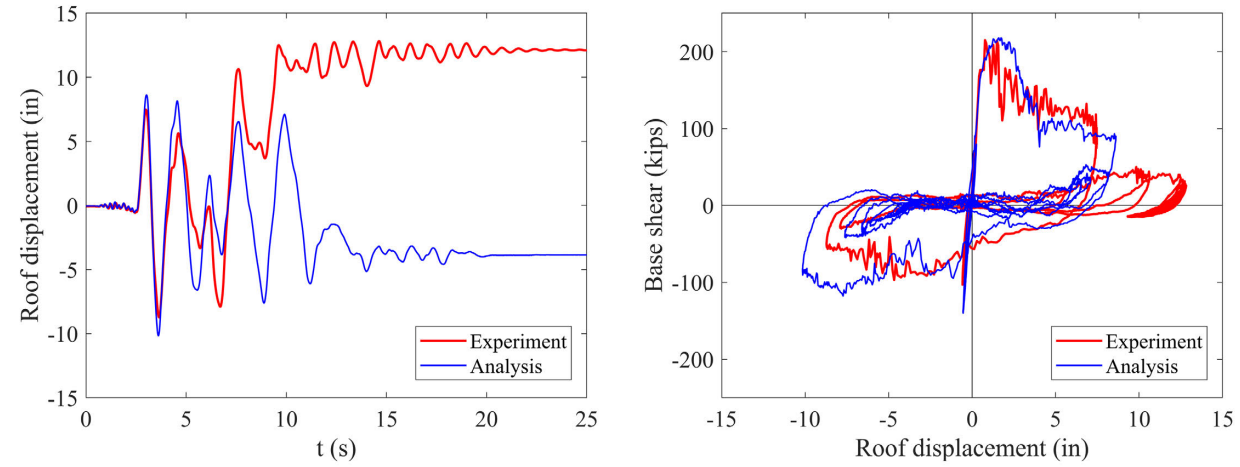

(c) Motion 7: Rinaldi 130%

Figure 3.34 Comparison of numerical to experimental results for the one-story shake-table test structure.

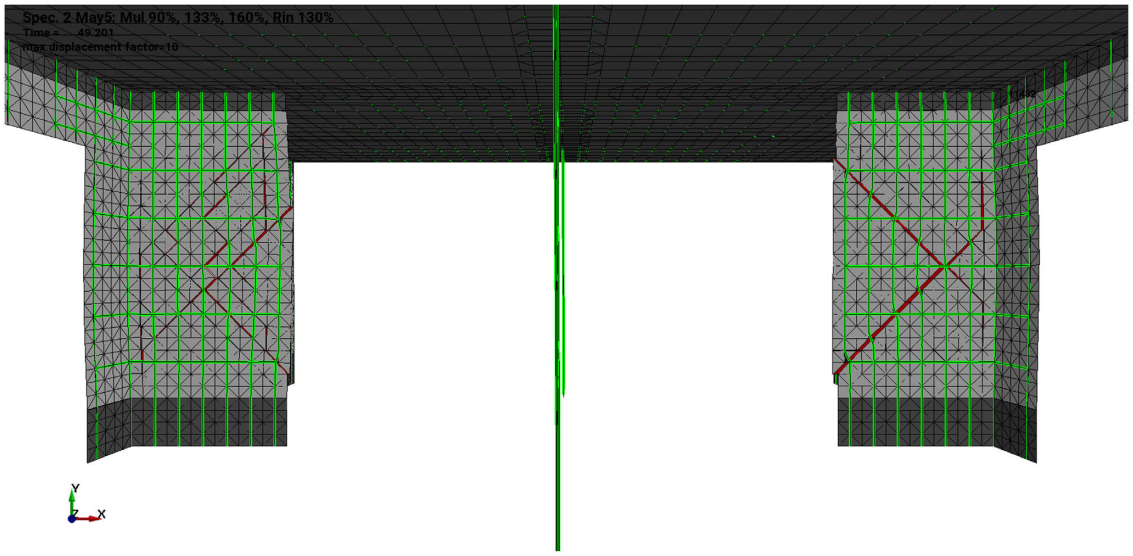

(a) Motion 6: Mulholland 160%

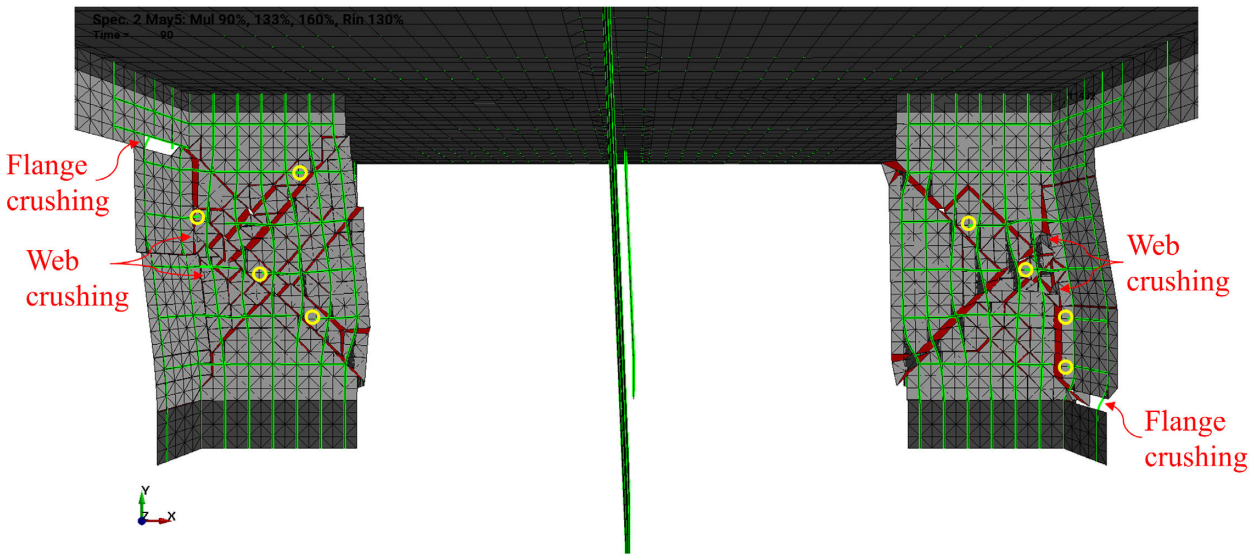

(b) Motion 7: Rinaldi 130%

Figure 3.35 Damage obtained in the analysis of the one-story shake-table test structure. Locations of reinforcement rupture are marked with yellow circles.

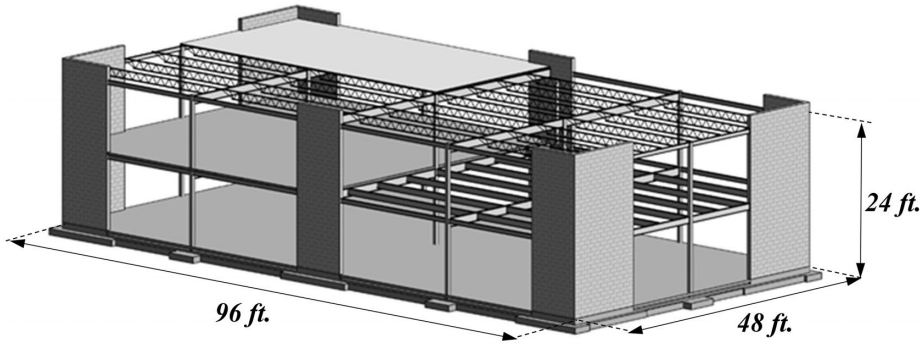

Figure 3.36 Configuration of the two-story commercial building archetype (courtesy of Dr. G. Kingsley).

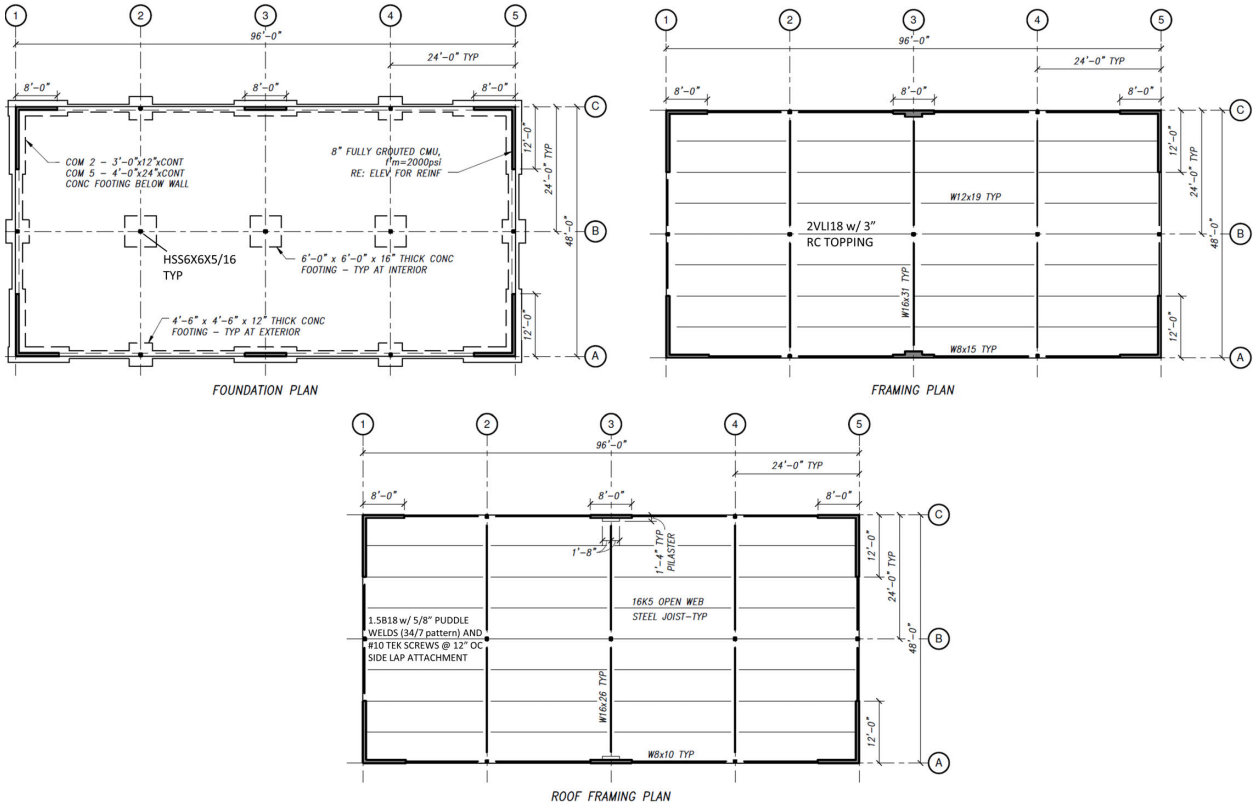

Figure 3.37 Foundation plan, floor framing plan, and roof framing plan of the commercial building archetype (courtesy of Dr. G. Kingsley).

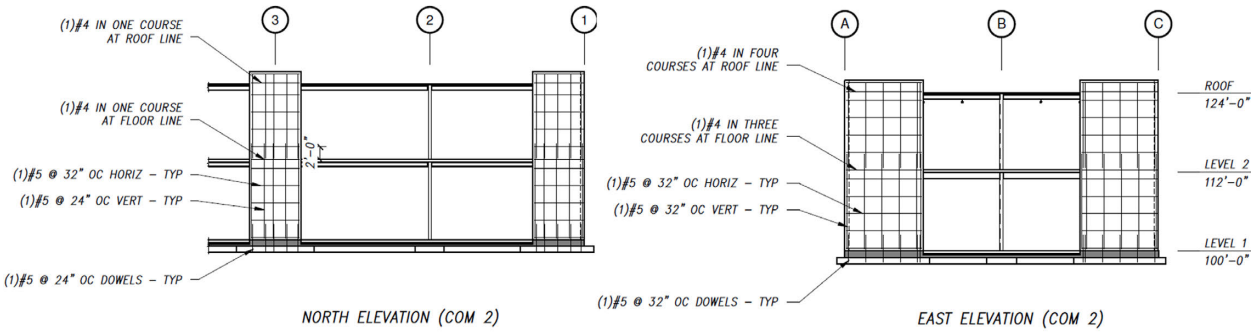

Figure 3.38 Reinforcing details of the RM shear walls of the commercial building archetype (courtesy of Dr. G. Kingsley).

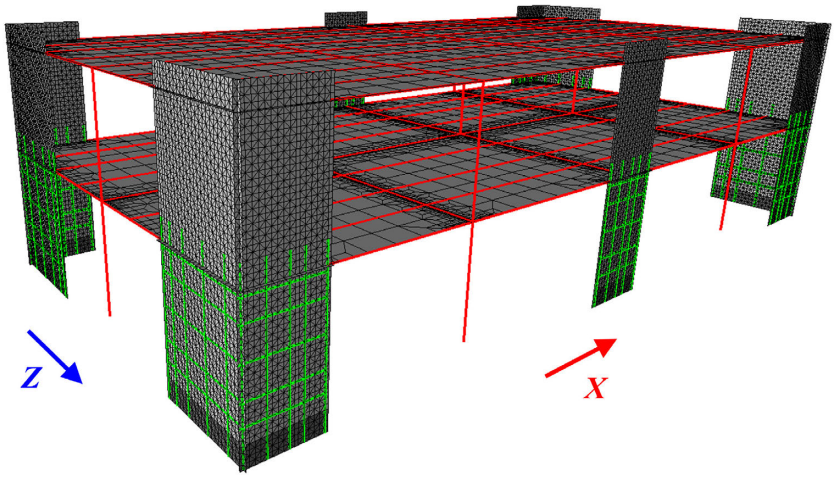

Figure 3.39 Finite element model of the commercial building archetype.

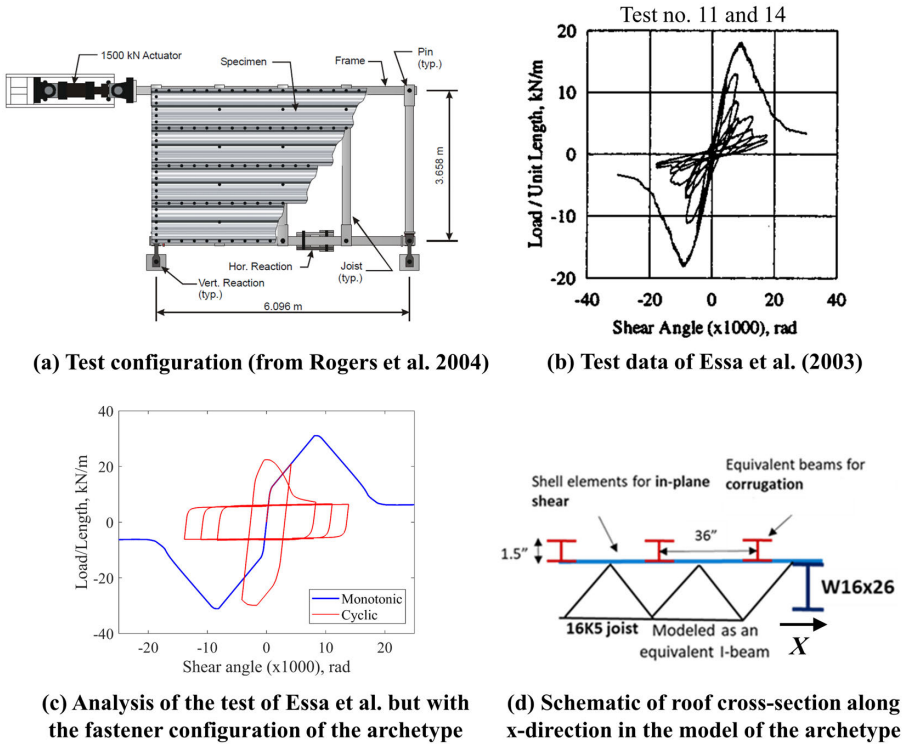

(a) Test configuration (from Rogers et al. 2004) **(b) Test data of Essa et al. (2003)**

(c) Analysis of the test of Essa et al. but with the fastener configuration of the archetype **(d) Schematic of roof cross-section along x-direction in the model of the archetype**

Figure 3.40 Modeling of the roof diaphragm of the commercial building archetype.

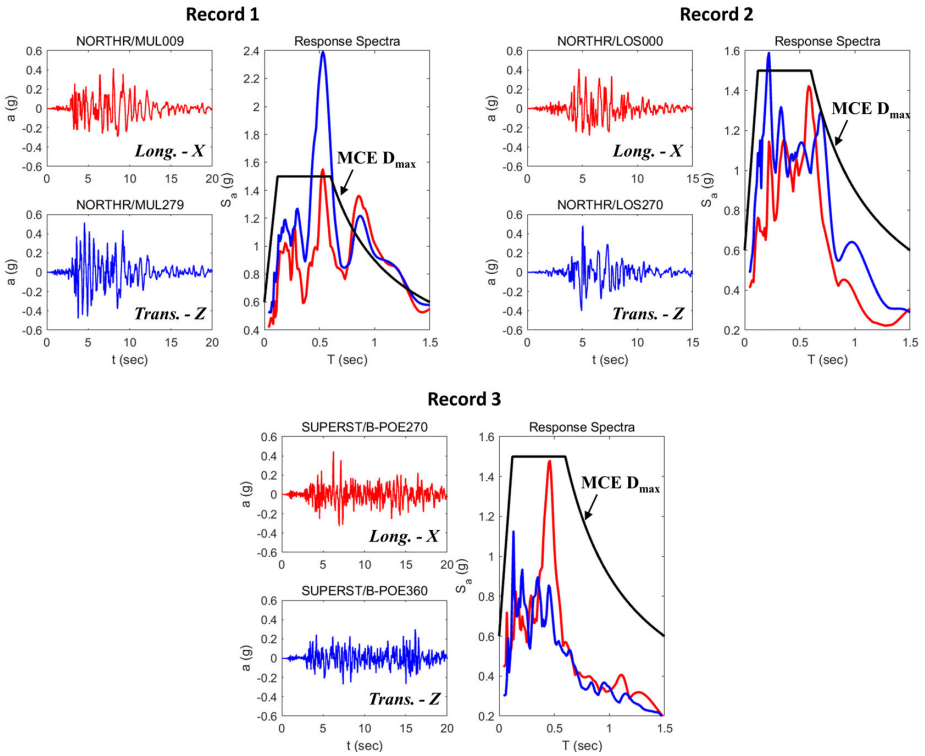

Figure 3.41 Earthquake records used for the time-history analyses of the commercial building archetype.

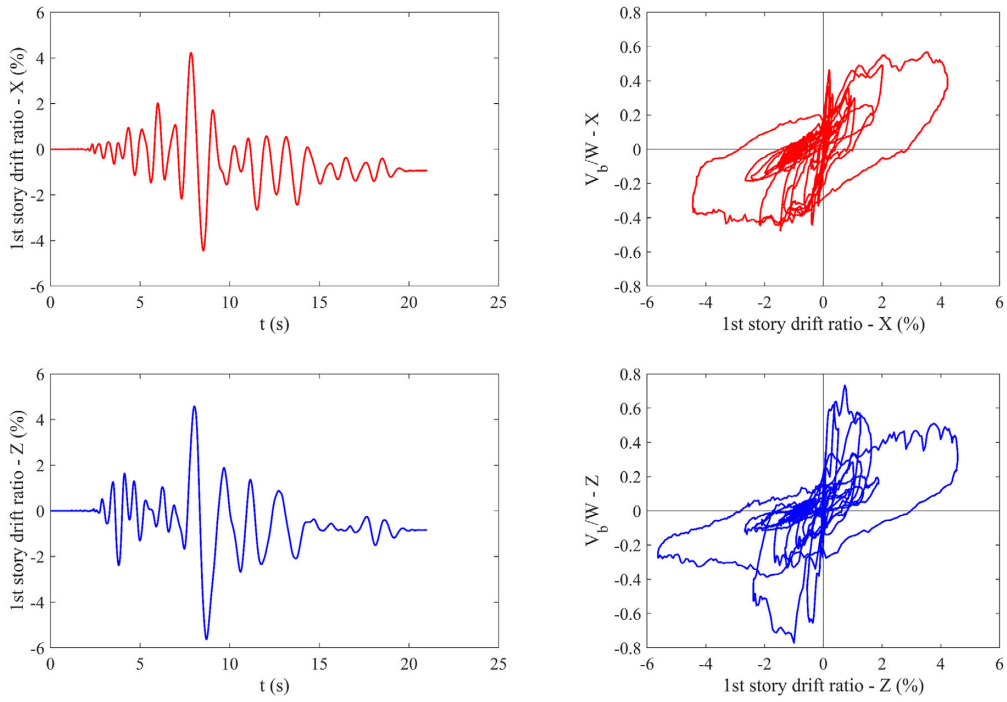

Figure 3.42 Response of the commercial building archetype during Record 1 scaled at MCE.

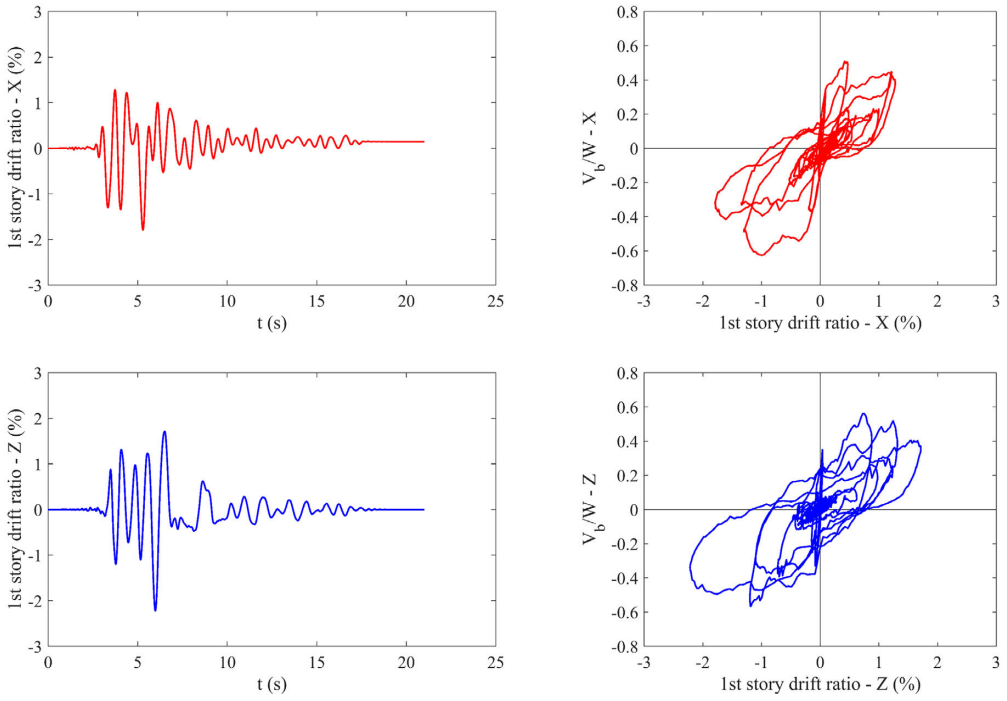

Figure 3.43 Response of the commercial building archetype during Record 2 scaled at MCE.

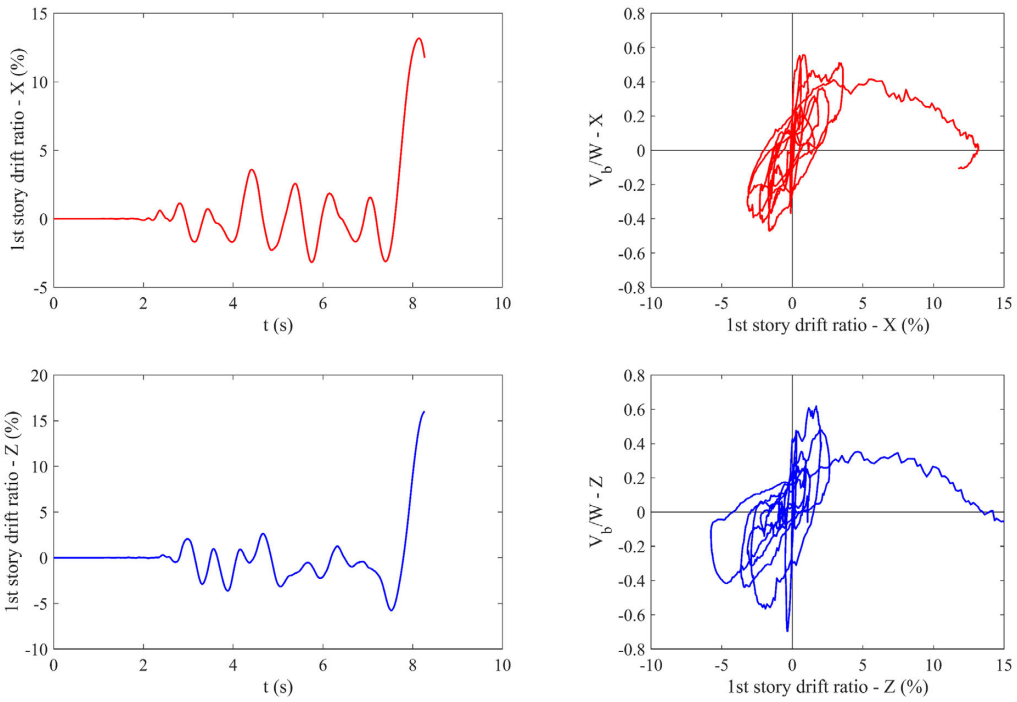

Figure 3.44 Response of the commercial building archetype during Record 1 scaled at 2xMCE.

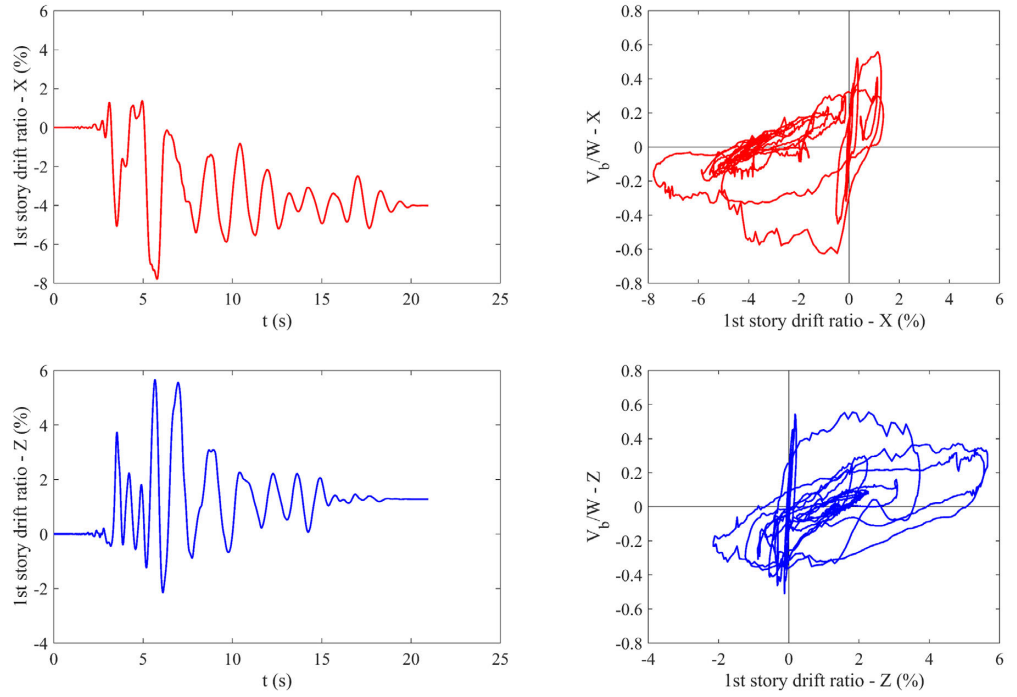

Figure 3.45 Response of the commercial building archetype during Record 1 scaled at 2xMCE.

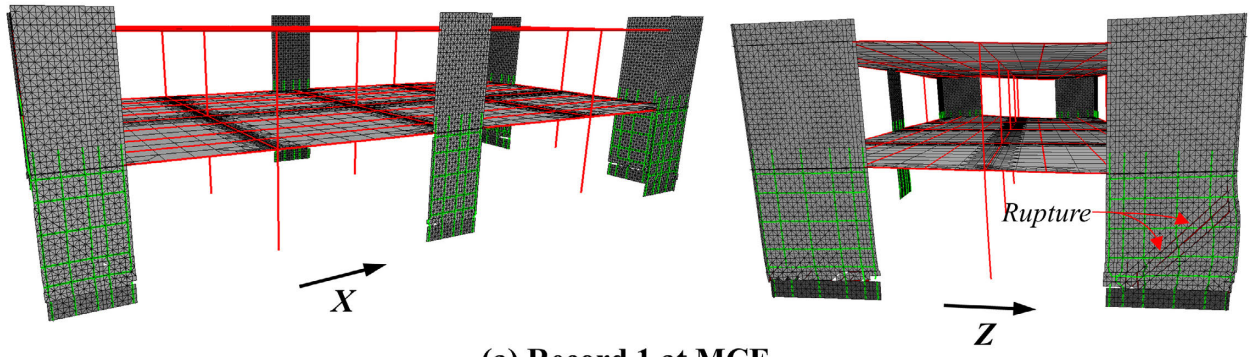

(a) Record 1 at MCE

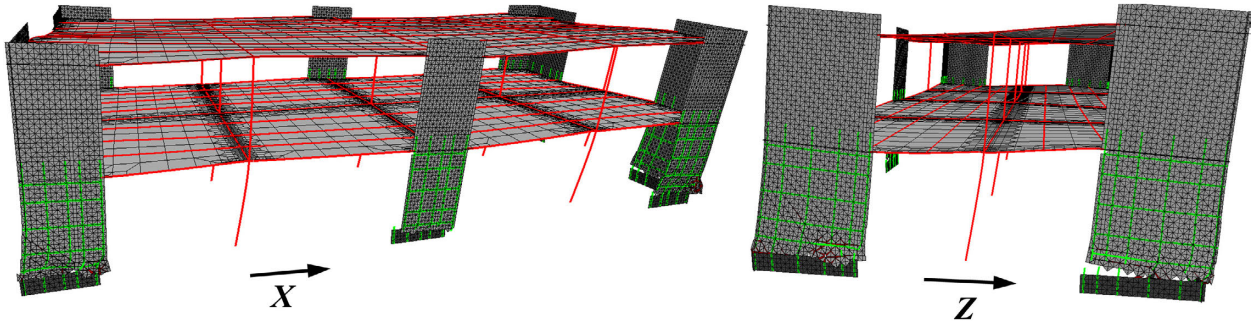

(b) Record 1 at 2xMCE

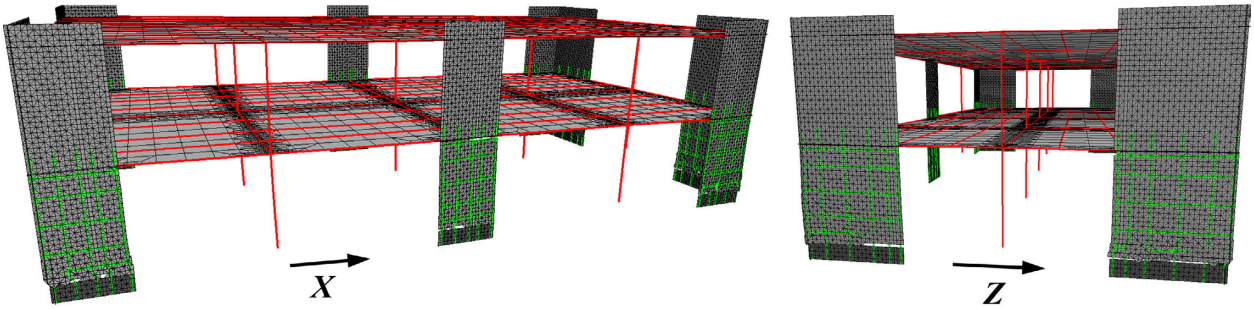

(c) Record 2 at 2xMCE

Figure 3.46 Damage at the end of the analyses of the commercial building archetype.

4 EXTENSION OF MODELING APPROACH TO PARTIALLY GROUTED MASONRY

4.1 State of Research on Partially Grouted Masonry

Most of the reinforced masonry (RM) structures in areas of high seismicity in California are fully grouted. Nonetheless, partially grouted masonry (PGM) constitutes the vast majority of RM construction outside the West Coast and is widely used for industrial, residential, and school buildings. In a partially grouted wall, only the reinforced vertical cells and reinforced horizontal courses (bond beams) are grouted. Partially grouted masonry walls may also have reinforcement in the form of steel wire (joint reinforcement) embedded in bed joints to serve as shear reinforcement or to satisfy the prescriptive requirement of the design code (TMS 402, 2016). Although the code does not prohibit the use of PGM in areas of high seismicity, PGM is mainly and predominantly used in areas of low to moderate seismicity, where the code permits the use of ordinary reinforced masonry walls, which have a larger permitted spacing of the vertical and horizontal reinforcement. Ordinary walls are permitted to have reinforcing bars spaced at 4 to 10 ft, and are permitted to be used for Seismic Design Categories (SDC) A, B, and C, as defined in ASCE/SEI 7-16. Such walls are not required to abide by the shear capacity-design provisions of TMS 402, and are thus more prone to shear-dominated behavior.

While a number of studies have been carried out to investigate the seismic performance of fully grouted RM structures, far less attention has been devoted to PGM. Understanding and predicting the seismic behavior of PGM is challenging due to its inherent heterogeneity and the interaction between the grouted and ungrouted parts. To evaluate the safety of such construction for a moderate seismic zone in the U.S., Gülkan et al. (1990) and Clough et al. (1990) conducted

shake-table tests on light-roof, single-story, PGM houses. They concluded that such construction could meet the safety standard of the then current code (1976 UBC). Recent experimental studies have shown that the behavior and failure modes of PGM walls strongly depend on the spacing of the grouted cells. When the spacing is large (over 4 ft), PGM walls tend to exhibit a behavior similar to RC infilled frames (Minaie et al. 2010). The PGM walls tested by Minaie et al. (2010), which had vertical grouted cells spaced at 4 ft on center, revealed that the shear-strength equation in the then design code (MSJC 2008) could overestimate their shear strength by a factor of 2. To address this issue, a strength-reduction factor of 0.75 was introduced in the shear-strength equation in the 2013 edition of TMS 402. Nolph and ElGawady (2011) tested quasi-statically shear-dominated PGM walls to investigate the influence of the spacing of the vertical grouted cells and of the amount of horizontal reinforcement on the shear capacity of the walls. They studied walls that had only one bond beam, which was located at the mid-height, and vertical grouted cells with spacings of 2 ft, 2.7 ft, and 4 ft on center, respectively. The results showed that the revised code equation (TMS 2013) could still overestimate the shear strength as the spacing of the vertical grouted cells increases and as the amount of horizontal reinforcement increases. However, the walls in these tests were only loaded to the point at which the load capacity was reached; the post-peak response was not examined. Bolhassani et al. (2016a, 2016b) carried out an experimental study to investigate the in-plane behavior of PGM walls that had aspect ratios of 0.6 and 1.0, and vertical grouted cells spaced at 6 ft on center. They tested walls with single, separately grouted, reinforced cells, as commonly done in practice, and walls with double, side-by-side, grouted cells and joint reinforcement in addition to bond beams as an improved design alternative. Their results showed that the shear capacity predicted by the revised equation in the code (TMS 2013) was up to 1.8 times higher than the experimental value. However, the revised equation accurately

predicted the capacity of a PGM wall assemblage tested by Johnson and Schultz (2014) that had a window opening, wall flanges, and the same spacing of vertical grouted cells as the walls of Bolhassani et al. (2016a, 2016b). The influence of different configurations of openings in PGM walls was investigated by Voon and Ingham (2008), but those walls were not subjected to an axial load and had a much smaller spacing of grouted cells than those studied by Bolhassani et al. (2016a, 2016b) and Johnson and Schultz (2014). The walls developed a shear-dominated response showing gradual load degradation with severe stair-stepped cracks along mortar joints in the ungrouted panels and less severe cracks in the bond beams. Nonetheless, according to the New Zealand building code, NZS 4229, the walls were expected to be dominated by flexure. Maleki (2008) tested PGM walls that had various aspect ratios and spacings of grouted cells. He reported that the shear-strength predictions of both the Canadian Masonry Standard and U.S. code (MSJC 2008) are acceptable.

From the past experimental studies, it is evident that the behavior of PGM walls is not well understood. One cannot conclude with certainty as to whether existing seismic design provisions for PGM structures are adequate and sufficiently safe. Accurate numerical modeling tools can help to enhance this understanding and to assess the safety of buildings with PGM shear walls under earthquake loads.

Limited work has been done on the numerical modeling of PGM walls subjected to lateral loads. Two approaches have been mainly used to model the inelastic behavior of these walls with finite elements. In the first approach, the walls are discretized purely with continuum elements, while in the second approach continuum elements are combined with discrete crack interface elements to model major cracks in a discrete fashion. Minaie et al. (2014) modeled PGM walls that were tested under quasi-static cyclic loading. Three-dimensional continuum elements were

used to represent the grouted and ungrouted part in a homogenized manner. The damage-plasticity constitutive law for concrete in the finite element program ABAQUS was used. Even though the proposed continuum model was able to reproduce the experimental cyclic load-vs.-displacement response of the walls, it was not able to represent cracks in a realistic fashion, especially the fracture behavior of the mortar joints. As a result, the failure mechanism of the walls could not be captured.

Shing and Cao (NIST 1997) used a finite element modeling scheme that combined smeared-crack plane-stress elements with cohesive-crack interface elements to model the fracture behavior of masonry units and mortar joints in PGM walls. The models were used to simulate PGM walls that were tested quasi-statically under cyclic loading. However, the analyses were conducted under monotonic loading only. In the analyses, although the wall models developed a realistic load resisting mechanism with the grouted parts acting as a frame and the ungrouted parts acting as infills, the models resulted in lateral strengths that were higher than those obtained in the tests. As explained in the report, the discrepancy between the numerical and experimental load-displacement curves was attributed partly to the different load histories and the partly to the discrepancy in the bond strength between the wall panels and the concrete loading beams.

Maleki (2008) used a similar modeling scheme with smeared-crack plane-stress elements to model the grouted parts of PGM walls and a combination of smeared-crack elements and cohesive-crack interface elements to model the ungrouted masonry units and the mortar joints in a discrete manner. The cohesive-crack interface model of Lotfi and Shing (1994) was adopted for modeling the behavior of the mortar joints. Although the proposed modeling scheme could represent the cracking of mortar joints in a realistic manner, it was restricted only to monotonic loading conditions.

Bolhassani et al. (2016a, 2016b) improved the modeling approach of Minaie et al. (2014) in ABAQUS by introducing cohesive-crack interface elements to simulate the behavior of the mortar joints in PGM walls in a discrete manner. They used interface elements whose response was described with the Coulomb friction law and a traction-separation law to model the cohesive and tensile resistance of the joints. Even though, the models were able to predict the peak lateral resistance of planar walls tested quasi-statically, they were only used for monotonic analyses. The response of the models under cyclic loading was not investigated. Furthermore, the interface elements used for the mortar joints did not account for the reversible joint dilatation caused by the wedging effect of the interface asperities and also for the irreversible joint compaction due to the loss of the damaged mortar material. Accounting for these phenomena is particularly important in simulating the cyclic response of shear-dominated PGM walls since the dilatation or compaction of the mortar joints will affect the stresses transmitted from the surrounding grouted masonry.

Contrary to limited attention devoted to partially grouted masonry, several studies have been conducted on the numerical modeling of unreinforced masonry, especially clay masonry. Numerous studies have used cohesive-crack interface elements to model the fracture behavior of mortar joints in unreinforced masonry panels that were subjected to static or earthquake loading conditions (e.g., Lotfi and Shing 1994; Lourenco 1996; Mehrabi and Shing 1997; Giambanco et al. 2001; Oliveira and Lourenco 2004; Chaimoon and Attard 2007; Stavridis and Shing 2010; Koutromanos and Shing 2012; Aref and Dolatshahi 2013). Other studies have developed methods to represent the composite behavior of the masonry units and mortar joints as an equivalent homogenized continuum (e.g., Gambarotta and Lagomarsino 1997; Lourenco et al. 1998; Zucchini and Lourenco 2002; Milani et al. 2007; Addessi and Sacco 2012). While this approach is more computationally efficient, its ability to capture the failure behavior of large masonry systems

remains to be validated. More refined modeling methods have been proposed to simulate the three-dimensional interaction between the mortar and masonry units that can influence the compression behavior of a masonry assembly. Such models are known as micro-mechanical models and aim to simulate in detail the three-dimensional mechanical behavior of each constituent material of the masonry (e.g. Zucchini and Lourenco 2002; Addessi and Sacco 2016). Because of the high computational cost of these methods, micromechanical models are mostly used to simulate the fracture behavior of small masonry assemblies or to calibrate less refined models.

Although considerable research has been done in modeling the seismic response of unreinforced masonry, most of the previous numerical studies on partially grouted masonry focus only on simulating the monotonic response of planar PGM wall segments. The objective of this study is to develop a finite element modeling scheme that is able to capture the cyclic load-displacement response of PGM walls and can simulate the failure mechanism of such walls in a realistic manner. The scheme should be sufficiently efficient and robust to be used for the assessment of the seismic behavior of three-dimensional PGM building systems that are subjected to earthquake excitation.

4.2 Finite Element Modeling Scheme for Partially Grouted Masonry

4.2.1 Discretization scheme

The finite element modeling scheme proposed for fully grouted RM walls is extended for the analysis of PGM walls. Figure 4.1 shows the finite element model of a PGM wall using a combination of smeared-crack shell elements and cohesive-crack interface elements. The wall shown is made of hollow 8 x 8 x 16 in. concrete masonry units placed in a running bond pattern and has vertical reinforced grouted cells and horizontal bond beams. The discretization scheme used for the grouted cells and the ungrouted panels is shown in Figure 4.2. As for fully grouted

walls, the grouted part of PGM walls is modeled with triangular smeared-crack shell elements to simulate the compressive behavior of grouted masonry as well as diffuse cracking. For walls made with concrete masonry units (CMU) that have a nominal length of 16 in. and a nominal height 8 in., each triangular element has two perpendicular 4-in. long sides. For the grouted part, cohesive-crack interface elements are used to simulate dominant cracks in a discrete fashion. They are placed at 45- and 135-degree angles to model shear cracks through the grouted part in a realistic manner, circumventing the stress locking that could introduced by the smeared-crack shell elements, and also in the horizontal and vertical directions to model possible sliding along horizontal and vertical cracks. The reinforcing bars are modeled with beams elements that are attached to the adjacent triangular shell elements through bond-slip/dowel-action interface elements, as shown in Figure 4.2a, in the same fashion as for fully grouted walls. Hooks at the ends of horizontal bars are assumed to provide strong anchorage and are simulated with bond-slip/dowel-action interface elements that have a high bond strength. The material models for the smeared-crack shell elements, cohesive-crack interface elements, bond-slip/dowel-action interface elements, and reinforcing steel beam elements are described in Chapter 2.

Each masonry unit in an ungrouted masonry panel is represented by two 8-by-8-in. quadrilateral smeared-crack shell elements. A vertical cohesive-crack interface is placed in-between the two shell elements to simulate possible splitting cracks through the unit. Only the thickness of the face shells of the CMU is considered for the ungrouted masonry. The thickness of each face shell is assumed to be 1.40 in., which represents the average face-shell thickness of typical concrete blocks. Cohesive-crack interface elements are also used to represent the horizontal and vertical mortar joints. Each of these interface elements has a void in the middle and two outer contact areas each with a width equal to the width of mortar on a face shell. In typical masonry

construction, the mortar joints have a nominal thickness of 3/8 in. In the model, the interface elements used for the mortar joints are assigned a zero thickness and the thickness of the mortar joints is included in the dimensions (8 x 8 in.) of the shells elements representing the masonry units. The actual length, height, and width of a typical 8 x 8 x 16 CMU are 15.625 in., 7.625 in., and 7.625 in., respectively.

To simulate the out-of-plane bending response of a PGM wall, each shell element is assigned three material layers through the thickness. For the triangular elements representing grouted masonry, the three layers have equal thickness with uniform material properties. A single Gauss point is assigned to each layer. For the quadrilateral shell elements representing ungrouted masonry units, the two exterior layers represent the face shells of the units, while the interior layer represents the void and has a material with zero resistance, as shown in Figure 4.2b. Each layer of the quadrilateral elements has four integration points; however, to avoid transverse shear locking, the element has only one integration point in each layer to calculate the transverse shear. Similar to the shell elements, the cohesive-crack interface elements that represent discrete cracks and mortar joints in the ungrouted masonry account for the void of the hollow units, as shown in Figure 4.2b. The interface element that is already available in LS-DYNA assumes uniform material properties along the width and does not allow for the simulation of the void. Therefore, in this study, a new interface element is implemented in LS-DYNA to be used for the analyses of PGM walls. The formulation of the proposed interface element is described in the following section. Details on the formulation of the quadrilateral and triangular shell elements can be found in LSTC (2018).

The ungrouted masonry is connected to the grouted masonry through cohesive-crack interface elements, as shown in Figure 4.3. Along these interfaces, the element size is 4 in. for the

grouted masonry, while it is 8 in. for the ungrouted masonry. The interface element implemented for this study can have unequal lengths on the two sides to accommodate this situation. The horizontal interface elements between the grouted and ungrouted parts represent the bed joints and are thus assigned the properties of the mortar joints. The properties for the vertical interface elements between the grouted and ungrouted parts depend on the construction details of the wall. In the construction of PGM walls, it is sometimes common to remove the end web of hollow units containing reinforcing bars to allow the placement of the units without the need to be threaded through the vertical bars. In this situation, the grout in the cavity is in contact with the adjacent ungrouted unit, and the vertical interface elements between the grouted and ungrouted units are assumed to have the properties of the face shells of the units, which are perceived to be the plane of weakness. Otherwise, the vertical interface elements between the grouted and ungrouted units are assigned the properties of the face shells in every other course and the properties of mortar joints in the remaining courses for a wall built with the running bond pattern.

4.2.2 Modeling of joint reinforcement in partially grouted masonry walls

The case of PGM walls that contain joint reinforcement is also investigated. Figure 4.4a shows the placement of joint reinforcement within a mortar bed joint during the construction of a PGM wall. The joint reinforcement shown consists of two longitudinal wires, called side wires, which are embedded in the mortar joints. The side wires are tied together with perpendicular wires, called cross wires, which are welded to the side wires. This type of joint reinforcement is called ladder-type joint reinforcement. The configuration of joint reinforcement that has the side wires welded in a zigzag pattern is called truss-type configuration. Typical wire diameters used in practice are 0.148 in. (9 gauge wire) or 3/16 in. The latter corresponds to half of the thickness of a typical bed joint. These wires are typically smooth wires. For modeling the joint reinforcement of

a wall in this study, the two side wires are lumped along the mid-thickness of the wall and are represented with a single row of beam elements. The beam elements have a cross-sectional area that is equivalent to the total area of the two side wires. The length of the beam elements used is 4 in. As shown in Figure 4.4b, the beam elements of the joint reinforcement are connected to the masonry shell elements through bond-slip/dowel-action interface elements. The bond-slip/dowel-action interface elements are attached to the nodes of masonry shell elements on the lower side of the bed joint. The bond and dowel resistances of an element are calculated for a single wire and multiplied by a factor of 2 to account for two wires. At the wall ends, the side wires are assumed to terminate with hooks that provide a strong anchorage. To describe the stress-strain response of a wire, an elastic-perfectly-plastic law is adopted. Tensile tests conducted on joint reinforcement wires have shown very little strain hardening after yielding.

In lack of experimental data, the bond-slip response of joint reinforcement is described based on the recommendation of Eligehausen and Bigaj-van Vliet in CEB/FIP MC90 (1999) for smooth cold-drawn wires embedded in concrete. In the absence of ribs on the wires, the bond strength is assumed to be provided solely by friction. With the formula proposed by Eligehausen and Bigaj-van Vliet, the maximum bond strength is calculated as $\tau_{\max} = 0.038\sqrt{f_{mor}}$ (f_{mor} in ksi), and it is developed at a slip equal to $s_{peak} = 0.0004$ in. To calculate the bond strength of joint reinforcement, the compressive strength of mortar (f_{mor}) is used. Figure 4.5a shows the resulting monotonic bond-slip response for a 3/16-in. diameter wire embedded in mortar with a compressive strength of 3 ksi. Under monotonically increasing slip, the bond strength remains constant once reached. To define the bond-slip response, Eq. 2.39 is used, which was originally proposed by Murcia-Delso and Shing (2014) to describe the frictional bond resistance as a function of slip of a deformed reinforcing bar embedded in concrete. Figure 4.5b shows the bond-slip response under

cyclic loading. The reduction in the friction resistance due to cyclic loading is accounted for through the reduction factor $\rho_{f,c}$ given in Eq. 2.44, as proposed by Murcia-Delso and Shing (2014). The reduction factor is applied to the bond stress only after a load reversal. Therefore, it does not affect the monotonic response curve of the bond-slip law. Parameter s_R in Eq. 2.44 is assumed to be equal to 0.04 in. Figure 4.5b also shows the influence of parameter s_R in the bond resistance under cyclic loading.

The dowel-action law used for the joint reinforcement is similar to that used for reinforcing bars, as described in Section 2.7.3, and is calibrated based on the dowel model of Dulacska (1972). For the calibration, the shearing plane is assumed to be perpendicular to the joint reinforcement. Since the dowel resistance of the joint reinforcement is expected to be small, the softening in the material law that describes the masonry bearing stress under dowel action is ignored.

4.2.3 Element removal scheme for partially grouted masonry

Element removal is triggered by masonry crushing, reinforcement rupture, or excessive relative displacement in a cohesive-crack interface element. For grouted masonry, the element removal criteria described in Chapter 2 apply. When all the integration points in a shell element representing grouted masonry satisfy the condition for compressive failure (i.e. the peak compressive strain has exceeded the strain threshold ε_u), the shell element, all the adjacent cohesive-crack interface elements, and all the connected bond-slip/dowel-action interface elements are removed. When all the integration points of a beam element representing the reinforcement have registered fracture, the beam element and the adjacent bond-slip/dowel-action interface elements are removed. A cohesive-crack interface element is removed when one of the integration points registers out-of-plane sliding that is larger than the thickness of the wall for the

grouted masonry. Finally, a shell element representing grouted masonry is removed when it is attached only on one side to another element.

Similar criteria are used for the removal of elements in ungrouted masonry. A shell element representing ungrouted masonry is removed when all the integration points that lie in one of the face shells satisfy the condition for compressive failure. The cohesive-crack and bond-slip/dowel-action interface elements that are adjacent to the shell element are also removed. A cohesive-crack interface is removed when one of the integration points registers out-of-plane sliding that is larger than the thickness of the face shell. In addition, an interface element representing a mortar bed joint is removed when its lower nodes drop by an average of 2 in. with respect to the top. As for grouted masonry, a shell element representing ungrouted masonry is removed when it is attached only on one side to another element. Furthermore, for ungrouted masonry, a shell element will be removed even if it remains connected to adjacent elements through two of its sides but the interface representing the bed joint below has been already removed.

4.3 A Cohesive-crack Interface Element for the Analysis of Ungrouted Concrete Masonry

A cohesive-crack interface element has been formulated and implemented in LS-DYNA for modeling the response of ungrouted and grouted concrete masonry. To capture the in-plane and out-of-plane behavior of ungrouted masonry, the element formulation accounts for the cavity between the face shells of a concrete unit. Furthermore, the interface element is formulated to allow the connection of sides of shell elements of different lengths. To have displacement compatibility with the connected shell elements, the interface element employs linear shape functions for the interpolation of the nodal displacements and rotations.

4.3.1 Element formulation

The interface element has a zero thickness and four nodes. As shown in Figure 4.6, nodes 1 and 2 define the bottom surface and nodes 3 and 4 define the top surface of the interface element. The deformation components of the interface consist of the differential sliding and differential opening between the top and bottom surfaces. The deformations and the corresponding stress components are calculated in terms of the element local coordinate system. The local system of the interface is defined by the three orthogonal unit vectors $\mathbf{v}_1$, $\mathbf{v}_2$, and $\mathbf{v}_3$, as shown in Figure 4.6. During the analysis, the local system is updated based on the displacements and rotations of the four nodes to account for the geometric nonlinearity associated with rigid-body rotations.

In the undeformed (initial) configuration of the interface element, the top and bottom surfaces are coincident. To define the initial local system of the element, unit vector $\mathbf{v}_1$ is specified to be normal to the plane of the wall that is modeled, vector $\mathbf{v}_2$ is defined along the direction pointing from node 1 to node 2 (or from node 4 to node 3), and vector $\mathbf{v}_3$ is calculated by the cross product $\mathbf{v}_1 \times \mathbf{v}_2$. In subsequent steps of the analysis, the local system of the element is calculated based on the nodal triads of the four nodes (shown in Figure 4.6a) with a procedure similar to the one described in Section 2.7.2 for updating the local system of the bond-slip/dowel-action interface element. Each nodal triad consists of three orthogonal unit vectors that is associated to a node and rotates with the node during the analysis. In the formulation presented, the unit vectors of a nodal triad are denoted by $\mathbf{r}_{I1}$, $\mathbf{r}_{I2}$, and $\mathbf{r}_{I3}$, where I is the node number (1, 2, 3, or 4) it is associated to. In the initial configuration of the element, the triads of the four nodes are defined to be coincident with the element local system, with $\mathbf{r}_{I1}$ coincident with $\mathbf{v}_1$, $\mathbf{r}_{I2}$ coincident with $\mathbf{v}_2$, and $\mathbf{r}_{I3}$ coincident with $\mathbf{v}_3$, as shown in Figure 4.6a. The formulation of the element will be presented for

a general situation in which the two sides of the interface have different lengths. For the convenience of the following discussion, the side defined by nodes 1 and 2 (bottom side) has the smaller length. The element has an isoparametric formulation. Similar to the bond-slip/dowel-action interface presented in Section 2.7.1, separate natural coordinates are introduced for the bottom side and the top side, as proposed by Mavros (2015).

The formulation of the interface element employs concepts for the formulation of a continuum-based beam element described in Belytschko et al. (2013). A similar formulation is used for the interface element that is available in LS-DYNA (LSTC 2018). At every node I, a nodal fiber is introduced, as shown in Figure 4.6b, which is a line of length *t* along the direction of the width of the associated surface. The length *t* is a constant for all 4 nodal fibers, representing the width of the interface. Each nodal fiber rotates with the node, with its direction defined by the unit vector $\mathbf{r}_{I1}$. The locations of nodes 1, 2, 3, and 4 in the global coordinate system are defined by the position vectors $\mathbf{x}_1$, $\mathbf{x}_2$, $\mathbf{x}_3$, and $\mathbf{x}_4$, respectively. The natural coordinate along the length of the nodal fiber is denoted by ξ, and the natural coordinates along the bottom and the top surfaces of the interface are denoted by η and η_m, respectively. Coordinate η corresponds to the short side of the element. Coordinate η_m is mapped to η through the expression $\eta_m = \alpha + \beta \cdot \eta$, in which $\alpha = \left(L_{14} - L_{23}\right)/L_{34}$ and $\beta = L_{12}/L_{34}$. The lengths L_{12}, L_{23}, L_{14}, and L_{34}, as defined in Figure 4.6a, are in terms of the physical coordinate system and are calculated once at the beginning of an analysis. The position of a point in the bottom or the top surface of the interface is defined by the respective position vector $\mathbf{x}_b$ or $\mathbf{x}_t$, which is calculated by linear interpolation functions as:

$$\mathbf{x}_b(\xi,\eta)=\left(\mathbf{x}_1+\xi\frac{t}{2}\mathbf{r}_{11}\right)\frac{1-\eta}{2}+\left(\mathbf{x}_2+\xi\frac{t}{2}\mathbf{r}_{21}\right)\frac{1+\eta}{2}$$

$$\mathbf{x}_t(\xi,\eta)=\left(\mathbf{x}_4+\xi\frac{t}{2}\mathbf{r}_{41}\right)\frac{1-\eta_m}{2}+\left(\mathbf{x}_3+\xi\frac{t}{2}\mathbf{r}_{31}\right)\frac{1+\eta_m}{2} \qquad 4.1$$

The deformation components of the interface consist of the differential displacement d_s between the top and the bottom surfaces along the direction of vector $\mathbf{v}_1$, and the differential displacements d_t and d_n along the directions of vectors $\mathbf{v}_2$ and $\mathbf{v}_3$, respectively. These components are collected in the deformation vector $\mathbf{d}=\{d_s \quad d_t \quad d_n\}^T$, which can be expressed as $\mathbf{d}=d_s\mathbf{v}_1+d_t\mathbf{v}_2+d_n\mathbf{v}_3$. The deformation vector at a point (ξ,η) is calculated by the expression:

$$\mathbf{d}(\xi,\eta)=\mathbf{Q}^T\left(\mathbf{x}_t(\xi,\eta)-\mathbf{x}_b(\xi,\eta)\right) \qquad 4.2$$

in which, $\mathbf{Q}=\begin{bmatrix}\mathbf{v}_1 & \mathbf{v}_2 & \mathbf{v}_3\end{bmatrix}$, with $\mathbf{v}_1$, $\mathbf{v}_2$, $\mathbf{v}_3$ being column vectors. Applying the principle of virtual work, we have:

$$\int_A \delta\mathbf{d}^T\boldsymbol{\sigma}\, dA=\delta\mathbf{U}^T\mathbf{F} \qquad 4.3$$

where $\delta\mathbf{d}$ is the vector of virtual deformations, $\delta\mathbf{U}$ is the vector of virtual nodal displacements and rotations, and $\mathbf{F}$ is the vector of nodal forces and moments. The displacement and force vectors are in terms of the global coordinate system and are given by:

$\mathbf{U}=\begin{bmatrix}\mathbf{u}_1^T & \boldsymbol{\theta}_1^T & \mathbf{u}_2^T & \boldsymbol{\theta}_2^T & \mathbf{u}_3^T & \boldsymbol{\theta}_3^T & \mathbf{u}_4^T & \boldsymbol{\theta}_4^T\end{bmatrix}^T$, and $\mathbf{F}=\begin{bmatrix}\mathbf{f}_1^T & \mathbf{m}_1^T & \mathbf{f}_2^T & \mathbf{m}_2^T & \mathbf{f}_3^T & \mathbf{m}_3^T & \mathbf{f}_4^T & \mathbf{m}_4^T\end{bmatrix}^T$, where $\mathbf{u}_I$, $\boldsymbol{\theta}_I$, $\mathbf{f}_I$, and $\mathbf{m}_I$ are 3x1 vectors of the displacements, rotations, forces, and moments at

node I . Vector $\boldsymbol{\sigma} = \{\sigma_s \quad \sigma_t \quad \sigma_n\}^T$ is the stress vector that is work conju4.4gate to the deformation vector $\mathbf{d}$. The vector of virtual deformations is given by:

$$\delta\mathbf{d} = \mathbf{Q}^T \left(\delta\mathbf{x}_t - \delta\mathbf{x}_b \right) \tag{4.5}$$

The variation of the local coordinate system is neglected. In other words, it is assumed that $\delta\mathbf{Q} = 0$. The virtual position vectors are calculated by the expressions:

$$\begin{aligned}
\delta\mathbf{x}_b &= \left(\delta\mathbf{x}_1 + \xi\frac{t}{2}\delta\mathbf{r}_{11} \right)\frac{1-\eta}{2} + \left(\delta\mathbf{x}_2 + \xi\frac{t}{2}\delta\mathbf{r}_{21} \right)\frac{1+\eta}{2} \\
&= \left(\delta\mathbf{x}_1 + \xi\frac{t}{2}\delta\boldsymbol{\theta}_1 \times \mathbf{r}_{11} \right)\frac{1-\eta}{2} + \left(\delta\mathbf{x}_2 + \xi\frac{t}{2}\delta\boldsymbol{\theta}_2 \times \mathbf{r}_{21} \right)\frac{1+\eta}{2} \\
&= \left(\delta\mathbf{u}_1 - \xi\frac{t}{2}S\left(\mathbf{r}_{11}\right)\delta\boldsymbol{\theta}_1 \right)\frac{1-\eta}{2} + \left(\delta\mathbf{u}_2 - \xi\frac{t}{2}S\left(\mathbf{r}_{21}\right)\delta\boldsymbol{\theta}_2 \right)\frac{1+\eta}{2}
\end{aligned} \tag{4.6}$$

$$\begin{aligned}
\delta\mathbf{x}_t &= \left(\delta\mathbf{x}_4 + \xi\frac{t}{2}\delta\mathbf{r}_{41} \right)\frac{1-\eta_m}{2} + \left(\delta\mathbf{x}_3 + \xi\frac{t}{2}\delta\mathbf{r}_{31} \right)\frac{1+\eta_m}{2} \\
&= \left(\delta\mathbf{x}_4 + \xi\frac{t}{2}\delta\boldsymbol{\theta}_4 \times \mathbf{r}_{41} \right)\frac{1-\eta_m}{2} + \left(\delta\mathbf{x}_3 + \xi\frac{t}{2}\delta\boldsymbol{\theta}_3 \times \mathbf{r}_{31} \right)\frac{1+\eta_m}{2} \\
&= \left(\delta\mathbf{u}_4 - \xi\frac{t}{2}S\left(\mathbf{r}_{41}\right)\delta\boldsymbol{\theta}_4 \right)\frac{1-\eta_m}{2} + \left(\delta\mathbf{u}_3 - \xi\frac{t}{2}S\left(\mathbf{r}_{31}\right)\delta\boldsymbol{\theta}_3 \right)\frac{1+\eta_m}{2}
\end{aligned}$$

In the expressions above, we have used the conditions that $\delta\mathbf{x}_I = \delta\mathbf{u}_I$ and $\delta\boldsymbol{\theta}_I \times \mathbf{r}_{I1} = -\mathbf{r}_{I1} \times \delta\boldsymbol{\theta}_I = -\mathbf{S}\left(\mathbf{r}_{I1}\right)\delta\boldsymbol{\theta}_I$ at each node *I*, where $\mathbf{S}\left(\mathbf{r}_{I1}\right)$ is the skew-symmetric matrix given by:

$$\mathbf{S}\left(\mathbf{r}_{I1}\right) = \begin{bmatrix} 0 & -\mathbf{r}_{I1}(3) & \mathbf{r}_{I1}(2) \\ \mathbf{r}_{I1}(3) & 0 & -\mathbf{r}_{I1}(1) \\ -\mathbf{r}_{I1}(2) & \mathbf{r}_{I1}(1) & 0 \end{bmatrix} \tag{4.7}$$

By substituting Eq. 4.6 into Eq. 4.5, we can relate the vector of virtual deformations to the virtual nodal displacement vector with the expression $\delta\mathbf{d} = \mathbf{B}\delta\mathbf{U}$. Matrix $\mathbf{B}$ is 3x24 and is given by:

$$\mathbf{B} = \left[-\frac{1-\eta}{2}\mathbf{Q}^T \quad \xi\frac{t}{2}\frac{1-\eta}{2}\mathbf{Q}^T\mathbf{S}(\mathbf{r}_{11}) \quad -\frac{1+\eta}{2}\mathbf{Q}^T \quad \xi\frac{t}{2}\frac{1+\eta}{2}\mathbf{Q}^T\mathbf{S}(\mathbf{r}_{21}) \ \ldots \right.$$
$$\left. \frac{1+\eta}{2}\mathbf{Q}^T \quad -\xi\frac{t}{2}\frac{1+\eta_m}{2}\mathbf{Q}^T\mathbf{S}(\mathbf{r}_{31}) \quad \frac{1-\eta_m}{2}\mathbf{Q}^T \quad -\xi\frac{t}{2}\frac{1-\eta_m}{2}\mathbf{Q}^T\mathbf{S}(\mathbf{r}_{41}) \right] \tag{4.8}$$

By substituting the above expression in Eq. 4.3, the element nodal force vector can be expressed as:

$$\mathbf{F} = \int_A \mathbf{B}^T\boldsymbol{\sigma}\, dA \tag{4.9}$$

The integral in Eq. 4.9 is evaluated with a four-point quadrature rule. A more refined quadrature rule can be used if higher resolution is desired in the distribution of contact stresses across the interface. The locations of the integration points and the integration domain depend on whether or not the interface has a cavity at the center as shown in Figure 4.7. For an interface without a cavity, Gauss quadrature is used and the element force vector is obtained by:

$$\mathbf{F} = \int_{-1}^{1}\int_{-1}^{1} \mathbf{B}^T\boldsymbol{\sigma}\cdot j\, d\xi d\eta = \sum_{i=1}^{4} \mathbf{B}^T(\xi_i,\eta_i)\boldsymbol{\sigma}(\xi_i,\eta_i)\cdot\frac{L_{12}\cdot t}{2} \tag{4.10}$$

where $j = L_{12}\cdot t/2$ the Jacobian determinant of the isoparametric formulation. For an interface element with a cavity, as shown in Figure 4.7b, the element force vector is obtained by Eq. 4.11.

$$\mathbf{F}=\int_{-1}^{1}\int_{-1}^{1}\mathbf{B}^T\boldsymbol{\sigma}\cdot j\;d\xi d\eta=\int_{-1}^{1}\int_{-1}^{-1+2\frac{t_f}{t}}\mathbf{B}^T\boldsymbol{\sigma}\cdot j\;d\xi d\eta+\int_{-1}^{1}\int_{1-2\frac{t_f}{t}}^{1}\mathbf{B}^T\boldsymbol{\sigma}\cdot j\;d\xi d\eta=$$

$$=\int_{-1}^{1}\int_{-1}^{1}\mathbf{B}^T\boldsymbol{\sigma}\cdot\frac{L_{12}\cdot t}{4}\cdot\frac{t_f}{t}\;dsd\eta+\int_{-1}^{1}\int_{-1}^{1}\mathbf{B}^T\boldsymbol{\sigma}\cdot\frac{L_{12}\cdot t}{4}\cdot\frac{t_f}{t}\;dpd\eta= \tag{4.11.}$$

$$=\mathbf{B}^T\boldsymbol{\sigma}\left(s=0,\eta=\frac{-1}{\sqrt{3}}\right)\cdot\frac{L_{12}\cdot t_f}{4}\cdot 2+\mathbf{B}^T\boldsymbol{\sigma}\left(s=0,\eta=\frac{1}{\sqrt{3}}\right)\cdot\frac{L_{12}\cdot t_f}{4}\cdot 2+$$

$$+\mathbf{B}^T\boldsymbol{\sigma}\left(p=0,\eta=\frac{-1}{\sqrt{3}}\right)\cdot\frac{L_{12}\cdot t_f}{4}\cdot 2+\mathbf{B}^T\boldsymbol{\sigma}\left(p=0,\eta=\frac{1}{\sqrt{3}}\right)\cdot\frac{L_{12}\cdot t_f}{4}\cdot 2$$

To calculate the integrals in Eq. 4.11, the change of variable is performed with $s=\frac{t}{t_f}(\xi+1)-1$ and $p=\frac{t}{t_f}(\xi-1)+1$, where t_f is the thickness of the face shell in the physical coordinate system. Note that the integration in Eqs. 4.10 and 4.11 is performed over the surface with the smaller initial length (i.e., the bottom surface).

4.3.2 Definition of element local coordinate system

The local coordinate system of the interface element is defined with a procedure similar to the one described in Section 2.7.2 for the bond-slip/dowel-action interface element. The local coordinate system is initially specified in the undeformed configuration of the element, and it is updated during the analysis based on the nodal triads, which are collected in the rotation matrix $\mathbf{R}_I=\begin{bmatrix}\mathbf{r}_{I1} & \mathbf{r}_{I2} & \mathbf{r}_{I3}\end{bmatrix}$ for each node I. At every displacement increment in the analysis, the element local system update is performed in two stages, as shown in Figure 4.8. In the first stage, assuming that matrices $\mathbf{R}_I$ have been already obtained, two new local systems are defined. One system corresponds to the bottom surface of the element and the other to the top surface. The system for

the bottom surface is described by matrix $\mathbf{Z}$ that collects unit vectors $\mathbf{z}_1$, $\mathbf{z}_2$, and $\mathbf{z}_3$, while the system for the top surface is described by matrix $\mathbf{T}$ that collects unit vectors $\mathbf{t}_1$, $\mathbf{t}_2$, and $\mathbf{t}_3$. Matrix $\mathbf{Z}$ is calculated as the average of the rotation matrices $\mathbf{R}_1$ and $\mathbf{R}_2$, while matrix $\mathbf{T}$ is the average of $\mathbf{R}_3$ and $\mathbf{R}_4$. To compute the average rotation matrices, the procedure described in Crisfield (1990) is followed. Matrices $\mathbf{Z}$ and $\mathbf{T}$ are corrected so that the unit vectors $\mathbf{z}_2$ and $\mathbf{t}_2$ are aligned with the directions of the bottom side (defined by nodes 1 and 2) and the top side (defined by nodes 3 and 4), respectively. The correction is performed using Eq. 2.36. In the second stage, matrix $\mathbf{Q}$ that collects the unit vectors of the element local system is calculated as the average of the rotation matrices $\mathbf{Z}$ and $\mathbf{T}$.

4.3.3 Drilling moments

To restrain the drilling degrees of freedom of the interface element (nodal rotations about the axes defined by unit vectors $\mathbf{r}_{I1}$), a penalty rotational stiffness is introduced at each node so that

$$M_{drill,I} = k_{drill} \cdot \theta_{drill,I} \tag{4.12}$$

in which k_{drill} is taken as a very small portion (e.g., 1/1000) of the interface material stiffness. Rotations $\theta_{drill,I}$ are calculated with Eq. 4.13 to obtain only the deformational part of the total rotations about each node. Assuming that the drilling rotations are small, we can replace the sine of an angle by the angle itself. After the drilling moments are computed, they are transformed to the global coordinate system and are added in the element force vector.

$$
\begin{aligned}
2\sin\theta_{drill,1} &= -\mathbf{r}_{13}^{T}\mathbf{z}_2 + \mathbf{z}_3{}^{T}\mathbf{r}_{12} \\
2\sin\theta_{drill,2} &= -\mathbf{r}_{23}^{T}\mathbf{z}_2 + \mathbf{z}_3{}^{T}\mathbf{r}_{22} \\
2\sin\theta_{drill,3} &= -\mathbf{r}_{33}^{T}\mathbf{t}_2 + \mathbf{t}_3{}^{T}\mathbf{r}_{32} \\
2\sin\theta_{drill,4} &= -\mathbf{r}_{43}^{T}\mathbf{t}_2 + \mathbf{t}_3{}^{T}\mathbf{r}_{42}
\end{aligned}
\tag{4.13}
$$

4.4 Validation of Modeling Scheme with Quasi-static Tests

The modeling scheme proposed for the analysis of PGM walls is validated with results from quasi-static wall tests. Four wall specimens are considered. The reinforcing details of the walls and the test setups are presented in Figure 4.9 to Figure 4.12. Walls SR67 and DR67 were tested by Bolhassani et al. (2016a). They were 224-in. long and 152-in. tall planar walls with an aspect ratio of 0.67. Walls SRU and DRU were tested by Johnson and Schultz (2014) and Schultz and Johnson (2019). They had a U-shaped cross section and a window opening within the web, as shown in Figure 4.11. The length and height of the specimens were 256 in. and 168 in., respectively. The wall flanges extended 40 in. from the web. The four wall specimens were subjected to a cyclic lateral displacement history at the top under the cantilever condition. All the wall specimens were tested under a constant vertical compressive load that was applied at the top of the walls.

The four walls are classified as ordinary walls according to TMS 402, since they had vertical and horizontal grouted cells spaced at a distance larger than 48 in. Walls SR67 and SRU represent the current masonry construction practice in that they had single separately grouted cells, while walls DR67 and DRU are considered as having improved design details with double side-by-side vertical grouted cells. In addition, wall DRU had joint reinforcement placed along the bed joints as shown in Figure 4.11. The joint reinforcement had a ladder-type configuration with longitudinal wires that had a diameter of 3/16 in. and cross wires that had a diameter of 0.148 in.

Table 4.1 shows the vertical loads that were applied to the walls and the material strengths as obtained from the respective test reports. The vertical load shown for walls SR67 and DR67 includes the weight of the RC beam placed on the masonry wall and the weight of the two additional grouted masonry courses right below the beam (see Figure 4.10).

Figure 4.13 shows the FE model developed for each wall specimen. Table 4.2 to Table 4.5 summarize the values of the material parameters used in the analyses of the walls. The parameters have been defined in Chapter 2. The values used for the tensile strength (f_t) of grouted masonry are in the range of 9% - 12% of f'_m. As in the analyses of fully grouted walls (see Chapter 3), the modulus of elasticity (E_m) of grouted masonry is taken to be $600 f'_m$ and the compressive stress (f_o) at the end of the linear branch of the stress-strain curve is assumed to be 2/3 of f'_m. The compressive strength for the shell elements representing the ungrouted masonry is taken to be the ungrouted masonry prism strength ($f'_{m,ungr}$). The tensile strength of the CMU is assumed to be 0.40 ksi based on data from the splitting tests conducted by Bolhassani et al. (2016a) on concrete masonry units. The initial stiffness of the CMU is set equal to 2000 ksi. The compressive strengths of the grouted and ungrouted masonry are determined from the respective prism tests. The interface elements simulating fracture of grouted masonry and ungrouted units are assigned a high initial stiffness to ensure displacement continuity before cracking and to minimize penetration when the interface is under compression. For the interfaces representing mortar joints, the elastic normal stiffness (D_{nn}) is selected so that the stiffness of the ungrouted masonry prism is equal to about $600 f'_{m,ungr}$. The tangential stiffness assigned is calculated from the normal stiffness with the assumption of a poisson's ratio of 0.2. The values of the parameters controlling the tensile strength of mortar joints, and the cohesion, friction and dilatation are selected based on the

recommendations of Koutromanos and Shing (2012), Drysdale and Hamid (2008), and Mehrabi (1994). The same properties are used for both the horizontal and vertical mortar joints. The mortar joints that contain joint reinforcement are assigned a reduced net width, which is equal to the full net width of the joints (2.5 in.) minus two diameters of the longitudinal wires of the joint reinforcement. For wall DRU, the reduced width is 2.13 in. A detailed description about the construction of the vertical grouted cells is not provided in the test reports for the four walls. Therefore, it is assumed that the grout in the vertical cells is not in contact with the adjacent ungrouted CMU. Therefore, the vertical interface elements that connect the grouted cells to the ungrouted masonry are assigned the properties of mortar joints and the properties of cracks in ungrouted blocks consistent with a running bond pattern.

Figure 4.14 to Figure 4.17 compare the numerical results to the experimental results in terms of the cyclic load-displacement response curves and damage patterns. The models predict reasonably well the experimental cyclic load-displacement response of the walls. In the models of SR67 and DR67, compressive failure occurs in the form of shear sliding along diagonal interfaces in the compression toes.

Parts of Chapter 4 are a reprint of the material that appears in the manuscript "Koutras A, Shing PB. Seismic Behavior of a Partially Grouted Reinforced Masonry Structure: Shake-Table Testing and Numerical Analyses" which has been submitted for publication to the Journal of Earthquake Engineering and Structural Dynamics in 2019. The author of this dissertation was the primary investigator and author of this manuscript.

Table 4.1 Material properties and applied vertical loads on the PGM wall specimens.

Wall properties	Wall ID			
	SR67	DR67	SRU	DRU
Estimated total roof weight and applied vertical load (kips)	18.0	18.0	29.0	29.0
Grouted masonry prism strength (ksi)	4.0	4.0	2.9	3.7
Ungrouted masonry prism strength (ksi)	3.0	3.0	2.1	3.0
Grout strength (ksi)	4.2	4.2	4.2	4.3
CMU strength (ksi)	2.9	2.9	n.a.	n.a.
Mortar strength (ksi)	1.9	1.9	1.8	1.9
Reinf. size	#6	#4	#4	#3
Reinf. yield and ultimate strengths (ksi)	Grade 60	Grade 60	70 / 98	68 / 104
Joint reinf. yield and ultimate strengths (ksi)	None	None	None	73 / 79

Table 4.2 Material parameters of the smeared-crack shell elements used in the analyses of PGM walls (see Figure 2.8 for the parameter definitions).

Shells elements	**Wall ID**	f_m **(ksi)**	f_o **(ksi)**	E_m **(ksi)**	f_t **(ksi)**	ε_o	ε_u	**Net width (in)**
Grouted masonry	SR67	4.0	2.7	2400	0.48	0.003	0.040	7.625
	DR67							
	SRU	2.9	1.9	1740	0.32			
	DRU	3.7	2.5	2220	0.32			
Ungrouted masonry	SR67	3.0	2.0	2000	0.40	0.003	0.015	2.8
	DR67							
	SRU	2.1	1.4					
	DRU	3.0	2.0					

Table 4.3 Material parameters of the cohesive-crack interface elements used in the analyses of PGM walls (see Section 2.5.2 for the parameter definitions).

Interface elements	**Wall ID**	D_{nn} / D_{tt} **(ksi/in)**	s_o **(ksi)**	μ_o / μ_r	r_o / r_r **(ksi)**	G_{fI} **(kips/in)**	G_{fII} **(kips/in)**	$\zeta_{dil,o}$ / $\zeta_{dil,r}$	d_o **(in)**	**Net width (in)**
Grouted masonry	SR67	5000	0.48	1.4 / 1.0	0.05 / 0.01	0.0004	0.004	0.4 / 0.001	0.4	7.625
	DR67									
	SRU		0.32	1.3 / 1.0						
	DRU									
Ungrouted units	SR67	5000	0.40	1.2 / 1.0	0.05 / 0.01	0.0004	0.004	0.2 / 0.001	0.2	2.8
	DR67									
	SRU									
	DRU									
Mortar joints	SR67	300 / 125	0.10	0.95 / 0.70	0.02 / 0.01	0.0002	0.002	0.10 / 0.001	0.035	2.5*
	DR67									
	SRU		0.07	0.95 / 0.80						
	DRU									
Base interface	SR67	5000	0.10	1.00 / 1.00	0.05 / 0.01	0.0002	0.002	0.4 / 0.001	0.4	7.625
	DR67									
	SRU									
	DRU									

* In the model of DRU, the mortar joints that contain joint reinforcement are assumed to have a net width of 2.13 in.

Table 4.4 Material parameters of the beam elements representing steel reinforcement in the analyses of PGM walls (see Section 2.6 for the parameter definitions).

Wall ID	Size	f_y (ksi)	f_u (ksi)	E_s (ksi)	ε_{sh}	(ε_{sh1}, f_{sh1})	ε_u	D_{cr}
SR67	#6	67	100	29000	0.01	(0.03, 84)	0.12	0.55
DR67	#4	67	100	29000	0.01	(0.03, 84)	0.12	0.55
SRU	#6	70	98	29000	0.01	(0.03, 84)	0.12	0.55
DRU	#4	68	104	29000	0.01	(0.03, 84)	0.12	0.55

Table 4.5 Material parameters of the bond-slip/dowel-action elements used in the analyses of PGM walls (see Section 2.7.3 for the parameter definitions).

Wall ID	Masonry compressive strength used for bond strength (ksi)	Confinement condition	Grout compressive strength used for dowel strength (ksi)	Displacement parameters for dowel law d_1 / d_u (in)
SR67	4.0	Unconfined	4.2	0.03 / 0.06
DR67	4.0	Confined	4.2	0.03 / 0.06
SRU	2.9	Unconfined	4.2	0.03 / 0.06
DRU	3.7	Confined	4.3	0.03 / 0.06

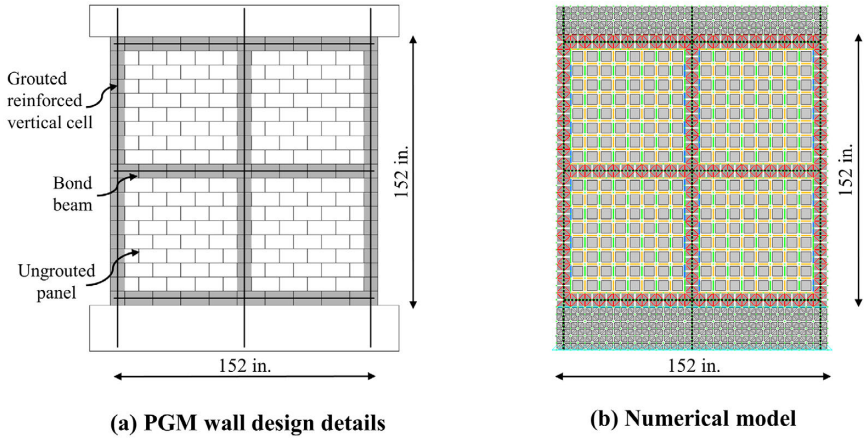

Figure 4.1 Design details and numerical model of a partially grouted reinforced masonry wall.

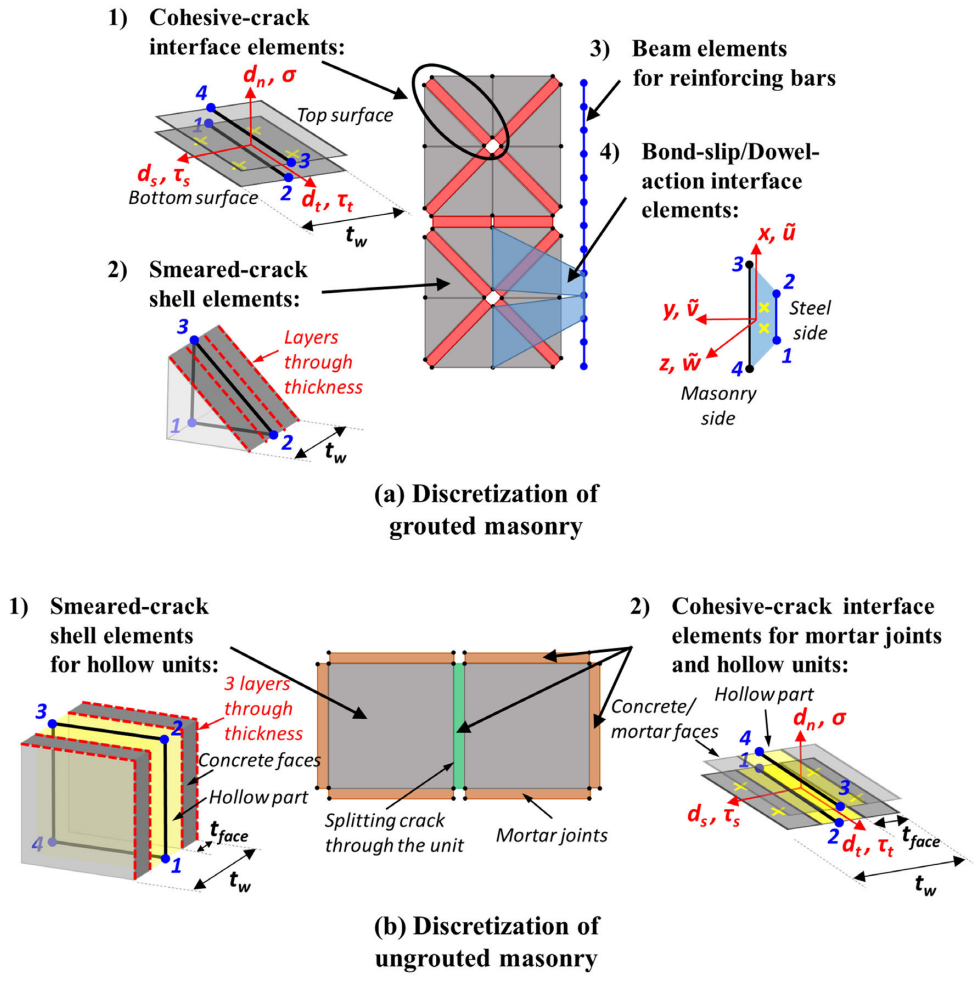

Figure 4.2 Finite element modeling scheme for partially grouted masonry.

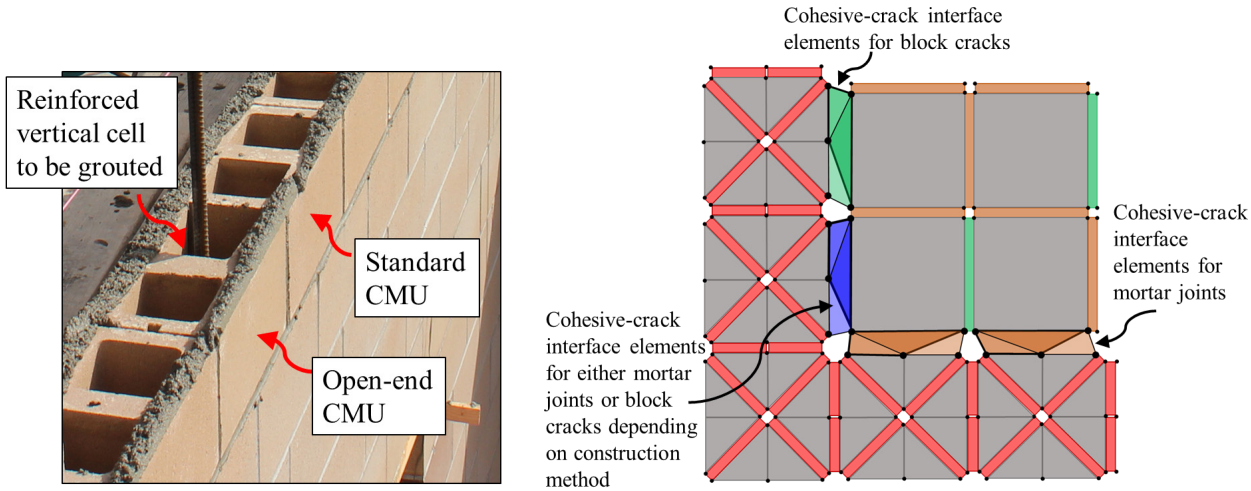

(a) Construction of PGM wall with running bond pattern

(b) Connection of grouted and ungrouted parts in the model

Figure 4.3 Discretization scheme for the interface between the grouted and ungrouted parts.

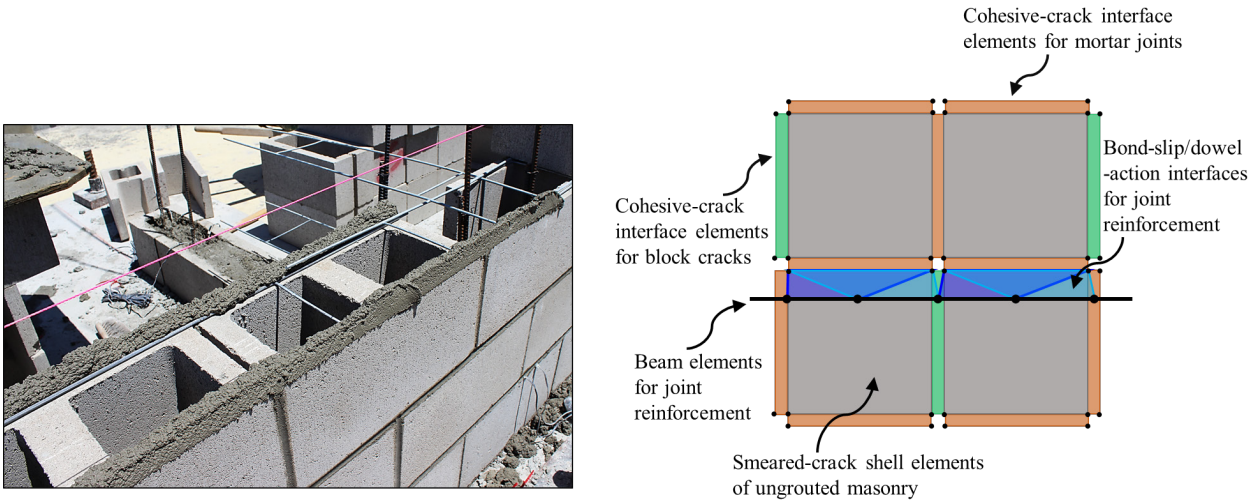

(a) Placement of joint reinforcement

(b) Discretization scheme with joint reinforcement

Figure 4.4 Placement of joint reinforcement in construction and in the numerical model.

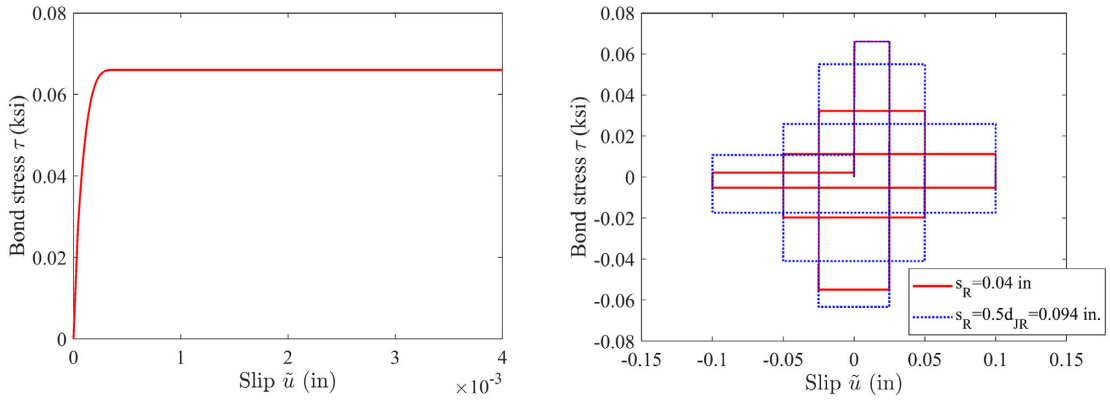

(a) Monotonic response **(b) Cyclic response**

Figure 4.5 Monotonic and cyclic response of the bond-slip law used for the joint reinforcement.

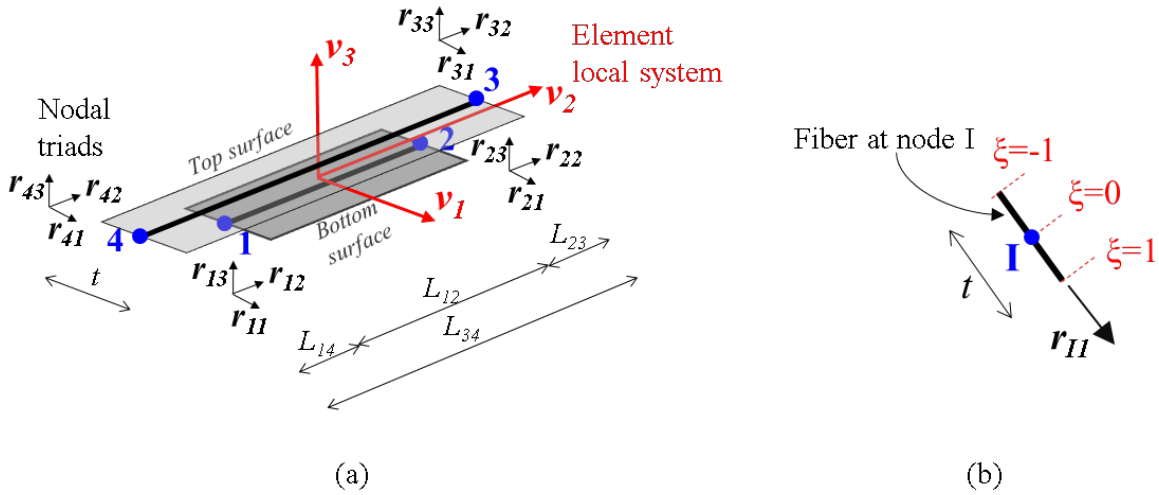

(a) (b)

Figure 4.6 Configuration of cohesive-crack interface element. (a) Element local coordinate system and nodal triads in the undeformed state; (b) fiber at node I of the interface.

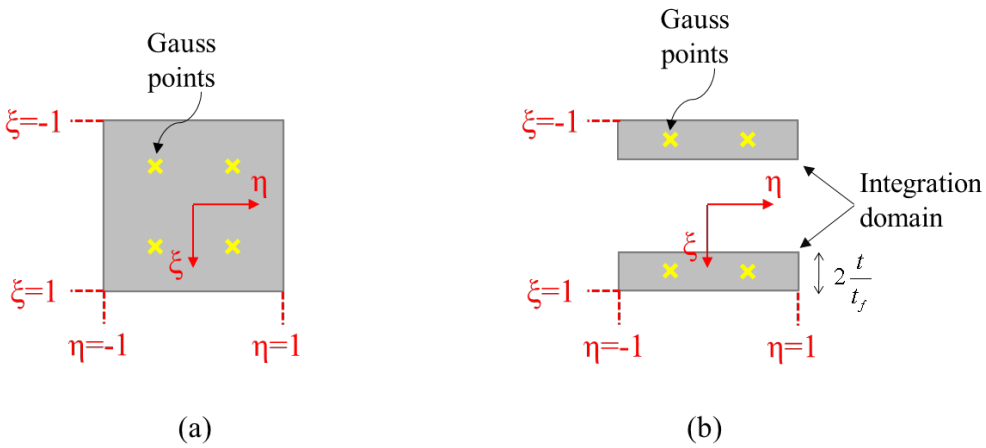

Figure 4.7 Cross section of interface element. (a) Interface for a grouted section; (b) interface for an ungrouted section with face shells.

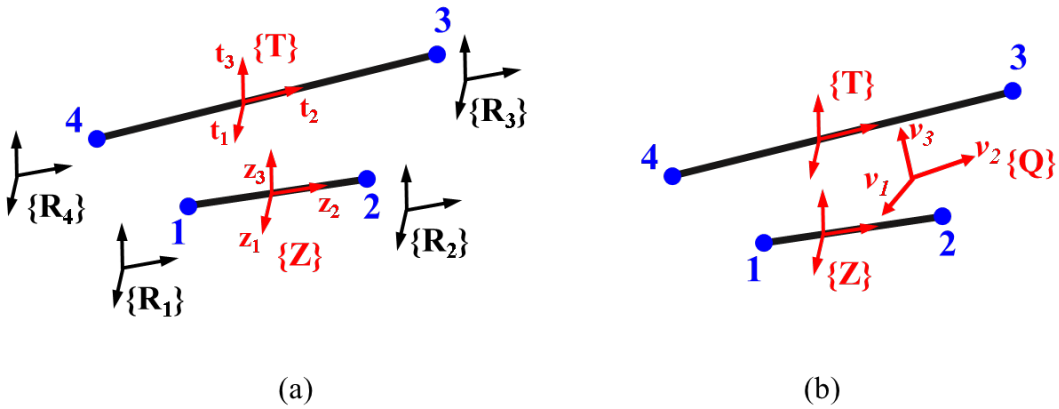

Figure 4.8 Definition of element local coordinate system. (a) Stage 1; (b) stage 2.

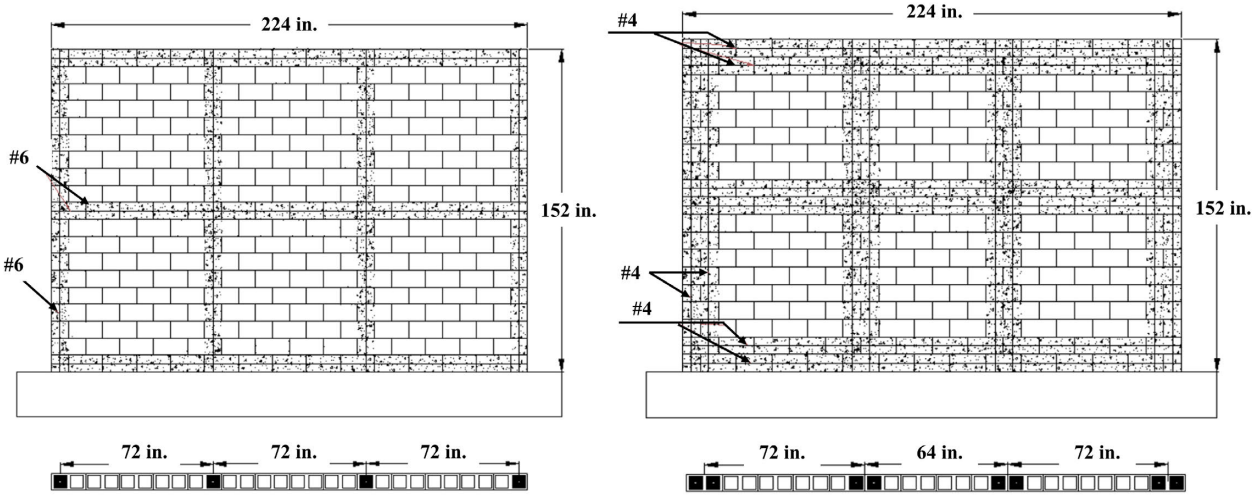

(a) Wall SR67 **(b) Wall DR67**

Figure 4.9 Reinforcement details of SR67 and DR67 (adapted from Bolhassani et al. 2016).

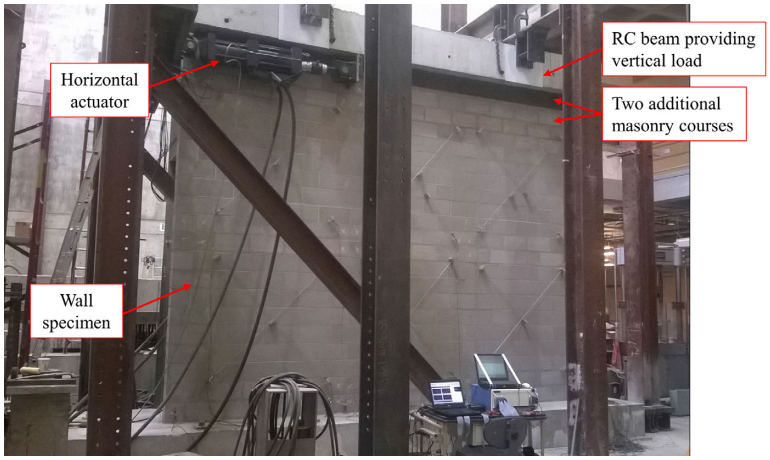

Figure 4.10 Test setup for walls SR67 and DR67 (adapted from Bolhassani 2015).

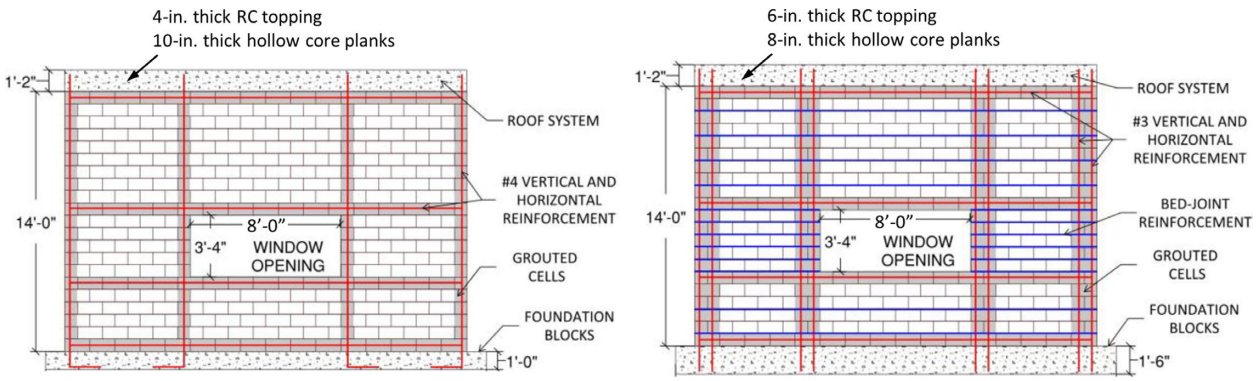

Front elevation views

Plan views

Side elevation views

(a) Wall SRU **(b) Wall DRU**

Figure 4.11 Reinforcement details of walls SRU and DRU (adapted from Schultz and Johnson 2019).

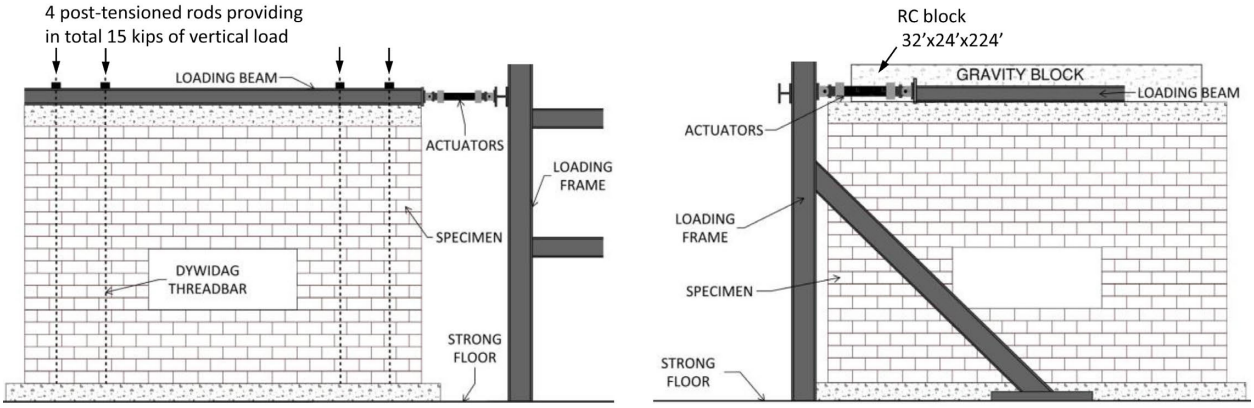

(a) Wall SRU **(b) Wall DRU**

Figure 4.12 Test setup for walls SRU and DRU (adapted from Schultz and Johnson 2019).

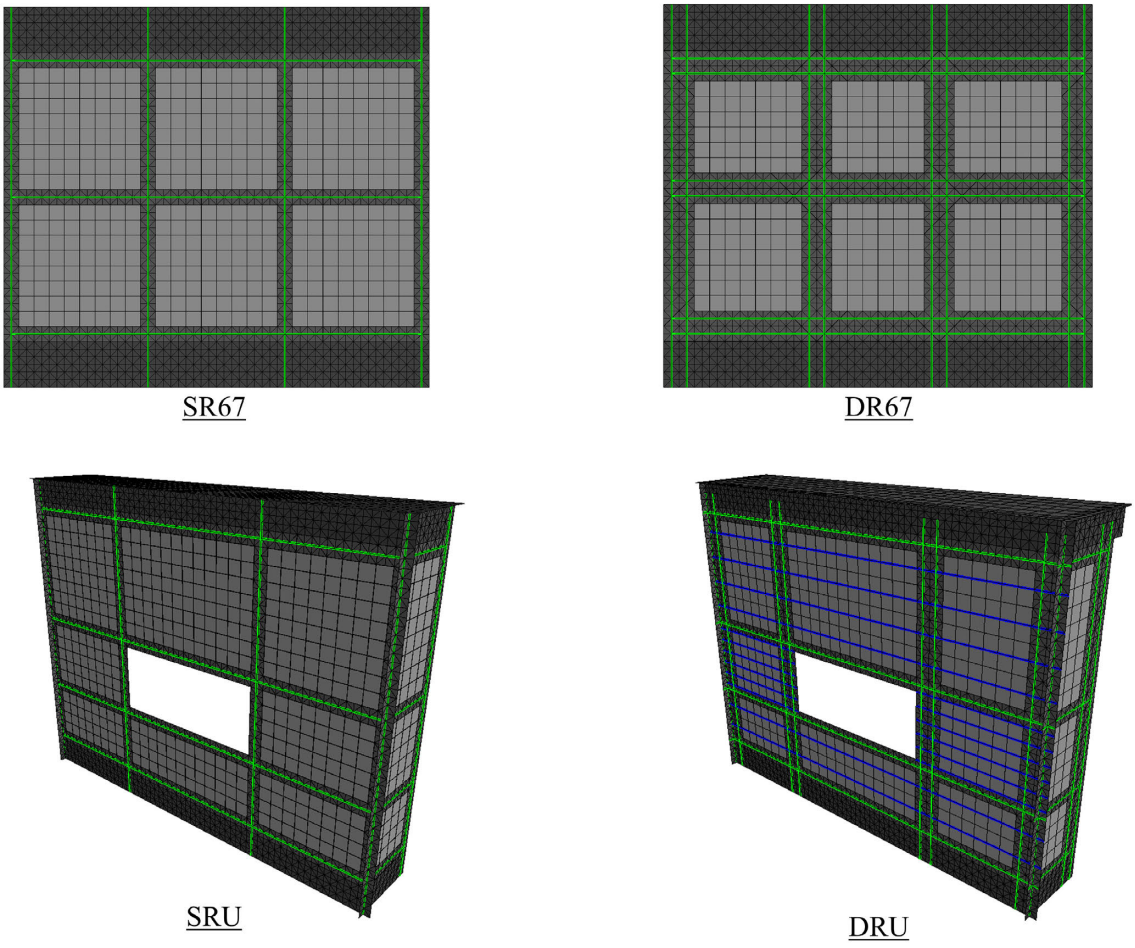

Figure 4.13 FE meshes for the PGM wall specimens.

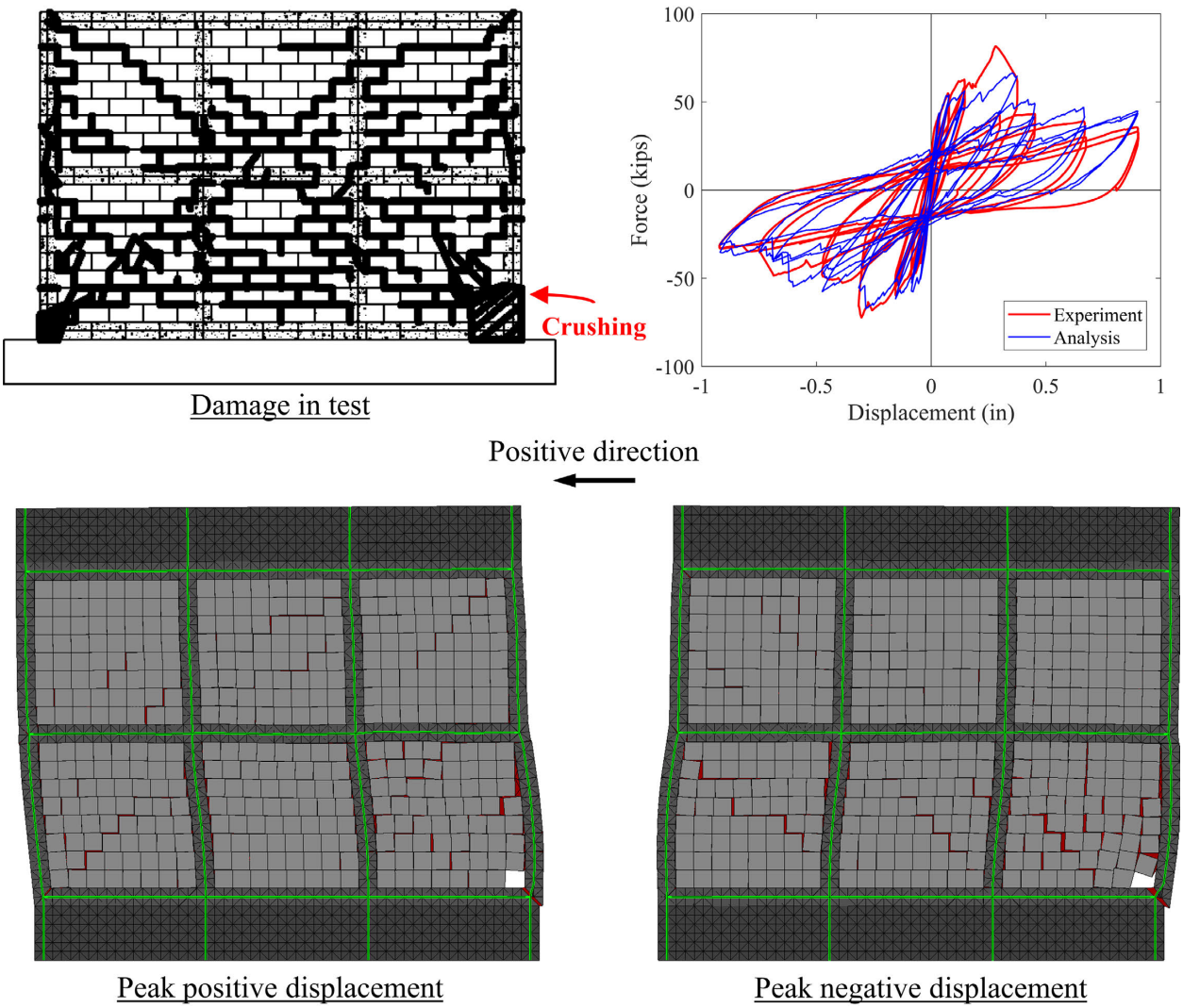

Figure 4.14 Comparison of numerical and experimental results for wall SR67 (deformation magnified by 12 times).

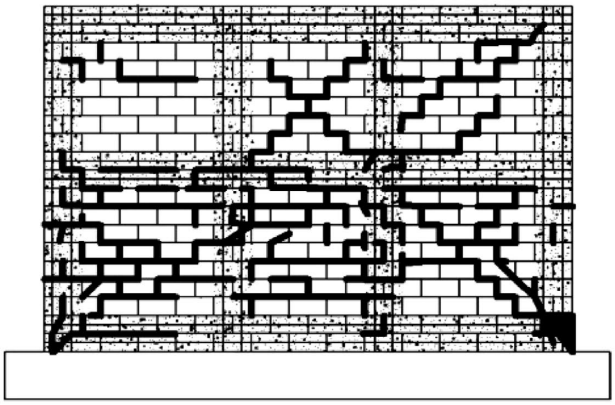

Damage in test

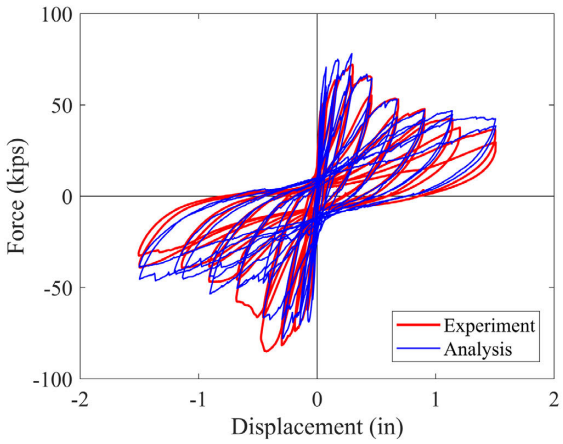

Positive direction

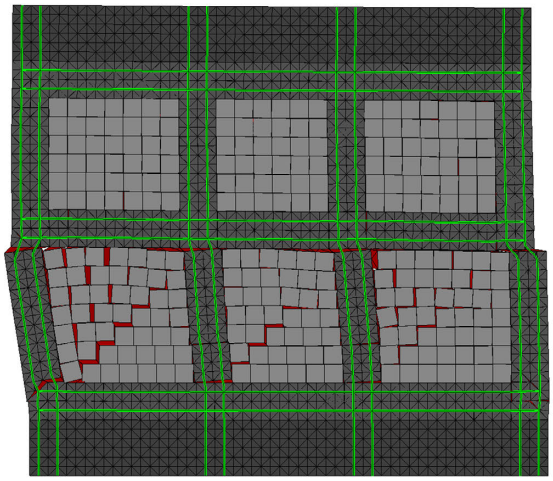

Peak positive displacement

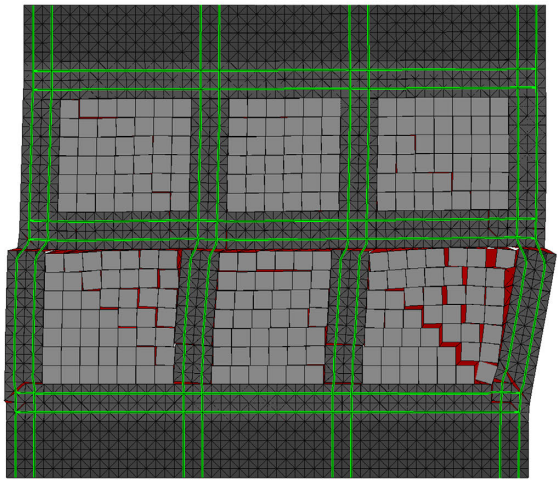

Peak negative displacement

Figure 4.15 Comparison of numerical and experimental results for wall DR67 (deformation magnified by 5 times).

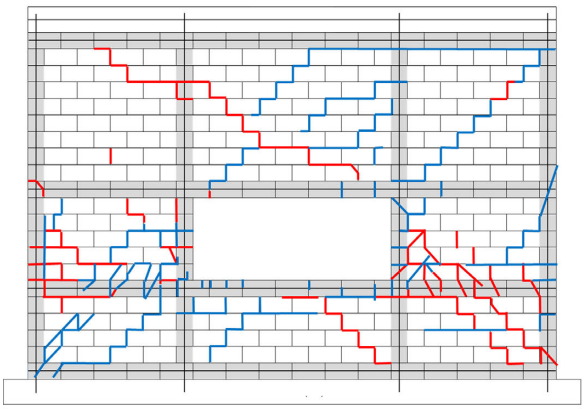

Damage in test

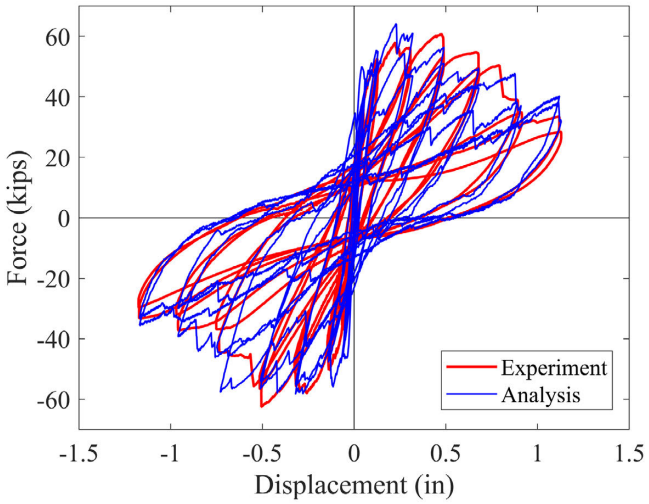

Damage in left pier

Damage in right pier

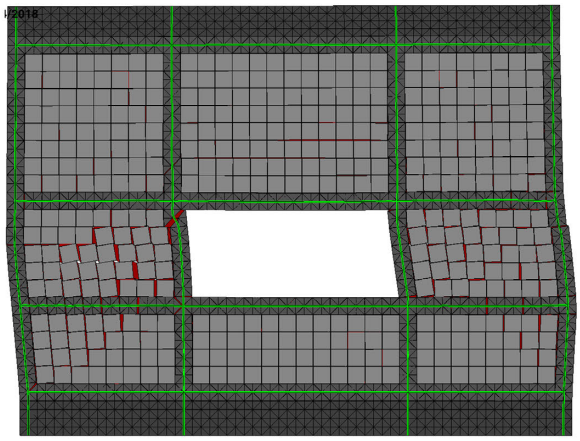

Peak negative displacement

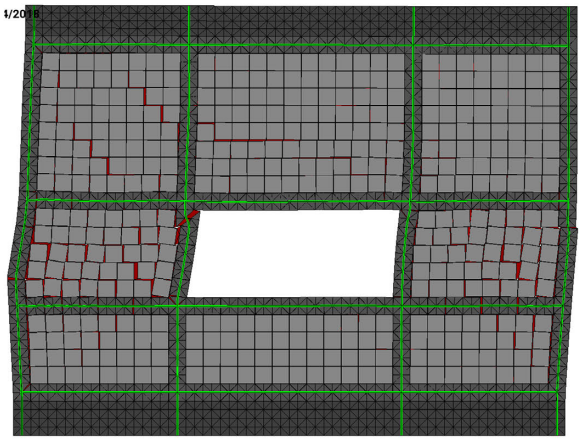

Peak positive displacement

Figure 4.16 Comparison of numerical and experimental results for wall SRU (deformation magnified by 5 times).

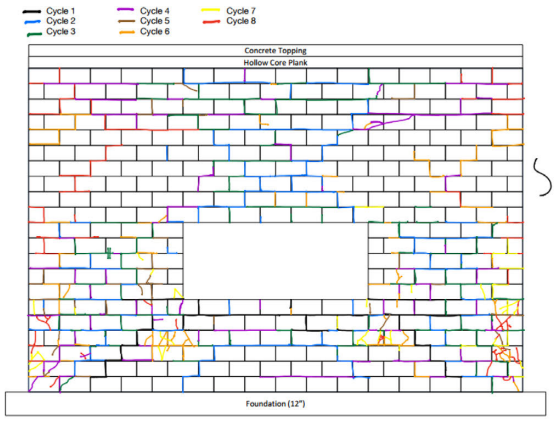

Damage in test

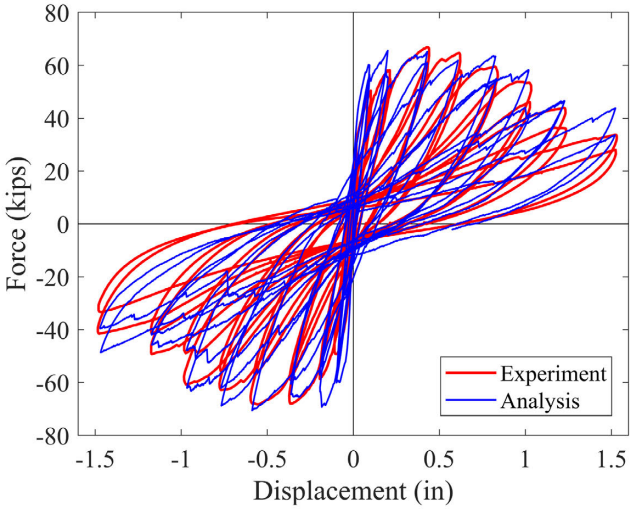

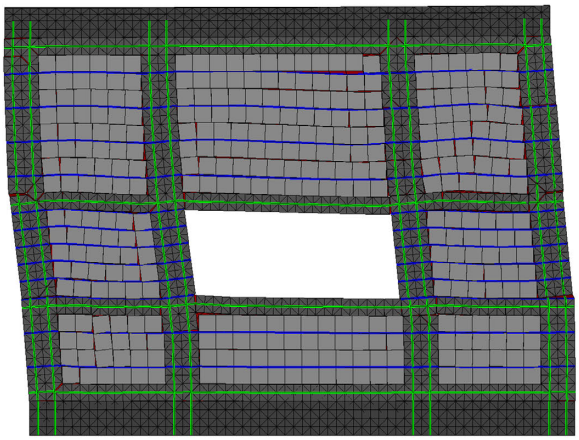

Peak negative displacement

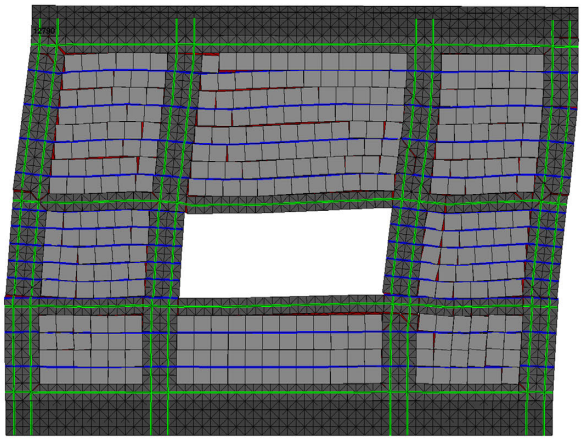

Peak positive displacement

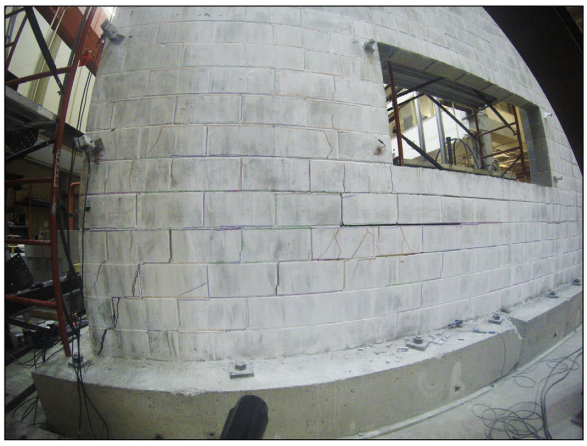

Damage in left pier

Figure 4.17 Comparison of numerical and experimental results for wall DRU (deformation magnified by 10 times).

5 SHAKE-TABLE TESTS OF A PARTIALLY GROUTED REINFORCED MASONRY BUILDING WITH TYPICAL REINFORCEMENT DETAILS

5.1 Introduction

Most of the previous experimental studies of partially grouted masonry (PGM) were limited to quasi-static cyclic tests of wall segments. Some experimental results showed that the previous and current shear-strength equations in TMS 402 could be unconservative for PGM walls when the spacing of the reinforced vertical cells is large, way over 4 ft (Minaie et al. 2010; Nolph and Elgawady 2012; Bolhassani et al. 2016a, 2016b). In some other studies, these equations appeared to be adequate even for walls with widely spaced reinforced vertical cells (Maleki 2008; Johnson and Schultz 2014). The behavior of PGM wall systems designed according to current standards in the U.S. under realistic earthquake load conditions has not been well studied. Shake-table tests conducted on fully grouted masonry wall systems revealed that a wall system could behave very differently than what was assumed in the design. For example, coupling forces exerted by horizontal diaphragms on shear walls could alter the behavior of a wall from the intended ductile flexural mode to a more brittle shear mode (Stavridis et al. 2016). In addition to the coupling forces, axial restraints exerted by walls orthogonal to the direction of the seismic action could change the axial forces in the walls parallel to the seismic force and thereby their resistance mechanism (Mavros et al. 2016).

This chapter presents the results and findings from the shake-table tests of a full-scale, one-story, PGM structure designed with the current code provisions and reinforced according to current practice. The experimental results are complemented with a numerical study. A nonlinear finite element model is developed using the modeling scheme presented in the previous chapter. The

model is validated with the test results, and is used to understand the load resistance mechanisms of the structure, the distribution of the shear resistance among the wall components, and the influence of bond beams on the seismic performance. The numerical results are also used to evaluate the shear-strength equation of the current code.

Based on TMS 402 (2016), the shear strength (V_n) of a PGM wall is calculated by the equation

$$V_n = \left(V_{nm} + V_{ns}\right)\gamma_g \tag{5.1}$$

in which V_{nm} is the shear resistance provided by masonry and calculated by

$$V_{nm} = \left[4.0 - 1.75\frac{M_u}{V_u d_v}\right] A_{nv}\sqrt{f'_m} + 0.25P_u \tag{5.2}$$

and V_{ns} the shear resistance provided by the shear reinforcement and calculated by

$$V_{ns} = 0.5\left(\frac{A_v}{s}\right) f_y d_v \tag{5.3}$$

The shear strength V_n should not be taken greater than $V_{n,\max}$ which is given by

$$V_{n,\max} = \begin{cases} \left(6A_{nv}\sqrt{f'_m}\right)\gamma_g & \text{for } M_u/\left(V_u d_v\right) \le 0.25 \\ \left(4A_{nv}\sqrt{f'_m}\right)\gamma_g & \text{for } M_u/\left(V_u d_v\right) \ge 1.00 \end{cases} \tag{5.4}$$

In the above equations, $\gamma_g = 0.75$ for PGM wall (while $\gamma_g = 1.00$ for fully grouted walls), A_{nv} is the net shear area of the wall, A_v is the cross-sectional area of shear reinforcement, *s* is the spacing of the shear reinforcement, d_v is the wall length in the direction of shear, $M_u/V_u d_v$ is the shear-

span ratio, and P_u is the axial load on the wall taken to be positive for compression and negative for tension.

5.2 Prototype Building and Specimen Design

5.2.1 Prototype building configuration

Figure 5.1 shows the prototype structure considered in the experimental study. It has one story and a building plan representative of industrial or commercial buildings in North America. The structural system consists of gravity frames in the outer area and reinforced masonry walls in the central part. The masonry walls are arranged in four modules, each designed to carry seismic forces as well as gravity loads. The roof consists of 6-inch thick precast hollow-core planks with a 2-inch cast-in-place concrete topping. Each masonry wall module carries a tributary gravity load of 76 kips from the roof, and has a tributary seismic weight (W) of 401 kips, which includes the weight of 1/4 of the entire roof and the self-weight of the masonry walls above the level of the window sills. The walls are partially grouted and were designed as ordinary load-bearing shear walls for SDC C according to ASCE/SEI 7 (2010) and TMS 402 (2013). The design spectral intensity is $S_{DS} = 0.5g$ and the seismic response modification coefficient is $R = 2$. Hence, the resulting design base shear for each wall module was $V_b = 100$ kips.

5.2.2 Design of test structure

As shown in Figure 5.1, the test structure represented one of the four masonry wall modules. It was symmetric about the center lines in the east-west and north-south directions, and had a door opening and a window opening in each of the south and north walls. The structure was tested on a shake table with the table motion applied in the east-west direction only. As shown in Figure 5.1 and Figure 5.2a, the wall components separated by openings are labeled as W1, W2,

and W3 on the south side, and W4, W5, and W6 on the north side. Each of the corner walls, W1, W3, W4, and W6, had an L-shaped cross section, and each of the middle walls, W2 and W5, had a T-shaped cross section. Lintels spanned along the north-south direction between W1 and W4, W2 and W5, and W3 and W6. The masonry walls had a height of 152 in. and a nominal thickness of 8 in. Figure 2 shows the exterior and interior of the test structure. As shown in Figure 5.2a, the whole panel consisting of W2 and W3 (or W5 and W6) including the window up to the elevation of the top of the window opening is referred to as the Main Wall, and the masonry panel above the openings is identified as the Top Panel.

For ordinary walls, shear-capacity design is not required by TMS 402. For the given wall configuration, one or more of the wall components were expected to be dominated by shear. A shear-dominated wall with light horizontal reinforcement may lose its lateral load resistance quickly after reaching the peak shear strength. Hence, it was prudent to assume in the design that the base-shear capacity of the structure would be reached when the shear demand on any of the shear-dominated wall components reached its shear strength. The design was assisted with an elastic analysis based on this premise. The resulting reinforcement details for the test structure are illustrated in Figure 3. The vertical and horizontal reinforcement consisted of Grade 60 #4 bars. The reinforcement met the prescriptive requirements of the code in that the area of the vertical reinforcement adjacent to the openings and wall intersections was at least 0.2 in.^{2}, and the vertical and horizontal bar spacing did not exceed 120 in. The building had four bond beams along the height. One was in the first course above the footing, the second and third were right below and above the window opening, and the fourth was in the upper-most course right below the roof. The bond beam in the top course was required to secure the dowel bars used to tie the roof diaphragm to the masonry walls. The bond beam at the bottom course was introduced to provide a better

performance (e.g., to reduce base crushing) if the walls were to develop base sliding. While the code requires that bond beams be placed right below and above a window or door opening, they need not be extended continuously along the entire wall length unless they are required to resist shear. For this structure, the two intermediate bond beams were not required to resist shear but they were deemed beneficial for resisting the strut action that could be developed by the ungrouted masonry panels.

The roof system consisted of 8-in-thick precast hollow-core planks with a 4-inch cast-in-place RC topping. It was much thicker than that of the prototype to attain the targeted roof weight of 76 kips without the need to include the tributary roof area outside the wall module. The actual seismic weight of the test structure was 120 kips. It included the weight of the roof and that of the masonry walls above the level of the window sills.

5.2.3 Supporting analysis

The reinforcement details were verified using an elastic analysis. Because of the symmetry of the structure, only the wall on one (the south) side was considered. A linearly elastic plane-frame model, as shown in Figure 5.2c, was employed to calculate the seismic force demand wall components W1, W2, and W3. Elastic Timoshenko beam elements were used to represent the wall components, while the Top Panel and the portion of W3 below the window sill were assumed to be rigid. For W1 and W2, the reinforcement in the two lower bond beams would contribute to the shear strength, while no bond beam would be present in W3 based on the wall height assumed. The net cross-sectional areas of the walls were considered. For calculating the flexural strengths of the walls, the entire flange width was considered effective, which complied with the code specification for the flange in tension (TMS 402). The equivalent lateral load was distributed in the way shown in Figure 5.2c, with V_1 proportional to the weight of one-half of the roof slab and

applied at the level of the roof, V_2 proportional to the weight of the Top Panel and half of the transverse lintels and applied at the mid-height of the Top Panel, and V_3 proportional to the weight of the walls between the Top Panel and the window sill and applied at the top of the door opening. This was based on the assumption that the roof and the Top Panel displaced as a rigid body. Forces V_2 and V_3 only account for 8.3% and 2.7% of the total base-shear demand.

The lateral seismic forces were applied in the positive and negative directions. The compressive strength of masonry was specified to be 1.83 ksi based on the net area of the walls. Table 5.1 shows the seismic load demands on W1, W2, and W3 when the lateral load applied to the entire structure is equal to the design base shear of 100 kips, the capacities of the wall components calculated according to the code-specified methods, and the capacity-to-demand ratios. It can be seen that all wall components were shear-dominated apart from W1, which was flexure dominated when subjected to positive loading. Furthermore, W3 had a capacity-to-demand ratio slightly greater than 1.0, while the other two wall components had much higher ratios. Hence, W3 controlled the design.

5.3 Construction, Material Properties, and Instrumentation

The walls of the test structure were constructed on RC footings that were post-tensioned onto the shake-table platen. Figure 5.4 shows pictures of the construction. The top surface of the footings was not intentionally roughened. The walls were constructed by masons and the whole construction took 12 days to complete. Standard 8 x 8 x 16 in. concrete masonry units (CMU) were used for the ungrouted part of the walls, double open-end units (H-blocks) were used for the bond beams, and open-end and half open-end units were used at the locations having vertical grouted cells. For both the head and bed joints, mortar was applied only at the face shell of the blocks. The units were laid in a running bond pattern with interlocking at the intersections of the orthogonal

walls at the four corners of the structure (see Figure 5.4b). However, the orthogonal walls in the middle of the structure were simply connected through the reinforcing bars in the bond beams without interlocking units (see Figure 5.4c and Figure 5.4d). The horizontal bars in the bond beams extended from the web into the flange with 90-degree bents, while standard 180-degree hooks were used at the wall ends. During construction, every bond beam course was grouted together with the vertical reinforced cells below. A net was placed under each bond-beam course (see Figure 5.4a) to prevent the grout from flowing into the cavity below. The vertical bars were lap-spliced above the footings over a length of 24 in, which was more than the minimum length specified in the code, while the horizontal bars were lap-spliced at the locations shown in Figure 5.3. The precast roof planks spanned along the north-south direction and were simply supported on the south and north walls (see Figure 5.4f). After the placement of the planks, the vertical dowel bars from the walls were bent 90 degrees. After the placement of reinforcement in the north-south and east-west directions on the planks, the concrete topping was poured.

Coarse grout with 3/8-in. aggregate and Type S mortar were used for the construction of the masonry walls. Material samples were taken during the construction and were tested during the period of the shake-table testing at an age exceeding 28 days. Compression tests were conducted on 2 x 4 in. mortar cylinders, 3.75 x 3.75 x 7.625 in. grout prisms prepared per ASTM C1019, grout cylinders, two-unit tall grouted and ungrouted masonry prisms per ASTM C1314, single CMU blocks, and concrete cylinders sampled from the footing concrete and the roof topping. All masonry prisms were prepared with half CMU blocks as shown in Figure 5.4e. The average compressive strength obtained for each sample type is summarized in Table 5.2. Furthermore, tension tests were conducted on samples of the reinforcing bars used in the masonry

walls. The average yield strength obtained was 70 ksi, and the average tensile strength was 100 ksi and was attained at a strain of 0.113.

The shake-table test structure was instrumented with an array of 393 sensors, consisting of 177 strain gages, 177 displacement transducers, and 39 accelerometers. The strain gages were attached on the vertical and horizontal reinforcing bars at locations where yielding could occur. The location of strain gages on the south wall are shown in Figure 5.5a. Linear potentiometers were used to measure sliding along bed joints and uplift of the walls at select locations. They were also mounted vertically along the two sides of W1 and W4 to determine the curvature along the height of these walls. Sliding at the base of the structure was also monitored with linear potentiometers installed along the base of the walls. The horizontal displacement of the roof with respect to the footings of the walls was measured at the top of the north and south walls with two string potentiometers (one per side). The potentiometers were installed at the top bond-beam course and the strings were attached to steel reference frames, which were 3.75 m (148 in) tall and mounted on the concrete footings. The acceleration at the base and the roof was measured with accelerometers placed on top of the footings and the roof slab, respectively. The instrumentation scheme for the south wall is shown in Figure 5.5b. The complete instrumentation plan can be found in Koutras and Shing (2015). In addition to the conventional sensors, the deformations of the walls on the north and west sides of the structure were monitored with a digital image correlation (DIC) system using high-speed cameras. However, the system was only employed for a limited number of tests before any major structural damage occurred. Further details on the DIC system are presented in Rajaram et al. (2017). Figure 5.6 shows pictures of sensors mounted on the walls, and the north and west sides of the structure that were painted in a black and white pattern for the DIC measurements.

5.4 Ground Motions and Scaling

The test structure was subjected to a sequence of 17 earthquake motions, referred to as Motions 1 to 17, which were historical records that were scaled to different intensity levels. The north-south component of the El Centro record from the 1940 Imperial Valley Earthquake (EC1940) was used in most of the tests. In addition, the El Centro Array #5 record component 140 from the 1979 Imperial Valley Earthquake (EC1979) was used for Motions 2 and 3, and also two records obtained from earthquakes outside the West Coast, which were the transverse component of the North Anna Nuclear Power Plant (NPP) record from the 2011 Mineral, Virginia Earthquake and the component 10 of the Nahanni Station #1 from the 1985 Nahanni Earthquake, were used for Motions 1, 7, and 10. These ground motion records have acceleration spectra with a shape similar to the shape of the design spectrum of ASCE/SEI 7 (2010). Before Motion 1 and after each earthquake motion, the structure was subjected to white-noise excitation with a root-mean-square amplitude of 0.05g to identify any change in the natural period. The initial fundamental period ($T_{initial}$) of the structure was identified to be 0.043 s. The transfer function of the structure was identified as the ratio of the Fourier amplitude of the average acceleration response history measured at the roof to the Fourier amplitude of the average acceleration measured at the footing with overlapping time windows.

The estimated actual seismic weight of the test structure was $W_{spec} = 120$ kips, while the seismic weight considered in the design of the wall module based on the prototype configuration was $W = 401$ kips. The difference is due to the tributary weight carried by the gravity columns, which was not included in the test structure. For the test structure to satisfy the dynamic similitude with the prototype, the applied base acceleration in the tests was scaled up by a factor of

$F_a = W/W_{spec} = 3.33$ and the time was compressed by a factor of $F_t = \left(1/F_a\right)^{0.5} = 0.55$. This time scaling was applied to the ground motion records prior to the construction of the specimen for the tuning of the shake table. The actual seismic weight of the test structure as constructed was calculated to be 125.8 kips, which was slightly higher than the initial estimation. Figure 5.7 shows the original ground motion records used in the tests after the similitude scaling was applied. The records are scaled to the Design Earthquake (DE) and their spectra are compared to design spectrum of ASCE/SEI (2010), which is also scaled according to the similitude law. The scaling to the DE is performed by matching the spectral acceleration of the record at the initial period of structure to the spectral acceleration of the design spectrum. A damping ratio of 5% is assumed for the response spectra. The fundamental period of the structure had been accurately predicted prior to test by a preliminary finite element model. The motions that used the EC1979, Mineral and Nahanni records did not induce any discernible damage to the structure and therefore are omitted from the following discussion. Figure 5.8 shows the time history of Motion 17 and compares the response spectra of Motions 8 and 17, which were obtained by the accelerometers placed on the footings of the test structure, to the spectra for the Maximum Considered Earthquake (MCE) and the DE, which were also scaled according to the similitude law. The MCE is 1.5 times the DE. The shake table was tuned with ground motions scaled to the DE with the procedure described in Luco et al. (2010). However, as the intensity of the motions increased, the table did not track the input motion closely, and the response spectra of the table motions showed a significant amplification in the frequency range of 10-20 Hz, where the resonance frequency of the oil column of the shake table resided. To quantify the intensity of the table motions in a meaningful manner, the ratio of the spectral acceleration of the table motion to the MCE spectral acceleration is used as an effective intensity measure (I_{eff}). The ratio is calculated as the average

value over the range of the structural period measured before and after the structure was subjected to the ground motion (Stavridis et al. 2012).

5.5 Structural Response and Analysis of Test Data

Testing was conducted in two phases. In Phase 1, the structure was tested in its original configuration. After a number of tests and before the walls reached their flexural or shear capacities, the response started to be dominated by the sliding of the Main Walls at the base. To restrain sliding in the subsequent tests, RC blocks (stoppers) were cast against the bottom course of the Main Walls on both sides, as shown in Figure 5.9. The subsequent tests are referred to as Phase 2. Some minor damage induced in Phase 1 near the toes of the Main Walls was repaired with grout patch. Rubber pads were placed between the concrete stoppers and the wall toes to allow for a uniform distribution of the contact forces. Before the first Phase-2 test, the fundamental period of the structure was measured to be 0.056 s, which was slightly longer than the fundamental period of 0.043 s measured at the beginning of Phase 1 indicating that the masonry walls had not sustained major damage. Table 5.3 shows the sequence of the major tests conducted in Phase 1 and all the tests in Phase 2, for which the EC1940 record was used, and summarizes peak response quantities along with the effective intensity of the motions and the value of the structural period measured after each test. It should be noted that the peak response quantities shown for each motion shown are not necessarily concurrent. For the calculation of the net roof drift ratio shown in the table and subsequent figures, the average sliding measured at the base of the Main Walls was subtracted from the roof displacement. The net roof drift was divided by the clear height of the roof, which was 152 in., to obtain the drift ratio. The base shear shown in the table is calculated from the measured roof acceleration considering the mass of the structure above the window sills, which is consistent with how the design base shear was determined. The change of the structural

period during Phase 1 and Phase 2 is shown in Figure 5.8c. The decrease of the structural period at the beginning of Phase 2 was mainly due to the repairs at the toes of the Main Walls.

5.5.1 Response in Phase 1

In Phase 1, the structure was subjected to twelve motions, which had the effective intensity I_{eff} ranging from 0.36 to 1.91. The structure developed sliding at the base when the effective intensity of the applied motion reached the MCE level (i.e., when I_{eff} was around 1.0). In the first eleven motions, no discernible damage was observed in the masonry walls, yet the sliding measured at the base of the Main Walls was consistently larger than that for W1 and W4. During Motion 12, which was the most demanding motion in Phase 1 with I_{eff}=1.91, the sliding at the base of the Main Walls increased drastically reaching 0.25 in, which was almost equal to the peak roof displacement, as shown in Table 5.3. The sliding at the base of W1 and W4 was much smaller and diagonal cracks formed in their webs. No significant damage was observed in the Main Walls apart from some fine cracks forming along mortar joints and the spalling of the grouted cells at the wall toes caused by the base sliding. Almost identical sliding displacements were obtained at the three transducer locations along the base of each Main Wall. Sliding was not observed in the wall flanges. Instead, fine stair-stepped cracks developed along mortar joints near the base of the flanges. The cracks propagated diagonally along the flange width and extended from the flange-web intersection at the base to the fourth or fifth course. Figure 5.10 shows the damage in the web of W4 after Motion 12, and compares the sliding response histories measured at the base of W4 and the north Main Wall to the total horizontal displacement response history measured at the roof during Motion 12. For the Main Wall, the average sliding measured by three transducers is shown. Figure 5.11shows the cracks formed on the south wall and wall flanges during Phase 1.

Figure 5.12 shows the shear force at the base plotted against the base sliding registered at the Main Walls during Motions 5 and 9. Both motions did not cause any visible cracking in any of the masonry walls, and Motion 5 was the motion during which base sliding initiated. The shear force in the figure is the total lateral force transmitted to the base of the structure and is calculated as the sum of the inertial force developed by the roof slab and the total inertial force by the walls. The figure shows a large shear force developed in the positive direction during an early cycle in Motion 5. The shear-friction resistance can be largely attributed to the clamping force exerted by the vertical reinforcement. However, as the grout surrounding the dowels at the wall base got damaged, the bond between the dowels and the grout deteriorated leading to a reduction of the clamping force and thereby a drop in the shear-friction resistance at the same displacement level in the subsequent cycles. The small increase in the shear resistance as sliding increased in one direction could be attributed to the restoring forces developed by W1 and W4 and the wall flanges, as well as the dowel action.

According to TMS 402 (2016), the shear-friction strength (V_{nf}) for walls with a low aspect ratio is given by $V_{nf} = \mu\left(A_{sp}f_y + P_u\right)$, where μ is the coefficient of friction, P_u is the axial load, and $A_{sp}f_y$ is the total area of vertical reinforcement crossing the sliding plane, excluding that in the wall flanges, times the yield strength, accounting for the clamping force of the vertical reinforcement crossing the sliding plane. Applying this formula here, only the 14 #4 vertical bars in the in-plane walls need to be considered. With the assumption that the coefficient of friction μ is 0.7, as recommended in TMS 402 (2016) for masonry walls laid on concrete surface that was not intentionally roughened, the formula results in a sliding resistance of 234 kips, which is very close to the maximum sliding resistance developed during Motion 5, as shown in Figure 5.12.

However, it should be noted that the wall flanges and dowel action could also contribute a little shear resistance once sliding had started. Furthermore, it should be noted that not all the vertical reinforcement crossing the sliding plane yielded during Motion 5. The strains in the vertical reinforcement measured 1 in. above the footing surface were in the range of 30% - 100% of the yield strain.

5.5.2 Response in Phase 2

In Phase 2, the structure was subjected to five motions with effective intensities above the MCE, as shown in Table 5.3. With the stoppers installed, the maximum sliding reached at the base of the Main Walls was 0.08 in. and was due to the deformation of the rubber pads that had been placed between the stoppers and the wall toes. At the maximum base shear, which was reached during Motion 16, the peak base sliding in the Main Walls constituted 24% of the total peak roof displacement. However, at the maximum roof drift, which was reached in Motion 17, the last run, the peak base sliding of the Main Walls was only 1% of the total roof displacement. The structure withstood Motions 14 and 15, which had effective intensities more than two times the MCE, without showing signs of major damage. Fine cracks developed mainly along mortar joints of the Main Walls in a stair-stepped pattern and diffused minor cracking developed in ungrouted and grouted masonry units. Similar level of damage was observed in Motion 16 with the peak net roof drift ratio reaching only 0.18%. Figure 5.13a and Figure 5.11 show the state of the structure after Motion 16 and the corresponding crack patterns. During Motion 17, the existing cracks propagated through the vertical grouted cells causing a rapid load degradation. A maximum net roof drift ratio of 2.25% was reached, which was accompanied by severe cracking of the vertical grouted cells, and cracking and crushing of ungrouted units, as shown in Figure 5.13b and Figure 5.13c. It appears that among the wall components, W3/W6 were the first ones to develop the most severe

damage and the other walls followed. By the end of Motion 17, severe damage had occurred in the grouted cells, and most of the ungrouted units within the height of the window openings in the Main Walls and below the mid-height of W1/W4 were damaged and dislocated from the walls, leaving large openings. The wall flanges experienced heavy damage too; yet, they were able to carry the weight of the roof after the end of the test averting total collapse of the building.

Figure 5.14 shows the time histories of the net roof drift ratio and the hysteresis curves obtained during Motions 16 and 17. The maximum base shear developed in the positive direction was 285 kips, which occurred in Motion 16 at 0.13% net roof drift. In the negative direction, the maximum base shear reached was 254 kips. During Motion 17, severe load degradation occurred within the first few cycles before the structure reached a net roof drift of 0.4%. The damage resulted in a significant reduction of the lateral stiffness, which led to large displacement oscillations even under very low base acceleration towards the end of the input motion (see Figure 5.8a), as shown by the response history after the first 20 s in Figure 5.14. At the time of the maximum net roof drift of 2.25%, the structure had lost about 50% of the maximum base-shear resistance in the positive direction. The drift ratio experienced by the Main Walls was 4% because most of the wall deformation concentrated below the top panel. This drift level is much higher than that reached in any of the previous experimental studies on PGM walls; yet the test structure was still able to retain a significant residual lateral strength, which was almost equal to 50% of the peak base shear, in its first major excursion in the positive direction. The resistance dropped significantly upon displacement reversal and in subsequent cycles due to the loss of masonry from the walls.

5.5.3 Yielding of reinforcement

The sequence of yielding in the reinforcing bars as recorded by the strain gages is illustrated in Figure 5.15. Only the information for the south wall and the connected flanges is shown since a similar yielding sequence was observed in the walls on the north side. The motion during which each strain gage registered yielding for the first time is indicated. The gages that did not record yielding as well as the faulty ones are also indicated. For brevity, the sequence of yielding during the different motions in Phase 1, as well as during Motions 13 through 16, is not identified. During the Phase-1 tests, the vertical bars yielded along the base of the wall due to tension induced by base sliding. In Phase 2, most of the additional yielding occurred during Motion 17. However, the yielding of the reinforcement in the 2nd bond beam (from the base) of W2 and W3 was first observed in Motion 16, during which the maximum base shear was reached.

Figure 5.16 shows the strains plotted against the net roof drift obtained during Motions 16 and 17 in the 2nd bond beam of W2 and W3 at the locations H1 and H2 marked in Figure 5.15. During Motion 16, the strains barely exceeded the yield strain. Furthermore, the plots show that the reinforcement in the 2nd bond beam of W3 was engaged primarily during drift in the positive direction (towards east). This could be because for positive drifts, diagonal shear cracks intercepted the bond beam, whereas for negative drifts, the shear cracks were localized within the panel next to the window. For the same reason, the bond beam of W2 was engaged when the drift was towards the negative direction. During Motion 17, the strain in the reinforcement of the bond beam of W3 increased drastically until the net roof drift reached 0.5% in the positive direction. Beyond that drift, the deformation of W3 localized in the masonry panel next to the window, which is consistent with the damage shown in Figure 5.13. Figure 5.16 also shows the strains developed in the two vertical bars in W6 at locations V1 and V2 indicated for W3 in Figure 5.15. The bars developed

significant strains after the net roof drift reached 1%, which was in the post-peak regime of the base shear-vs.-net roof drift curves.

5.6 Numerical Analyses of the Behavior of the Test Structure

The maximum base shear developed in the tests was 2.8 times the design base shear. The fact that the actual material strengths for the test structure were higher than the nominal strengths, and the strength reduction factors introduced in the design can only explain part of this overstrength. The main contributing factor is the conservative design assumption that the capacity of the structure was limited by the capacity of walls W3/W6, while W1/W4 and W2/W5 had reserve capacities, as shown in Table 5.1. To acquire a better understanding of the lateral load resisting mechanism of the structural system, a detailed finite element (FE) model has been developed for the test structure. The model is used to examine the lateral resistance developed in each wall component, which is hard to deduce from the test data. Nonlinear time-history and nonlinear static (pushover) analyses are conducted. The modeling assumptions and numerical resutls are presented in the following sections.

5.6.1 Modeling approach and material properties

Figure 5.17 shows the FE model developed in LS-DYNA for the analysis of the test structure using the modeling scheme presented in the previous chapter. Because of the symmetry of the structure and the loading, only the south half of the structure is modeled, with the nodes at the plane of symmetry free to translate and rotate only within the plane of symmetry. The grouted and ungrouted parts are modeled with the discretization scheme presented in the previous chapter. The grouted cells are modeled with triangular smeared-crack shell elements that have a 4-in. long vertical and horizontal side and cohesive-crack interface elements are placed in the 45-degree angles as well as in the horizontal and vertical directions. Each ungrouted CMU is represented

with two 8 x 8 in. smeared-crack cell elements that are connected through a vertical cohesive-crack interface element to model possible splitting cracks through the unit. The mortar joints are modeled in a discrete fashion with horizontal and vertical shell elements. The cohesive-crack interface elements have the interface formulation presented in the previous chapter. The proposed formulation accounts for the void in the hollow CMU when modeling discrete cracks through the CMU or mortar joints. The reinforcing bars are modeled with 2-in. long beam elements that are connected to the adjacent smeared-crack shell elements through bond-slip/dowel-action interface elements. The same discretization scheme is used for both the in-plane and out-of-plane walls. The vertical interface elements between the grouted and ungrouted masonry assume the properties of ungrouted masonry units, which are perceived to constitute the plane of weakness. This is assumed because the vertical grouted cells of the test structure had been constructed with open-end blocks that allowed for the grout to be in contact with the web of the adjacent ungrouted CMU, as shown in Figure 5.4b. However, the vertical interface elements between the in-plane wall and the ungrouted panels of the middle flange assume the properties of the mortar joints since in the actual structure there was no unit interlocking between the middle flange and the in-plane wall. The element removal scheme that has been described in the previous chapter and has been used in the analysis of the quasi-static wall tests is also used in the analyses of the shake-table test structure.

The footings and the roof slab are modeled with elastic shell elements. The walls are connected to the footings through cohesive-crack interface elements, while stiff elastic interface elements are used to connect the walls to the roof slab. The lap-splices at the bottom of the walls are modeled explicitly. However, the 180-degree hooks and the 90-degree bends of the horizontal bars around the vertical bars are considered in an approximate manner by directly attaching the node of the horizontal bar to the node of the vertical bar. The weights of the roof slab and of the

masonry walls are distributed over the respective areas. Since the roof planks were initially supported only by the in-plane walls during construction (see Figure 5.4f), the interface elements that are placed between the slab and the out-of-plane walls are activated in the analysis after the vertical loads have been applied.

The material models of the smeared-crack shell elements, cohesive-crack interface elements, bond-slip/dowel-action interface elements, and reinforcing steel beam elements have a number of parameters that need to be specified. The values of the materials parameters used for the analyses of the test structure are summarized in Table 5.4 to Table 5.7. These values are in general determined in a way consistent with that for the analyses of the quasi-static wall tests. Some generic parameters assume the same values while the values of other parameters are determined based on the strengths of the material samples using the same relations as those used for the quasi-static wall tests. In the analyses of the test structure, due to the significant difference between the compressive strengths of grouted masonry prisms and grout prisms, the tensile strength of grouted masonry in the model is taken to be 12% of the average of the compressive strength of the grout (6.1 ksi) and that of the grouted masonry prisms (2.6 ksi). The tensile strength of the CMU is assumed to be 12% of the compressive strength of the CMU (3.2 ksi). For the same reason, in determining the bond strength of the bond-slip model, the average of the compressive strengths of the grout and the masonry prisms is used. For calculating the dowel strength, the compressive strength of the grout is used.

5.6.2 Nonlinear time-history analysis

The time-history analysis is performed with the implicit time-integration scheme proposed by Bathe (2007). The scheme has a desirable numerical damping characteristic to suppress spurious high-frequency modes that could be induced by the sudden stress release caused by the

cracking of masonry. Additionally, Rayleigh damping is prescribed with a damping ratio of 0.1% for the first and second modes. The initial fundamental period and second-mode period of the model are calculated to be 0.044 s and 0.033 s, respectively. The stiffness proportional part of the damping is based on the initial stiffness of the shell and beam elements. However, for the cohesive-crack and bond-slip/dowel-action interface elements, no stiffness proportional damping is applied because of their high initial stiffness. It should be mentioned that the mass of the model is 6% higher than that of the test structure because of the meshing scheme.

Ground motion histories measured at the base of the structure during the shake-table tests are used for the time-history analysis. Since the structure did not sustain any major damage during Phase 1, only the Phase-2 tests are considered. Instead of explicitly modeling the concrete stoppers, the surface of the footings is assumed to be sufficiently rough to prevent base sliding. To this end, a coefficient of friction of 1.0 is used in the cohesive-crack interface elements placed along the base. The structure is subjected to Motions 13 and 17 in a single run. Motion 14 through 16 are not considered because the damage observed in the analysis with Motion 13 is slightly more severe than that obtained with Motion 15 in the test. Figure 5.18 compares the net roof drift time histories and the hysteresis curves obtained from the analysis and the tests. For Figure 5.18a, only the response for the first 10 s is shown for clarity. The lateral resistance is calculated by summing the shear forces developed in the horizontal interface elements at the top of the second bond beam course (the level of the window sill) and the shear forces developed by the dowel action of the vertical reinforcement at the same elevation. This is consistent with the method used to calculate the seismic force from the experimental data by considering only the seismic mass above that line. The damage obtained during the analysis is shown in Figure 5.19.

Under Motion 13, the model develops a maximum lateral drift that is about 2.4 times the net drift attained by the actual test structure under the same motion. This is because the base sliding developed in the test comprised almost 50% of the total horizontal displacement measured at the roof, while in the analysis, base sliding is prevented. As Figure 5.18a shows, the peak lateral drift obtained in the analysis with Motion 13 is in-between the values obtained for Motions 15 and 16 in the tests. The model, however, predicts well the base-shear capacity of the test structure. For Motion 17, the model captures the response in the first 10 s of the motion, and is also able to reproduce the rapid loss of lateral resistance observed in the test. However, for the rest of the motion, it overestimates the stiffness and thereby the response frequency of the structure. This could be attributed to the less severe damage induced in the vertical grouted cells and wall flanges of the model as compared to the actual test structure (see Figure 5.13 and Figure 5.19). Nonetheless, the analysis captures the extent of damage in the ungrouted panels of the in-plane walls reasonably well. As in the test, the crushing and removal of the shell elements occurred primarily after reaching the maximum positive roof drift.

5.6.3 Distribution of forces among wall components

To gain insight into the distribution of the seismic force among the wall components and also the lateral load capacity of each wall component, a pushover analysis is performed with the FE model. The displacement is applied at the level of the roof, in the positive and negative directions (as defined in Figure 5.2). Figure 5.20 compares the shear and axial forces developed in each wall component at the level of the window sill. The total lateral resistance of the structure and the total vertical load are also shown. The axial force in each wall is calculated by summing the normal forces in the horizontal interface elements in the web and the flange of the wall and the forces of the vertical bars. It can be observed that the pushover analysis shows a more gradual load

degradation and a higher peak resistance than the time-history analysis (as compared in Figure 5.18). However, for the positive direction, the difference in the strength is small (with 293 kips versus 272 kips).

The numerical results show that W1/W4 and W3/W6 develop a higher strength in the respective loading direction that induces axial compression, while the resistance of W2/W5, the middle wall components, shows a very small difference in the two loading directions, as the axial load is always compressive but varies in magnitude. Figure 5.21 shows the deformed meshes obtained for each loading direction. It can be seen that the diagonal cracks in W2 spread along the height of the window for positive loading, but those associated with negative loading spread over the height of the door opening. Wall component W3 behaves in the opposite way. The analysis shows that the horizontal reinforcement in the 2nd bond beam of W3 is engaged only when the building is subjected to positive loading. This behavior is consistent with what was observed in the tests. Yielding in the reinforcement of the bond beam occurs before the structure develops its maximum load capacity. The reinforcement eventually ruptures at a roof drift ratio of 2.5%.

To evaluate the code provisions, the shear and flexural strengths of each wall component are calculated with the methods recommended in TMS 402 using the axial force developed in the pushover analysis at the peak lateral resistance of each wall component. The wall components are assumed to have fixed-fixed end conditions. Based on the observations from the pushover analysis and the tests, different heights are assumed for each of W2 and W3 depending on the direction of loading. For positive loading, W2 is assigned the height of the window and W3 the height of the door. For negative loading, W2 is assigned the height of the door and W3 the height of the window. The height of W1 is assumed to be the same as the door opening. The masonry prism strengths and the yield strength of the steel reinforcement obtained from the material tests are used. The

shear capacity is calculated based on the ungrouted masonry prism strength, while the flexural capacity is based on both the ungrouted and grouted masonry prism strengths depending on the wall cross-sectional area under compression.

Table 5.8 shows the code-based shear strength (V_n) and flexural strength (V_{flex}) as compared to the wall strengths obtained from the pushover analysis. Based on the code-based capacities, W2 and W3 are shear dominated for both loading directions, while W1 is shear dominated for negative loading and flexure dominated for positive loading. The shear-strength equation of TMS 402 overestimates the capacity of W3 by 14% when the building is subjected to negative loading and W3 is under tension. For the rest of the shear-dominated cases, the code equation gives a lower value. The difference between the code value and the numerical result is higher for W1 under negative loading and for W3 under positive loading. This could be due to the beneficial influence of the wall flange, which enhances the shear-compression resistance at the wall toe but is ignored by the code. Furthermore, assuming that W3 has the height of the door opening when the building is subjected to positive loading is also a conservative hypothesis. For W1 loaded in the positive direction, the code-based flexural capacity is slightly higher than the analysis result. This can be explained by the mixed flexural-shear mode developed by W1 in the pushover analysis and also by the fact that the top of W1 is not perfectly fixed in reality but is assumed to be fixed in the calculation.

The results obtained from the pushover analysis reveal that the distribution of the shear resistance among W1, W2, and W3 is different from that assumed in the design, which was based on an elastic analysis (see Table 5.1). The design assumed that the capacity of the system was reached once the shear capacity of one wall component was reached. Based on this premise, the design was governed by the shear capacity of W3 for both loading directions. For the negative

loading direction, the pushover analysis shows that W3 indeed reaches its load capacity before W1 and W2 because it is subjected to tension; however, the capacity of W3 is relatively small and the wall is able to maintain a portion of its resistance as the displacement increases. The capacity of the structure is reached when both W1 and W2 almost reach their capacities as shown in Figure 5.20. At that point, the two wall components together provide 87% of the lateral load resistance of the structure. For loading in the positive direction, the analysis shows that the maximum load resistance of the structure develops when W2 reaches its peak strength. In this case, W2 together with W3 provide 90% of the maximum total load resistance. Wall component W1 that is in tension reaches its maximum load after W2 and W3 have lost their peak strengths. For either loading direction, the wall component in tension provides only a small portion of the lateral resistance. However, the wall component in tension contributes to a higher axial compression in the other two wall components, and therefore, indirectly enhances the shear resistance of the structure.

5.6.4 Influence of bond beams

As previously discussed, the wall components would still meet the design load demand and the prescriptive requirements of TMS 402 even if the first and second bond beams (from the base) were not present, as long as there was a bond beam right under each of the window openings. To evaluate the influence of the continuous bond beams on the performance of the structure, two code-compliant design alternatives are considered. The first alternative has the bond beam under the window openings extend only 24 in. beyond the left and right sides of the openings rather than through the entire length of the Main Walls. Furthermore, the second bond beam in W1/W4 is removed. The second bond beam is also removed from all the wall flanges except for the middle flange, which requires a bond beam to connect to the Main Wall because the wall joint has no interlocking masonry units. This design is referred to as the Intermediate Design. The second

alternative is the same as the first but has all the bond beams at the base course (except for that in the middle flange) removed as well. This is referred to as the Minimum Reinforcement Design.

To compare the two alternative designs with the original design of the test structure, time-history analyses are performed with FE models representing the three designs using the original 1940 El Centro record scaled by a factor of 1.6. This motion corresponds to a spectral intensity of 1.22 times the MCE at the fundamental period of the model. The ground motion is scaled to comply with the dynamic similitude with the prototype building. Similar to the previous analyses, the interface between the wall and the footing is assumed to be rough. Figure 5.22 compares the response histories and load-displacement hysteresis curves. The damage induced for each case is shown in Figure 5.23. One can see that the second bond beam can significantly improve the performance of the structure. It provides a horizontal tie to effectively confine the ungrouted masonry. The influence of the bond beam at the base is not as significant but it is still beneficial in that it slightly reduces the drift level. However, the Intermediate Design, which includes the base bond beam, has more crushing in the ungrouted masonry, resulting in a more extensive element removal than the Minimum Reinforcement Design. Base sliding is not observed in any case.

5.7 Summary and Conclusions

This chapter presents an experimental and numerical study on the seismic performance of a partially grouted reinforced masonry structure. The structure was designed according to the current code provisions in the U.S. for areas of moderate seismicity and design details conforming to current practice. It had a single story and widely spaced vertical grouted cells and bond beams. The design of the masonry walls was based on an elastic frame model and the assumption that the capacity of the wall system would be reached when one of the shear-critical wall components first

reached its shear capacity. The structure was tested on a shake table with a sequence of ground motions of progressively increasing intensity. Under an MCE-level motion, the structure developed a response dominated by base sliding. The sliding resistance calculated with the shear-friction equation in TMS 402 (2016) using a coefficient of friction of 0.7 closely matches the shear-friction resistance deduced from the test data. In the second phase of testing, base sliding was restrained with RC stoppers, and the test structure developed its ultimate load capacity showing fine cracks along the mortar joints and some limited yielding of the reinforcement in the bond beams. The base-shear capacity reached by the structure was 2.8 times the design base shear. In Phase 2, the structure was able to withstand four motions with an effective intensity above the MCE level before failing in a brittle manner. Two of the motions had an effective intensity two times the MCE. The structure exhibited sudden load degradation at a roof drift of about 0.4%. However, it was able to maintain almost 50% of its lateral load capacity at a roof drift of 2.25%, which corresponds to a local drift ratio of 4% for the Main Walls.

The behavior of the structure has been further studied with nonlinear FE analyses. The FE model gives a reasonable prediction of the response histories and the strength of the structure, as well as the load degradation observed in the tests. A pushover analysis has been conducted to investigate the contribution of the wall components to the lateral load capacity of the structural system. The analysis shows that the elastic frame model used in the design did not give the correct load distribution among the wall components. Furthermore, it shows that the shear-dominated wall components are able to retain a substantial portion of their load capacities at displacements beyond the point of their peak lateral resistance. This allows different wall components of the structure to develop significant lateral resistance at the same time, and the resistance continues to increase as the axial compressive loads in the walls increase, resulting in a base-shear capacity much higher

than the design base shear (2.8 times). The numerical results have also been used to assess the shear-strength equation of TMS 402 (2013, 2016). It has been found that the shear strength of the wall components calculated with the code equation is slightly lower than those given by the FE model, except for wall components W3/W6 when they are subjected to tension. The results also indicate a possibility that the wall flange might improve the shear resistance when it is in compression. Furthermore, the FE analyses show that the continuous bond beams right below the window openings appear to significantly improve the performance of the structure. The benefit of a bond beam in the first course above the footing is negligible.

Even though conservative, the assumptions used to design the structure appear to be adequate considering the brittle behavior exhibited in the tests after the roof drift exceeded 0.4%. The overstrength factor of 2.8 is close to the value of 2.5 suggested in ASCE/SEI 7 for ordinary load-bearing reinforced masonry shear walls. In spite of the fact that the shear-strength equation in TMS 402 has been found to be adequate when compared to the FE analysis results for this structure, further studies are needed to understand why it overestimates the shear capacities of PGM wall components tested in some other studies. In particular, the influence of the spacing of grouted cells, and of the wall aspect ratio and boundary conditions should be investigated. The behavior of PGM structures under bidirectional earthquake excitation should also be studied. Developing design details that can improve the ductility of partially grouted wall systems is also worthwhile for future investigation. The next chapter presents the design, testing, and numerical analyses of a second shake-table test structure that has design details introduced to improve the ductility of the structure.

Parts of Chapter 5 are a reprint of the material that appears in the manuscript “Koutras A, Shing PB. Seismic Behavior of a Partially Grouted Reinforced Masonry Structure: Shake-Table

Testing and Numerical Analyses" which has been submitted for publication to the Journal of Earthquake Engineering and Structural Dynamics in 2019. The author of this dissertation was the primary investigator and author of this manuscript.

Table 5.1 Load demands versus capacities of the wall components in the two lateral directions (positive is east) of the masonry building.

Wall	Axial load, P_u (kips)		Lateral load demand, V_u (kips)		Flexural capacity, V_{flex} (kips)		Shear capacity, V_n (kips)		Capacity-to-demand ratio, min(V_{flex}, V_n)/V_u	
	Neg.	Pos.	Neg.	Pos.	Neg.	Pos.	Neg.	Pos.	Neg.	Pos.
W1	30.8	7.3	9.0	9.0	47.0	35.3	36.7	37.3	4.08	3.91
W2	25.0	18.2	18.7	18.8	109.1	99.3	65.9	65.5	3.53	3.49
W3	4.3	34.6	22.4	22.3	74.3	107.5	25.9	30.8	1.15	1.38

Note: Strength factors of 0.9 and 0.8 were used in the calculation of the flexural and shear capacities, respectively. Axial loads with positive sign represent compression.

Table 5.2 Average compressive strengths obtained from material samples.

Sample	Strength (ksi)	Sample	Strength (ksi)	Sample	Strength (ksi)	Sample	Strength (ksi)
Mortar cylinder	4.0	Grout prism	6.1	Ungrouted prism	2.0	Concrete footing	6.3
Grout cylinder	4.2	Grouted prism	2.6	CMU block	3.2	Concrete roof	4.7

Table 5.3 Summary of structural response during the tests.

Motion No.	Test ID (EC1940 record)	Testing phase	Specimen period after test (s)	Eff. Intensity I_{eff} (x MCE)	PGA (g)	Peak roof accel. (g)	Peak roof disp. (in)	Peak base sliding (in)		Peak net roof drift ratio (%)	Peak base shear (kips)
								W1	Main Walls		
1	Mineral 127%	Phase 1	0.043	0.53	-1.09	1.25	-0.01	0.00	0.00	-0.01	157.3
2	EC1979 51%		0.045	0.36	0.66	0.89	-0.01	0.00	0.00	-0.01	-111.9
3	EC1979 77%		0.045	0.49	0.93	1.19	-0.01	0.00	0.00	-0.01	-149.3
4	125%-A		0.046	0.81	-1.36	-1.37	-0.03	0.00	0.00	-0.02	172.4
5	188%-A		0.049	1.05	-1.91	-1.96	0.06	0.01	-0.03	0.02	246.1
6	84%-A		0.049	1.15	0.94	-1.73	0.08	0.01	0.03	0.03	218.1
7	Nahanni 22%		n.a.	n.a.	0.64	-1.37	0.06	0.01	0.02	0.03	172.9
8	84%-B		0.050	0.69	0.95	-1.30	0.06	0.01	0.03	0.04	158.8
9	125%-B		0.051	1.23	1.33	-1.79	0.11	0.03	0.06	0.04	225.2
10	Nahanni 33%		0.052	1.89	-1.06	1.79	0.09	0.02	-0.06	0.03	-224.8
11	125%-C		0.052	1.46	1.29	-1.79	0.16	0.05	0.09	0.05	225.7
12	164%-A		0.066	1.91	-1.73	-1.94	-0.28	-0.06	-0.25	0.06	244.3
13	125%-D	Phase 2	0.062	1.52	-1.49	-1.98	0.17	0.08	0.07	0.06	248.5
14	164%-B		0.066	2.04	-1.88	-2.16	0.22	0.10	0.07	0.10	272.0
15	188%-B		0.097	2.07	-2.09	-2.22	0.26	0.13	-0.08	0.13	278.7
16	202%		0.118	1.43	-2.16	-2.27	-0.35	0.16	-0.08	-0.18	285.2
17	214%		n.a.	1.17	-2.24	-2.21	3.44	0.28	-0.07	2.25	277.8

Note: Test ID indicates the scaling of the original record in addition to the similitude scaling. Apart from Motions 1, 2, 3, 7, and 10, the EC1940 record was used for all motions. The letter A, B, C, or D next to the percentage indicates the 1st, 2nd, 3rd, or 4th time the same motion was applied. Motions 4 and 5 had the positive and negative directions flipped as compared to the other records.

Table 5.4 Material parameters for smeared-crack shell elements (see Figure 2.8 for the parameter definitions).

Shells elements	f_m **(ksi)**	f_o **(ksi)**	E_m **(ksi)**	f_t **(ksi)**	ε_0	ε_u	**Net width (in)**
Grouted masonry	2.64	1.76	1584	0.50	0.003	0.040	7.625
Ungrouted units	2.03	1.35	1920	0.38	0.003	0.015	2.8

Table 5.5 Material parameters for cohesive-crack interface elements (see Section 2.5.2 for the parameter definitions).

Interface elements	D_{nn} / D_{tt} **(ksi/in)**	s_o **(ksi)**	μ_o / μ_r	r_o / r_r **(ksi)**	$G_{f,I}$ **(kips/in)**	$G_{f,II}$ **(kips/in)**	$\zeta_{dil,o}$ / $\zeta_{dil,r}$	d_o **(in)**	**Net width (in)**
Grouted masonry	5000	0.50	1.4 / 1.0	0.05 / 0.01	0.0004	0.004	0.4 / 0.001	0.4	7.625
Ungrouted units	5000	0.38	1.4 / 1.0	0.05 / 0.01	0.0004	0.004	0.2 / 0.001	0.2	2.8
Mortar joints	300 / 125	0.10	0.95 / 0.85	0.02 / 0.01	0.0002	0.002	0.10 / 0.001	0.035	2.5
Base interface	5000	0.20	1.00 / 1.00	0.05 / 0.01	0.0002	0.002	0.4 / 0.001	0.4	7.625

Table 5.6 Material parameters for beam elements representing reinforcing steel (see Section 2.6 for the parameter definitions).

Size	f_y **(ksi)**	f_u **(ksi)**	E_s **(ksi)**	ε_{sh}	$(\varepsilon_{sh1}, f_{sh1})$	ε_u	D_{cr}
#4	69.7	100	29000	0.01	(0.03, 84)	0.12	0.55

Table 5.7 Material parameters for bond-slip/dowel-action interface elements (see Section 2.7.3 for parameter definitions).

Masonry compressive strength used for bond strength (ksi)	**Confinement condition**	**Grout compressive strength used for dowel strength (ksi)**	**Displacement parameters for dowel law, d_l / d_u (in)**
4.3	Confined	6.1	0.03 / 0.06

Table 5.8 Comparison of lateral load capacities of the wall components based on TMS 402-16 with capacities from the finite element model.

Wall	**V_{max} analysis (kips)**		**P_{Vmax} analysis (kips)**		**Shear span ratio**		**Effective hor. reinf.**		**V_{flex} TMS 402 (kips)**		**min(V_n,$V_{n,max}$) TMS 402 (kips)**		**min(V_n,$V_{n,max}$, V_{flex})/V_{max}**	
	Neg.	**Pos.**	**Neg.**	**Pos.**	**Neg.**	**Pos.**	**Neg.**	**Pos.**	**Neg.**	**Pos.**	**Neg.**	**Pos.**	**Neg.**	**Pos.**
W1	67.8	26.0	76.9	-10.4	0.55	0.55	2 #4	2 #4	102.8	28.1	50.9	38.2	0.75	1.08
W2	79.2	80.9	26.1	26.9	0.29	0.13	2 #4	None	136.9	304.0	76.3	70.8	0.96	0.88
W3	29.0	66.8	-9.2	66.2	0.25	0.55	None	2 #4	64.1	93.9	33.1	50.9	1.14	0.76

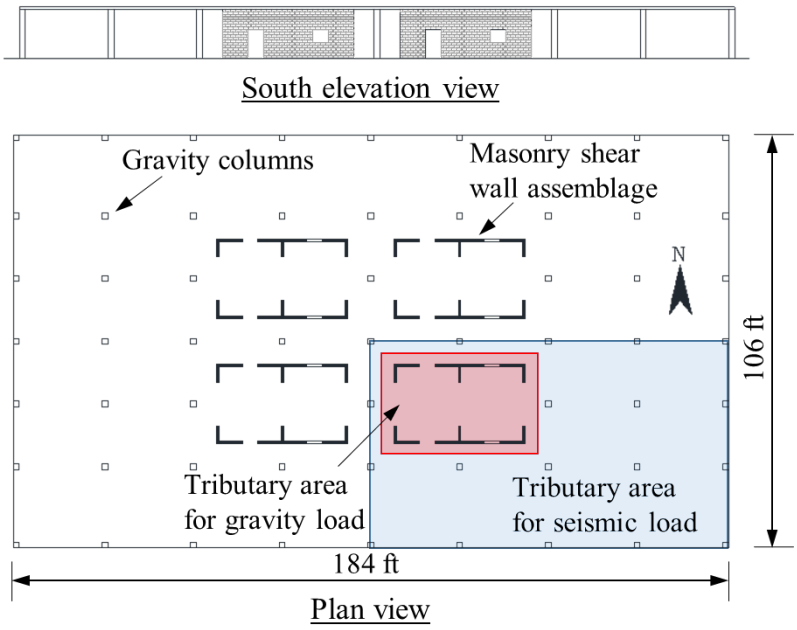

(a) Prototype building

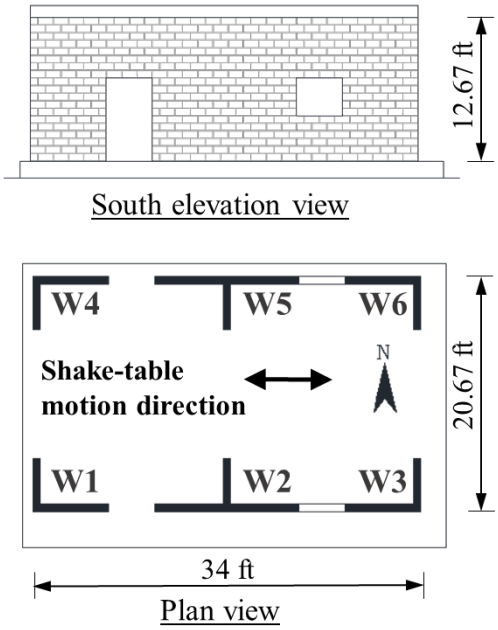

(b) Test structure

Figure 5.1 Prototype building and reinforced masonry test structure.

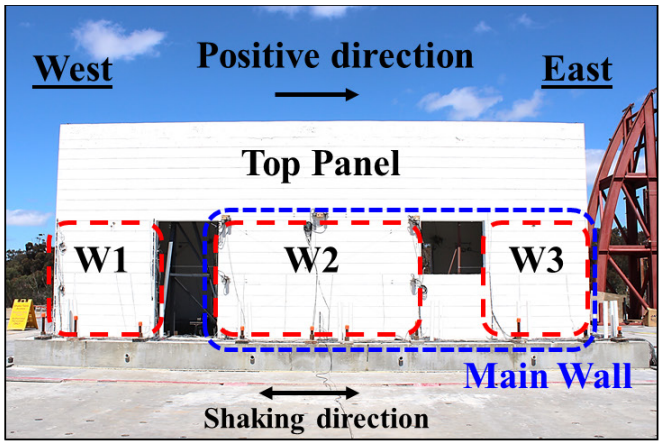

(a)

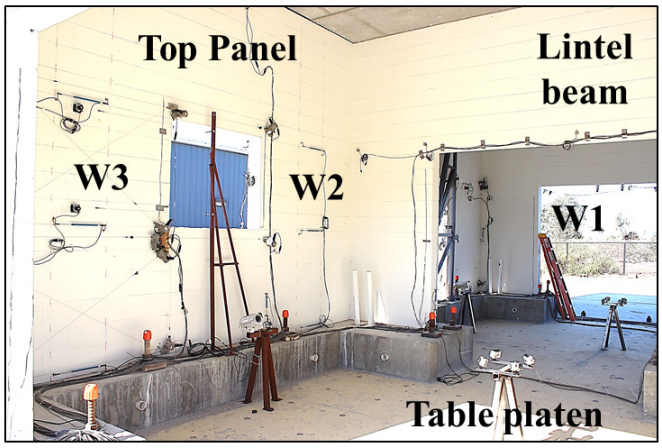

(b)

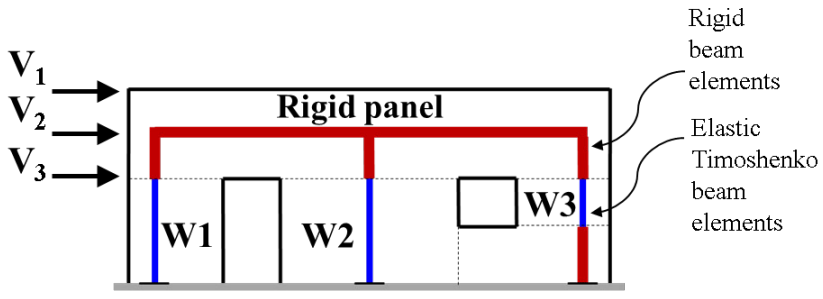

(c)

Figure 5.2 Shake-table test specimen and frame model used for the design. (a) South view of specimen; (b) south-east view of interior of specimen; (c) plane frame model.

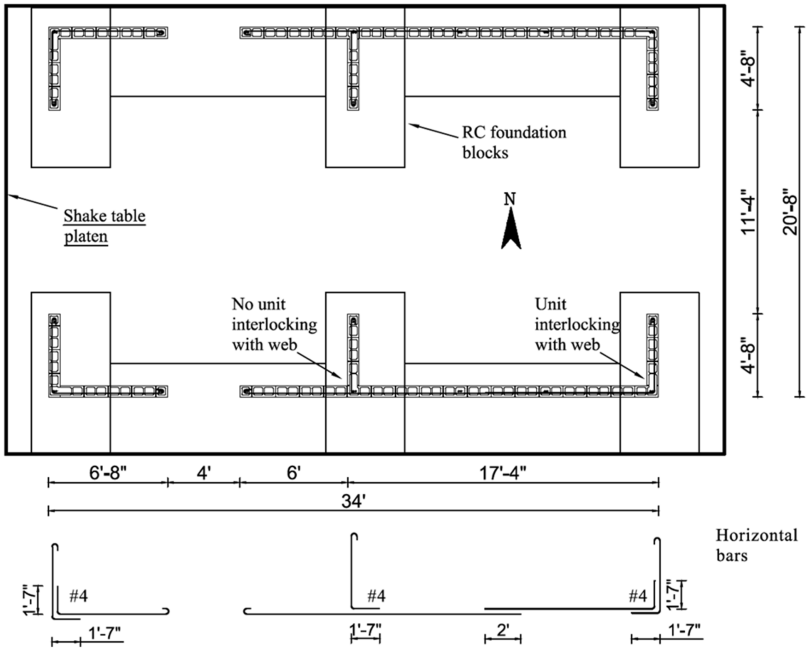

(a) Plan view (base grouted course)

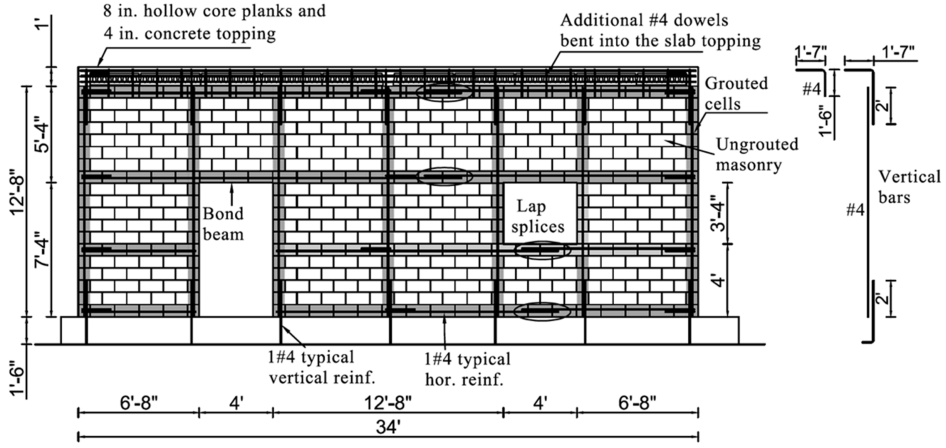

(b) South elevation view

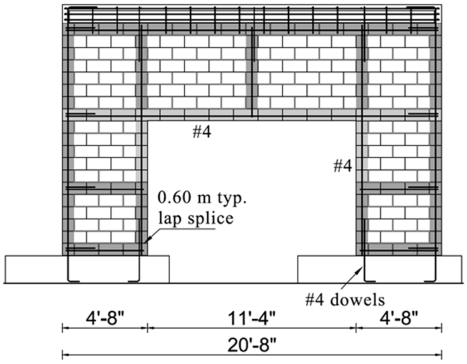

(c) East elevation view

Figure 5.3 Reinforcement details of test specimen.

Figure 5.4 Construction of the structure on the shake table. (a) Construction of the second bond beam course; (b) construction of a corner wall; (c) grouting of the second bond beam in a T-wall; (d) south main wall under construction; (e) grouted and ungrouted masonry prisms; (f) placement of the precast hollow-core roof planks.

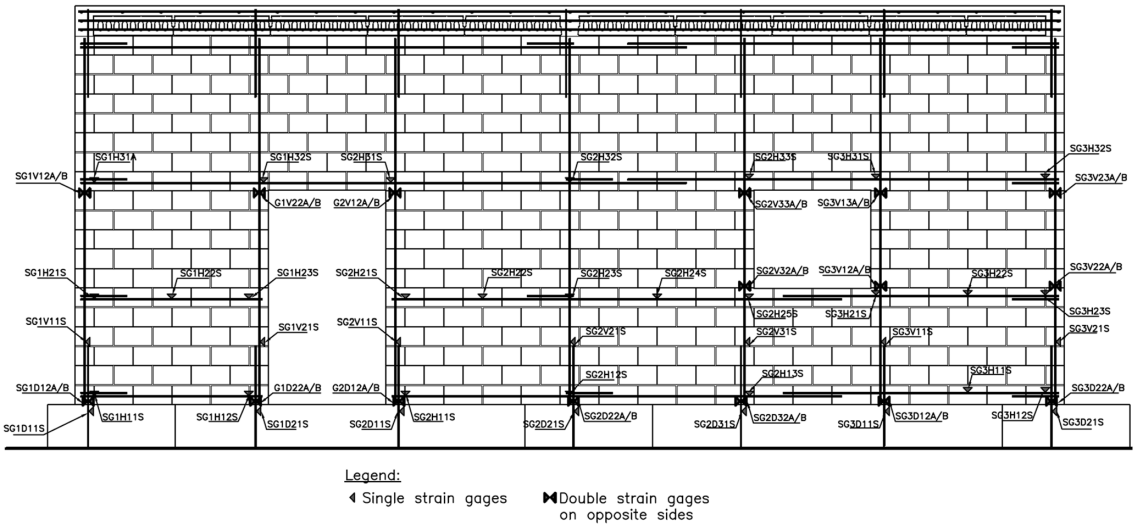

(a)

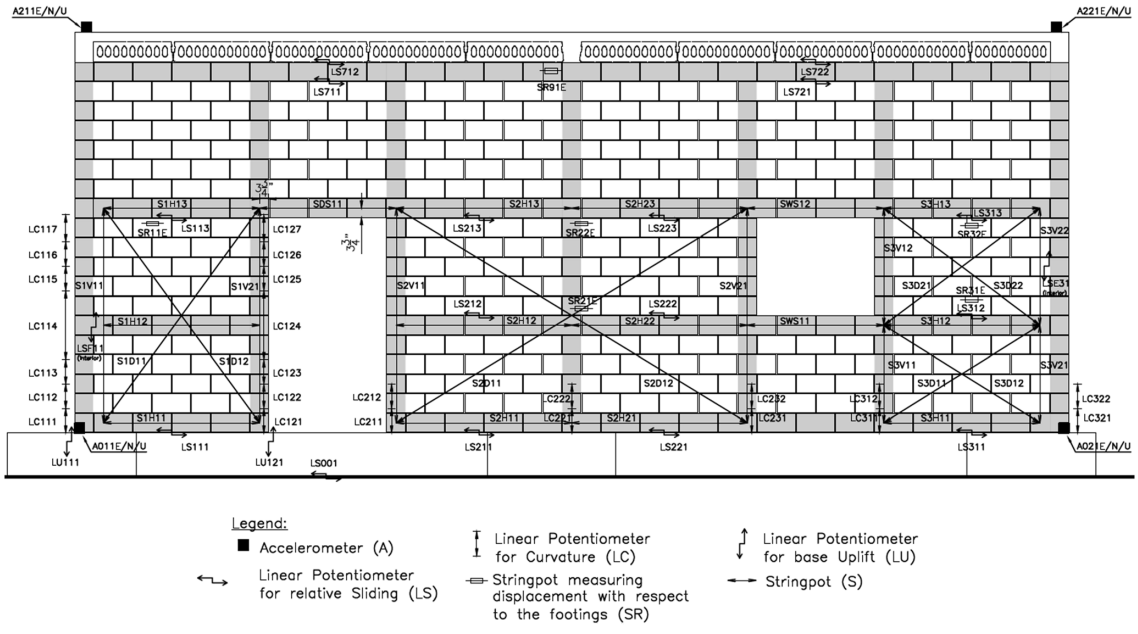

(b)

Figure 5.5 Instrumentation plan for the south wall. (a) Strain gages; (b) displacement transducers and accelerometers.

(a)

(b)

(c)

Figure 5.6 Instrumentation of test structure. (a) Displacement transducers mounted on the north wall; (b) displacement transducers mounted on W1; (c) north and west elevation monitored using the DIC system.

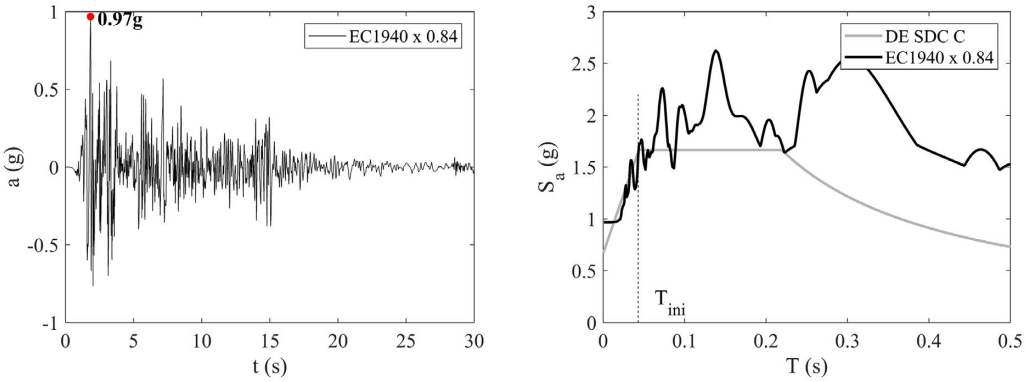

(a) El Centro record, 1940 Imperial Valley Earthquake

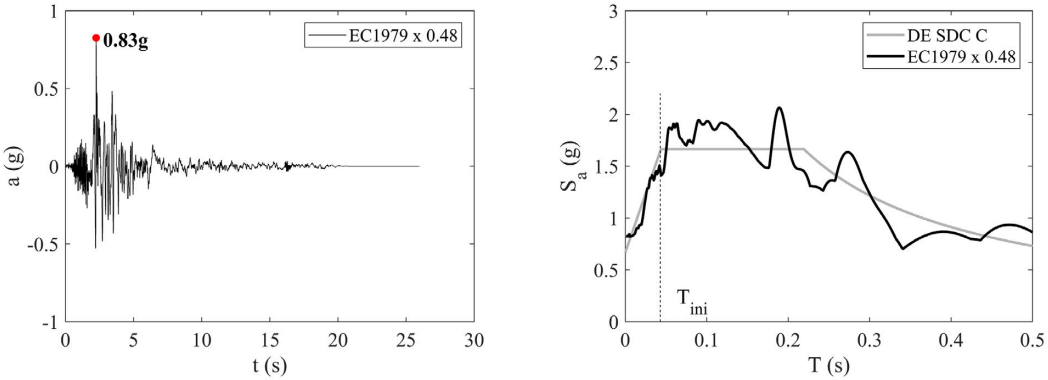

(b) El Centro record, 1979 Imperial Valley Earthquake

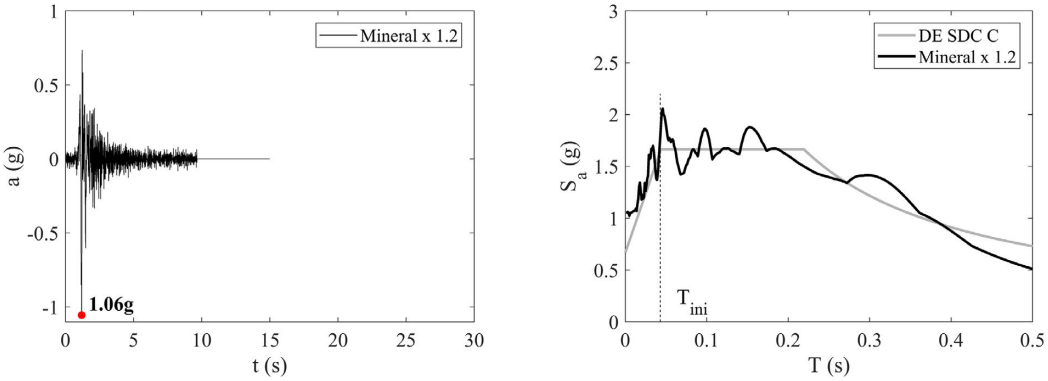

(c) NPP record, 2011Mineral Earthquake

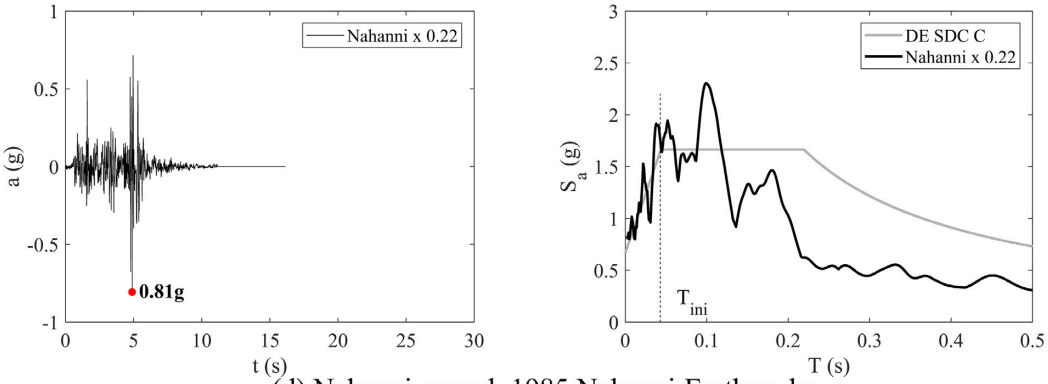

(d) Nahanni record, 1985 Nahanni Earthquake

Figure 5.7 Earthquake records scaled to the DE including similitude scaling.

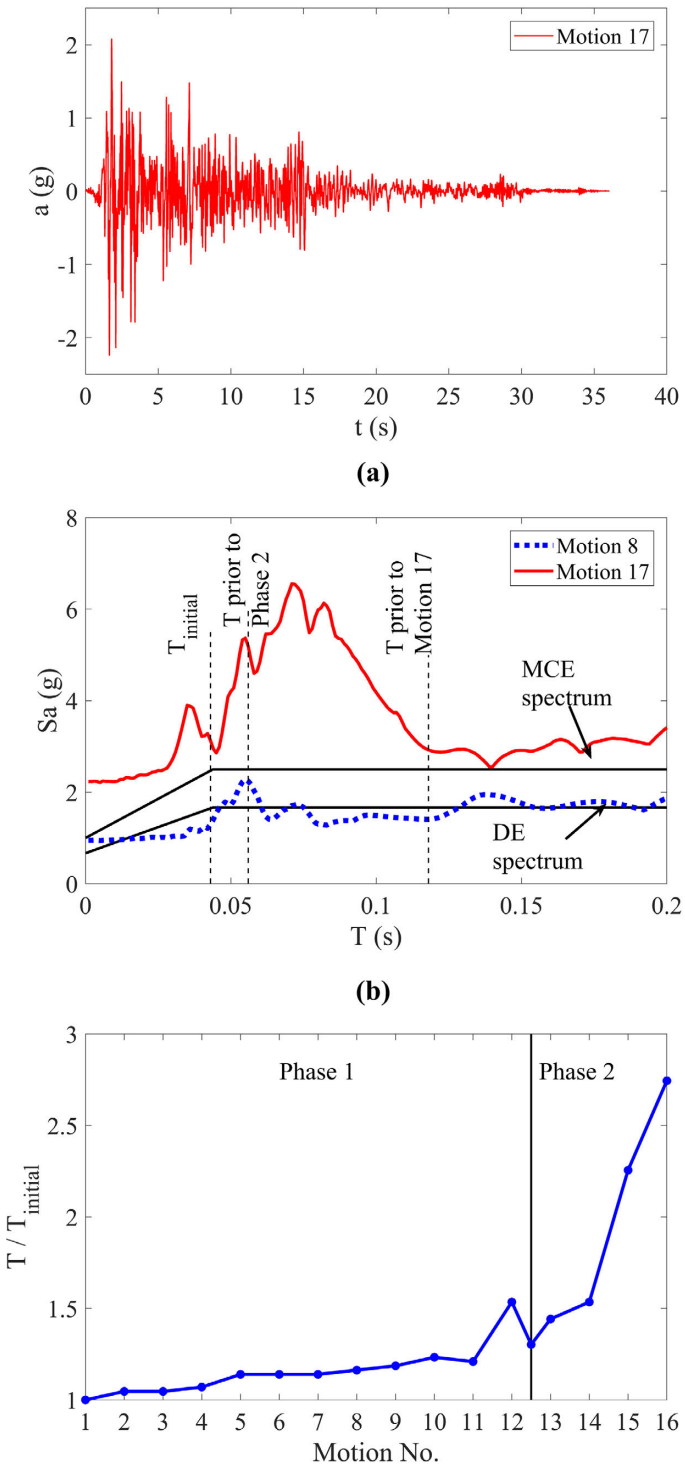

Figure 5.8 Sample ground motions and structural period change. (a) Acceleration time history of Motion 17; (b) acceleration response spectra of Motions 8 and 17; (c) structural period change during the test sequence.

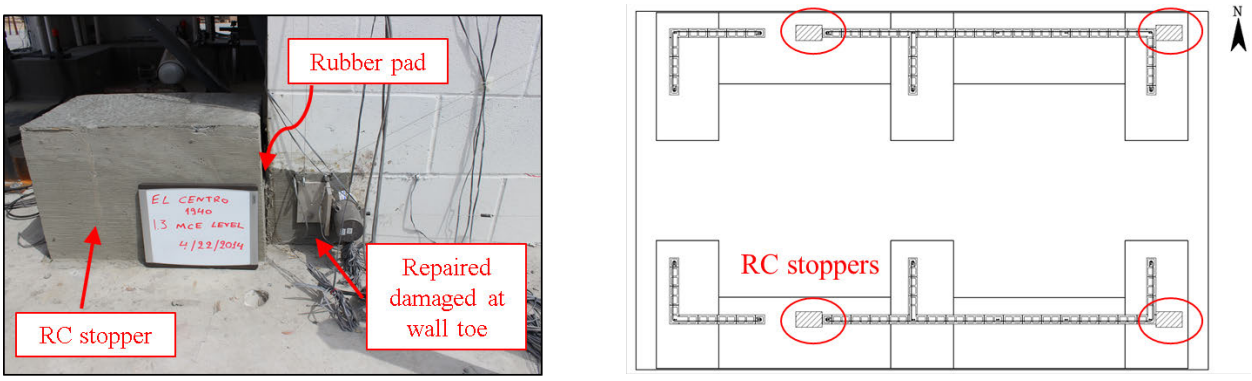

(a) **(b)**

Figure 5.9 Concrete stoppers installed after Phase-1 tests. (a) Stopper near a toe of a Main Wall; (b) locations of stoppers.

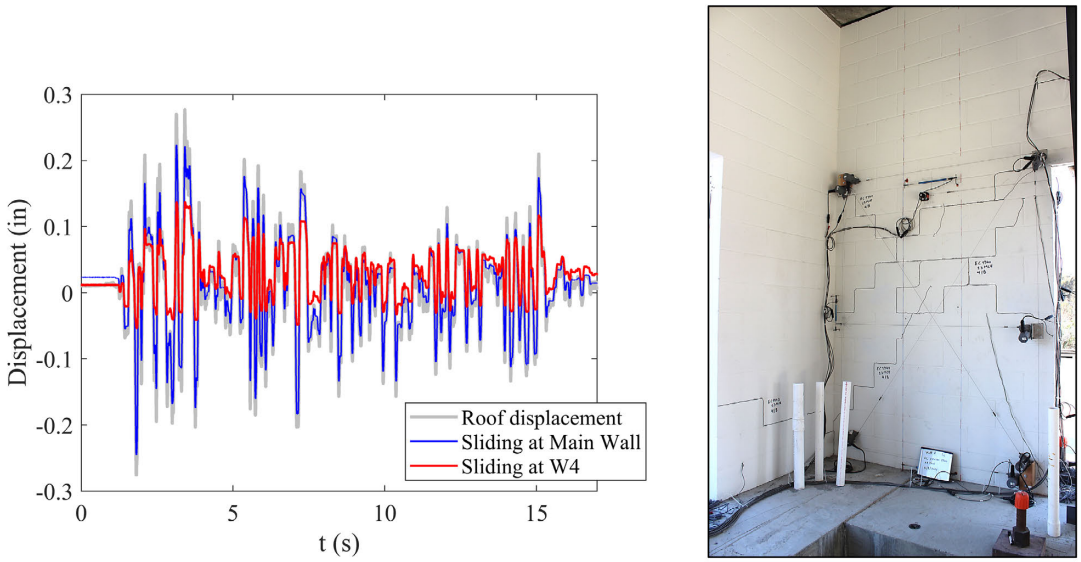

(a) **(b)**

Figure 5.10 Response to Motion 12. (a) roof displacement response history and sliding at the base of north wall; (b) damage in W4.

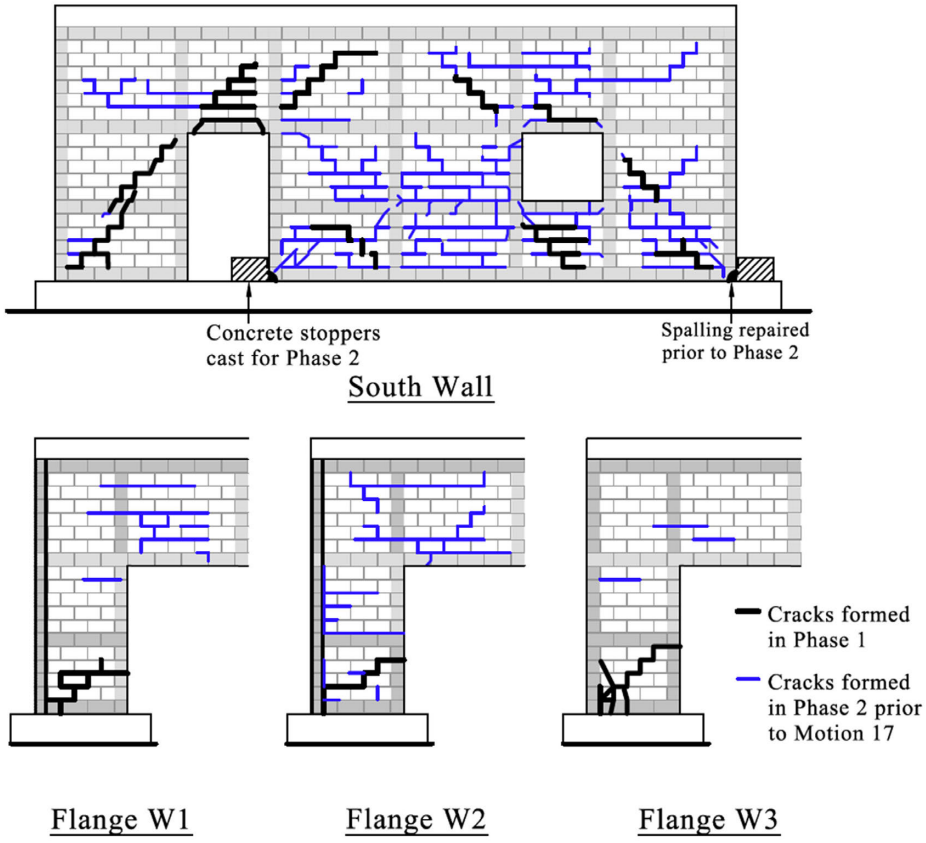

Figure 5.11 Cracks formed in the south wall and wall flanges in Phase 1 and Phase 2 up to Motion 16.

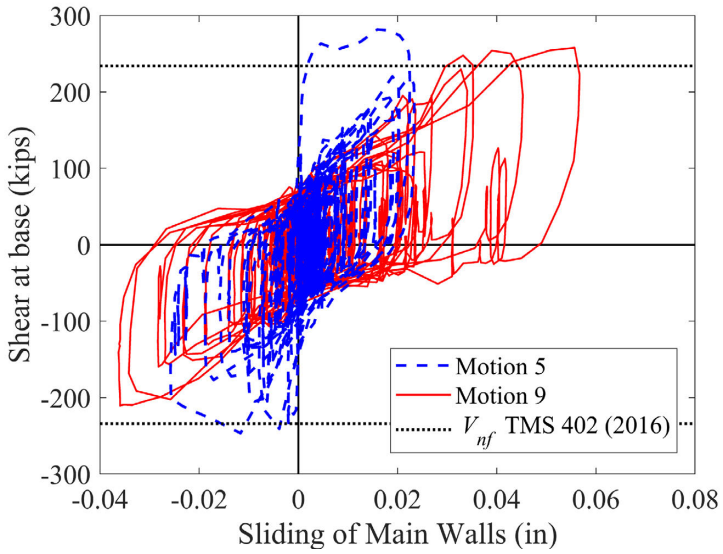

Figure 5.12 Shear force at base - versus - average base sliding curves for Motions 5 and 9.

(a)

(b)

(c)

(d)

(e)

(f)

Figure 5.13 Damage states of the test structure. (a) South-east interior view before Motion 17; (b) south-east exterior view at the maximum roof drift during Motion 17; (c) south-east exterior view at the first negative cycle right after the occurrence of the maximum roof drift; (d) south exterior view after Motion 17; (e) south-east exterior view after Motion 17; and (f) north-west interior view after Motion 17.

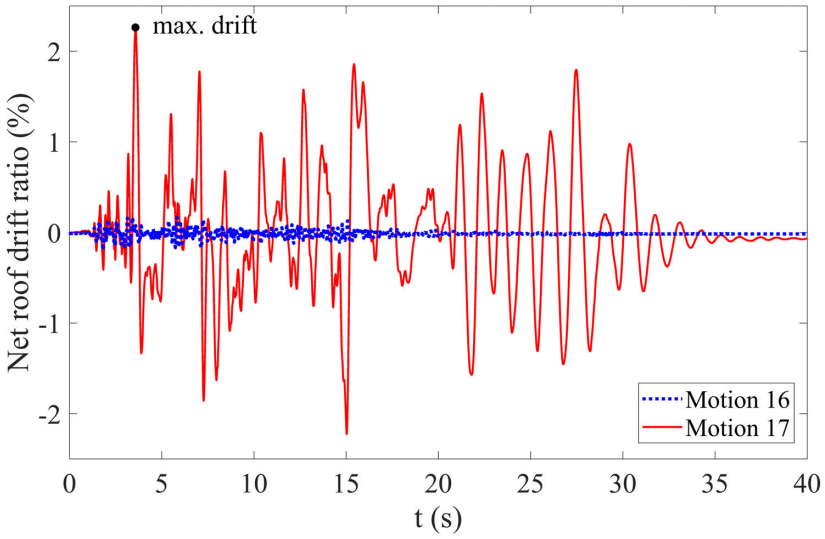

(a)

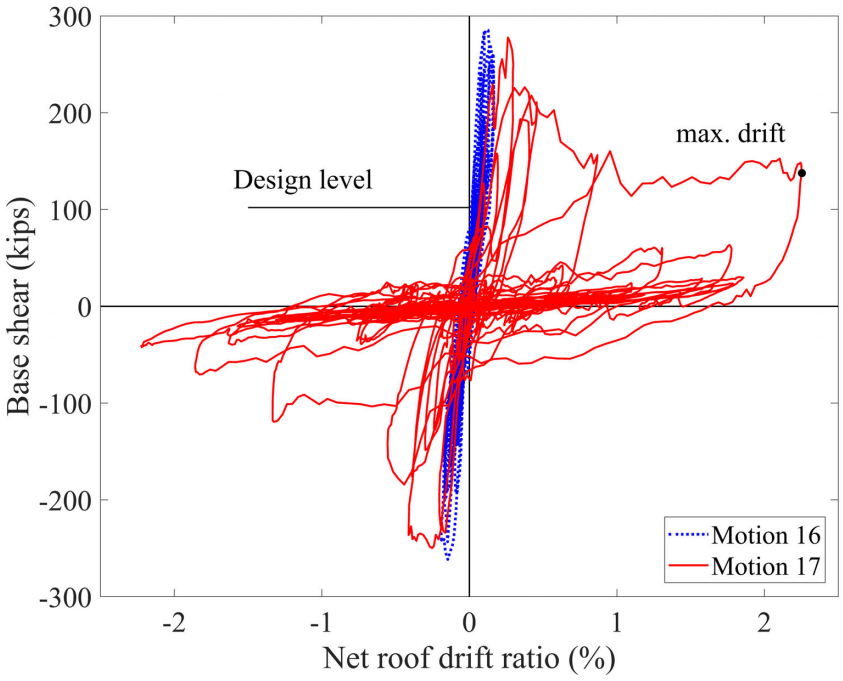

(b)

Figure 5.14 Structural response during Motions 16 and 17. (a) Net roof drift ratio response history; (b) base shear - versus - net roof drift hysteresis curves.

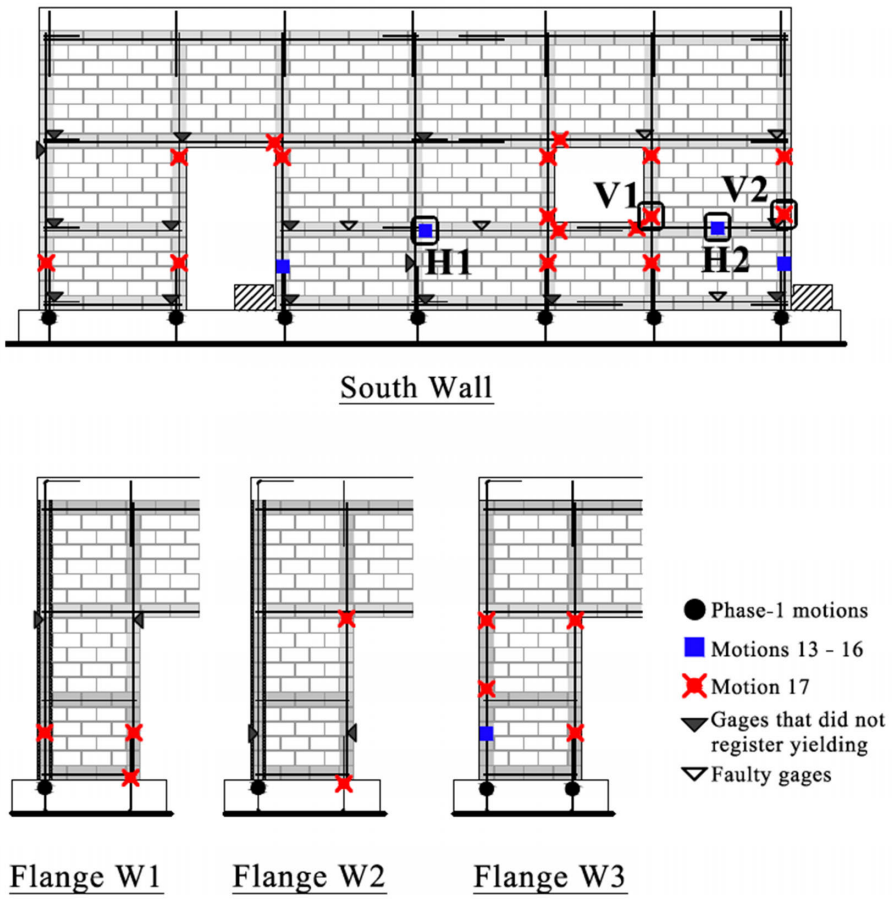

Figure 5.15 Yielding of reinforcement at locations of strain gages on the south wall and wall flanges.

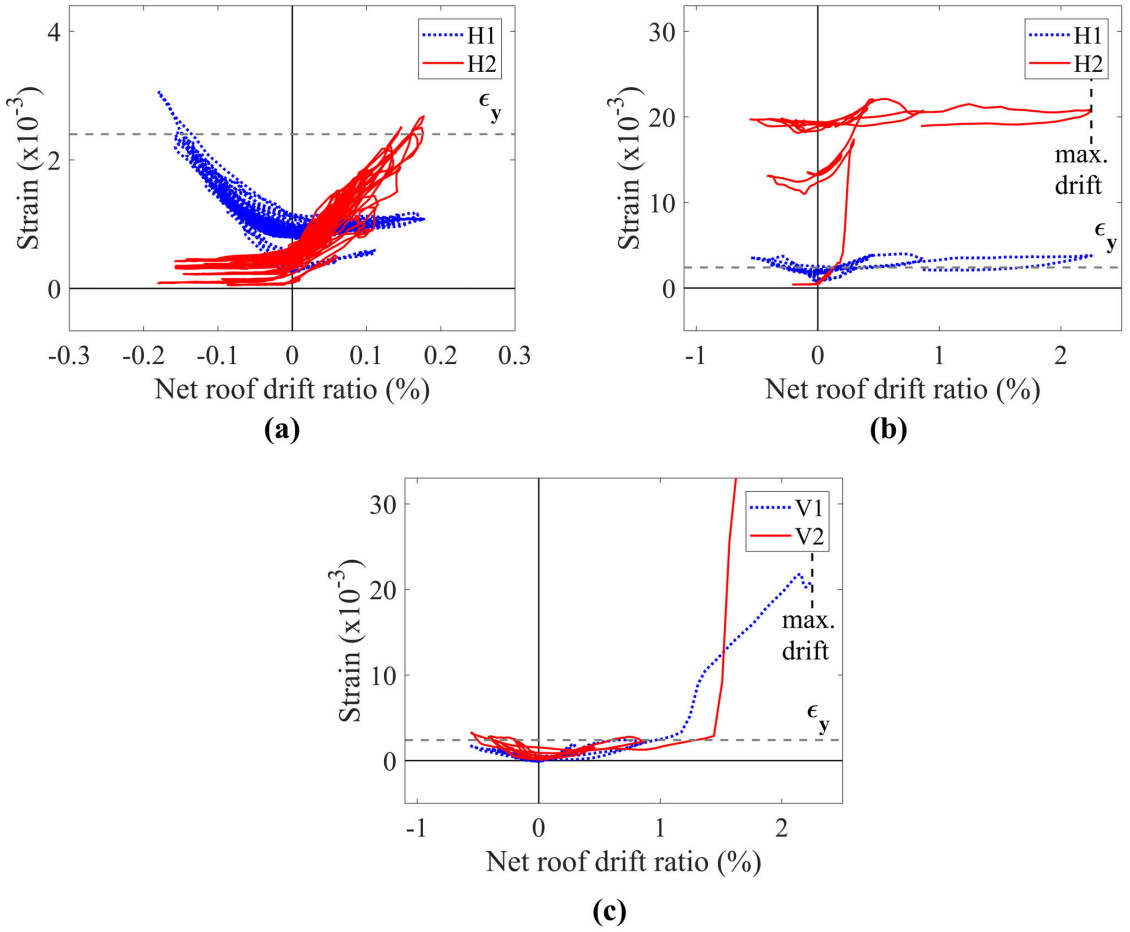

Figure 5.16 Strains from select strain gages plotted against the net roof drift ratio. (a), (b) Strains recorded by gages H1 and H2 in W2 and W3 during Motions 16 and 17, respectively; (c) strains recorded during Motion 17 in the vertical bars of W6 at the same locations as V1 and V2 in W3.

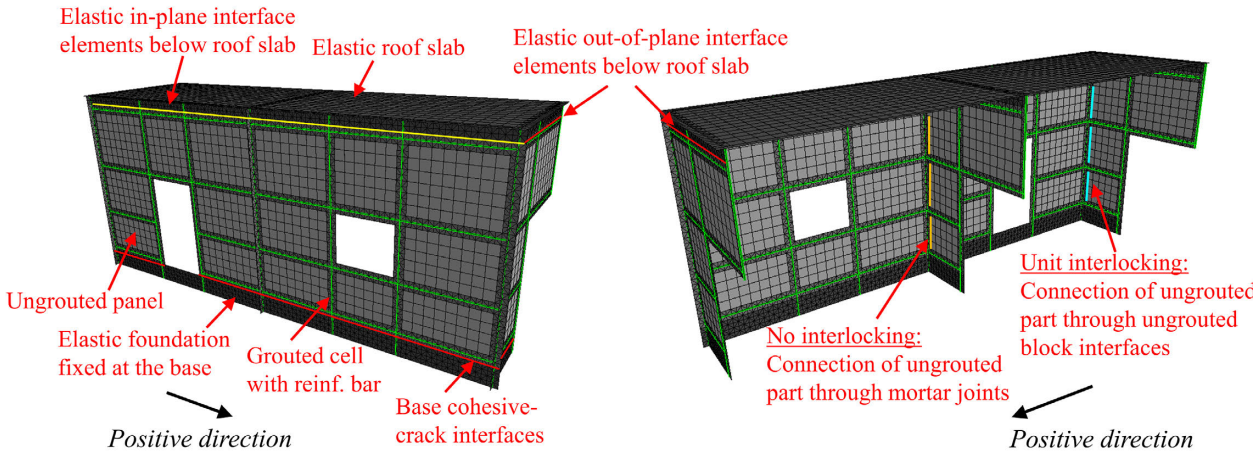

Figure 5.17 Front and back views of the FE model of the test structure.

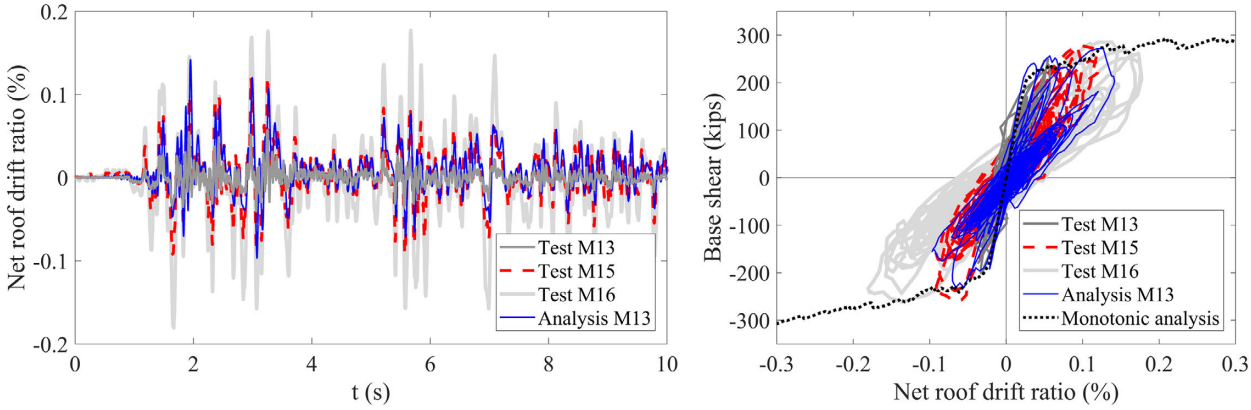

(a) Motion 13

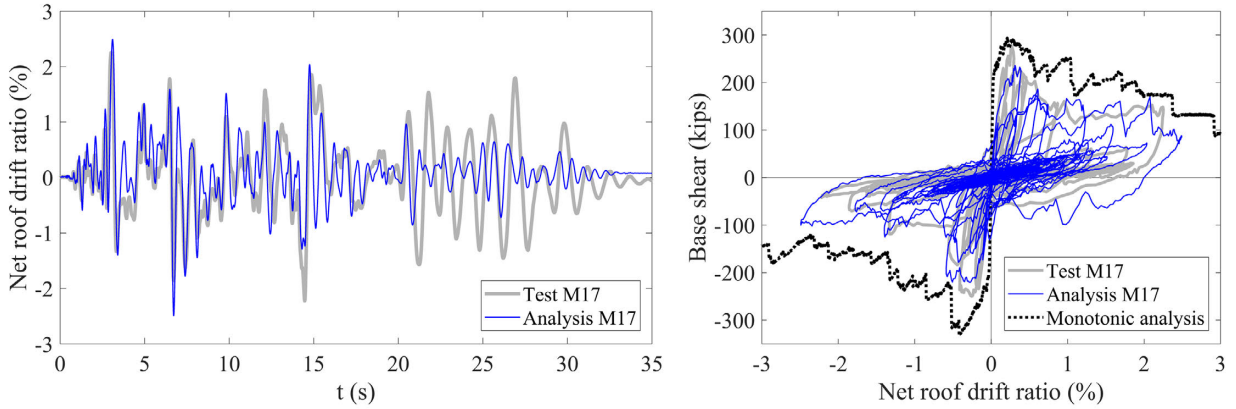

(b) Motion 17

Figure 5.18 Comparison of the results from the time-history analysis with the experimental results.

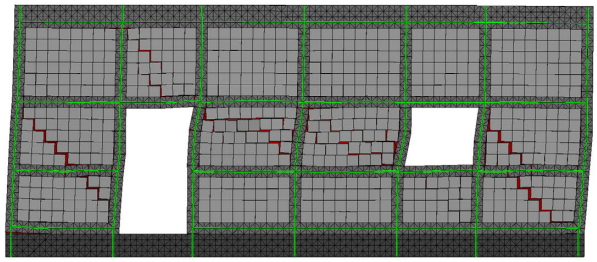

(a) M13 at drift +0.14%

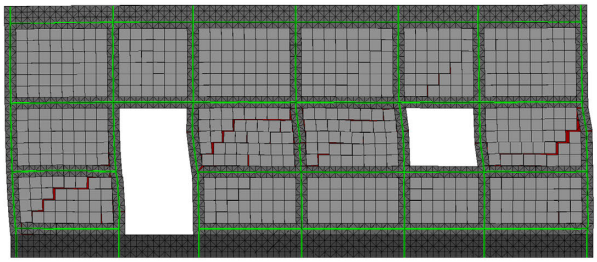

(b) M13 at drift -0.10%

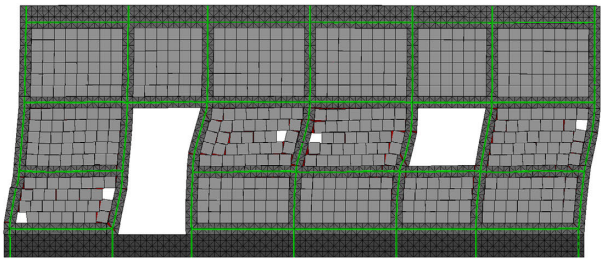

(c) M17 at drift +2.49%

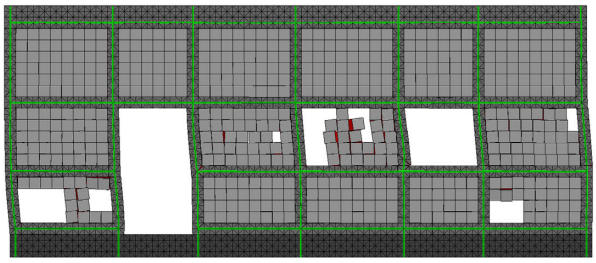

(d) M17 at drift -2.49%

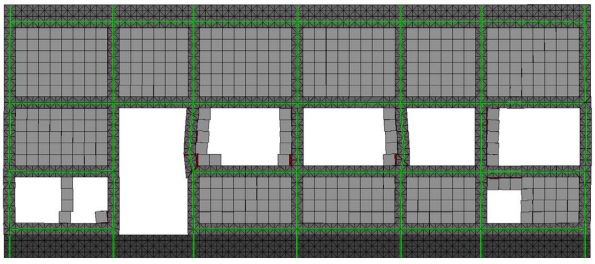

(e) M17 end

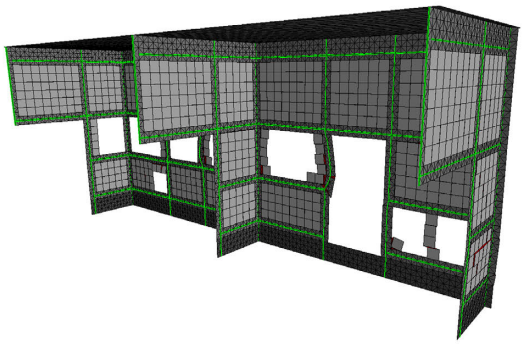

(f) M17 end

Figure 5.19 Damage shown in the time-history analysis: (a), (b) at the peak positive and negative roof drift during Motion 13 (deformation magnified by 30 times); (c) at the peak positive roof drift during Motion 17 (deformation magnified by 3 times); (d) at the peak negative roof drift during Motion 17; (e), (f) at the end of Motion 17.

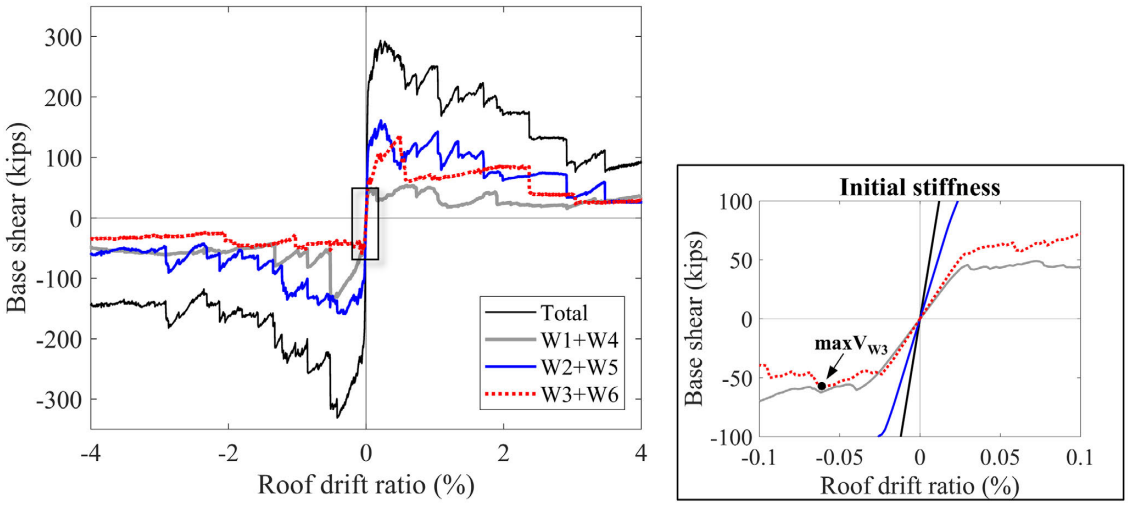

(a)

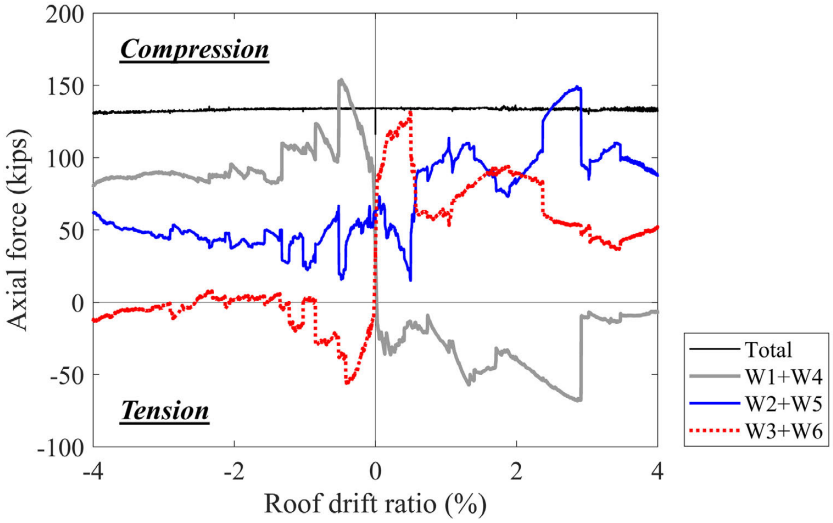

(b)

Figure 5.20 Shear and axial force developed in each wall component in the pushover analysis.

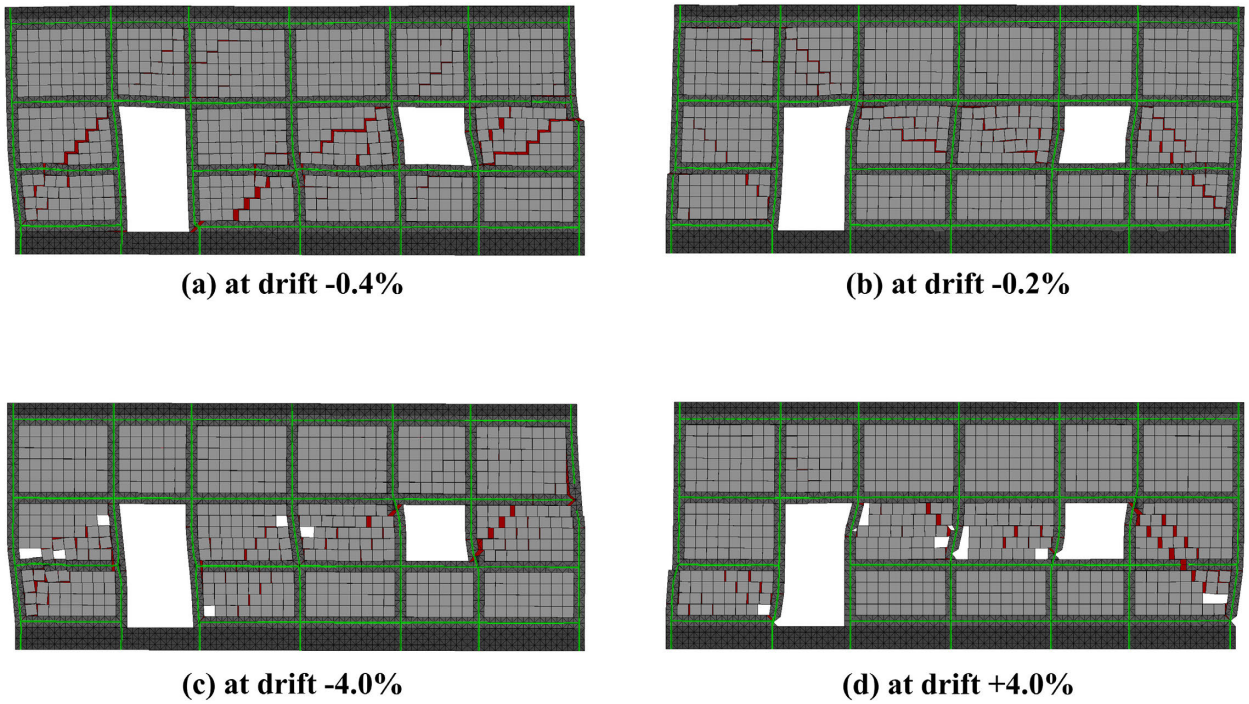

Figure 5.21 Damage in the pushover analysis: (a), (b) at the peak resistance in the negative and positive directions (magnified by 20 times); (c), (d) at a roof drift of 4% in the negative and positive directions.

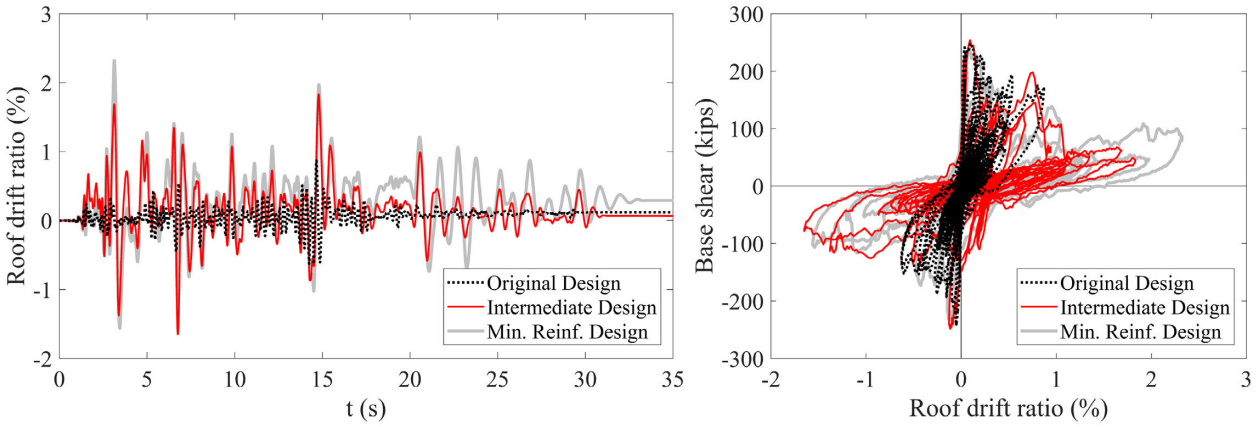

Figure 5.22 Comparison of responses of different designs subjected to the 1940 El Centro scaled by a factor of 1.6.

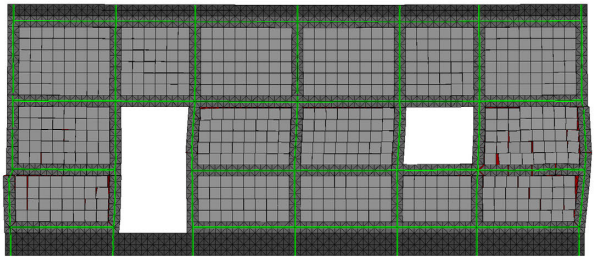

(a) Original design

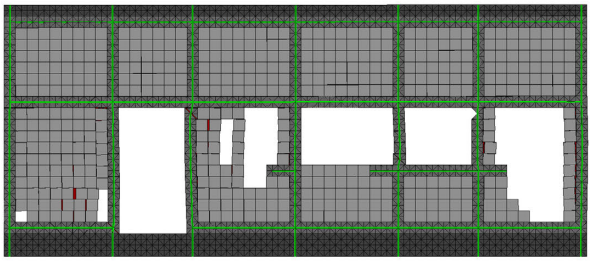

(b) Intermediate design

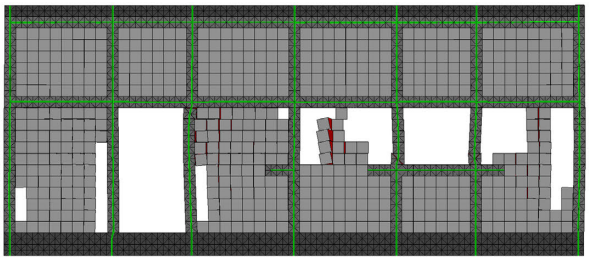

(c) Minimum reinf. design

Figure 5.23 Damage induced by the 1940 El Centro record scaled by 1.6 for the: (a) original design (magnified by 10 times); (b) intermediate design; (c) minimum reinforcement design.

6 SHAKE-TABLE TESTS OF A PARTIALLY GROUTED REINFORCED MASONRY BUILDING WITH IMPROVED DESIGN DETAILS

The previous chapter presented the behavior of a partially grouted masonry (PGM) structure that was tested on a shake table under a sequence of 17 ground motions. The structure was designed according to the current code provisions for Seismic Design Category (SDC) C and had design details conforming to current practice. It had widely spaced vertical grouted cells as well as reinforced bond beams located at four courses along the height. During testing, when the effective intensity of the applied motions exceeded the level of the Maximum Considered Earthquake (MCE), the structure developed a response dominated by base sliding and showed only minor damage in the walls. In subsequent tests, base sliding was restrained by constructing concrete stoppers against the wall toes. During these tests, referred to as Phase 2, the structure developed an adequate base-shear capacity that was 2.8 times the design base shear. The structure was able to withstand four motions with effective intensity above the MCE level including two motions with intensity 2 times the MCE. However, the structure failed in a brittle manner in the last motion of the sequence. The structure experienced a rapid load degradation at a roof drift of 0.4% which was primarily attributed to the sudden shear failure of the vertical grouted cells and the crushing of ungrouted masonry units.

This chapter presents the results from the shake-table tests conducted on a second structure that had design details aimed to improve the ductility of the building. In particular, this study was to investigate the effectiveness of using side-by-side double grouted cells and joint reinforcement to improve the seismic performance of a building system. The performance of walls with double grouted vertical cell has been assessed in a small number of quasi-static tests (Bolhassani et al.

2016a and 2016b; Schultz and Johnson 2019). It has been shown in these studies that walls with double vertical grouted cells developed higher ductility than walls with single grouted cells. However, double grouted cells have not been used in practice. Joint reinforcement is commonly used in partially grouted masonry walls to satisfy the prescriptive requirement of the code (TMS 402-16) or to control the size and spacing of cracks due to shrinkage. The code also permits the use of joint reinforcement as primary shear reinforcement to resist lateral earthquake or wind loads. Experimental studies on PGM walls have shown that joint reinforcement can contribute to the shear capacity and increase the ductility of a wall (Schultz and Hutchison 2001; Baenzinger and Porter 2010; Bolhassani et al. 2016b). However, the aforementioned studies focused on single wall segments, and the performance of wall systems with double grouted cells and joint reinforcement have not been examined.

The first and second test structures will be hereafter referred to as Specimen 1 and Specimen 2. A finite element (FE) model has been developed for Specimen 2 and validated with the test results. The model is used to gain insight into the seismic load resisting mechanisms of the structure.

6.1 Design of Specimen 2

Figure 6.1 shows the configuration and the numbering of the wall components of Specimen 2. The reinforcement details of the test structure are shown in Figure 6.2. The masonry walls of the structure had the same dimensions as in Specimen 1. However, two changes were introduced in the reinforcement details with the goal to enhance the seismic performance of the building. First, the cross-sectional area of the vertical grouted elements was increased to delay or prevent the shear failure of the vertical grouted elements and to enhance the frame action provided by the grouted cells. In Specimen 1, each vertical grouted element had a single grouted cell that contained a #4

(0.20 in^2) bar. In Specimen 2, each vertical grouted element consisted of two side-by-side vertical grouted cells. At the wall intersections, three vertical cells were grouted in an L or T configuration, as shown in Figure 6.2. Each vertical grouted cell contained a #3 (0.11 in^2) reinforcing bar so that Specimen 2 had a similar amount of total vertical reinforcement as Specimen 1.

The second change for Specimen 2 was the placement of joint reinforcement in every course. This was done to control the opening of stair-stepped cracks in the ungrouted panels, which were observed during the Phase-2 tests of Specimen 1. Specimen 2 retained the bond beams used in Specimen 1. Each bond beam had a #4 bar. The joint reinforcement had longitudinal wires and cross wires in a ladder-type configuration. The longitudinal wires had a 3/16-in. diameter, while the cross wires had a 0.148-in. diameter. Joint reinforcement was placed in both the in-plane and out-of-plane walls, as shown in Figure 6.2.

Specimen 2 had a heavier roof slab than Specimen 1. The roof slab of Specimen 2 consisted of 8-in. thick precast hollow core planks as in Specimen 1, but had a 12-in. thick cast-in-place RC topping, while Specimen 1 had a 4-in. thick topping. The roof weight of Specimen 2 was 147 kips, while that of Specimen 1 was 79 kips. The increase in the roof weight was to reduce the peak ground acceleration required to reach the capacity of the structure and thereby the force demand on the horizontal actuators of the shake table. It was observed that the actuator force developed in the tests of Specimen 1 approached the load capacity of the actuators. The larger roof weight also increased the sliding resistance at the base.

6.2 Construction, Material Properties, and Instrumentation

Specimen 2 was constructed in the same way as Specimen 1 by the same masons. The structure was built on the same RC footings built for Specimen 1. The dowel bars were pre-installed during the footing construction and were offset for a short distance from the dowels for

Specimen 1. To ensure that no base sliding would occur in the tests of Specimen 2, the footing surface was intentionally roughened. To further increase the sliding resistance, additional #3 vertical dowels with 180-degree hooks were placed in epoxy-filled drilled holes in the footing along the length of the Main Walls, as shown in Figure 6.3a. The dowels extended within the height of the base bond beam and hooked around the horizontal bar. The vertical reinforcing bars of the walls were lap-spliced above the footings and below the roof slab a lap length of 24 in. The horizontal bars were lap-spliced in the wall webs at the same locations as in Specimen 1 and were extended into the flanges with 90-degree bents, while 180-degree hooks were used in the wall ends. The joint reinforcement was placed so that the longitudinal wires were embedded within the mortar placed on top of the face shells of the concrete masonry units (CMU), as shown in Figure 6.3b. The joint reinforcement was provided in 10-foot long prefabricated segments that were lap-spliced over a length of at least 10 in. At the wall intersections, joint reinforcement segments were arranged in the form of an L or T, as shown in Figure 6.3c. At the wall ends, the longitudinal wires were bent to form 90-degree hooks. The ungrouted parts of the masonry walls were constructed with standard masonry units (8 x 8 x 16 in.), while H-blocks were used for the bond beam courses, and U-blocks or open-end blocks were used for the construction of the double grouted cells, as shown in Figure 6.3d and Figure 6.3e. As in Specimen 1, the roof planks spanned across the north-south direction and were simply supported on the north and south walls.

Grout, mortar, and masonry prism samples were taken during the construction and were tested in compression at an age exceeding 28 days. The average material strengths are summarized in Table 6.1. Samples of the reinforcing bars and the longitudinal wires of the joint reinforcement were tested in tension up to the point of rupture. The average yield (f_y) and ultimate tensile stress

(f_u), as well as the strain at the ultimate stress (ε_u) are shown in Table 6.2. Rupture of the samples of joint reinforcement occurred at an average strain of 0.06.

The instrumentation scheme for Specimen 2 is similar to that for Specimen 1. The locations of strain gages in the south wall are shown in Figure 6.4. Strain gages were placed on vertical bars at locations close to the wall-footing interface, above the second bond beam (level of the window sill), and at the elevation of the top of the openings right below the third bond beam from the base. The wall flanges had strain gages placed only on the vertical bars close to the wall-foundation interface. Strains gages were also placed on the horizontal bars of the first, second, and third bond beams within the in-plane walls as shown in Figure 6.4. The strains in the joint reinforcement were not monitored. Further details can be found in Koutras and Shing (2015b).

6.3 Ground Motions and Scaling

The test structure was subjected to a sequence of 17 motions, referred to as Motions 1 to 17. Two earthquake records were used in the tests, the north-south component of the El Centro record from the 1940 Imperial Valley Earthquake (EC1940), and the El Centro Array #5 record component 140 from the 1979 Imperial Valley Earthquake (EC1979). Record EC1940 is more severe than EC1979 in terms of the duration of strong shaking and it was primarily used in the tests of Specimen 1. However, because of the brittle behavior observed in the tests of Specimen 1, record EC1979 was used for the high intensity tests of Specimen 2. Record EC1940 was used for Motions 1, 3, 4, 6, and 9. The specimen was subjected to white-noise excitation before Motion 1 and after each motion of the sequence to identify any change in the natural period of the structure. The fundamental period of the structure before the application of Motion 1 was found to be 0.062 s.

The f_y masonry wall system of Specimen 2 was designed for the prototype building configuration assumed for Specimen 1. The actual seismic weight of the test structure was calculated to be $W_{spec} = 197$ kips , which is by 3.5% higher than the weight initially assumed based on the prototype and used for scaling the ground motions. To satisfy the dynamic similitude with the prototype, the applied base acceleration in the tests was amplified by a factor of $F_a = W/W_{spec} = 2.11$ and the time was compressed by a factor of $F_t = \left(1/F_a\right)^{0.5} = 0.69$. Figure 6.5 shows the acceleration time histories and response spectra of records EC1940 and EC1979 after the similitude scaling has been applied. In the figure, the records are scaled to the level of the Design Earthquake (DE) of the code (ASCE 7-10) for SDC C. The scaling factor indicated in the figure is in addition to that for the similitude scaling. In the figure, the polarity of record EC1979 is inverted as it was applied in the shake table tests. Figure 6.6a compares the acceleration response spectra of Motions 8 and 16, which were obtained from the accelerometers placed on the footings, to the code-based spectra for the DE and MCE. Both motions were from the EC1979. As the intensity of the applied motion increased, the shape of the response spectrum of the table motion deviated from the target motion (shown in Figure 6.5) in the vicinity of 10 Hz, which was close to the oil column resonance frequency of the table oil column. The same issue had been observed during the testing of Specimen 1.

6.4 Structural Response and Analysis of Test Data

6.4.1 Test observations and global response

Table 6.3 shows the sequence of the 17 ground motions used in the testing of Specimen 2. The table includes the structural period measured after each motion, the effective intensity (I_{eff}) of each ground motion with respect to the level of the MCE, and summarizes the peak ground and

roof accelerations as well as the peak roof drift ratio and peak base shear measured during each ground motion. The effective intensity (I_{eff}) of a motion is calculated as described in Chapter 4. The change of the structural period of Specimen 2 during the test sequence is also illustrated in Figure 6.6b. It can be observed that the structural period measured with the white-noise excitations showed a gradual increase during the sequence. During the entire test sequence, the sliding measured along the base of the Main Walls was practically zero, while the sliding measured at the base of W1 and W4 did not exceed 0.02 in. and 0.05 in., respectively. The roof drift ratio shown in Table 6.3 is calculated as the displacement measured at the roof divided by the clear height of the masonry walls, which was 152 in. The base shear is calculated from the average acceleration measured by the accelerometers placed on the roof slab and the mass of the structure above the level of the window sills. The positive direction for the acceleration, drift, and base shear is assumed to be towards East.

As shown in Table 6.3, Motions 1 through 7 had an effective intensity lower than the DE. They were low-level tests that were performed to improve the tuning of the shake table.. During these tests, the specimen did not sustain any discernible damage; however, the structural period increased from 0.062 s to 0.088 s. This increase could be due to the opening of flexural cracks at the base of the walls, bond deterioration between the bars and the grout, or minor cracking in the mortar joints of ungrouted masonry that was not visible. Motion 8 had the intensity of the DE and did not cause any visible damage. Visible but minor cracking along mortar joints was first detected after Motion 9, for which the EC1940 record was used. It had an effective intensity of 0.89 x MCE. Among the next four motions, Motions 10 to 13, Motion 10 was the strongest and had an effective intensity at the level of the MCE. During these motions, cracks propagated further in the mortar joints. A few fine cracks in some ungrouted units were also observed. In addition, horizontal

flexural cracks were found along the flange of W3 and W6 at the level of the window sill. These cracks extended to the grouted cells in the wall webs. No new cracks occurred until Motion 15, which had an effective intensity of 1.34 x MCE. During Motion 15, the structural period increased by 35% with respect to the period measured before the motion. The motion induced additional vertical cracks in the hollow masonry units and horizontal cracks in the vertical grouted cells of W2/W5 and W3/W6 at the bottom and top of the window openings. Cracks developed in the south wall at the end of Motion 15 are shown in Figure 6.7. During Motion 15, the structure developed its ultimate base shear capacity of 337 kips. Motion 16 had an effective intensity of 1.5 x MCE and caused further cracking in the ungrouted masonry units. The mortar joints along the height of the wall components experienced significant damage due to the excessive sliding that occurred along the joints during the motion. In several locations along the bed joints, the mortar material had completely disintegrated exposing the longitudinal wires of the joint reinforcement. In Motion 17, the final motion, the excitation used for Motion 15 was reapplied. During that test, cracking mainly occurred in the ungrouted units. In addition, a diagonal crack started to form at the mid-height of the double grouted vertical cell of W5 adjacent to the door opening and also in the vertical grouted cell of W6 adjacent to the window opening (see Figure 6.8). As shown in Figure 6.6b, the structural period measured after Motion 17 was 6.4 times the initial period.

Figure 6.8 shows pictures of the damage of Specimen 2 at the end of the test sequence. Figure 6.7 compares the cracks formed at the end of Motion 15 in the south wall and the flanges of W1 and W3 to the final crack pattern. It can be seen that in the ungrouted panels of the wall components, the cracks were uniformly distributed along the mortar joints of the in-plane walls. In addition, with the exception of the diagonal cracks that started to form in the grouted cells of W5 and W6, no other diagonal cracks were observed in the grouted vertical cells. However, all the

vertical grouted cells had horizontal flexural cracks at distinct locations at the top and bottom of the openings. No crushing or block detachment occurred in the tests, and no rupture of the joint reinforcement or reinforcement bars was observed.

Figure 6.9 shows the roof drift response history during Motion 17, the final motion, and compares the hysteresis curves obtained in Motions 14 through 17. In these tests, the EC1979 record was used. The maximum base shear of 337 kips developed in the negative direction (pointing west) during Motion 15 at a roof drift of 0.27%. In the positive direction, the peak base shear was 312 kips, which occurred in Motion 15 as well. It can be also observed that the drift developed towards the negative direction was more severe. This is consistent with the strong direction of the base excitation. It also appears that during Motion 17, the structure was not excited enough to attain its ultimate lateral load resistance in the positive direction. Compared to Specimen 1, the maximum base shear capacity of Specimen 2 was higher by 18%. Figure 6.9c compares the hysteresis loops for Specimen 2 from Motions 14 through 17 to those for Specimen 1 from Motions 16 and 17, the last two. The peak base shear capacity of Specimen 1 developed in Motion 16. In calculating the roof drift ratio of Specimen 1, the small base sliding (no more than 0.08 in.) of the Main Walls was subtracted from the roof displacement. It should be noted that the response of Specimen 1 was obtained with the EC1940 record. The record has a longer duration than EC1979 and is equally strong in both the positive and negative directions. Unlike the behavior of Specimen 1, Specimen 2 showed a gradual load and stiffness degradation. The hysteresis curves for Specimen 2 demonstrated significant pinching especially during the last two motions. This could be attributed to the opening and closing of the horizontal flexural cracks that appeared in the double grouted vertical cells. The pinched shape also indicates that despite the significant sliding developed along the mortar joints during the last two motions, there was no significant energy

dissipation through friction. This could be because of the severe damage in the mortar joints resulting in the loss of mortar and therefore a low amount of vertical compressive force transmitted to the joints.

6.4.2 Yielding of reinforcement

Figure 6.10 shows the sequence of yielding in the reinforcing bars as registered by the strain gages attached on the bars. The figure indicates the motion during which each strain gage registered yielding for the first time. For brevity, the sequence of yielding during Motions 11 through 13 is not distinguished. As shown in the figure, yielding was first registered during Motion 10 that had an effective intensity at the MCE level. Yielding initiated in the vertical bars of W1, W3, W4, and W6, including bars in the respective flanges. During the following motions, yielding was gradually registered in the vertical bars of the other wall components. It can be observed that by the end of Motion 15, during which Specimen 2 developed its peak load capacity, most of the strain gages on the vertical bars had showed yielding. Strain gages attached on the horizontal bar of the second (from the base) bond beam in the Main Walls registered yielding as well; however, the strains measured were much lower than those measured in some of the vertical bars. Furthermore, it can be seen that the yielding of the horizontal bars was registered only after several of the vertical bars had already yielded.

Figure 6.10 shows seven locations in the North Wall, identified as Section 1 through Section 7, where the strains in the reinforcing bars are further examined. Sections 1 and 2 are at the base of W4, Sections 3 and 4 are at the two ends of W5 at the level of the window sill, Sections 5 and 6 are at the two ends of W6 at the level of the window sill, and Section 7 is at the base and west end of W6. The two vertical bars in the side-by-side vertical grouted cells at each section are referred to as the West and the East bars based on their positions. The strains developed in the

vertical bars depended on the deformation of the wall component, the deformation of the grouted columns, and the level of the axial load transmitted to the wall component due to the overturning moment developed in the building system.

Figure 6.11 shows the strains measured at the select sections plotted against the roof drift ratio for Motions 15 and 17. During Motion 15, the maximum base shear was developed, while during Motion 17, the peak roof drift ratio was reached. It can be seen that the strains in the two vertical bars at Sections 1, 2, and 5 varied in an out-of-phase manner, with the West bars developing higher tensile strains when the displacement was towards the positive direction (east) and lower strains when the displacement was towards the negative direction (west). The East bars behaved in the opposite manner. The strain variation at Sections 1 and 2 indicates localized bending of the vertical grouted elements in W4 as well as the flexural deformation of W4 as a whole. The former can be attributed to the weakening of the ungrouted panels in W4 caused by the extensive sliding along the mortar joints. The V-shaped strain-vs.-roof drift curves were caused by the combination of these two mechanisms. At Sections 3, 4, and 6, the strains in the East and West bars varied in phase, with higher tension in both bars when the structure was displaced in one direction. However, the trends at Sections 3 and 4 are opposite to one another. Except for the West bar at Section 5, the trends of the bar strains at Sections 5 and 6 are in phase with one another, with higher tensile strains in all bars when the structural displacement was towards the negative direction (west). The trends observed for Sections 3, 4, 5, and 6 were most likely caused by the axial forces induced by the global overturning moment developed in the building as the roof was displaced laterally. The fact that the strain in the West bar was much smaller than that in the East bar at Section 5 could be due to the superposition of localized bending of the grouted element at that section.

6.5 Numerical Studies

It is evident that during the shake-table tests, Specimen 2 showed a more favorable performance compared to Specimen 1. Specimen 2 reached a peak load capacity that was 18% higher than Specimen 1 and also developed a more ductile load-displacement response. The increased cross-sectional area of the double grouted vertical cells delayed the occurrence of shear cracks in the grouted masonry and allowed the grouted vertical cells to behave in a flexure-dominated manner. This was indicated by the opening and closing of dominant horizontal cracks and by the yielding of the vertical bars from an early stage of testing. However, significant cracking and sliding were observed along the mortar joints of the ungrouted panels in Specimen 2. The cracks were uniformly distributed along the panels. Unlike Specimen 1, Specimen 2 had no crushing of masonry units during the tests. Nonetheless, it should be noted that the two structures were tested under different sequences of ground motions and had different roof weights. Specimen 2 had a roof weight which was almost 2 times that of Specimen 1. Furthermore, Specimen 1 developed base sliding over a large number of motions, while it was prevented in Specimen 2 by using intentionally roughened footing surface and additional dowels at the wall base. All these differences could affect the seismic behavior of a structure. Moreover, the role of the double grouted cells and of the joint reinforcement in improving the strength and ductility of the structure cannot be determined from the test data alone. To determine the factors that contributed to the better performance of Specimen 2, a nonlinear finite element (FE) model is developed to conduct numerical parametric studies.

6.5.1 Modeling of Specimen 2 and validation analysis

Figure 6.12 shows the FE model developed for Specimen 2. Due to the symmetry of the structure and the loading condition, only the south half of the structure is modeled. The

discretization scheme used for the modeling of Specimen 1, as described in Chapter 5, is used here. However, the modeling of the joint reinforcement for Specimen 2 requires additional considerations, as described in Chapter 4. The two longitudinal wires embedded in each bed joint are modeled with a single line of beam elements that have an elastic-perfectly plastic material law. The beam elements are attached to the masonry shell elements using bond-slip/dowel-action interface elements. The bond-slip response has a peak resistance of $\tau_{\max} = 0.038\sqrt{f_{mor}}$, where f_{mor} is the mortar compressive strength, which remains constant once reached under monotonic loading conditions. The bond-slip model accounts for the deterioration of the bond resistance under cyclic loading, as described in Chapter 4. In the FE model, the interface elements representing the mortar joints in ungrouted masonry that contain joint reinforcement have a net mortar width equal to the total width of the two face shells minus 2 times the diameter of a longitudinal wire. Within the region of the double grouted vertical cells, the joint reinforcement in the model is assumed to have a strong anchorage (i.e., a high bond strength) to simulate either the 90-degree hook that was used at the wall end or the side rod that was embedded (in most of the courses) in the grout. To reduce the number of elements in the model, the joint reinforcement placed in the out-of-plane walls of the test structure is ignored.

Rupture of the joint reinforcement is modeled in the same manner as for the reinforcing bars (see Chapter 2). Rupture is triggered when a work-based damage parameter D exceeds a specified value D_{cr}. For the beam elements representing the joint reinforcement, the critical value D_{cr} is set equal to 0.06. This results in a rupture strain of about 0.06 when subjected to monotonically increasing tension.

Table 6.4 to Table 6.8 summarize the values assumed for the material parameters for the smeared-crack shell elements, cohesive-crack interface elements, beam elements representing the steel reinforcement, and bond-slip/dowel-action interface elements. The values adopted are determined in the same way as those for the Specimen 1 model (see Chapter 5) and are based on the strengths of the material samples shown in Table 6.1 and Table 6.2. The cohesive-crack interface elements for the wall-footing interface have a sufficiently high coefficient of friction to prevent base sliding. The additional dowel bars placed along the base of the Main Walls in the actual structure are not modeled.

For the time-history analyses, the implicit time-integration scheme proposed by Bathe (2007) is used. Rayleigh damping with a damping ratio of 0.1% is prescribed for the first and second modes. The stiffness proportional part of the damping model is based on the initial stiffness of the shell and beam elements, and is ignored for the interface elements. The initial fundamental period and the second-mode period, calculated with eigenvalue analysis, are equal to 0.050 s and 0.029 s. The fundamental period of the model is lower than the initial period of 0.064 s measured from the specimen.

The time-history analysis is performed by subjecting the model to the last five motions of the test sequence, Motions 13 to 17. The five motions are applied in sequence and in a single run using the base acceleration measured on the concrete footings during the tests. Although applying the complete sequence of 17 motions will be desirable, it will greatly increase the duration of the analysis. Figure 6.13 and Figure 6.14 compare the roof drift ratio histories and hysteresis curves obtained from the analysis and the tests. The lateral resistance of the model is obtained by summing the shear forces developed along the interface elements at the level of the window sill and the shear forces developed by dowel action of the vertical reinforcement at the same elevation. This is

consistent with the method used to calculate the seismic base shear from the experimental results by considering only the mass of the structure above that line. Figure 6.15 shows the deformation of the model at the peak positive and negative resistance, at the peak positive and negative roof drift, and at the end of the analysis.

As shown in Figure 6.13 and Figure 6.14, the response of the model is initially stiffer than the experimental response. This is due to the cracking and yielding that occurred in the test structure during motions prior to Motion 13. However, the stiffness of the model gradually approaches the stiffness of the test structure. Eventually, during Motions 15 to17, the model is able to capture both the roof drift history and the hysteretic response. In the analysis, the peak load capacity occurs in Motion 13 and has similar values in both directions, i.e., 326 kips for the negative direction and 325 kips for the positive direction. Furthermore, the damage obtained in the analysis is similar to that observed in the tests. As in the tests, significant sliding occurs along the mortar joints, and the vertical double grouted cells behave in a flexure-dominated manner. Figure 6.16 shows the strains developed in the vertical reinforcing bars of the model during Motion 17 at the seven sections identified in Figure 6.10. The shapes of the strain - vs. - roof drift curves obtained resemble those from tests (see Figure 6.11) but do not provide a close match for each section. In the analysis, crushing was limited to only a few ungrouted units and occurred at the peak roof drift during Motion 17, as can be seen in Figure 6.15. Yielding of the beam elements representing the joint reinforcement was registered in the last two motions of the time-history analysis. However, no rupture of joint reinforcement occurred. This is consistent with the test observations.

Figure 6.13 and Figure 6.14 show the monotonic load-displacement response curves obtained from pushover analyses. The pushover analyses are performed by controlling the

horizontal displacement at the roof. It can be observed that the pushover analyses produce a higher strength than the one obtained in the time-history analysis. In the pushover analyses, the model reached a peak lateral load of 465 kips and 462 kips in the positive and negative directions, respectively. In the time-history analysis, the peak load was 326 kips. The difference is significant and can be attributed to the more severe deterioration of the mortar joints in the ungrouted panels under cyclic loading.

6.5.2 Influence of double grouted cells and joint reinforcement

A numerical study is conducted to assess the influence of the double grouted cells and joint reinforcement on the seismic behavior of the building. To this end, three design alternatives are considered in addition to the design of Specimen 2. The first design alternative has double grouted vertical cells and bond beams as in Specimen 2, but without joint reinforcement. The second design alternative has single grouted cells with #4 bars as in Specimen 1 but has the same roof weight as Specimen 2. The third design alternative is the same as the second but with the addition of 3/16-in. joint reinforcement in every course. The three alternative designs will be hereafter referred to as the DG (double grouted cells) design, SG (single grouted cells) design, and SG/JR (single grouted cells with joint reinforcement) design, respectively. The design of Specimen 2 will be called the DG/JR design, which stands for double grouted cells and joint reinforcement. The respective FE models assume the material properties and mass used in the analysis of Specimen 2 (see Table 6.4 to Table 6.8). The net width of the mortar joints that contain joint reinforcement is reduced by two times the diameter of a longitudinal wire. Pushover and time-history analyses are performed to compare the response of the three design alternatives to the response of model of Specimen 2.

Figure 6.17 compares the pushover load-displacement curves for the four designs. Table 6.9 summarizes the peak load capacities that the models develop when displaced towards the positive and negative directions. Figure 6.18 to Figure 6.21 show the damage developed in the analyses at the peak load capacity and at a roof drift ratio of 1.5%. The locations at which the joint reinforcement ruptured are indicated in the figures. The drift at which the peak load capacity is reached is also shown. It can be observed that the introduction of double grouted cells, joint reinforcement, or both has a beneficial influence on the lateral resistance of the structure. However, the improved behavior of the DG/JR design compared to the SG design is primarily attributed to the double grouted cells. Joint reinforcement seems to be more beneficial and to be activated more extensively when it is used with single grouted cells as indicated in Table 6.9. This is also shown by the fact that in SG/JR design, the rupture of joint reinforcement occurs at a lower drift than it does in DG/JR design. In SG/JR, rupture is first registered at a drift of 0.42% and 0.63% in the positive and negative directions, respectively, while in DG/JR, rupture first occurs at drifts of 0.70% and 1.38% in each of the two directions, respectively. The results for SG/JR and DG/JR also show that the addition of joint reinforcement leads to less localized shear cracks at the peak load capacity of the structure (see Figure 6.18 to Figure 6.21). Figure 6.19 and Figure 6.21 indicate that the joint reinforcement helps to restrain the opening of shear cracks in the grouted vertical cells of DG/JR. Finally, it should be noted that the models containing joint reinforcement reach their peak strengths at a larger drift than the models that do not contain joint reinforcement.

A time-history analysis is performed to compare the response of the four designs under the same earthquake excitation. The four models were subjected to the original 1940 El Centro record with the acceleration scaled by a factor of 2.3. The motion corresponds to 1.8 times the MCE at the fundamental period of model of Specimen 2. The ground motion history and spectrum scaled

to comply to the dynamic similitude with the prototype building can be found in Figure 6.5a. Figure 6.22 compares the response histories and load-displacement hysteresis curves for the models. The analyses of the SG/JR and DG/JR stop before the end of the motion due to convergence issues. This is likely related to the vibration of the beam elements representing the joint reinforcement after the crushing and removal of the adjacent masonry elements.

The time-history results show that all models apart from the SG design develop a lower base shear capacity than in the pushover analyses. The DG, SG/JR, and DG/JR have the base shear capacities reduced by 8%, 12%, and 17%, respectively. The four models also show a lower ductility in the time-history analyses. The SG/JR performs better than the SG, developing a higher resistance, especially in the post-peak regime. As shown in Figure 6.22b, the SG/JR developed lower roof displacements than the SG after the initial cycles. In the first few cycles, the displacements of the SG/JR are larger. This could be attributed to the smaller width assumed for the horizontal mortar joints because of the presence of the joint reinforcement, which results in earlier joint cracking. The performance of the DG and DG/JR is better than their single grouted counterparts. Both models behave in a similar manner with the latter developing slightly higher resistance in the post-peak regime due to the joint reinforcement.

Figure 6.23 and Figure 6.24 show the damage that the four models develops at the peak base shear and peak drift in the positive direction. Figure 6.25 shows the damage of SG and SG/JR at the end of the analysis. At the peak load capacity, the cracks along the mortar joints appear to be more localized in the SG and DG and more distributed in the SG/JR and DG/JR, which contain joint reinforcement. The more localized cracks in the SG and DG could explain the more severe crushing and subsequent removal of the shell elements for the ungrouted masonry, as shown in

Figure 6.24. Rupture of joint reinforcement occurs only in the SG/JR but is limited to the wire located at the base course next to the wall toes.

Finally, it should be mentioned that the base shear capacity developed by DG/JR under the 2.3 x 1940 El Centro ground motion is 18% higher than that under the sequence of Motions 13 through 17. This demonstrates the load history effect.

6.5.3 Behavior of wall components and assessment of the code shear-strength equation

The monotonic and time-history analyses presented previously demonstrate that the use of double grouted cells or joint reinforcement improves the seismic performance of the PGM structure as compared to the performance obtained using single grouted vertical cells and bond beams only (SG design). In the previous chapter, the strength of the wall components of Specimen 1 are calculated with the methods in TMS 402 (2016). It has been found that for the walls of Specimen 1 that had single grouted cells, the shear strength calculated with the code equation is slightly lower than those given by the finite element model, except for wall components W3/W6 when they are subjected to tension. In this section, the results of the monotonic analyses are used to assess the accuracy of the shear-strength equation in TMS 402 (2016) for wall components containing double grouted vertical cells, joint reinforcement, or both. The SG has the reinforcement as Specimen 1 but has a higher roof weight and material strengths different from those for Specimen 1.

Figure 6.26 shows the shear and axial forces developed in each wall component at the level of the window sill as computed from the pushover analyses of the four design alternatives. The axial force in each wall is calculated by summing the normal forces in the horizontal interface elements of the in-plane and out-of-plane walls and the forces in the vertical bars. In the figure, axial force with the positive sign represents compression. The shear force in each wall is calculated

from the shear forces in the horizontal interface elements and in the vertical bars. It can be seen that the axial forces in the walls vary with the direction of loading. Under positive loading, the axial force in W1/W4 is tensile, while that in W3/W6 is compressive. The opposite is observed when the structure is subjected to negative loading. Furthermore, it can be seen that when W1/W4 and W3/W6 are under compression, the shear force and axial force in each wall vary with a similar trend, showing the interdependence between the shear resistance and the axial load exerted on a wall component. The axial load in W2/W5, the middle walls, remains compressive throughout the analysis, varying slightly with the displacement.

Comparing the responses of the walls in the four design alternatives, it is clear that the double grouted cells and the joint reinforcement improve the shear resistance in all wall components. In Figure 6.26c, W3/W6 in the DG/JR appears to be weaker than that in the DG when loaded in the negative direction because of the higher tensile force developed in the DG/JR. Figure 6.26c shows that W3/W6 in the SG/JR is stronger than that in the SG by 22.5 kips when the structure is loaded in the positive direction. Apart from the higher amount of horizontal reinforcement, the higher strength of W3/W6 in the SG/JR is attributed to the higher compression, which in turn is due to a higher lateral resistance of the SG/JR. The interdependence of the axial and shear forces is due to the overturning moment introduced by the lateral loading on the structure.

The shear and flexural strengths of each wall component are calculated based on the code prescribed methods (TMS 402-16) using the axial force ($P_{V\max}$) developed in the pushover analysis at the peak load resistance ($V_{\max}$) of each wall component. To determine the shear-span ratio ($M_u / V_u d_v$) in the shear strength equation, all wall components are assumed to have fixed-fixed

end conditions. Wall component W1/W4 is assigned the height of door opening. For walls W2/W5 and W3/W6, different heights are assumed depending on the direction of loading. For positive loading, W2/W5 is assigned the height of the window, while W3/W6 is assigned the height of the door. For negative loading, W2/W5 is assigned the height of the door, while W3/W6 is assigned the height of the window. As explained in the previous chapter, this is consistent with the height over which the dominant diagonal cracks span when the walls reach their load capacities in the finite element analyses. Based on TMS 402 (2016), the shear strength of a PGM wall is calculated with Eqs. 5.1 and 5.4. In the calculation, the cross-sectional areas of the vertical grouted cells are considered as part of the net shear area, and the joint reinforcement is treated as shear reinforcement. The masonry prism strengths and the yield strengths of the steel reinforcement and joint reinforcement obtained from the material tests are used. The shear capacity is calculated based on the ungrouted masonry prism strength, while the flexural capacity is based on both the ungrouted and grouted masonry prism strengths depending on the wall cross-sectional area under compression.

Table 6.10 to Table 6.13 show the code-based shear strength (V_n) as calculated from Eq. 5.1, the upper limit of the shear strength ($V_{n,\max}$) as calculated from Eq. 5.4, and the flexural strength (V_{flex}). The code-based lateral load capacity of a wall component is equal to the minimum of V_n, $V_{n,\max}$, and V_{flex}. The code-based capacity is compared to the wall strength ($V_{\max}$) obtained from the respective pushover analysis by taking the ratio of former to the latter. Strength ratios below 1.0 indicate that the code-based strength is conservative with respect to strength obtain from the analysis. The tables also include the shear strength provided by the joint reinforcement (V_{JR}). For all four designs, the calculated strengths show that wall components W2/W5 and W3/W6 are

shear-dominated, while W1/W4 is shear-dominated for negative loading and flexure-dominated for positive loading. In most cases, the code-based strength is lower than that calculated in the pushover analysis. When wall W1/W4 is subjected to negative loading and W3/W6 is subjected to positive loading, the strength ratio is in the range of 0.6 - 0.8. In these cases, the code-based strength is governed by the upper limit $V_{n,\max}$. The higher strength from the pushover analysis could be attributed to the beneficial influence of the wall flange, which enhances the shear-compression resistance at the wall toe. The same observation is made in the previous chapter for W1/W4 and W3/W6 of Specimen 1. For W2/W5, the code-based strength is closer to the pushover analysis result with the strength ratio in the range of 0.7 - 1.1. It can also be observed that for W2/W5, the code-based strength is more conservative for the cases with double grouted cells (DG and DG/JR) than for the cases with single grouted cells (SG and SG/JR). The code equation slightly overestimates the shear strength of wall W3/W6 in the DG/JR and SG/JR when the wall is subjected to negative loading and is under tension. However, for the DG, even when W3/W6 is under tension, the code prediction is conservative.

In most of the cases examined, the code-based shear strength of the wall components has been found to be lower (or equal) than the strength obtained from the pushover analyses. Exception to this is W1/W4 in the SG/JR and DG/JR when it is subjected to tension and W2/W5 in the SG/JR when it is subjected to positive loading. For these walls, the code-based strength is only slightly higher than the strength obtained from the pushover analysis. However, it should be noted that under an earthquake excitation, the shear strengths of the wall components are likely to be lower than the strengths from the pushover analysis. This is because the shear strengths of PGM walls can be significantly affected by the loading history. The amount of reduction in strength under an earthquake scenario will depend on the number and amplitude of displacement cycles the structure

is subjected to before the walls reach their peak strengths. Therefore, the values of the strength ratios shown in Table 6.10 through Table 6.13 are expected to be higher when the structure is subjected to an earthquake excitation.

6.6 Summary and Conclusions

This chapter presents an experimental and numerical study on the seismic performance of a one-story partially grouted reinforced masonry building that had improved design details. It was the second building specimen tested on a shake table for the study of PGM wall systems. The first building (Specimen 1) represented the current masonry design and construction practice in the U.S. for areas of low to moderate seismicity. Both buildings had the same geometry but different design details. Specimen 1 had horizontal bond beams and single grouted vertical cells, all of which contained a #4 bar. During testing, the building developed a sufficient base shear capacity; however, it failed in a very brittle manner as soon as the drift became larger than 0.4%. The objective of the second shake-table test structure was to evaluate the improved design details aimed to enhance the ductility of the structure. Specimen 2 was reinforced with double grouted vertical cells instead of the traditional single grouted vertical cells. Each vertical cell contained a #3 bar. Furthermore, in addition to the horizontal bond beams, as used in Specimen 1, joint reinforcement was placed in every bed joint. Although joint reinforcement is allowed by the code and used in practice, its effectiveness in improving seismic performance has not been investigated thoroughly.

The shake-table testing of Specimen 2 was performed with a sequence of ground motions of progressively increasing intensity. The structure was tested up to a roof drift ratio of 1.1% and behaved in a relatively ductile manner without sudden drops in the lateral resistance. It developed a base shear capacity that was 18% higher than the capacity reached by Specimen 1. During the testing, significant sliding was observed along the mortar joints of the ungrouted panels and fine

cracking in the ungrouted units. The double grouted cells behaved in a flexure-dominated manner. Horizontal cracks related to flexure were formed at distinct locations along the height of the grouted cells and high tensile strains were registered by the strain gages attached on the vertical bars. At some locations, the recorded strains exceeded the value of 0.02. During the last motion of testing, in which the peak roof drift was reached, diagonal cracks started to form in some of the vertical grouted cells. Overall, the structure developed a superior performance compared to Specimen 1 and behaved like an RC frame with a weak infill.

The behavior of the test structure has been further studied with nonlinear FE analyses. The FE model developed for Specimen 2 was subjected to a sequence of motions obtained from the shake-table tests. The results show that the model can predict reasonably well the response histories, load capacity, and damage pattern observed in the testing sequence. The model was used to investigate the influence of the loading history on the response of the structure. Nonlinear pushover analyses as well as an additional time-history analysis using a single ground motion of high intensity were conducted. The results show that the lateral load resistance of the structure is influenced by the number and amplitude of the displacement cycles that the structure experiences. In the pushover analyses, the model develops a capacity that is 40% higher than that developed in the time-history analysis using a sequence of ground motions. Under a single high-intensity motion record, the model reaches a strength that is 18% higher than that under a sequence of ground motions.

Further analyses have been performed to demonstrate the influence of double grouted vertical cells and joint reinforcement on the seismic behavior of the structure. The results show that the superior performance observed in the shake-table test of Specimen 2 (compared to Specimen 1) is mainly attributed to the double grouted cells. The joint reinforcement may have

some beneficial influence by restraining the opening of cracks during the post-peak regime of the response. In particular, the pushover analyses indicate that joint reinforcement also contributes the shear strength. The effect of joint reinforcement has been also investigated for a structure that has single grouted vertical cells. It has been found that joint reinforcement is more beneficial when used with single grouted vertical cells than with double grouted cells for this structure. The numerical results are further used to assess the accuracy of the shear-strength equation of TMS 402 (2016). For most of the cases considered, with or without joint reinforcement and with single or double vertical grouted cells, the shear strengths of the wall components calculated with the code equation are lower than the strengths given in the pushover. However, it should be noted that the code equation is evaluated with results from pushover analyses. Under an earthquake excitation the load capacity of the wall components can be lower due to the cyclic deterioration of the wall resistance.

Table 6.1 Average compressive strengths obtained from material samples of Specimen 2.

Sample	Strength (ksi)	Sample	Strength (ksi)	Sample	Strength (ksi)	Sample	Strength (ksi)
Mortar cylinder	3.7	Grout prism	4.8	Ungrouted prism	1.5	Concrete footing	6.3
Grout cylinder	4.7	Grouted prism	2.4	CMU block	3.2	Concrete roof	3.7

Table 6.2 Average properties of the reinforcement of Specimen 2.

Reinforcement	f_y (ksi)	f_u (ksi)	ε_u
Vertical bars #3	65.5	104.2	0.11
Horizontal bars #4	66.3	97.2	0.12
Joint reinforcement	70.0	75.0	0.06

Table 6.3 Summary of structural response of Specimen 2 during the tests.

Motion No.	Test ID	Specimen period after test (s)	Eff. Intensity I_{eff} (x MCE)	PGA (g)	Peak roof accel. (g)	Peak roof drift ratio (%)	Peak base shear (kips)
1	EC1940 63%-A	0.068	0.31	0.43	-0.53	-0.01	104.6
2	EC1979 36%-A	0.068	0.34	0.43	0.56	-0.01	-110.9
3	EC1940 84%-A	n.a.	0.38	0.59	-0.72	0.02	140.9
4	EC1940 63%-B	n.a.	0.35	0.42	-0.63	n.a.	123.9
5	EC1979 36%-B	0.070	0.36	0.41	0.68	-0.01	-134.3
6	EC1940 63%-C	n.a.	0.46	-0.52	-0.71	0.03	139.2
7	EC1979 36%-C	0.088	0.59	0.43	1.09	-0.04	140.3
8	EC1979 48%-A	0.090	0.69	0.54	1.28	-0.06	-251.5
9	EC1940 84%-B	0.108	0.89	-0.66	-1.48	0.08	290.9
10	EC1979 72%-A	0.140	1.05	1.13	1.68	-0.14	-331.5
11	EC1979 72%-B	n.a.	0.82	0.78	1.43	-0.14	-281.3
12	EC1979 72%-C	0.146	0.81	0.76	1.45	-0.15	-285.1
13	EC1979 86%	0.166	0.94	0.89	1.56	-0.18	-308.2
14	EC1979 108%	0.185	1.08	1.06	1.66	-0.24	-327.3
15	EC1979 122%-A	0.249	1.34	1.19	1.71	-0.34	-336.6
16	EC1979 137%	0.352	1.52	1.27	-1.56	-0.60	308.1
17	EC1979 122%-B	0.398	1.24	1.06	1.31	-1.02	-258.0

Note: Test ID indicates the scaling of the original record in addition to the similitude scaling. The letters A, B, or C next to the percentage indicates the 1st, 2nd, and 3rd time the same motion was applied.

Table 6.4 Material parameters for smeared-crack shell elements in the model of Specimen 2 (see Figure 2.8 for the parameter definitions).

Shells elements	f_m **(ksi)**	f_o **(ksi)**	E_m **(ksi)**	f_t **(ksi)**	ε_o	ε_u	**Net width (in)**
Grouted masonry	2.39	1.59	1434	0.40	0.003	0.040	7.625
Ungrouted units	1.54	1.03	924	0.40	0.003	0.015	2.8

Table 6.5 Material parameters of cohesive-crack interface elements in the model of Specimen 2 (see Section 2.5.2 for the parameter definitions).

Interface elements	D_{nn} / D_{tt} **(ksi/in)**	s_o **(ksi)**	μ_o / μ_r	r_o / r_r **(ksi)**	G_{fI} **(kips/in)**	G_{fII} **(kips/in)**	$\zeta_{dil,o}$ / $\zeta_{dil,r}$	d_o **(in)**	**Net width (in)**
Grouted masonry	5000	0.4	1.4 / 1.0	0.05 / 0.01	0.0004	0.004	0.4 / 0.001	0.4	7.625
Ungrouted units	5000	0.4	1.2 / 1.0	0.05 / 0.01	0.0004	0.004	0.2 / 0.001	0.2	2.8
Mortar joints	300 / 125	0.1	0.95 / 0.85	0.02 / 0.01	0.0002	0.002	0.10 / 0.001	0.035	2.5 (head) / 2.13 (bed)
Base interface	5000	0.4	1.5 / 1.5	0.05 / 0.01	0.0004	0.004	0.4 / 0.001	0.4	7.625

Table 6.6 Material parameters for beam elements representing reinforcing steel in the model of Specimen 2 (see Section 2.6 for the parameter definitions).

Size	f_y **(ksi)**	f_u **(ksi)**	E_s **(ksi)**	ε_{sh}	(ε_{sh1}, f_{sh1})	ε_u	D_{cr}
Vertical: #3	65.5	104.2	29000	0.01	(0.03, 84)	0.11	0.55
Horizontal: #4	66.3	97.2	29000	0.01	(0.03, 84)	0.12	0.55

Table 6.7 Material properties of bond-slip/dowel-action interface elements in the model of Specimen 2 (see Section 2.7.3 for parameter definitions).

Masonry compressive strength used for bond strength (ksi)	**Confinement condition**	**Grout compressive strength used for dowel strength (ksi)**	**Displacment parameters for dowel model law d_1 / d_u (in)**
2.39	Confined	4.8	0.03 / 0.06

Table 6.8 Material parameters for beam elements and bond-slip/dowel action interface elements of the joint reinforcement in the model of Specimen 2.

Wire diameter (in)	**f_y (ksi)**	**Mortar strength, f_{mor} (ksi)**	**Bond strength (ksi)**
0.1875	71	3.7	0.073

Table 6.9 Load capacities reached in the pushover analyses of the four design alternatives.

Loading direction	**Lateral load capacity (kips)**			
	DG/JR	**DG**	**SG/JR**	**SG**
Positive	464.5	441.2	337.8	269
Negative	-461.5	411.2	358.6	310

Table 6.10 Comparison of lateral load capacities of the wall components based on TMS 402-16 with capacities from the finite element model of the DG/JR design.

Wall	V_{max} (kips) analysis		P_{Vmax} (kips) analysis		Shear span ratio (M/Vd)		V_{JR} (kips) TMS 402		V_n (kips) TMS 402 (Eq. 5.1)		$V_{n,max}$ (kips) TMS 402 (Eq. 5.4)		V_{flex} (kips) TMS 402		min(V_n,$V_{n,max}$, V_{flex})/V_{max}	
	Neg.	Pos.	Neg.	Pos.	Neg.	Pos.	Neg.	Pos.	Neg.	Pos.	Neg.	Pos.	Neg.	Pos.	Neg.	Pos.
W1	86.9	41.8	101.7	-26.5	0.55	0.55	14.7	14.7	76.3	52.2	55.7	55.7	128.8	21.5	0.64	0.51
W2	112.2	118.6	27.5	42.4	0.29	0.13	27.9	27.9	107.4	105.3	108.6	110.5	153.2	388.6	0.96	0.89
W3	42.4	86.3	-15.1	94.3	0.25	0.55	14.7	14.7	50.0	74.9	64.3	55.7	69.3	112.6	1.18	0.65

Note: Axial loads with positive sign represent compression.

Table 6.11 Comparison of lateral load capacities of the wall components based on TMS 402-16 with capacities from the finite element model of the DG design.

Wall	V_{max} (kips) analysis		P_{Vmax} (kips) analysis		Shear span ratio (M/Vd)		V_n (kips) TMS 402 (Eq. 5.1)		$V_{n,max}$ (kips) TMS 402 (Eq. 5.4)		V_{flex} (kips) TMS 402		min(V_n,$V_{n,max}$,V_{flex})/V_{max}	
	Neg.	Pos.	Neg.	Pos.	Neg.	Pos.	Neg.	Pos.	Neg.	Pos.	Neg.	Pos.	Neg.	Pos.
W1	82.1	36.3	97.8	-25.8	0.55	0.55	60.8	37.6	55.7	55.7	127.8	22.1	0.7	0.6
W2	99.0	111.0	33.1	42.6	0.29	0.13	80.5	77.4	108.6	110.5	162.1	389.3	0.8	0.7
W3	58.2	81.7	-6.8	85.2	0.25	0.55	36.9	58.5	64.3	55.7	85.2	115.7	0.6	0.7

Note: Axial loads with positive sign represent compression.

Table 6.12 Comparison of lateral load capacities of the wall components based on TMS 402-16 with capacities from the finite element model of the SG/JR design.

Wall	V_{max} (kips) analysis		P_{Vmax} (kips) analysis		Shear span ratio (M/Vd)		V_{JR} (kips) TMS 402		V_n (kips) TMS 402 (Eq. 5.1)		$V_{n,max}$ (kips) TMS 402 (Eq. 5.4)		V_{flex} (kips) TMS 402		min(V_n,$V_{n,max}$,V_{flex})/V_{max}	
	Neg.	Pos.	Neg.	Pos.	Neg.	Pos.	Neg.	Pos.	Neg.	Pos.	Neg.	Pos.	Neg.	Pos.	Neg.	Pos.
W1	62.0	36.0	85.5	-2.8	0.55	0.55	14.7	14.7	65.8	49.3	43.2	43.2	107.3	32.5	0.7	0.9
W2	84.9	81.1	30.6	38.8	0.29	0.13	27.9	27.9	95.2	91.0	87.3	88.8	138.5	333.8	1.0	1.1
W3	40.9	78.2	-6.0	89.1	0.25	0.55	14.7	14.7	43.1	66.6	49.8	43.2	65.2	110.1	1.1	0.6

Note: Axial loads with positive sign represent compression.

Table 6.13 Comparison of lateral load capacities of the wall components based on TMS 402-16 with capacities from the finite element model of the SG design.

Wall	V_{max} (kips) analysis		P_{Vmax} (kips) analysis		Shear span ratio (M/Vd)		V_n (kips) TMS 402 (Eq. 5.1)		$V_{n,max}$ (kips) TMS 402 (Eq. 5.4)		V_{flex} (kips) TMS 402		min(V_n,$V_{n,max}$,V_{flex})/V_{max}	
	Neg.	Pos.	Neg.	Pos.	Neg.	Pos.	Neg.	Pos.	Neg.	Pos.	Neg.	Pos.	Neg.	Pos.
W1	61.2	24.8	82.8	-3.8	0.55	0.55	50.6	34.4	43.2	43.2	105.1	31.6	0.7	1.3
W2	71.0	73.2	29.5	40.8	0.29	0.13	67.1	63.5	87.3	88.8	136.7	341.0	0.9	0.9
W3	37.4	55.7	22.6	55.7	0.25	0.55	33.8	45.6	49.8	43.2	119.9	82.6	0.9	0.8

Note: Axial loads with positive sign represent compression.

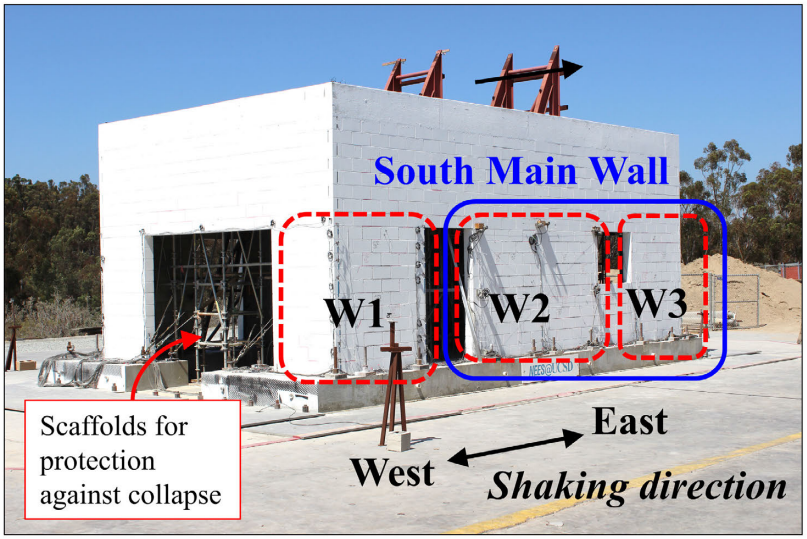

(a) South wall

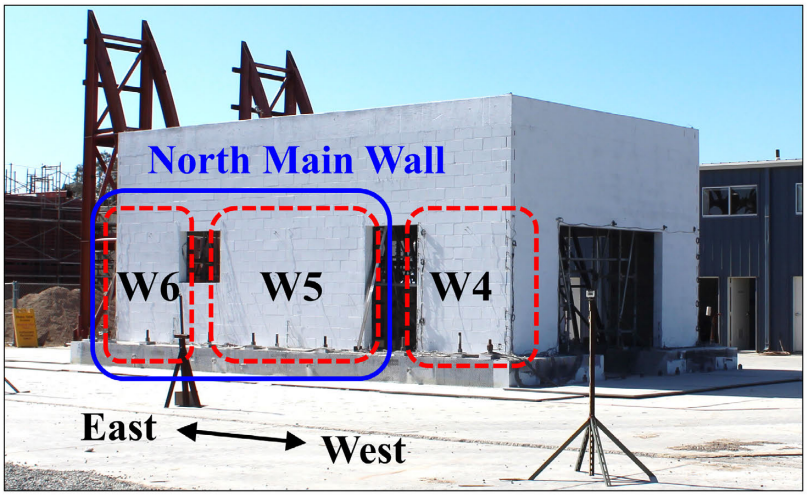

(b) North wall

Figure 6.1 Configuration and wall components of the test structure.

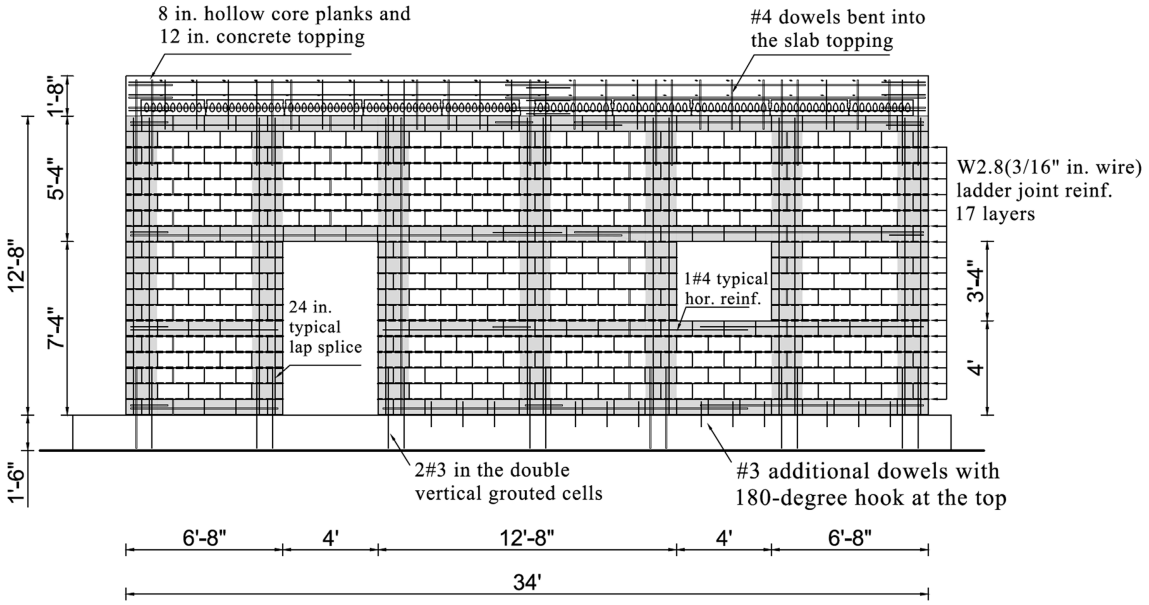

(a) South wall

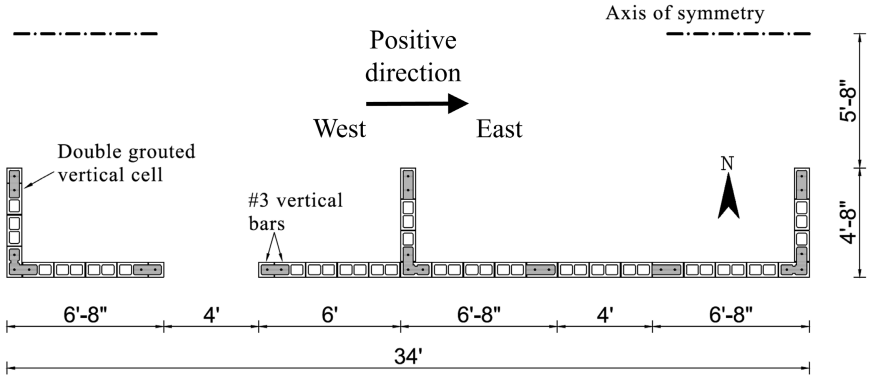

(b) Plan view of the south wall

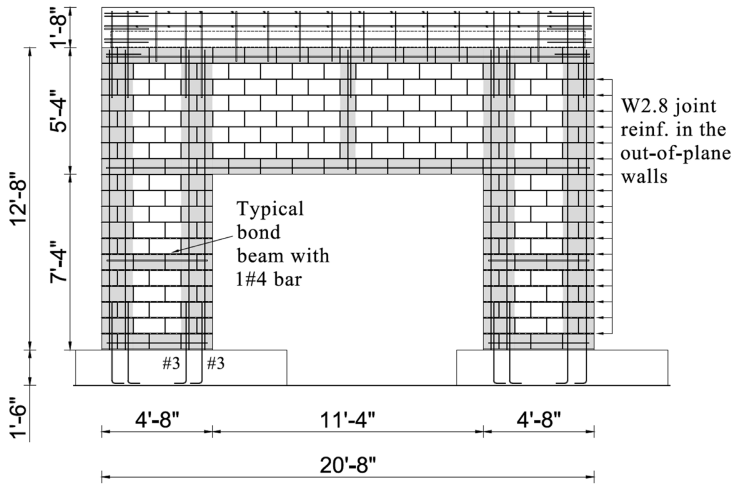

(c) East wall

Figure 6.2 Reinforcement details of Specimen 2.

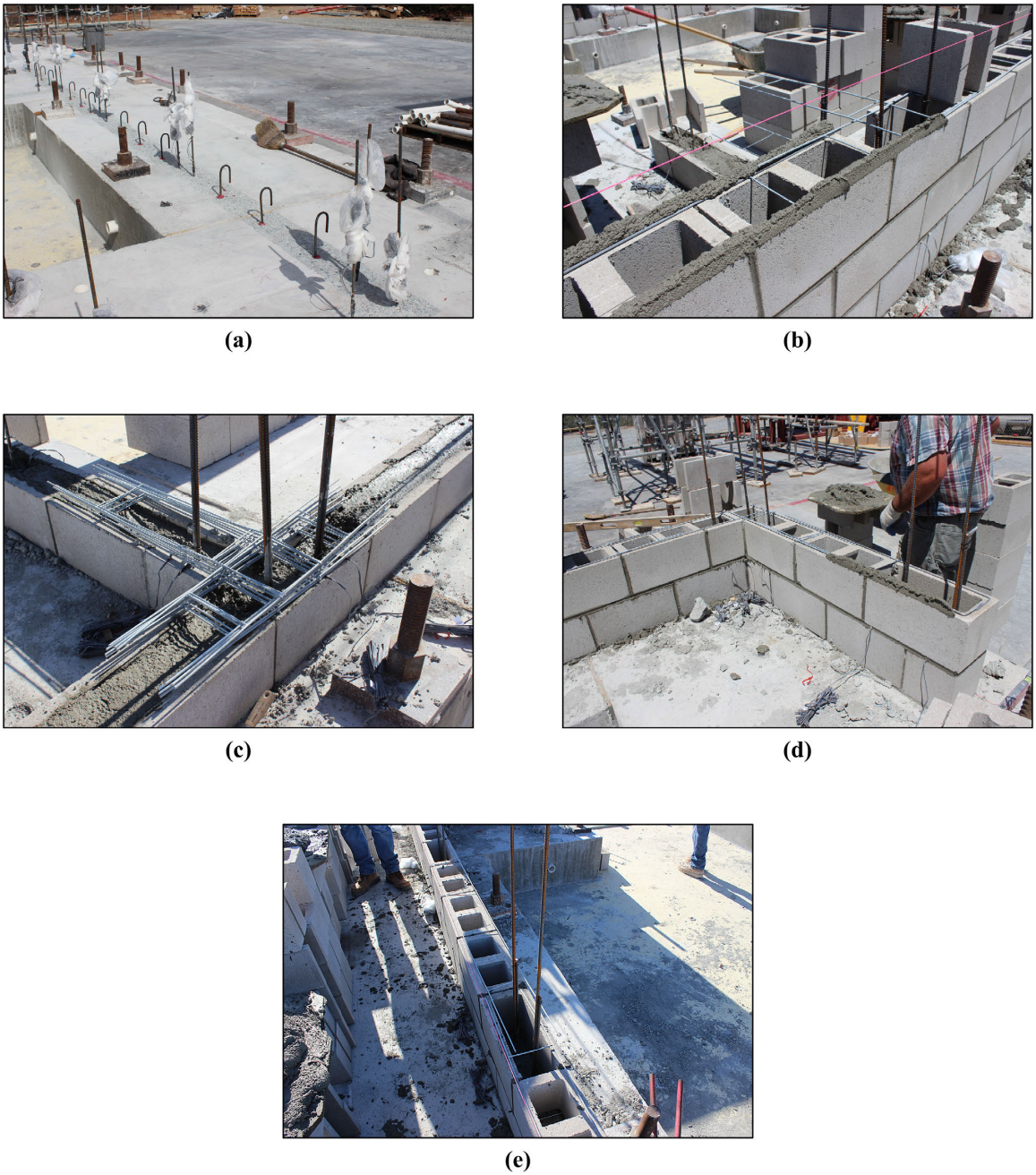

Figure 6.3 Construction of Specimen 2. (a) Roughening of footing surface and dowel bars in Main Walls; (b) ladder-type joint reinforcement embedded in a mortar joint; (c) prefabricated joint reinforcement segments at a T-wall; (d) construction of W4; (e) construction of W5.

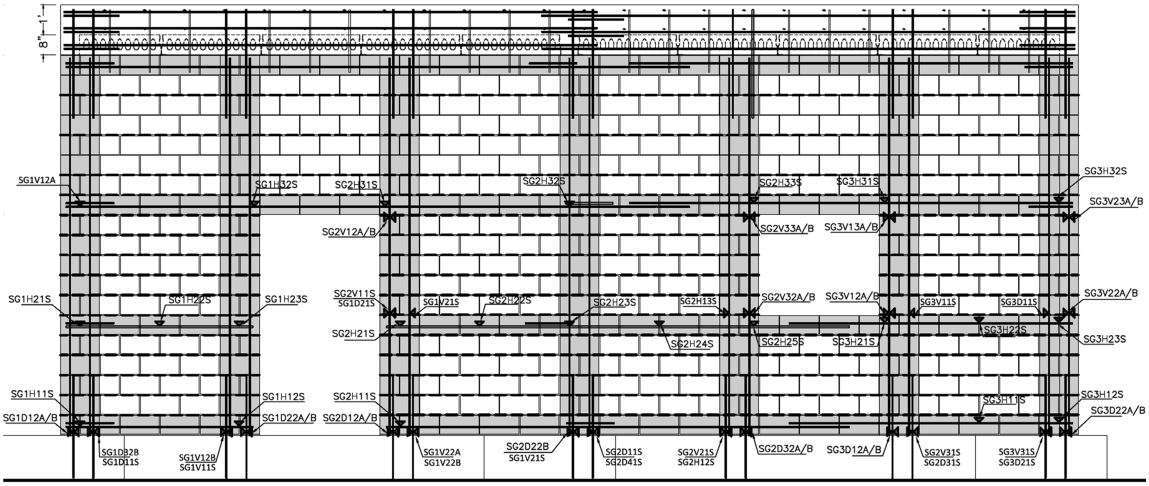

Figure 6.4 Locations of strain gages at the south wall of Specimen 2.

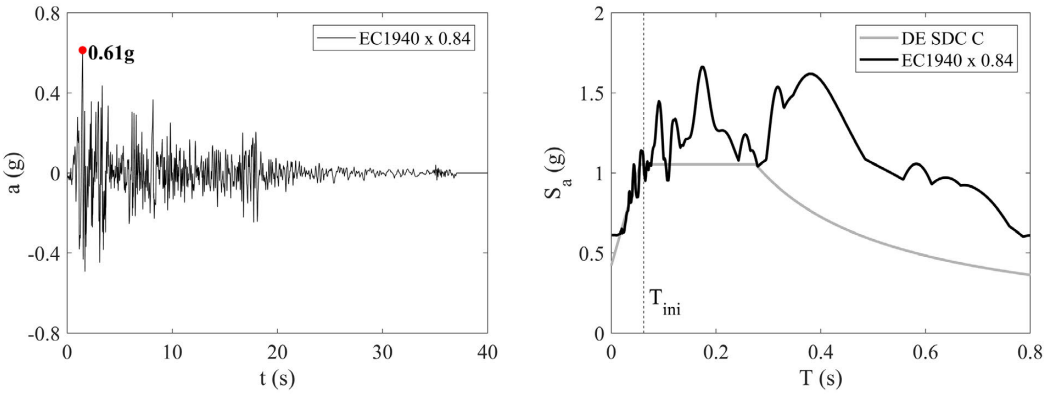

(a) El Centro 1940 record

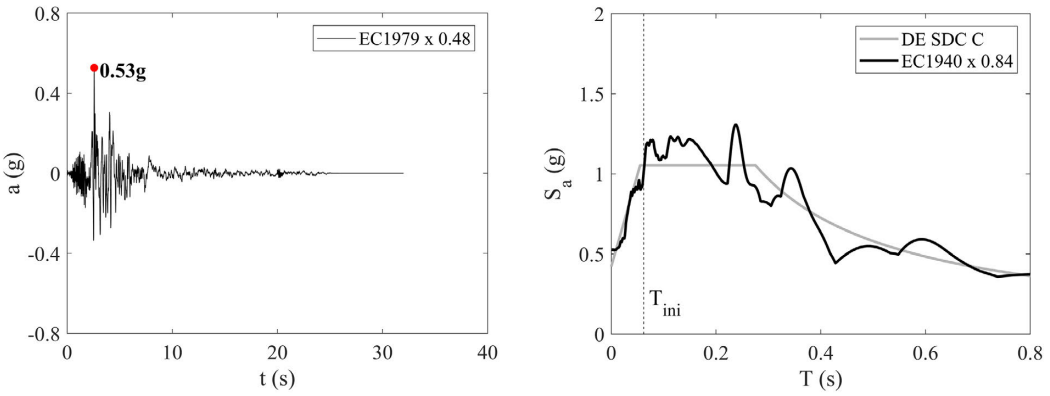

(b) El Centro 1979 record

Figure 6.5 Earthquake records used for testing Specimen 2 and scaled to the DE after the similitude scaling is applied.

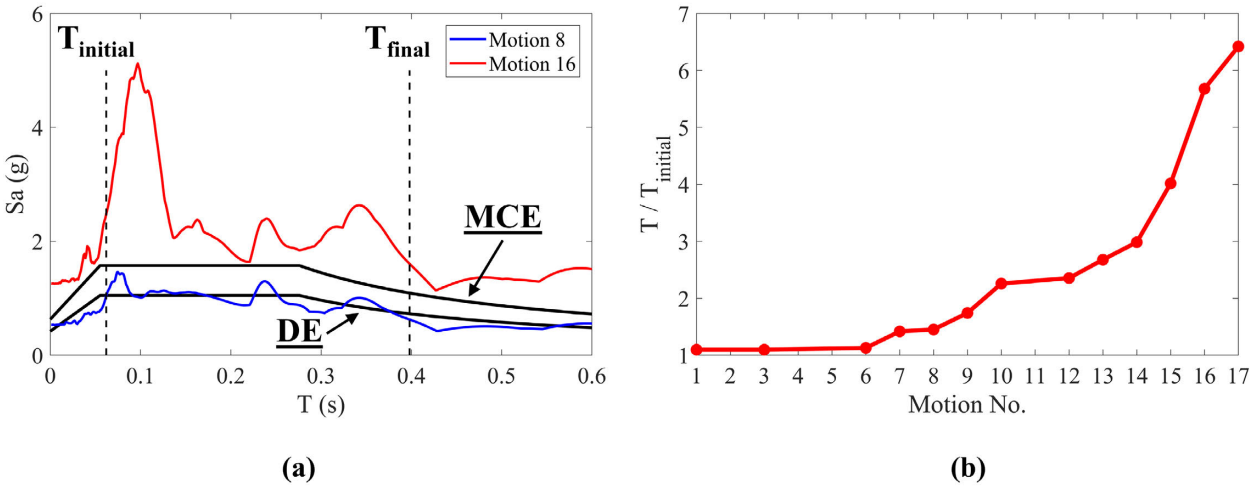

Figure 6.6 Ground motion and structural period change of Specimen 2. (a) Acceleration response spectra of Motion 8 and 16; (b) change of structural period.

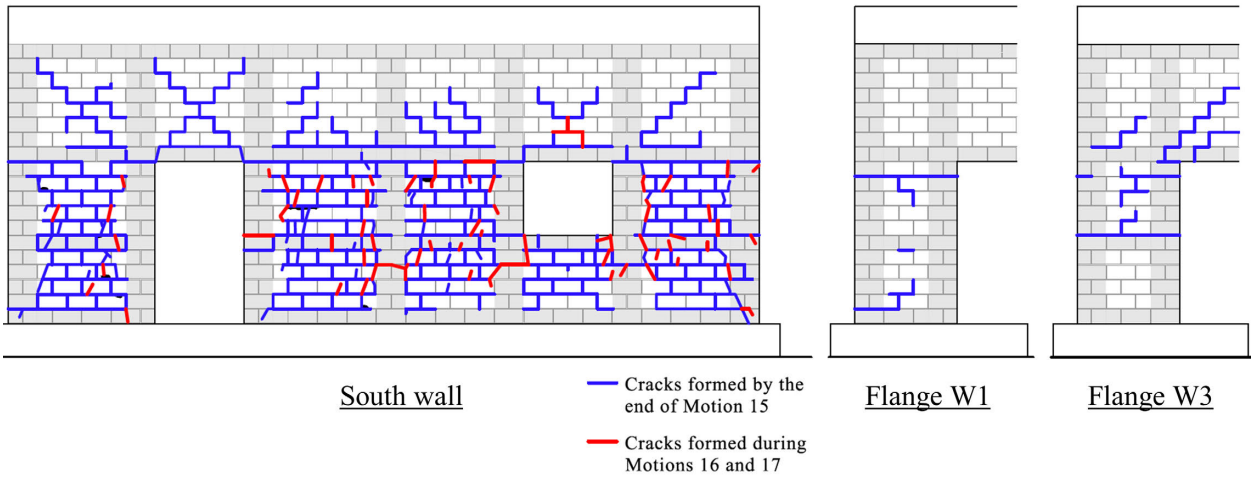

Figure 6.7 Crack pattern of Specimen 2 in south wall and flanges.

South wall

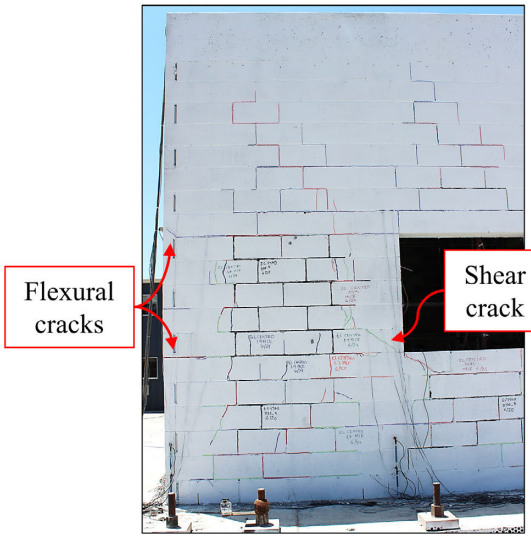

W6

W4

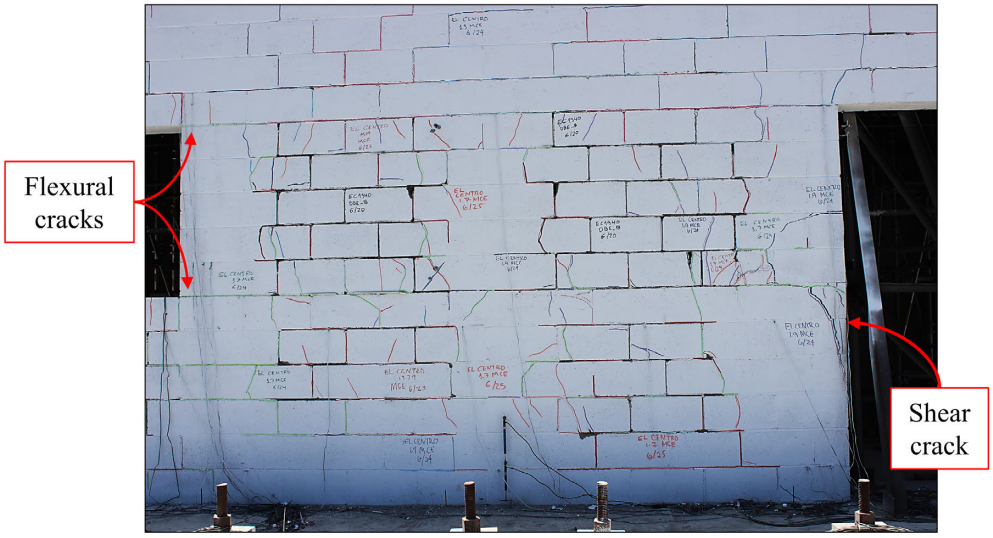

W5

Figure 6.8 Damage in Specimen 2 at the end of testing.

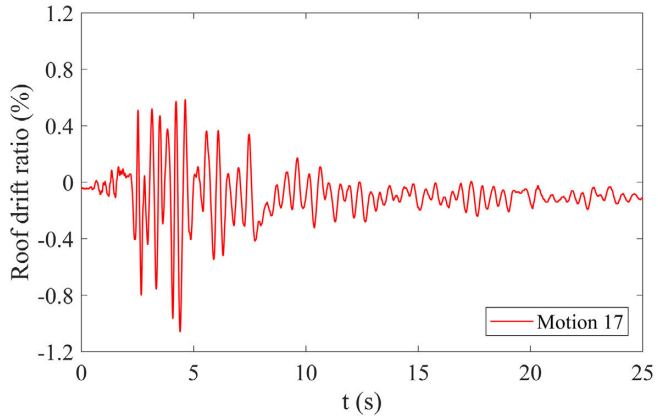

(a)

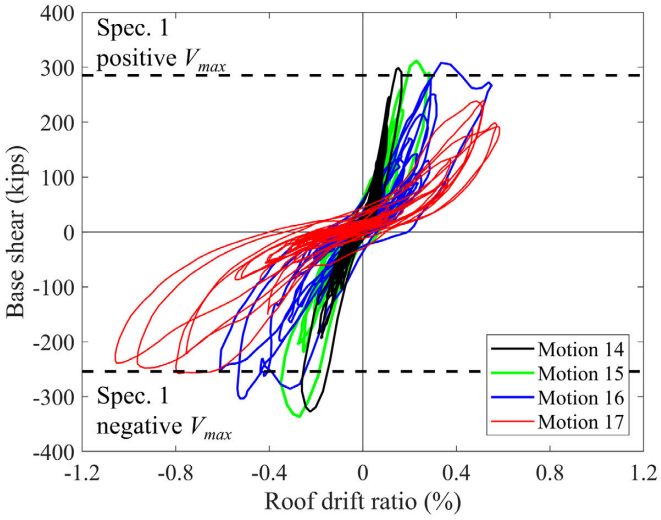

(b)

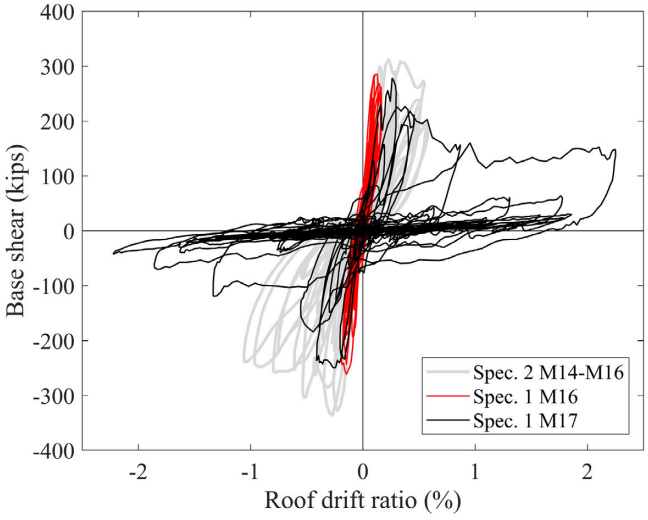

(c)

Figure 6.9 Global response of Specimen 2. (a) Time history of roof drift ratio during Motion 17; (b) hysteresis curves for Motions 14 through 17; (c) comparison with Specimen 1.

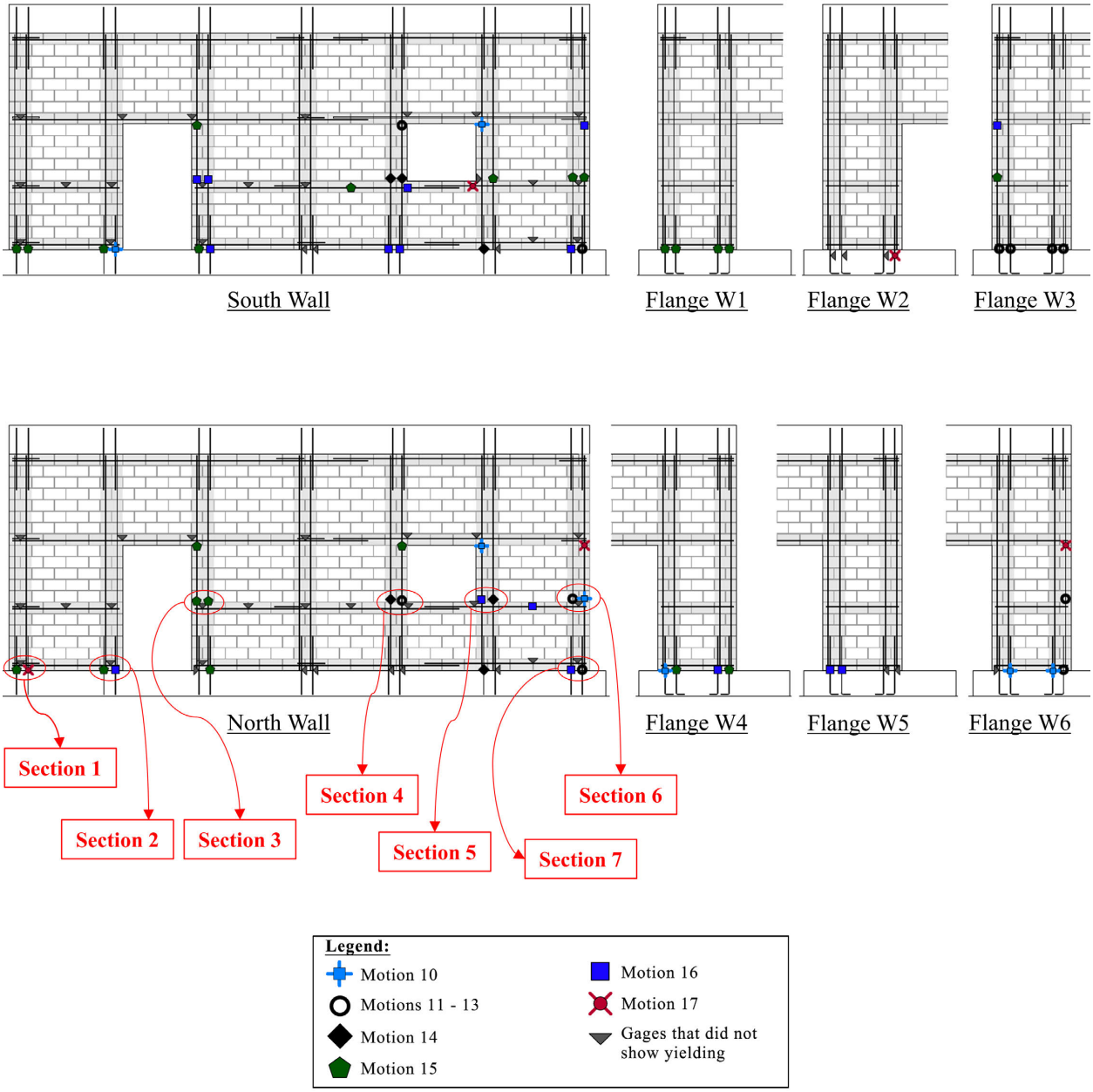

Figure 6.10 Yielding of reinforcement at the locations of the strain gages of Specimen 2.

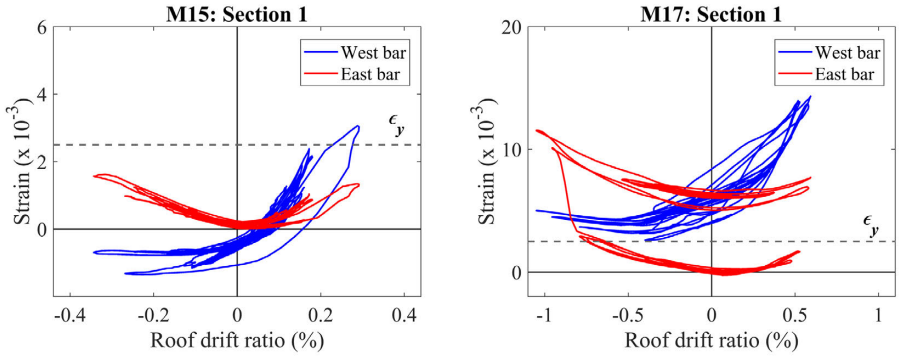

(a) Section 1

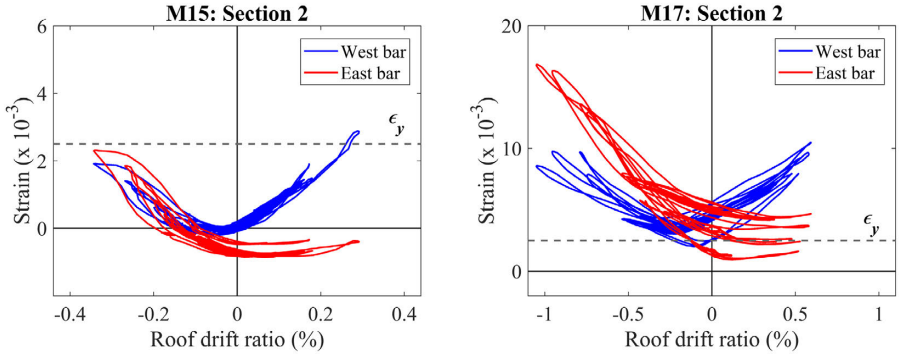

(b) Section 2

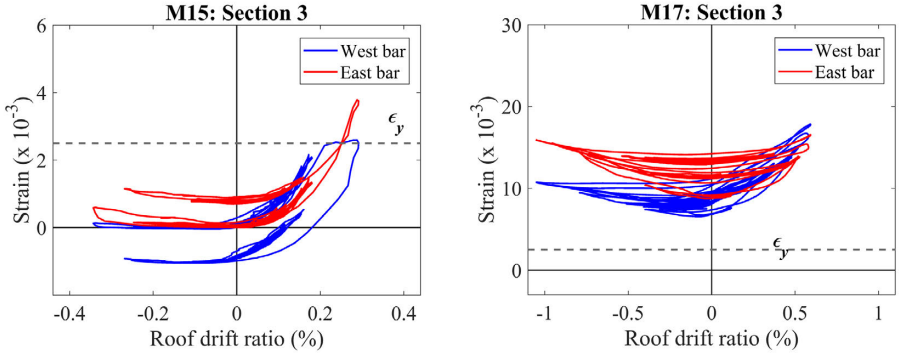

(c) Section 3

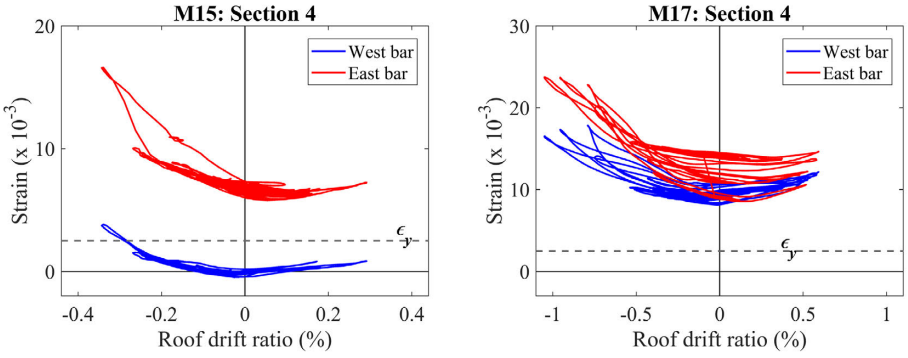

(d) Section 4

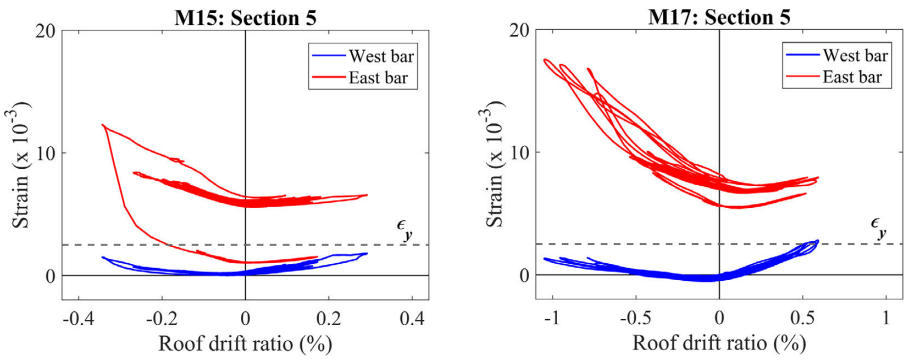

(e) Section 5

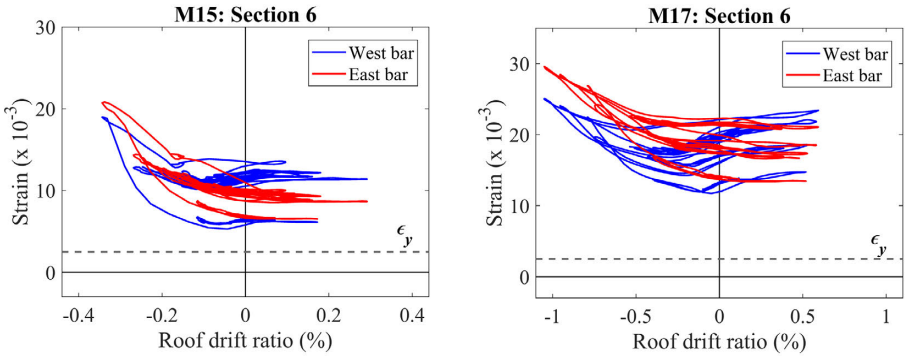

(f) Section 6

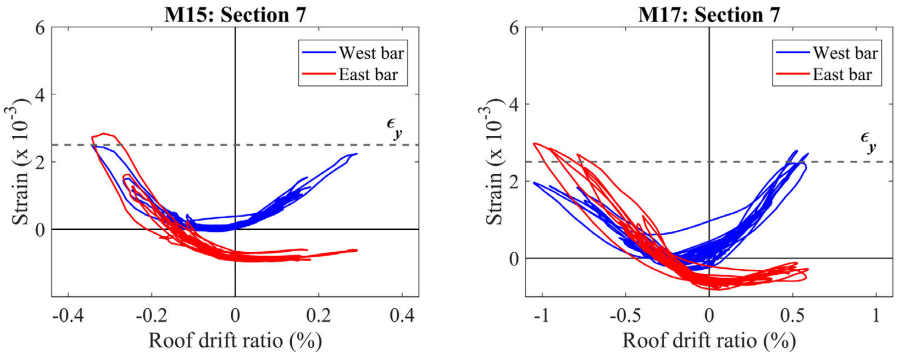

(g) Section 7

Figure 6.11 Strains in vertical bars of Specimen 2 measured during Motions 15 and 16.

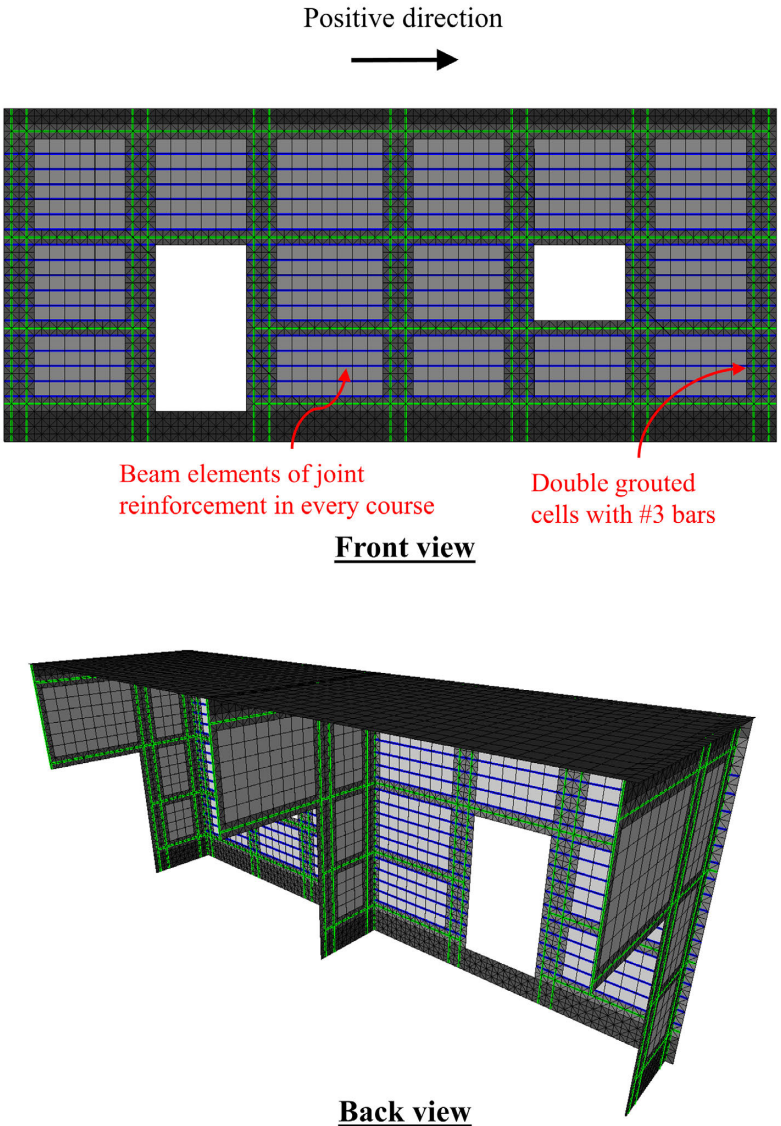

Figure 6.12 Finite element model of Specimen 2.

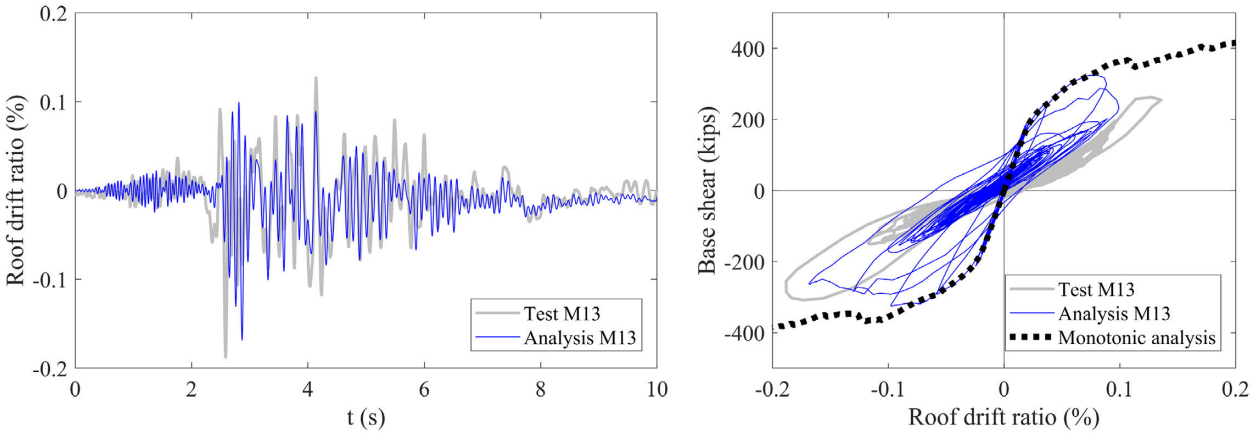

(a) Motion 13

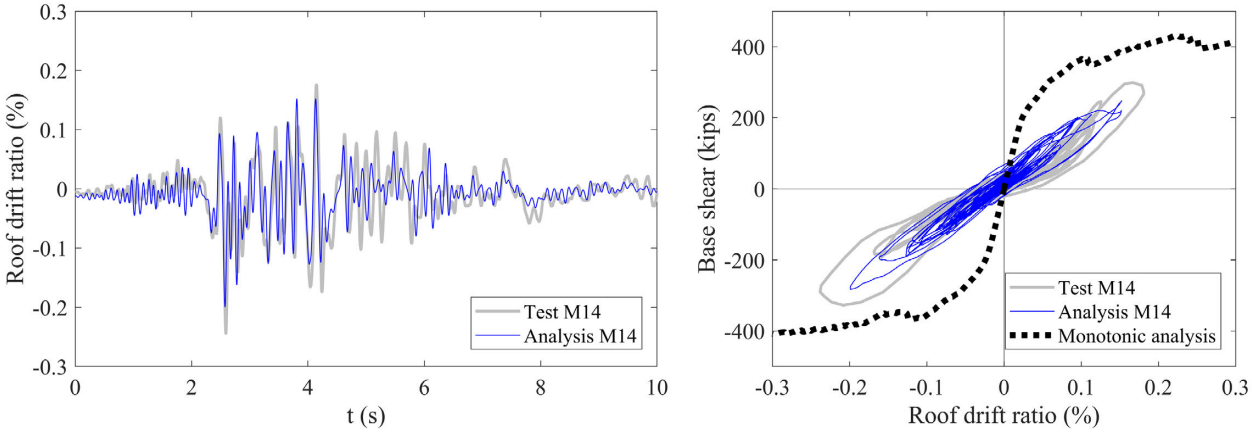

(b) Motion 14

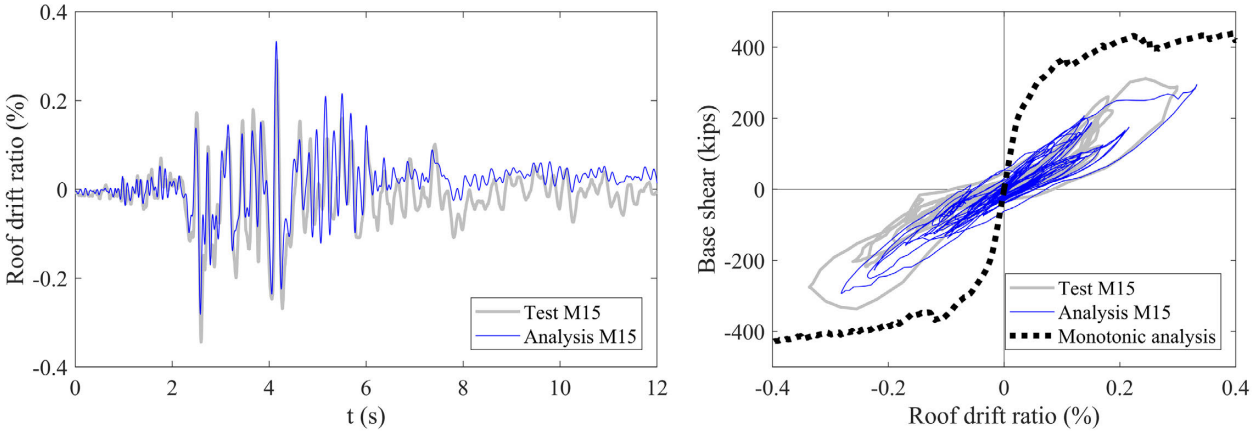

(c) Motion 15

Figure 6.13 Comparison of numerical and experimental results for: (a) Motion 13; (b) Motion 14; and (c) Motion 15.

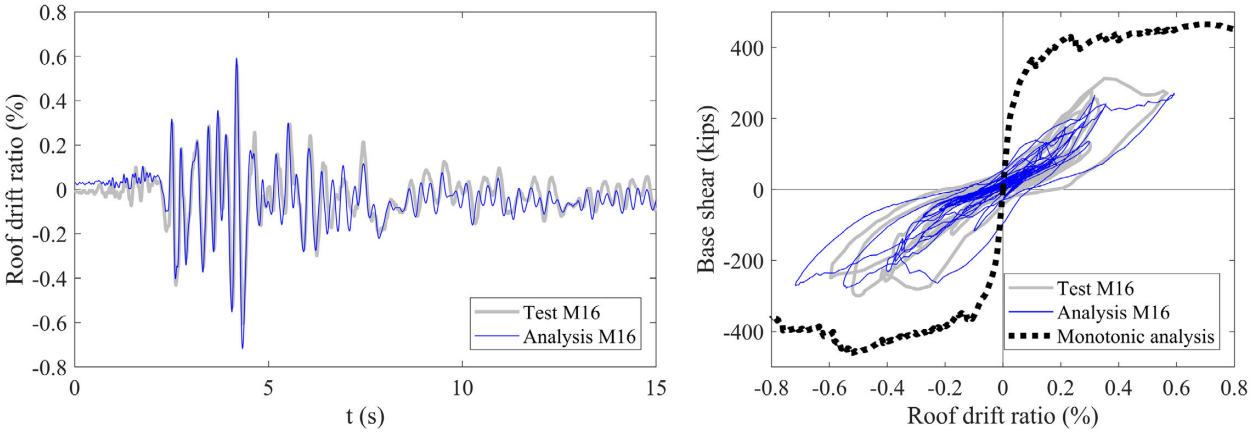

(a) Motion 16

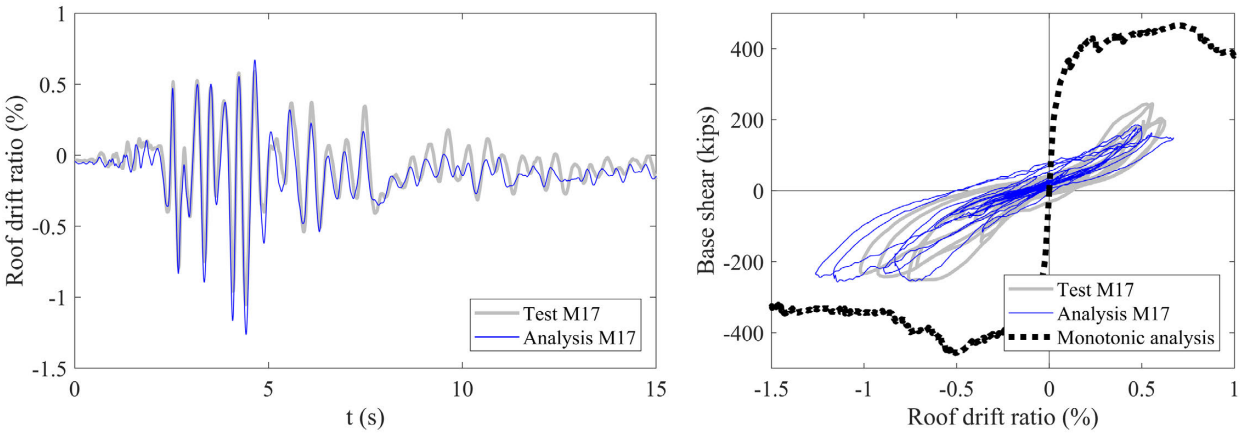

(b) Motion 17

Figure 6.14 Comparison of numerical and experimental results for: (a) Motion 16; and (b) Motion 17.

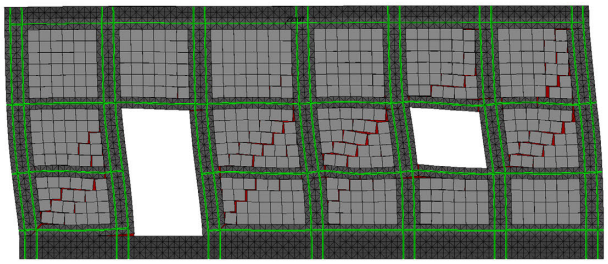

(a) At peak negative load

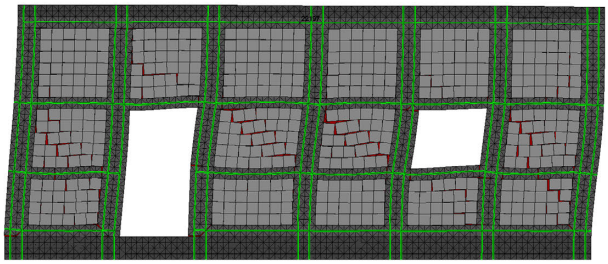

(b) At peak positive load

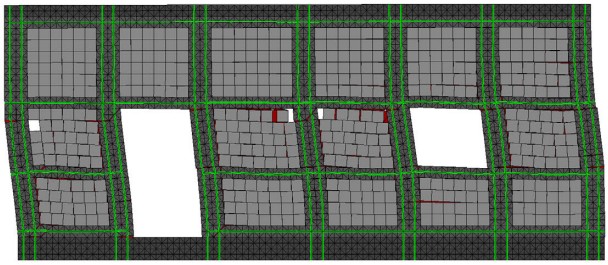

(c) At peak negative drift

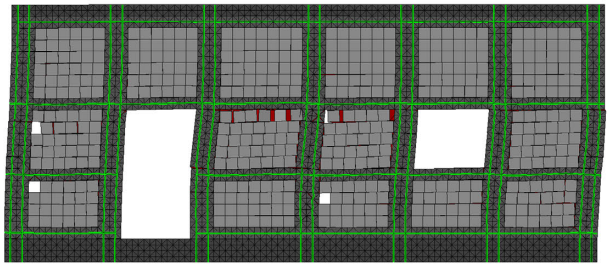

(d) At peak positive drift

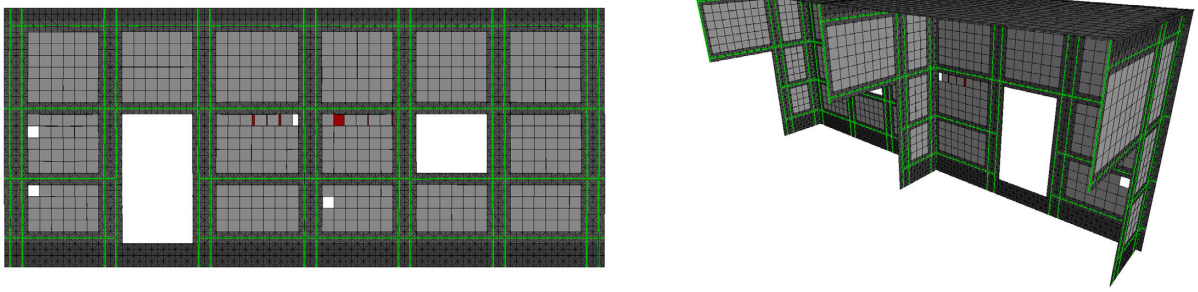

(e) At the end of the analysis

Figure 6.15 Damage shown by the time-history analysis. Deformations are magnified by 70 times in (a) and (b), and by 5 times in (c), and (d). The joint reinforcement is not shown for clarity.

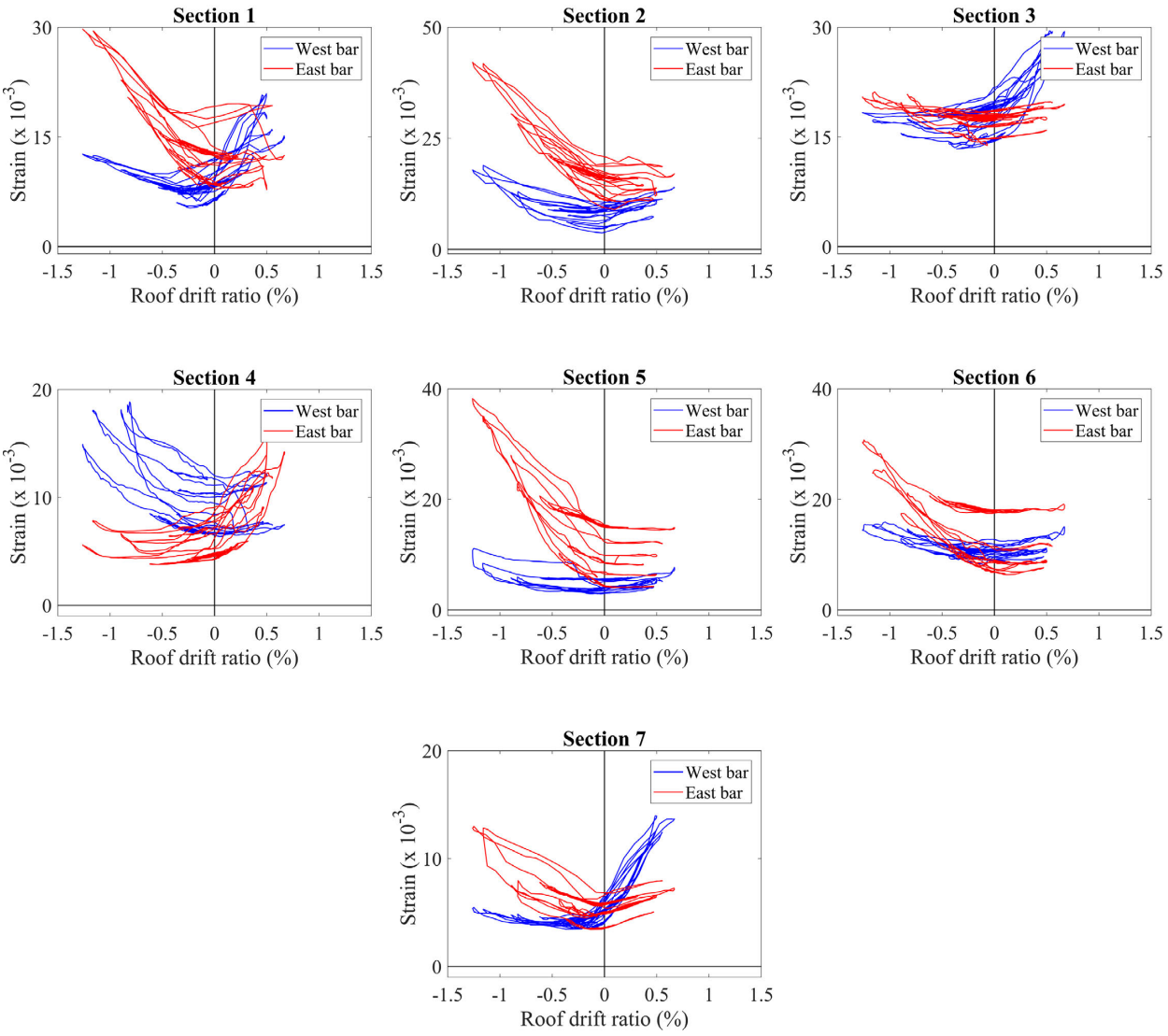

Figure 6.16 Strains developed in the vertical bars of the model during the time-history analysis with Motion 17.

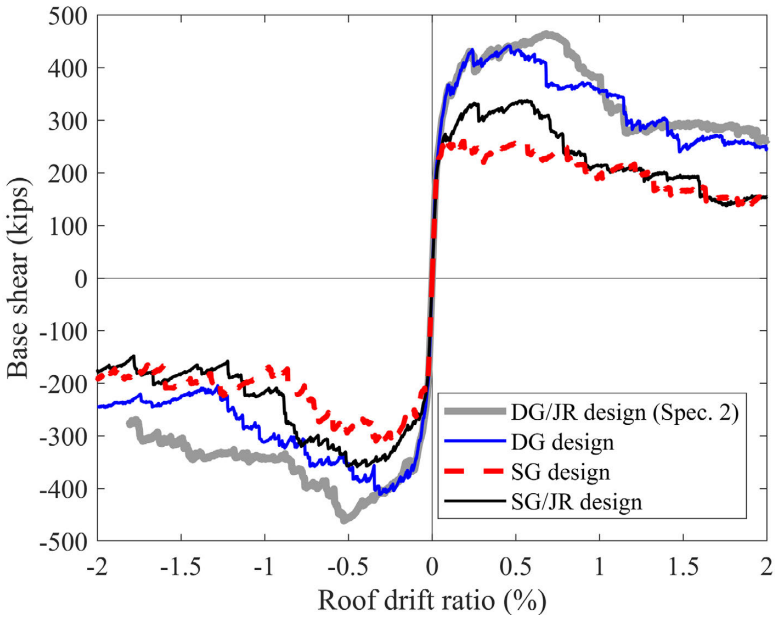

Figure 6.17 Comparion of pushover load-displacement response of the DG/JR (Specimen 2), DG, SG, and SG/JR designs.

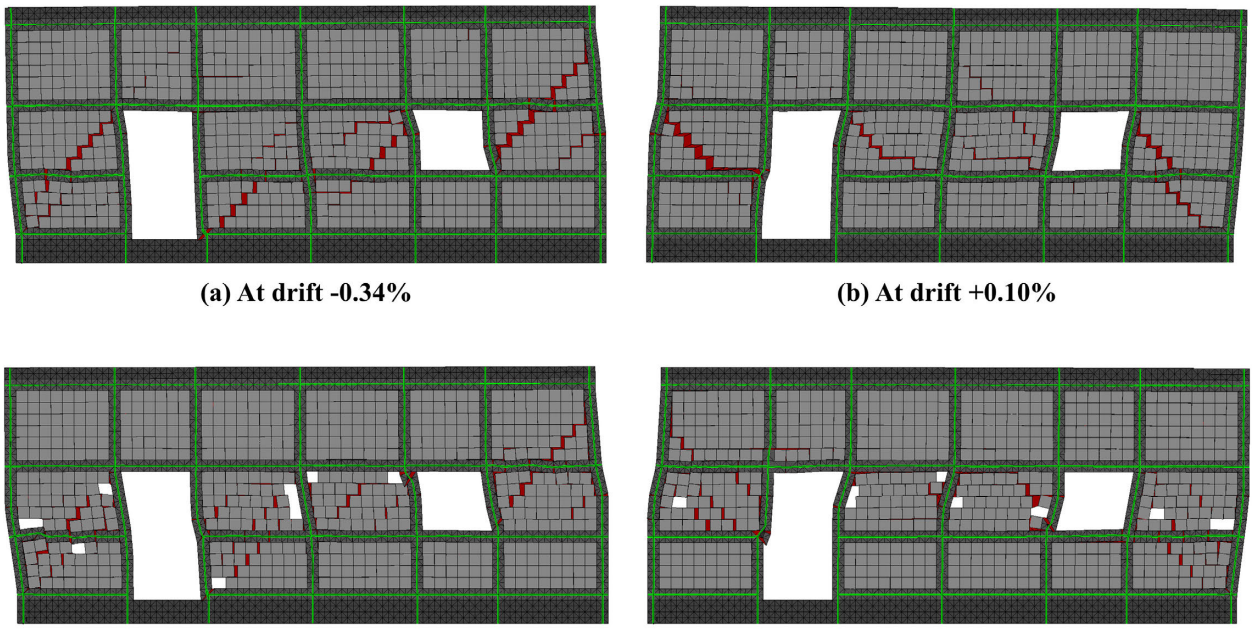

(a) At drift -0.34%

(b) At drift +0.10%

(c) At drift -1.50%

(d) At drift +1.50%

Figure 6.18 Damage in the pushover analysis of the SG design at: (a) the peak strength in the negative direction (magnified by 15); (b) the peak strength in the positive direction (magnified by 70); (c), (d) at drift 1.50% in the negative and positive direction (magnified by 4).

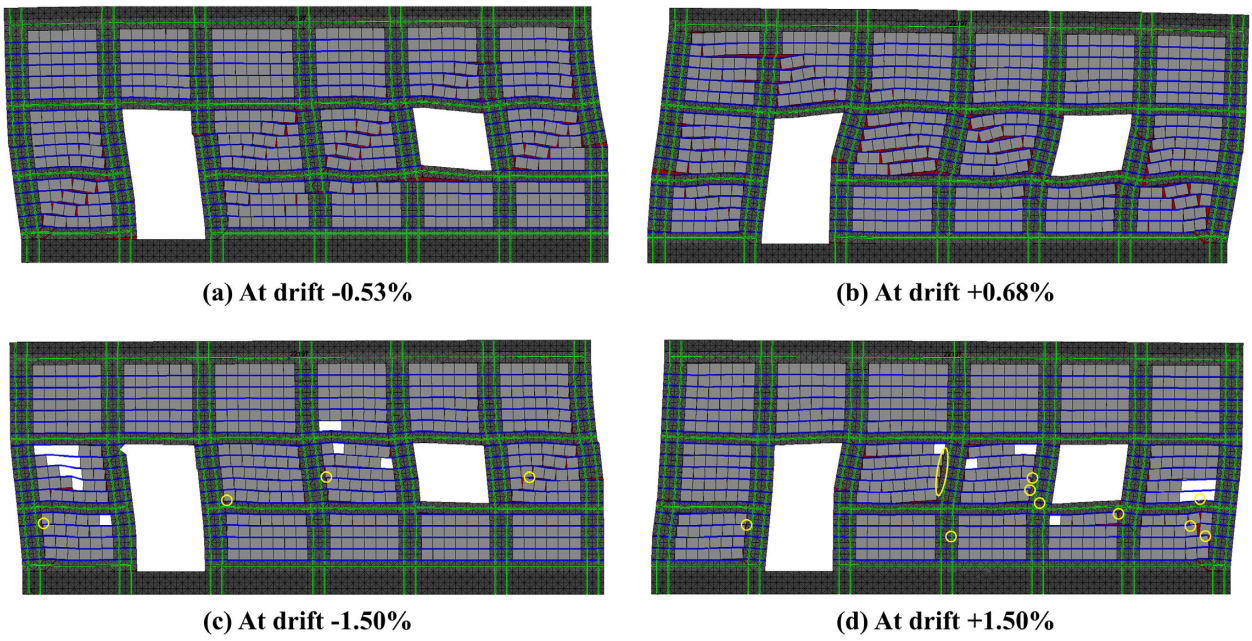

(a) At drift -0.53%

(b) At drift +0.68%

(c) At drift -1.50%

(d) At drift +1.50%

Figure 6.19 Damage in the pushover analysis of Specimen 2 at: (a), (b) the peak strength in the negative and positive direction (magnified by 15); (b); (c), (d) drift 1.50% in the negative and positive direction (magnified by 4). Locations of joint reinforcement rupture are indicated.

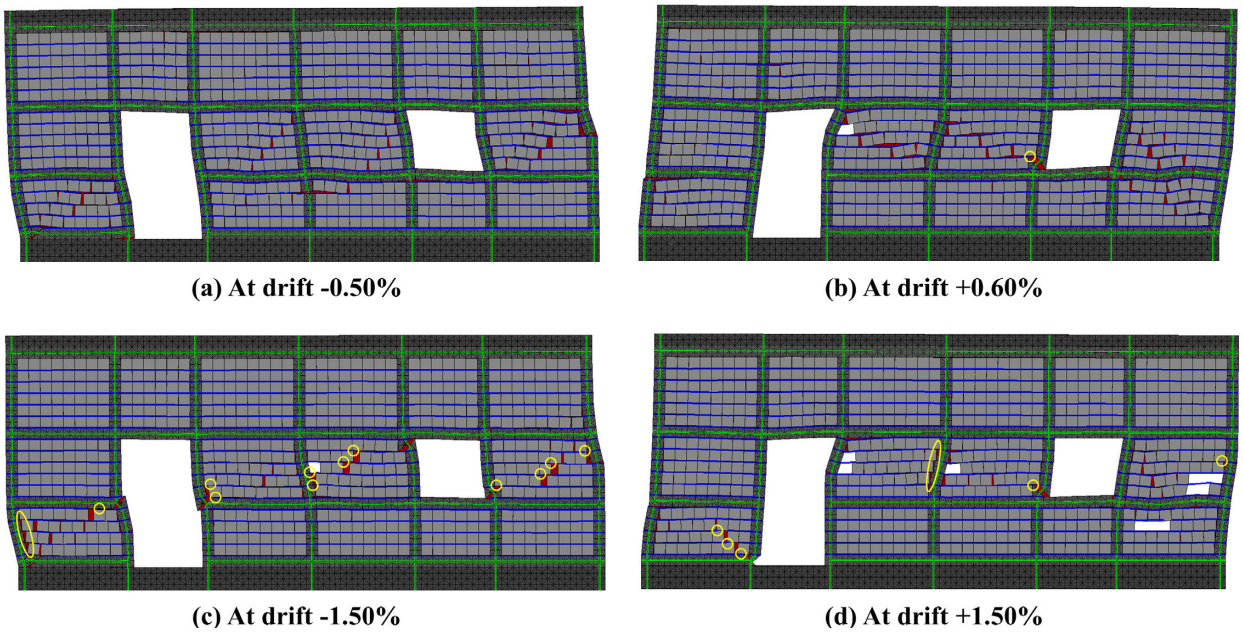

(a) At drift -0.50%

(b) At drift +0.60%

(c) At drift -1.50%

(d) At drift +1.50%

Figure 6.20 Damage in the pushover analysis of the SG/JR design at: (a), (b) the peak strength in the negative and positive direction (magnified by 15); (b); (c), (d) drift 1.50% in the negative and positive direction (magnified by 4). Locations of joint reinforcement rupture are indicated.

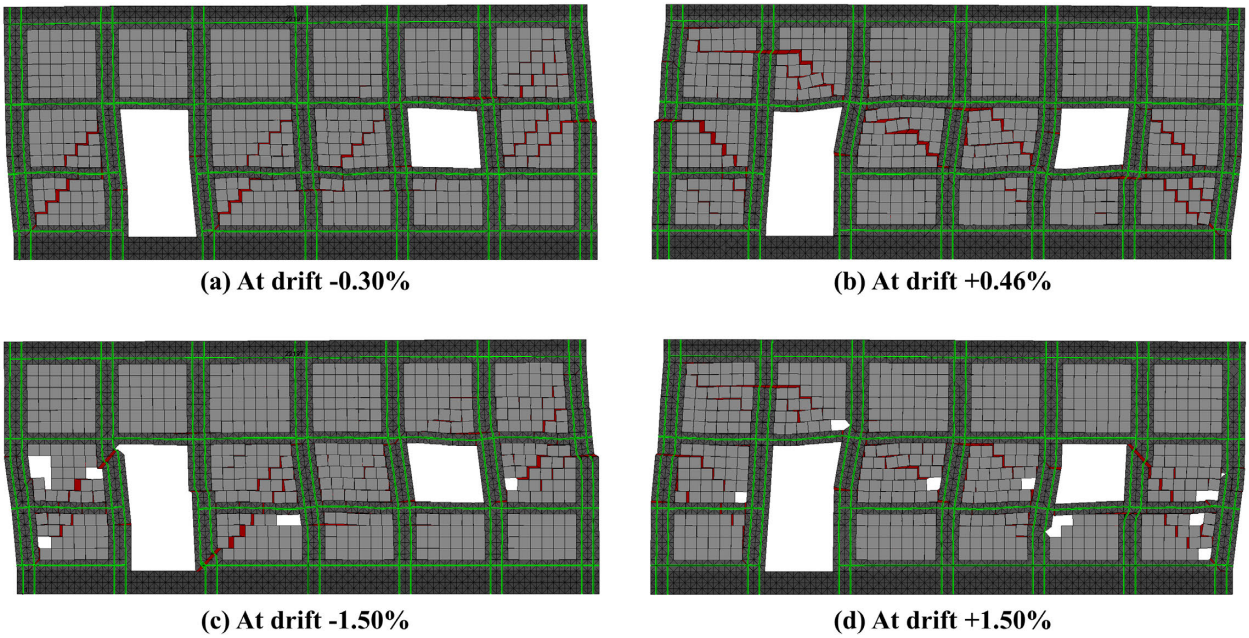

Figure 6.21 Damage in the pushover analysis of the DG design at: (a), (b) the peak strength in the negative and positive direction (magnified by 15); (b); (c), (d) drift 1.50% in the negative and positive direction (magnified by 4).

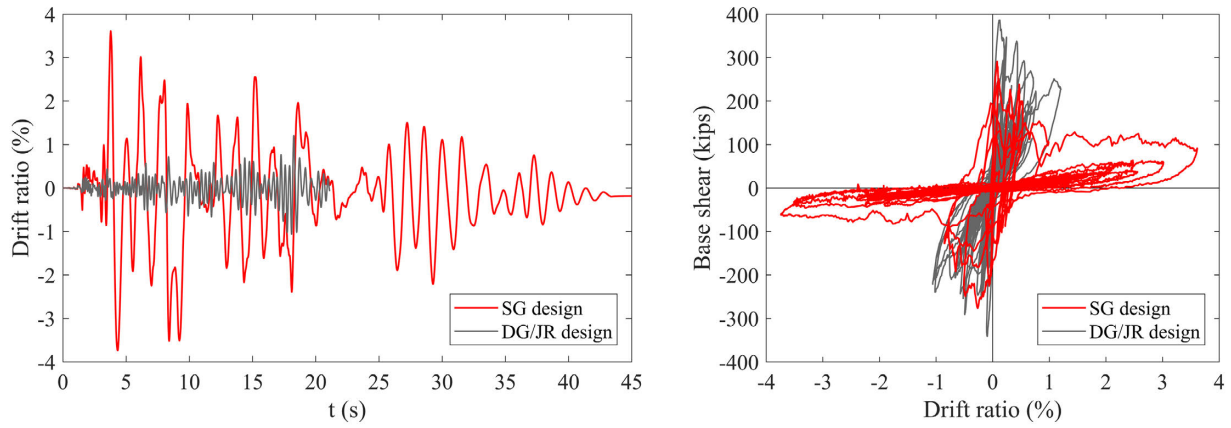

(a) SG and DG/JR

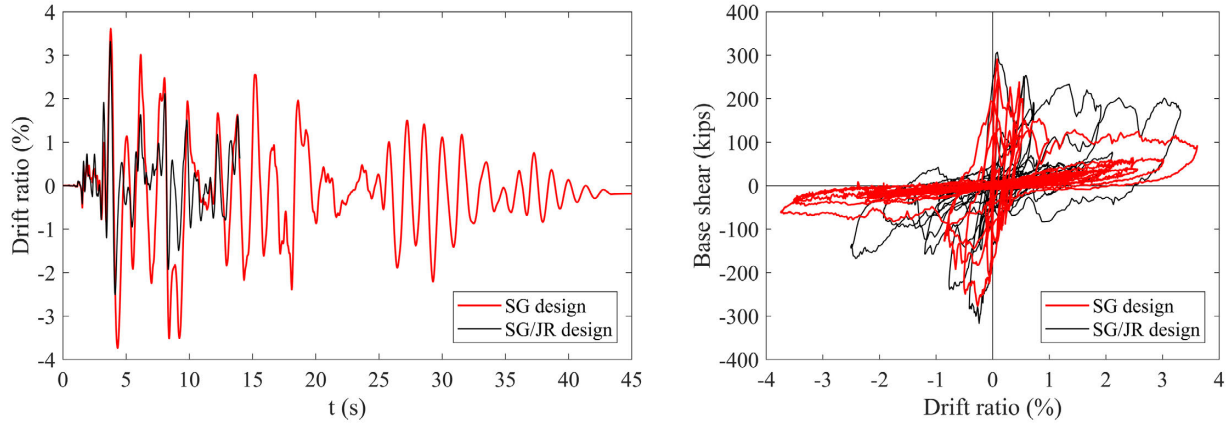

(b) SG and SG/JR

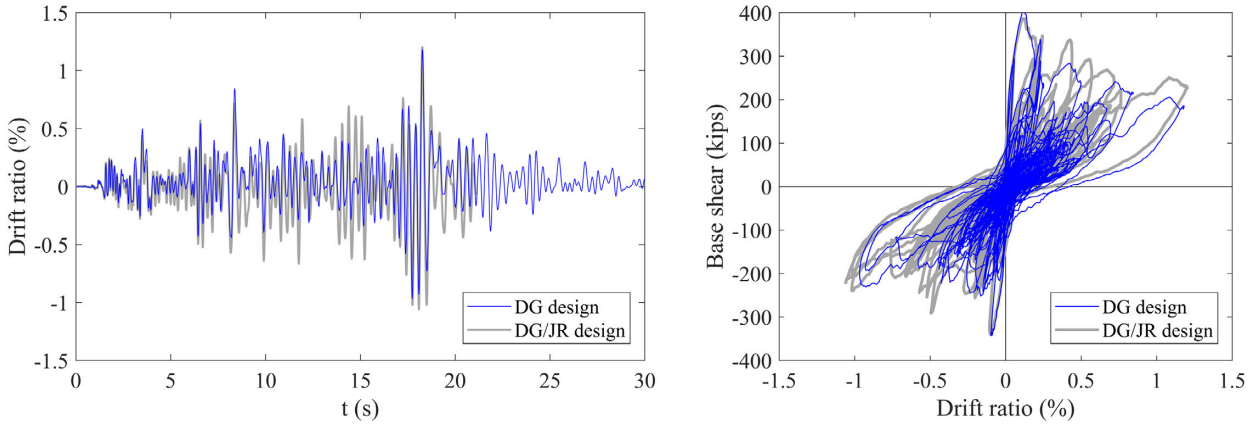

(c) DG and DG/JR

Figure 6.22 Comparison of the SG, SG/JR, DG, and DG/JR designs under 1940 El Centro scaled by a factor of 2.3.

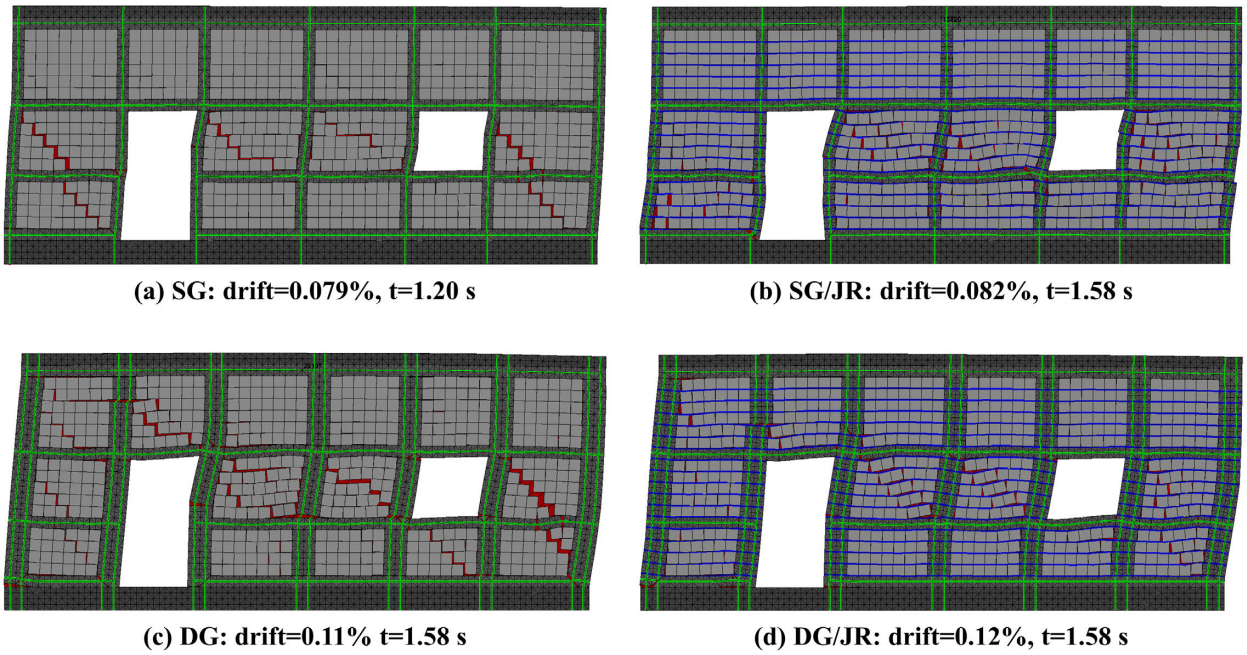

(a) SG: drift=0.079%, t=1.20 s **(b) SG/JR: drift=0.082%, t=1.58 s**

(c) DG: drift=0.11% t=1.58 s **(d) DG/JR: drift=0.12%, t=1.58 s**

Figure 6.23 Damage at the peak base shear of SG, SG/JR, DG, and DG/JR designs under 1940 El Centro scaled by a factor of 2.3 (deformation magnified by 40 times).

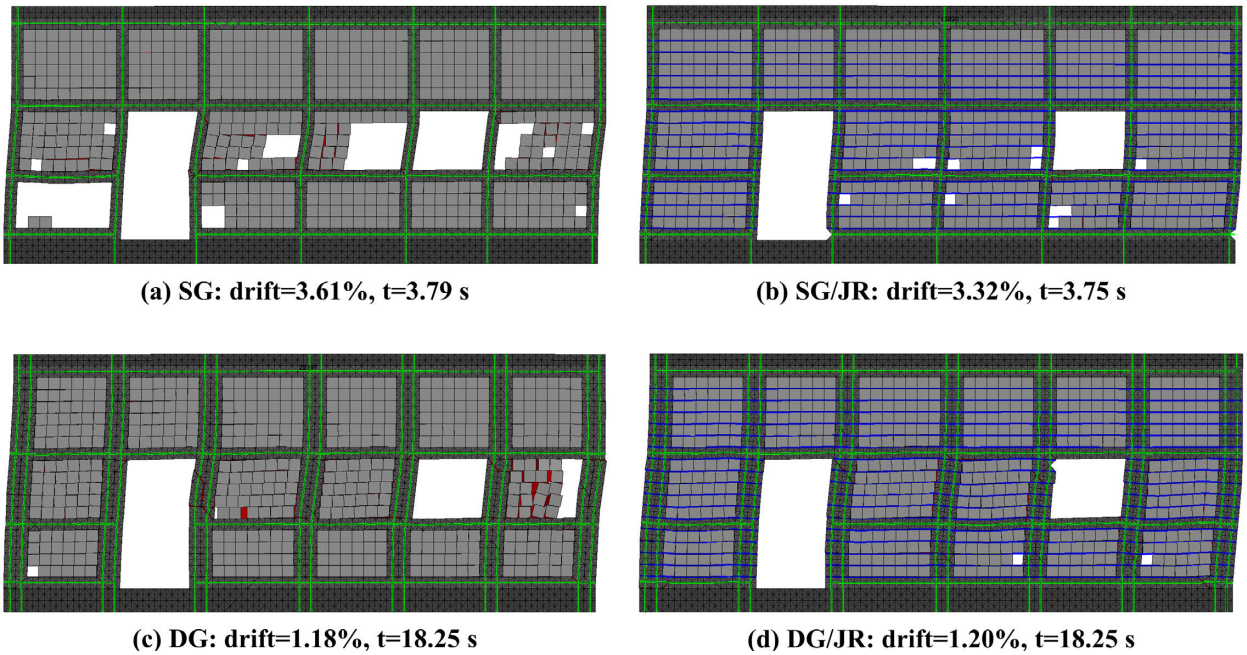

(a) SG: drift=3.61%, t=3.79 s **(b) SG/JR: drift=3.32%, t=3.75 s**

(c) DG: drift=1.18%, t=18.25 s **(d) DG/JR: drift=1.20%, t=18.25 s**

Figure 6.24 Damage at the peak roof drift of SG, SG/JR, DG, and DG/JR designs under 1940 El Centro scaled by a factor of 2.3 (deformation of DG and DG/JR magnified by 4 times).

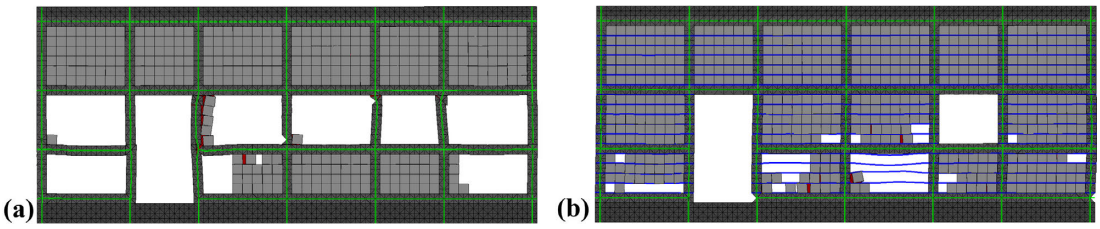

Figure 6.25 Damage at the end of the analysis under under 1940 El Centro scaled by a factor of 2.3 for the designs of: (a) SG and (b) SG/JR.

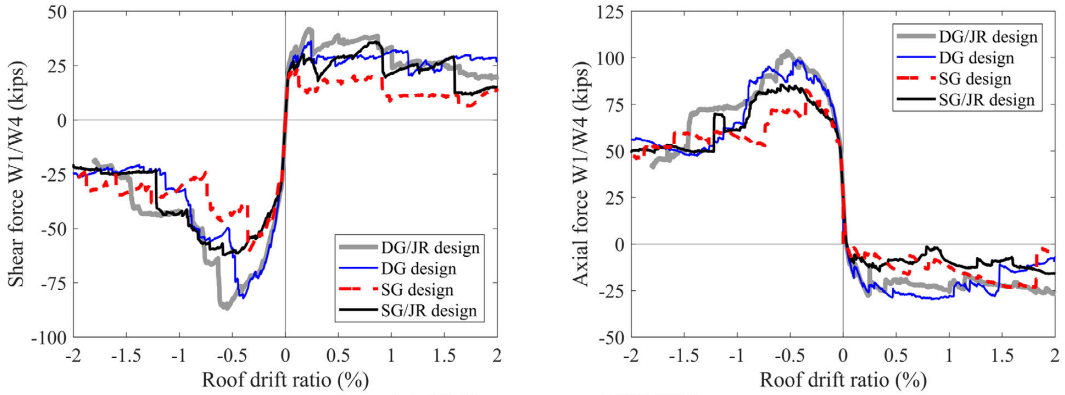

(a) Wall component W1/W4

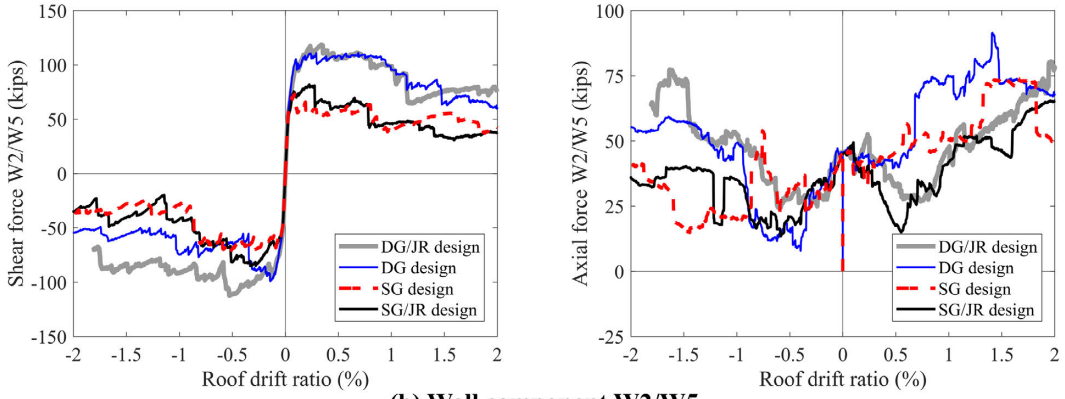

(b) Wall component W2/W5

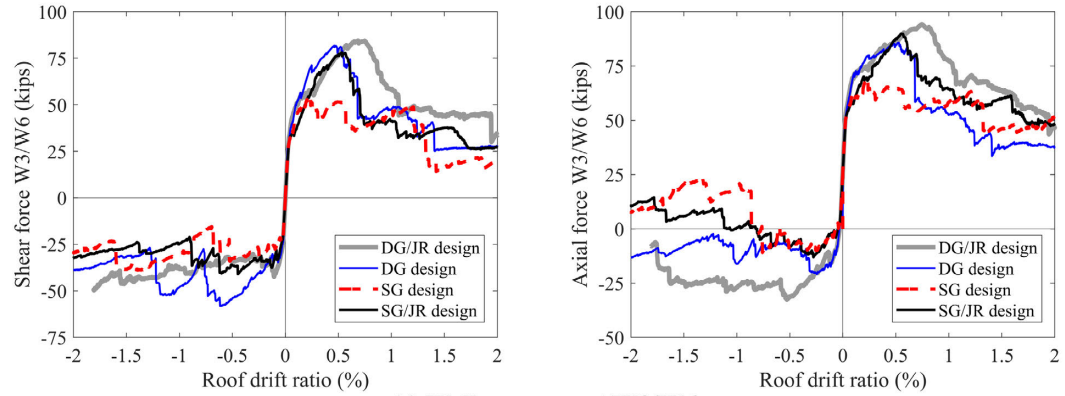

(c) Wall component W3/W6

Figure 6.26 Shear and axial forces of the wall components in DG/JR, DG, SG, and SG/JR.

7 SUMMARY, CONCLUSIONS, AND RECOMMENDATIONS FOR FUTURE RESEARCH

7.1 Summary

This dissertation presents a numerical and experimental study on the seismic behavior of modern reinforced masonry (RM) structures. Both fully grouted and partially grouted masonry (PGM) structures have been examined. Objectives of this research were to develop numerical tools that can predict the response of RM structures under rare, high intensity earthquakes, and to investigate the seismic performance of PGM building systems through large-scale shake-table tests and numerical analyses.

A detailed finite element (FE) modeling framework has been developed for the simulation of the inelastic response of RM structures under severe earthquake loading through collapse. The framework has been developed with the goal to predict the response of wall components developing flexure-dominated or shear-dominated modes of failure and to simulate the seismic behavior of existing building systems in a refined manner. To this end, smeared-crack shell elements are combined with cohesive-crack interface elements to capture the compressive behavior and tensile fracture of masonry. A robust and numerically efficient orthotropic concrete law has been implemented to be used with the shell elements, while a previously proposed cohesive-crack constitutive law has been adopted for the interface elements. The cohesive-crack law adopted is able to represent the opening and closing of cracks in masonry or mortar joints and the sliding along cracks in a realistic fashion. Reinforcing bars are modeled with fiber-section beam elements with material and geometric nonlinearities to capture bar buckling in a natural manner. A material law that can reproduce the uniaxial behavior of steel and accounts for rupture

due to low-cyclic is adopted. The reinforcement beam elements are attached to the masonry shell element through interface elements that simulate the bond-slip and dowel-action effects. An existing bond-slip interface element formulation is improved to account for large rigid-body rotations than may occur in analyses. The smeared-crack shell elements and cohesive-crack interface elements account for large rigid-body rotations as well. The uniaxial bond-slip law adopted was originally developed for reinforcing bars embedded in well-confined concrete. In this study, assumptions are made to indirectly account for the opening of splitting cracks and the subsequent loss of the bond resistance for bars embedded in masonry, which normally has unconfined conditions. A new element removal procedure is introduced to help avoid numerical problems created by element distortion and unrestrained degrees of freedom and to simulate severe masonry crushing, bar buckling, and bar rupture in an accurate manner. The FE program LS-DYNA is used as the analysis platform in which the aforementioned material models, interface elements, and element removal procedure have been implemented as user-defined features.

The proposed modeling scheme has been validated with data from several quasi-static cyclic tests on shear-dominated and flexure-dominated wall segments. The values used for the parameters of the constitutive laws have been reported in detail and were assigned in a consistent manner throughout the analyses. As in a FE model involving softening, strain localization can occur. This results in the concentration of masonry crushing and subsequent bar buckling in the first row of shell elements above the base of a wall failing in flexural. To circumvent this issue, an improved element removal scheme is developed so that the unsupported length of the bars as a result of masonry crushing can be specified *a priori* as a modeling parameter. The use of the proposed scheme has been demonstrated in the analyses of flexure-dominated cantilever wall tests. Walls with lap splices within the plastic hinge region have also been examined.

The behavior of the proposed modeling framework under dynamic loading has been assessed with data from the shake-table tests of two RM wall structures. The first structure had two stories, door and window openings, and was tested by Mavros et al. (2016) up to a first-story drift ratio of 1.9%. The second structure had one story, two T-walls, and six rectangular walls perpendicular to the direction of the applied motion and was tested by Cheng et al. (2019), including the author of this dissertation, to the verge of collapse with a roof drift exceeding 13%. The damage of the latter structure primarily involved wide diagonal cracks, crushing, and rupture of several horizontal bars.

The proposed modeling framework has been applied to gain insight into the seismic performance and collapse potential of a two-story commercial archetype building which was designed (by KL&A Inc.) for a high seismic zone following the current code provisions and design practice. The archetype building had six RM walls to resist lateral forces and gravity loads and a system of steel beams and columns that were designed to carry only gravity loads. The FE model developed for the structure has been subjected to three bidirectional earthquake records that have been scaled to the level of the maximum considered earthquake (MCE) and two times the MCE.

The FE modeling scheme has been extended for the analyses of PGM walls. A new zero-thickness interface element has been developed to model the mortar joints in a discrete fashion and to also model discrete cracks though the ungrouted concrete blocks. The new interface element accounts for the cavity between the face shells of a concrete unit; thereby, a single element can be used to model contact along the two parallel face shells. A co-rotational element coordinate system has been adopted for the element to handle large rigid-body rotations. The modeling scheme has been validated with results from the quasi-static cyclic tests of two rectangular PGM walls and two wall assemblies that had wall flanges and a window opening. One of the wall assemblies had

also joint reinforcement in the form of steel wires embedded in the horizontal mortar joints. The joint reinforcement is represented with beam elements that are connected to the masonry shell elements through bond-slip/dowel-action interface elements. The models are able to predict reasonably well the experimental response and failure mechanisms.

The seismic behavior of PGM wall systems has been studied through large-scale shake-table tests and additional numerical analyses. Two full-scale, one-story, PGM structures were tested on the shake table of the NEES facility at UC San Diego. The two structures had the same wall geometry, but different reinforcement details. The first structure, Specimen 1, was tested to acquire a better understanding on the seismic performance of a PGM building built according to current design provisions and practice. The structure was designed according to the current code provisions in the U.S. for areas of moderate seismicity and had widely spaced vertical grouted cells and bond beams. The design of the masonry walls was based on an elastic analysis and the assumption that the capacity of the wall system would be reached when one of the shear-critical wall components first reached its shear capacity. During the tests, under an MCE-level motion, the structure developed a response dominated by base sliding. After base sliding was restrained, in Phase 2 of testing, the structure reached a peak base shear that was 2.8 times the design base shear. In Phase 2, the structure was able to withstand four motions with effective intensities above the MCE-level, including two motions with an effective intensity above two times the MCE-level. Nonetheless, in a subsequent motion, the structure exhibited significant load degradation at a roof drift of about 0.4% due to shear cracks that propagated through the vertical grouted cells. The load drop was followed by the severe crushing and detachment of the ungrouted masonry units.

The second structure was tested to assess alternative reinforcing details aimed to result in a more ductile response. Specimen 2 had stronger vertical grouted elements, each consisting of

two side-by-side (double) grouted vertical cells. Furthermore, joint reinforcement with 3/16" longitudinal wires was placed in every horizontal mortar joint in addition to the horizontal bond beams, which were also present in Specimen 1. The structure was tested up to a roof drift of 1.1% showing gradual load degradation and no sudden shear failures. It developed a peak base shear resistance that was 18% higher than the capacity reached by Specimen 1.

The behavior of the two structures was further studied with nonlinear FE analyses. FE models were developed for the two structures and validated with the results from the shake-table tests. The models were used to understand the distribution of the lateral resistance among the wall components and to assess the shear-strength equation of TMS 402 (2016). Additional time-history and nonlinear static analyses were conducted to evaluate the influence of the continuous bond beams below the window openings, the double grouted vertical cells, and the joint reinforcement on the seismic performance of the test structures.

7.2 Main Observations and Conclusions

7.2.1 Finite element modeling

The detailed FE modeling framework developed in LS-DYNA has been extensively validated with results from quasi-static tests of wall segments and wall assemblies, and results from shake-table tests of fully and partially grouted masonry wall systems. The detailed models presented in this study capture the failure behavior of RM masonry structures with details beyond any of the previous works. The results demonstrate that the proposed modeling scheme can predict the cyclic load-displacement response of RM wall segments and systems, including the peak lateral load capacity, load degradation, and damage pattern, with a satisfactory level of accuracy. The models were also able to predict severe failures such as the rupture of several horizontal reinforcing bars, which occurred in the second fully grouted shake-table test structure considered, and the

extensive crushing and detachment of ungrouted masonry units observed in the final motion of the shake-table tests of the first PGM specimen. In addition, the use of geometrically nonlinear beam elements for modeling the reinforcing bars helped in capturing the reinforcement buckling observed in the tests of flexure-dominated walls. The validation analyses are also valuable in determining the values of material parameters that are otherwise hard to obtain from tests on material samples, such as the friction coefficient along a crack, the fracture energy under tension, or the parameters controlling the dilatation of a mortar joint. Furthermore, the proposed modeling scheme in LS-DYNA has been proven to be robust under static and dynamic loading scenarios.

The modeling approach together with the proposed values for the material parameters can be used as predictive tools. The framework can be applied to evaluate the seismic performance of existing RM structures, whose behavior may be different than what was assumed in the design, to assess the design-code provisions, and to calibrate or validate simplified models. The numerical case study of the two-story commercial building archetype revealed that the structure is able to develop a base shear capacity that was three times the design base shear. This is because the design considered the RM shear walls as cantilevers, while in reality, the rotational restraints exerted by the floor diaphragm at the top of the first-story walls reduce the shear-span ratio of the walls and increased the shear capacity. Nonetheless, the structure performed well in the analyses. The walls developed either a flexure-dominated response or a response governed by combined flexure and shear. The structure collapsed under the most demanding record that has been scaled to two times the MCE. The first-story drift ratio at the moment of incipient collapse exceeds 10%.

7.2.2 Shake-table tests and analyses of partially grouted masonry wall systems

The shake-table tests of the first PGM specimen showed that a PGM system with ordinary walls can withstand several MCE-level motions without significant damage because of the

overstrength. Although the structure eventually failed in a brittle manner at a roof drift ratio of only 0.4%, it was able to retain a significant residual lateral strength which was equal to 50% of the peak base shear capacity until the roof drift ratio reached 2.25%. At that point, the local drift ratio experienced by the wall components was 4%, which is much higher than that reached in any of the previous experimental studies on PGM walls.

The high overstrength achieved in the tests was due to conservative assumptions and the use of an elastic frame model in the design in that the capacity of the structure was assumed to be reached when the critical wall component reached the shear capacity in the analysis. However, it has been shown that the wall components can maintain a substantial portion of their load capacity at displacements beyond the point of their peak load resistance. This allowed different wall components to develop significant lateral resistance at the same time, and the resistance continued to increase as the axial compressive loads in the walls increased, resulting in a base-shear capacity much higher than the design base shear (2.8 times). The nonlinear pushover analysis has also showed that a wall component in tension provides only a small portion of the lateral resistance. However, within a wall system, a wall component in tension may contribute to a higher axial compression in the other wall components and therefore it may indirectly enhance the shear resistance of the system. Such effects cannot be captured by elastic analyses. Conservative the assumptions made in the design of Specimen 1 appear to be adequate considering the brittle behavior exhibited in the test. The overstrength factor of 2.8 is close to the value of 2.5 suggested by ASCE/SEI 7 for ordinary load-bearing RM shear walls.

The continuous bond beams introduced below the window openings in PGM walls are found to be beneficial to the performance of the building. This was indicated by the large strains (exceeding 2%) registered in the horizontal reinforcement of Specimen 1 during the last motion of

the test and was further verified through a parametric study conducted with the FE model. The model also shows that the benefit of a bond beam in the first course above the footing is negligible if sliding does not occur.

The test results of Specimen 1 also showed that lightly reinforced PGM wall structures can be prone to base sliding if their foundation surface is not intentionally roughened and their weight is not sufficiently high. It was found that the shear-friction equation in TMS 402 (2016) predicts well the shear-friction resistance deduced from the test data (before base sliding was restrained) if a coefficient of friction of 0.7 is assumed.

The design proposed for the second PGM test structure enhanced the performance in terms of lateral strength and ductility as compared to Specimen 1. The double grouted vertical cells introduced in Specimen 2 developed a flexure-dominated response. Horizontal cracks related to flexure formed at distinct locations along the height of the vertical cells inducing high tensile strains in the vertical bars. Uniform cracks developed in the ungrouted masonry and significant sliding was observed between the masonry units in the ungrouted panels. No crushing of masonry units occurred. In the tests, the joint reinforcement may have been beneficial in restraining the opening of cracks in ungrouted masonry. Nonetheless, its contribution during the later and most demanding motions of the sequence is questionable because the mortar joints had been significantly weakened from prior motions of lower intensity.

The pushover analyses and the time-history analyses conducted with a single earthquake motion reveal that joint reinforcement can contribute to the lateral load resistance of the structure and can reduce the width of the shear cracks in ungrouted masonry. However, the benefit from the placement of joint reinforcement is shown to be higher when used with single grouted vertical cells. The results also indicate that the loading history can influence the lateral load resistance of

a PGM structure. As discussed in Chapter 6, higher capacities are achieved in the monotonic pushover analyses than in the time-history analyses.

With the assumption that the pushover analyses are accurate, the shear-strength equation of TMS 402 (2016) appears to be adequate for different design details, including designs with single grouted vertical cells with and without joint reinforcement, and designs with double grouted vertical cells with and without joint reinforcement. In general, the shear strength of the wall components calculated with the code equation is lower than those given by the FE model, except for a few cases where the wall components are subjected to tension. Furthermore, the code equation appears to be more conservative for wall components with double grouted vertical cells. The results also indicate that the wall flange may improve the shear resistance when it is in compression.

7.3 Recommendations for Future Research

In spite of the fact that the shear-strength equation in TMS 402 (2016) has been found to be adequate for PGM when compared to the FE analysis results, further studies are needed to understand why it overestimates the shear capacities of PGM wall components tested in some other studies. In particular, the influence of the spacing of grouted cells, wall aspect ratio, boundary conditions, and wall flanges should be investigated. The effect of the loading history on the shear strength of PGM walls is another factor that should be further examined experimentally and analytically.

Simplified methods should be developed to predict the lateral load capacity of a PGM system in an accurate and efficient manner. The use of a strut-and-tie approach can be a viable means to evaluate the load capacity of a perforated wall system. Results from the shake-table tests and FE models can be used to validate such an approach.

In this dissertation, the seismic behavior of modern PGM wall systems under uniaxial base excitation has been studied. The behavior of PGM structures under bidirectional earthquake excitations should also be investigated. The proposed modeling scheme can be employed to provide insight into that and can be used as a tool for the design of future shake-table tests.

Tests should also be conducted to characterize the cyclic bond-slip and dowel-action behaviors of reinforcing bars embedded in masonry. The influence of the bar size, grout strength, and clear cover should be among the variables to consider. Furthermore, the bond-slip behavior of joint reinforcement embedded in mortar joints has not been studied so far and needs to be investigated. Having such data will improve the design-code provisions and lead to more accurate and reliable numerical models.

The verification analyses presented in this dissertation are conducted without an accompanying sensitivity study. Such a study will be desirable to demonstrate the influence of various material parameters and the element size on the numerical results.

REFERENCES

ACI Committee, International Organization for Standardization. Building code requirements for structural concrete (ACI 318-19) and commentary. American Concrete Institute, Farmington Hills, MI; 2019.

Addessi D, Sacco E. A multi-scale enriched model for the analysis of masonry panels. International Journal of Solids and Structures. 2012;49(6):865-80.

Addessi D, Sacco E. Nonlinear analysis of masonry panels using a kinematic enriched plane state formulation. International Journal of Solids and Structures. 2016;90:194-214.

Ahmadi F. Displacement-based seismic design and tools for reinforced masonry. PhD Thesis, The Univerisy of Texas at Austin; 2012.

Applied Technology Council, United States. Federal Emergency Management Agency. Quantification of building seismic performance factors. US Department of Homeland Security, FEMA; 2009.

Aref AJ, Dolatshahi KM. A three-dimensional cyclic meso-scale numerical procedure for simulation of unreinforced masonry structures. Computers & Structures. 2013;120:9-23.

ASCE (2010, 2016). Minimum design loads for buildings and other structures. ASCE/SEI Standard 7, Reston VA; 2010, 2016.

Baenziger G, Porter ML. In-Plane Structural Testing of Joint Reinforcement in Concrete Masonry Shear Walls. A Report—for Sponsors and MSJC Discussion, Iowa State University; 2010.

Banting BR, El-Dakhakhni WW. Force- and displacement-based seismic performance parameters for reinforced masonry structural walls with boundary elements. ASCE Journal of Structural Engineering, 2012; 138(12):1477-1491.

Bathe KJ. Conserving energy and momentum in nonlinear dynamics: a simple implicit time integration scheme. Computers & Structures. 2007;85(7-8):437-45.

Bažant ZP, Lin FB. Nonlocal smeared cracking model for concrete fracture. ASCE Journal of Structural Engineering. 1988;114(11):2493-510.

Bažant ZP, Planas J. Fracture and Size Effect in Concrete and Other Quasibrittle Materials. London: CRC Press, 1998.

Belytschko T, Liu WK, Moran B, Elkhodary K. Nonlinear finite elements for continua and structures. John Wiley & Sons; 2013.

Blaauwendraad J, Hoogenboom PC. Stringer panel model for structural concrete design. ACI Structural Journal. 1996;93(3):295-305.

Bolhassani M, Hamid AA, Johnson C, Moon FL, Schultz AE. New design detail to enhance the seismic performance of ordinary reinforced partially grouted masonry structures. ASCE Journal of Structural Engineering. 2016b;142(12):04016142.

Bolhassani M, Hamid AA, Johnson C, Schultz AE. Shear strength expression for partially grouted masonry walls. Engineering Structures. 2016c;127:475-94.

Bolhassani M, Hamid AA, Moon FL. Enhancement of lateral in-plane capacity of partially grouted concrete masonry shear walls. Engineering Structures. 2016a;108:59-76.

Bolhassani M. Improvement of seismic performance of ordinary reinforced partially grouted concrete masonry shear walls. PhD Thesis, Drexel Univesiry; 2015.

Burchnall D. Formulation and validation of a nonlinear shell element for the analysis of reinforced concrete and masonry structures. MS Theis, Virginia Tech, Blackburg; 2014.

Burton H, Deierlein G. Simulation of seismic collapse in nonductile reinforced concrete frame buildings with masonry infills. ASCE Journal of Structural Engineering. 2013;140(8):A4014016.

Caliò I, Marletta M, Pantò B. A new discrete element model for the evaluation of the seismic behaviour of unreinforced masonry buildings. Engineering Structures. 2012;40:327-38.

Caner FC, Bažant ZP. Microplane model M7 for plain concrete. I: Formulation. ASCE Journal of Engineering Mechanics. 2012;139(12):1714-23.

Carol I, Prat PC, Lopez CM. Normal/shear cracking model: application to discrete crack analysis. ASCE Journal of Engineering Mechanics. 1997;123(8):765-73.

Centeno J, Ventura CE, Ingham JM. Seismic performance of a six-story reinforced concrete masonry building during the Canterbury earthquake sequence. Earthquake Spectra. 2014;30(1):363-81.

Cervenka J. Mixed mode discrete crack propagation in concrete structures. PhD Thesis, University of Colorado at Boulder; 1994.

Chaimoon K, Attard MM. Modeling of unreinforced masonry walls under shear and compression. Engineering structures. 2007;29(9):2056-68.

Chen JS, Pan C, Wu CT, Liu WK. Reproducing kernel particle methods for large deformation analysis of non-linear structures. Computer methods in applied mechanics and engineering. 1996;139(1-4):195-227.

Chen WF. Plasticity in reinforced concrete. J. Ross Publishing; 2007.

Cheng J, Koutras A, Shing PB. A shake-table test investigating the drift capacity of reinforced masonry wall systems. Proceedings of the Thirteenth North American Masonry Conference, Salt Lake City, Utah; 2019.

Clough RW, Gülkan P, Manos GC, Mayes RL. Seismic testing of single-story masonry houses: Part 2. Journal of Structural Engineering. 1990 Jan;116(1):257-74.

Colotti V. Shear behavior of RC structural walls. ASCE Journal of Structural Engineering. 1993;119(3):728-46.

Crisfield MA. A consistent co-rotational formulation for non-linear, three-dimensional, beam-elements. Computer methods in applied mechanics and engineering. 1990;81(2):131-50.

Cyrier WB. Performance of concrete masonry shear walls with integral confined boundary elements. MS Thesis, Washington State University; 2012.

D'Ambrisi A, Filippou FC. Modeling of cyclic shear behavior in RC members. ASCE Journal of Structural Engineering. 1999;125(10):1143-50.

De Borst R, Mühlhaus HB. Gradient-dependent plasticity: formulation and algorithmic aspects. International Journal for Numerical Methods in Engineering. 1992;35(3):521-39.

Dizhur D, Ingham J, Moon L, Griffith M, Schultz A, Senaldi I, Magenes G, Dickie J, Lissel S, Centeno J, Ventura C. Performance of masonry buildings and churches in the 22 February 2011 Christchurch earthquake. Bulletin of the New Zealand Society for Earthquake Engineering. 2011;44(4):279-96.

Dodd LL, Restrepo-Posada JI. Model for predicting cyclic behavior of reinforcing steel. ASCE Journal of Structural Engineering. 1995;121(3):433-45.

Drysdale R, Hamid AA. Masonry structures behavior and design 3rd Edition. The Masonry Society, 2008.

Dulacska H. Dowel action of reinforcement crossing cracks in concrete. ACI Journal. 1972;69(12):754-757.

EERI. The M 6.3 Christchurch, New Zealand, Earthquake of February 22, 2011. EERI special earthquake report; 2011.

ElGawady MA. Shear strength equations for partially grouted masonry walls. Proceedings of the Twelfth North American Masonry Conference, Denver, Colorado; 2015.

Elwood KJ, Moehle JP. Dynamic collapse analysis for a reinforced concrete frame sustaining shear and axial failures. Earthquake Engineering & Structural Dynamics. 2008;37(7):991-1012.

EN 1992-1-1. Eurocode 2: design of concrete structures–part 1-1: general rules and rules for buildings. European Committee for Standardization; 2004.

Essa HS, Tremblay R, Rogers CA. Behavior of roof deck diaphragms under quasistatic cyclic loading. ASCE Journal of Structural Engineering. 2003;129(12):1658-66.

Faria R, Oliver J, Cervera M. Modeling material failure in concrete structures under cyclic actions. ASCE Journal of Structural Engineering. 2004;130(12):1997-2005.

Feenstra PH, de Borst R. Constitutive model for reinforced concrete. ASCE Journal of Engineering Mechanics. 1995;121(5):587-95.

FEMA (2009). Quantification of Building Seismic Performance Factors, FEMA P-695, prepared by the Applied Technology Council for the Federal Emergency Management Agency, Washington, D.C; 2009.

FEMA (2019). Developing Solutions to the Short-Period Building Performance Paradox: Study of Reinforced Masonry Buildings. Federal Emergency Management Agency, Washington, D.C.; 2019 (under publication).

Fries TP, Belytschko T. The extended/generalized finite element method: an overview of the method and its applications. International journal for numerical methods in engineering. 2010;84(3):253-304.

Gambarotta L, Lagomarsino S. Damage models for the seismic response of brick masonry shear walls. Part II: the continuum model and its applications. Earthquake engineering & structural dynamics. 1997;26(4):441-62.

Giambanco G, Rizzo S, Spallino R. Numerical analysis of masonry structures via interface models. Computer methods in applied mechanics and engineering. 2001;190(49-50):6493-511.

Girgin SC, Moharrami M, Koutromanos I. Nonlinear Beam-Based Modeling of RC Columns Including the Effect of Reinforcing-Bar Buckling and Rupture. Earthquake Spectra. 2018;34(3):1289-309.

Grassl P, Jirásek M. Plastic model with non-local damage applied to concrete. International Journal for Numerical and Analytical Methods in Geomechanics. 2006;30(1):71-90.

Gülkan P, Clough RW, Mayes RL, Manos GC. Seismic testing of single-story masonry houses: Part 1. Journal of Structural Engineering. 1990;116(1):235-56.

He L, Priestley MN. Seismic behavior of flanged masonry walls. Dept. of Applied Mechanics & Engineering Sciences, University of California, San Diego; 1992.

Hillerborg A, Modéer M, Petersson PE. Analysis of crack formation and crack growth in concrete by means of fracture mechanics and finite elements. Cement and concrete research. 1976;6(6):773-81.

Huang Y, Mahin SA. Simulating the Inelastic Seismic Behavior of Steel Braced Frames Including the Effects of Low-Cycle Fatigue, PEER Report 10/104. Berkeley, CA: Pacific Earthquake Engineering Research Center, University of California; 2010.

Hughes TJ, Winget J. Finite rotation effects in numerical integration of rate constitutive equations arising in large-deformation analysis. International journal for numerical methods in engineering. 1980;15(12):1862-7.

Ibarra LF, Medina RA, Krawinkler H. Hysteretic models that incorporate strength and stiffness deterioration. Earthquake Engineering & Structural Dynamics. 2005;34(12):1489-511.

Jiang H, Kurama YC. Analytical Modeling of Medium-Rise Reinforced Concrete Shear Walls. ACI Structural Journal. 2010;107(4).

Johnson CA, Schultz AE. Partially-grouted masonry shear wall performance with a basalt-reinforced repair overlay. Proceedings Eleventh U.S. National Conference on Earthquake Engineering, Los Angeles, California; 2018.

Johnson CA, Schultz AE. Seismic resistance of an FRP repair of a partially grouted masonry sub-assemblage. Proceedings Twelfth North American Masonry Conference, Denver, Colorado; 2015.

Johnson CA, Schultz AE. Simulated seismic testing of partially-grouted masonry sub-assemblages. Proceedings Tenth U.S. National Conference on Earthquake Engineering, Anchorage, Alaska; 2014.

Kabeyasawa T, Otani S, Aoyama H. Nonlinear earthquake response analyses of R/C wall-frame structures. Transactions of the Japan Concrete Institute. 1983;5:277-84.

Kapoi CM. Experimental performance of concrete masonry shear walls under in-plane loading. MS Thesis, Washington State University; 2012.

Kennedy JM, Belytschko T, Lin JI. Recent developments in explicit finite element techniques and their application to reactor structures. Nuclear Engineering and Design. 1986;97(1):1-24.

Kim SH, Koutromanos I. Constitutive model for reinforcing steel under cyclic loading. ASCE Journal of Structural Engineering. 2016;142(12):04016133.

Kolozvari K, Orakcal K, Wallace JW. Modeling of cyclic shear-flexure interaction in reinforced concrete structural walls. I: Theory. ASCE Journal of Structural Engineering. 2014;141(5):04014135.

Kolozvari K, Tran TA, Orakcal K, Wallace JW. Modeling of cyclic shear-flexure interaction in reinforced concrete structural walls. II: experimental validation. ASCE Journal of Structural Engineering. 2014;141(5):04014136.

Kottari A, Mavros M, Murcia-Delso J, Shing PB. Interface model for bond-slip and dowel-action behavior. ACI Structural Journal. 2017; 114(4)

Kottari A. Horizontal load resisting mechanisms of external shear keys in bridge abutments. PhD Thesis, University of California San Diego, La Jolla; 2016.

Koutras A, Shing PB. Shake-Table Test of a Partially Grouted Reinforced Masonry Building with Double Side-by-Side Vertical Grouted Cells. DesignSafe Dataset, DOI: 10.4231/D3RJ48W1F, 2015b.

Koutras A, Shing PB. Shake-table test of a partially grouted reinforced masonry building with separated single grouted cells. DesignSafe Dataset, DOI: 10.4231/D3W950P43, 2015a.

Koutromanos I, Shing PB. Cohesive crack model to simulate cyclic response of concrete and masonry structures. ACI Structural Journal. 2012;109(3).

Koutromanos I, Stavridis A, Shing PB, Willam K. Numerical modeling of masonry-infilled RC frames subjected to seismic loads. Computers & Structures. 2011;89(11-12):1026-37.

Kunnath SK, Reinhorn AM, Park YJ. Analytical modeling of inelastic seismic response of R/C structures. ASCE Journal of Structural Engineering. 1990;116(4):996-1017.

Kwan WP, Billington SL. Simulation of structural concrete under cyclic load. ASCE Journal of Structural Engineering. 2001;127(12):1391-401.

LeBorgne MR, Ghannoum WM. Calibrated analytical element for lateral-strength degradation of reinforced concrete columns. Engineering Structures. 2014;81:35-48.

Lee J, Fenves GL. Plastic-damage model for cyclic loading of concrete structures. ASCE Journal of Engineering Mechanics. 1998;124(8):892-900.

Lotfi HR, Shing PB. An appraisal of smeared crack models for masonry shear wall analysis. Computers & Structures. 1991;41(3):413-25.

Lotfi HR, Shing PB. Interface model applied to fracture of masonry structures. ASCE Journal of Structural Engineering. 1994;120(1):63-80.

Lourenço PB, Rots JG, Blaauwendraad J. Continuum model for masonry: parameter estimation and validation. ASCE Journal of Structural Engineering. 1998;124(6):642-52.

Lourenco PB. Computational strategies for masonry structures. PhD Thesis, TU Delft; 1996.

LSTC. LS-DYNA theory manual. Livermore Software and Technology Corporation, Livermore, CA; 2018.

Lu Y, Panagiotou M. Three-dimensional cyclic beam-truss model for nonplanar reinforced concrete walls. ASCE Journal of Structural Engineering. 2013;140(3):04013071.

Luco JE, Ozcelik O, Conte JP. Acceleration tracking performance of the UCSD-NEES shake table. ASCE Journal of Structural Engineering. 2009;136(5):481-90.

Luttrell LD. Steel Deck Institute Diaphragm Design Manual Second Edition. Steel Deck Institute, Illinois; 1995.

Maleki M. Behaviour of partially grouted reinforced masonry shear wall under cyclic reversed loading. PhD Thesis, McMaster University, Hamilton, Ontario, Canada; 2008.

Manzoli OL, Shing PB. A general technique to embed non-uniform discontinuities into standard solid finite elements. Computers & Structures. 2006;84(10-11):742-57.

Marini A, Spacone E. Analysis of reinforced concrete elements including shear effects. ACI Structural Journal. 2006;103(5):645.

Masonry Standards Joint Committee (MSJC) 2008. Building code requirements for masonry structures. ACI 530/ASCE 5, TMS 402.

Massone LM, Orakcal K, Wallace JW. Shear-flexure interaction for structural walls. Special Publication. 2006;236:127-50.

Mavros M, Ahmadi F, Shing PB, Klinger RE, McLean D, Stavrids A. Shake-table tests of a full-scale two-story shear-dominated reinforced masonry wall structures. ASCE Journal Structural Engineering, 2016, 142(10).

Mavros M. Experimental and numerical investigation of the seismic performance of reinforced masonry structures. PhD Thesis, University of California San Diego, La Jolla; 2015.

Mazars J, Kotronis P, Davenne L. A new modelling strategy for the behaviour of shear walls under dynamic loading. Earthquake Engineering & Structural Dynamics. 2002;31(4):937-54.

Mehrabi AB, Shing PB. Finite element modeling of masonry-infilled RC frames. ASCE Journal of Structural Engineering. 1997;123(5):604-13.

Mehrabi AB. Behavior of masonry-infilled reinforced concrete frames subjected to lateral loadings. PhD Thesis, University of Colorado at Boulder; 1994.

Miki T. Nonlinear analysis of reinforced concrete structures subjected to seismic loads by using three-dimensional lattice model. PhD Thesis, Tokyo Institute of Technology, Japan; 2004.

Milani G, Lourenço P, Tralli A. 3D homogenized limit analysis of masonry buildings under horizontal loads. Engineering Structures. 2007;29(11):3134-48.

Minaie E, Moon FL, Hamid AA. Nonlinear finite element modeling of reinforced masonry shear walls for bidirectional loading response. Finite Elements in Analysis and Design. 2014;84:44-53.

Minaie E, Mota M, Moon FL, Hamid AA. In-plane behavior of partially grouted reinforced concrete masonry shear walls. ASCE Journal of Structural Engineering. 2010; 136(9):1089-97.

Minaie E. Behavior and vulnerability of reinforced masonry shear walls. PhD Thesis, Drexel University; 2009.

Moharrami M, Koutromanos I, Panagiotou M, Girgin SC. Analysis of shear-dominated RC columns using the nonlinear truss analogy. Earthquake Engineering & Structural Dynamics. 2015;44(5):677-94.

Moharrami M, Koutromanos I, Panagiotou M. Nonlinear truss modeling method for the analysis of shear failures in reinforced concrete and masonry structures. Proceedings Improving the Seismic Performance of Existing Buildings and Other Structures 2015 (pp. 74-85).

Moharrami M, Koutromanos I. Finite element analysis of damage and failure of reinforced concrete members under earthquake loading. Earthquake Engineering & Structural Dynamics. 2017;46(15):2811-29.

Moharrami M, Koutromanos I. Triaxial constitutive model for concrete under cyclic loading. ASCE Journal of Structural Engineering. 2016;142(7):04016039.

Monti G, Spacone E. Reinforced concrete fiber beam element with bond-slip. ASCE Journal of Structural Engineering. 2000;126(6):654-61.

Murcia-Delso J, Benson Shing P. Bond-slip model for detailed finite-element analysis of reinforced concrete structures. ASCE Journal of Structural Engineering. 2014;141(4):04014125.

Neuenhofer A, Filippou FC. Evaluation of nonlinear frame finite-element models. ASCE Journal of Structural Engineering. 1997;123(7):958-66.

Ngo D, Scordelis AC. Finite element analysis of reinforced concrete beams. In Journal Proceedings 1967; 64(3):152-163.

NIST (1997). GCR 97-710. Analysis of partially grouted masonry shear walls. Prepared by Shing PB and Cao L for the National Institute of Standards and Technology, Gaithersburg, MD.

NIST (2012). Tentative framework for development of advanced seismic design criteria for new buildings. National Institute of Standards and Technology Report No. GCR 12-917-20, Gaithersburg, MD; 2012.

NIST (2014). Seismic design of special reinforced masonry shear walls, a guide for practicing engineers. National Institute of Standards and Technology Report No. GCR 14-917-31, Gaithersburg, MD, 2014.

Noguchi H, Uchida K. Finite element method analysis of hybrid structural frames with reinforced concrete columns and steel beams. ASCE Journal of Structural Engineering. 2004;130(2):328-35.

Nolph SM, ElGawady MA. Static cyclic response of partially grouted masonry shear walls. ASCE Journal of Structural Engineering. 2011;138(7):864-79.

NZS 4229:1999 (1999). Concrete masonry buildings not requiring specific engineering design. Standards Association of New Zealand, Wellington, New Zealand.

Oliveira DV, Lourenço PB. Implementation and validation of a constitutive model for the cyclic behaviour of interface elements. Computers & Structures. 2004;82(17-19):1451-61.

Orakcal K, Wallace JW, Conte JP. Flexural modeling of reinforced concrete walls-model attributes. ACI Structural Journal. 2004;101(5):688-98.

Panagiotou M, Restrepo JI, Schoettler M, Kim G. Nonlinear cyclic truss model for reinforced concrete walls. ACI Structural Journal. 2012;109(2):205.

Park H, Eom T. Truss model for nonlinear analysis of RC members subject to cyclic loading. ASCE Journal of Structural Engineering. 2007;133(10):1351-63.

Paulay T, Priestley MJN. Seismic design of concrete and masonry structures. John Wiley and Sons. New York; 1992.

Peerlings RH, De Borst R, Brekelmans WA, Geers MG. Gradient-enhanced damage modelling of concrete fracture. Mechanics of Cohesive-frictional Materials: An International Journal on Experiments, Modelling and Computation of Materials and Structures. 1998;3(4):323-42.

Penna A, Lagomarsino S, Galasco A. A nonlinear macroelement model for the seismic analysis of masonry buildings. Earthquake Engineering & Structural Dynamics. 2014;43(2):159-79.

Petrangeli M, Pinto PE, Ciampi V. Fiber element for cyclic bending and shear of RC structures. I: Theory. ASCE Journal of Engineering Mechanics. 1999;125(9):994-1001.

Puntel E, Bolzon G, Saouma VE. Fracture mechanics based model for joints under cyclic loading. ASCE Journal of Engineering Mechanics. 2006;132(11):1151-9.

Rajaram S, Vanniamparambil PA, Khan F, Bolhassani M, Koutras A, Bartoli I, Moon F, Hamid A, Benson Shing P, Tyson J, Kontsos A. Full-field deformation measurements during seismic loading of masonry buildings. Structural Control and Health Monitoring. 2017;24(4):e1903.

Rashid YR. Ultimate strength analysis of prestressed concrete pressure vessels. Nuclear engineering and design. 1968;7(4):334-44.

Rogers CA, Tremblay R, Yang W, Martin E. Ductile design of steel roof deck diaphragms for earthquake resistance. In Proc. 13th world conf. on earthquake eng , Vancouver, Canada; 2004.

Rose BD. A constitutive model for the analysis of reinforced concrete beam-columns subjected to lateral loads. PhD Thesis, University of Colorado at Boulder; 2001.

Rots JG, Blaauwendraad J. Crack models for concrete, discrete or smeared? Fixed, multi-directional or rotating?. HERON. 1989;34 (1).

Schlaich J, Schäfer K, Jennewein M. Toward a consistent design of structural concrete. PCI Journal. 1987;32(3):74-150.

Schultz AE, Hutchinson RS. Seismic Behavior of Partially-Grouted Masonry Shear Walls: Phase 2 - Effectiveness of Bed-Joint Reinforcement, NIST GCR 01-808, National Institute of Standards and Technology;2001.

Schultz AE, Johnson CA. Seismic resistance mechanisms in partially grouted shear walls with new design details. Proceedings Thirtheenth North American Masonry Conference, Salt Lake City, UT; 2019.

Schultz AE. Seismic performance of partially-grouted masonry shear walls. Proceedings Eleventh World Conference on Earthquake Engineering, Acapulco, Mexico; 1996.

Seible F, Kingsley GR. Modeling of concrete and masonry structures subjected to seismic loading. Kluwer, Dordrecht; 1991.

Seible F, LaRovere HL, Kingsley GR. Nonlinear analysis of reinforced concrete masonry shear wall structures—monotonic loading. The Masonry Society Journal. 1990;9(1):60-69.

Sherman JD. Effects of key parameters on the performance of concrete masonry shear walls under in-plane loading. MS Thesis, Washington State University, 2011.

Shing PB, Noland JL, Spaeh HP, Klamerus EW, Schuller MP. Response of single-story reinforced masonry shear walls to in-plane lateral loads. U.S. - Japan Coordinated Program for Masonry Building Research Report No. 3.1(a)-2, University of Colorado at Boulder, 2011

Sivaselvan MV, Reinhorn AM. Hysteretic models for deteriorating inelastic structures. ASCE Journal of Engineering Mechanics. 2000;126(6):633-40.

Spacone E, Filippou FC, Taucer FF. Fibre beam–column model for non-linear analysis of R/C frames: Part I. Formulation. Earthquake Engineering & Structural Dynamics. 1996;25(7):711-25.

Stavridis A, Ahmadi F, Mavros M, Shing PB, Klinger RE, McLean D. Shake-table tests of a full-scale three-story reinforced masonry shear wall structure. ASCE Journal of Structural Engineering, 2016, 142(10).

Stavridis A, Koutromanos I, Shing PB. Shake-table tests of a three-story reinforced concrete frame with masonry infill walls. Earthquake Engineering & Structural Dynamics. 2012;41(6):1089-108.

Stavridis A, Shing PB. Finite-element modeling of nonlinear behavior of masonry-infilled RC frames. ASCE Journal of Structural Engineering. 2010;136(3):285-96.

Sveinsson BI, McNiven HD, Sucuoglu H. Cyclic loading tests of masonry single piers volume 4. Earthquake Engineering Research Center Report No. UCB/EERC-85/15, University of California, Berkeley; 1985.

Takayanagi T, Schnobrich WC. Non-linear analysis of coupled wall systems. Earthquake Engineering & Structural Dynamics. 1979;7(1):1-22.

TMS 402 (2013, 2016). Building code requirements for masonry structures. The Masonry Society, Longmont, CO; 2013, 2016.

To NH, Sritharan S, Ingham JM. Strut-and-tie nonlinear cyclic analysis of concrete frames. ASCE Journal of Structural Engineering. 2009;135(10):1259-68.

Tremblay R, Martin E, Yang W, Rogers CA. Analysis, testing and design of steel roof deck diaphragms for ductile earthquake resistance. Journal of Earthquake Engineering. 2004;8(05):775-816.

Uniform building code. (1976). Int. Conf. of Building Officials, Whittier, CA.

Vecchio FJ, Collins MP. The modified compression-field theory for reinforced concrete elements subjected to shear. ACI Journal. 1986;83(2):219-31.

Vecchio FJ, Emara MB. Shear deformations in reinforced concrete frames. ACI Structural Journal. 1992;89(1):46-56.

Vecchio FJ. Towards cyclic load modeling of reinforced concrete. ACI Structural Journal. 1999;96:193-202.

Voon KC, Ingham JM. Experimental in-plane shear strength investigation of reinforced concrete masonry walls. ASCE Journal of Structural Engineering. 2006;132(3):400-8.

Voon KC, Ingham JM. Experimental in-plane strength investigation of reinforced concrete masonry walls with openings. ASCE Journal of Structural Engineering. 2008;134(5):758-68.

Voon KC. In-plane seismic design of concrete masonry structures. PhD Thesis, The University of Auckland; 2007.

Vulcano A, Bertero VV. Analytical models for predicting the lateral response of RC shear walls: Evaluation of their reliability. Earthquake Engineering Research Center, University of California at Berkeley; 1987.

Yun YM. Nonlinear strut-tie model approach for structural concrete. ACI Structural Journal. 2000;97(4):581-90.

Zeris CA, Mahin SA. Analysis of reinforced concrete beam-columns under uniaxial excitation. ASCE Journal of Structural Engineering. 1988;114(4):804-20.

Zhao J, Sritharan S. Modeling of strain penetration effects in fiber-based analysis of reinforced concrete structures. ACI Structural Journal. 2007;104(2):133.

Zienkiewicz OC, Taylor RL, Taylor RL, Taylor RL. The finite element method: solid mechanics. Butterworth-heinemann; 2000.

Zucchini A, Lourenço PB. A micro-mechanical model for the homogenization of masonry. International journal of Solids and Structures. 2002;39(12):3233-55.